UNIVERSITY OF OKLAHOMA

GRADUATE COLLEGE

SELECTIVE HYDRODEOXYGENATION OF BIOMASS-DERIVED COMPOUNDS OVER PROMOTED METAL OXIDE CATALYSTS

A DISSERTATION

SUBMITTED TO THE GRADUATE FACULTY

in partial fulfillment of the requirements for the

Degree of

DOCTOR OF PHILOSOPHY

By

LAURA ALEJANDRA GOMEZ GOMEZ
Norman, Oklahoma
2023

Downloaded from SHAREOK. Persistent Handle URL: https://hdl.handle.net/11244/337705

SELECTIVE HYDRODEOXYGENATION OF BIOMASS-DERIVED COMPOUNDS
OVER PROMOTED METAL OXIDE CATALYSTS

A DISSERTATION APPROVED FOR THE
SCHOOL OF CHEMICAL, BIOLOGICAL AND MATERIALS ENGINEERING

BY THE COMMITTEE CONSISTING OF

Dr. Steven P. Crossley, Chair

Dr. Daniel E. Resasco

Dr. Lance L. Lobban

Dr. Bin wang

Dr. Daniel T. Glatzhofer

© Copyright by Laura Alejandra Gomez Gomez 2023
All Rights Reserved.

I would like to dedicate this dissertation to my family and friends, especially my mom, grandmother, and aunt, for their unconditional love and unwavering belief in me.

Acknowledgements

I would like to express my sincere gratitude to all the wonderful people who have been an integral part of my graduate student life and helped me achieve my dissertation. Your contribution and support have made this journey an enjoyable and unforgettable experience.

First and foremost, I would like to express my deepest gratitude to my academic advisor and mentor, Dr. Crossley, for his kindness, patience, and support throughout my academic journey. I will always be thankful for giving me the privilege and honor of being part of his group. Thanks for showing us the love of science and the beauty of catalysis, which has been inspiring. I am particularly grateful to him for his faith in my abilities, which has lifted my confidence and helped me become who I am today.

I would also like to express my deep appreciation to Dr. Resasco for allowing me to join his research group when I approached him in search of an opportunity as an undergraduate student. He did not hesitate to offer me a chance, and thanks to him, I am now achieving my doctorate. I would also like to thank him for his guidance and wonderful suggestion throughout my academic journey. You are truly an inspiration and a role model for all of us.

I am grateful to Dr. Lance Lobban and Dr. Bin Wang for their invaluable feedback and insights during my academic journey. I would also like to thank Dr. Daniel Glatzhofer for being part of my committee member.

I also want to thank Andrew D'Amico for his invaluable assistance and diligence with instruments and reactors. I am also grateful to the department staff for their help with purchasing and paperwork, which has ensured the smooth progress of my research.

I would especially like to thank all current and former research group members with whom I have had the pleasure t work and collaborate. Daniela, Ana, Caleb, Tram, Ismael, Han,

Ethan, Dai Phat, Ximo, Nilson, Nabihan, Thomas, Phoung, Yu Yan, Luis, Felipe, Redwan, Valeria, Santiago, Monica, Lawrence, Reda, Mali, Diken, and Gengnan, thank you for your help, support, and enjoyable friendship.

I would like to express my gratitude to all my friends who have been crucial to my journey here in the USA. You have all been there for me in different ways and have supported me in ways I cannot express in words. Cristian, Gio, Shangshuang, Wen, Ziqui, Elena, Alex, Paul, Pabel, Daniel, Jiang, Yuli, and Feshua, I thank you for the lovely friendship, deep conversations, companionship, and unwavering support throughout my career.

I feel incredibly grateful to my family, whose unconditional love, understanding, and support have been instrumental in getting me to where I am today. Their unwavering presence in my life is a constant source of blessings, and I cannot thank them enough for their amazing support. Your encouragement and inspiration have been invaluable to me, and I am truly grateful to have you all in my life.

I want to thank the National Science Foundation for funding my work and the University of Oklahoma for the opportunity to contribute to academia.

Finally, I would like to express my gratitude to all my friends and individuals who provided valuable assistance during my time at OU. Your support has been truly appreciated, and I apologize for not being able to acknowledge everyone by name.

Contents

Acknowledgements v

List of Tables xii

List of Figures xiii

ABSTRACT xxi

CHAPTER I 1

A. Introduction 1

A.1.1 Furfural upgrading 3

A.1.2 Ring opening of γ-valerolactone (GVL) to produce pentenoic acids 6

A.1.3 Selective HDO: A promising technique for upgrading biomass 8

A.1.4 Active sites on reducible metal oxides 9

A.1.5 Hydrogen spillover 13

CHAPTER II 16

B. Selective reduction of carboxylic acids to aldehydes over MoO_3 catalysts 16

B.1 Introduction 16

B.2 Experimental section 19

B.2.1 Chemical and catalyst materials 19

B.2.2. Catalyst synthesis 19

B.2.3 Kinetic measurements 20

B.2.4 Pulse reaction experiments 21

B.2.5 Catalyst characterization 22

B.2.6 DFT Calculations 25

B.3 Results 25

B.3.1 Pentanoic acid conversion over MoO_3 catalysts 25

B.3.2 Influence of metal cluster (Pt) over MoO_3-based catalysts 28

B.3.3 Catalytic activity for HDO using a promoted MoO_3 catalyst 34

B.3.4 Density functional theory study for pentanoic acid over MoO_3 41

B.3.5 Role of intermediate hydrogen pulses on acid conversion chemistry 44

B.4 Conclusions 46

CHAPTER III 48

C. Revealing the mechanistic details for the selective deoxygenation of carboxylic acids over dynamic MoO_3 catalysts. 48

C.1 Introduction 48

C.2 Experimental section 50

C.2.1 Chemical and catalyst materials 50

C.2.2 Catalyst synthesis 51

C.2.3 Kinetic measurements 51

C.2.4 Catalyst characterization 52

C.3 Results 52

C.3.1 Inhibition effect of pentanoic acid (PA) 52

C.3.2 H_2 effect on reaction order 57
C.3.3 Water inhibition 58
C.3.4 Site requirements for deoxygenation of carboxylic acids 59
C.3.5 Elementary steps and reaction mechanism 61
C.4 Conclusions 67
CHAPTER IV 69
D. Quantifying the influence of surface and subsurface H on selective C-O bond scission rates over MoO_3-x catalysts 69
D.1 Introduction 69
D.2 Experimental section 72
D.2.1 Chemical and catalysts materials 72
D.2.2 Catalyst synthesis 72
D.2.3 Oxygen chemisorption experiments 72
D.2.4 Kinetic measurements 73
D.2.5 Catalyst characterization 73
D.3 Results 74
D.3.1 Partially reduction of MoO_3 74
D.3.2 Quantification of oxygen vacancies 75
D.3.3 Quantification of hydrogen molybdenum bronzes 78
D.3.4 Oxidation kinetics of partially reduced MoO_3-x 81

D.3.5 Reaction order with respect to O_2 82

D.4 Conclusions 86

D.5 Future work 86

CHAPTER V 88

E. Use of carbon nanotubes hydrogen highways to identify active sites over bifunctional catalysts. 88

E.1 Introduction 88

E.2 Experimental 90

E.2.1 Chemicals and catalysts materials 90

E.2.2 Catalyst synthesis 91

E.2.3 Characterization 93

E.2.4 Kinetic measurements 94

E.3 Discussion 95

E.3.1 Evidence for hydrogen spillover 96

E.3.2 Furfural conversion over Pd/TiO_2: Metal-support interfaces sites 98

E.3.3 The promoting effect of Cu on anisole conversion over TiO_2 catalysts 100

E.3.4 Promoter effect in the deoxygenation of pentanoic acid over Pt/MoO_3 102

E.5 Conclusions 106

CHAPTER V 107

F. Vapor-phase ring rearrangement of furfural to cyclic over Ru/TiO_2 catalyst 107

F.1 Introduction 107

F.2 Experimental 109

F.2.1 Chemicals and catalysts materials 109

F.2.2 Catalyst synthesis 110

F.2.3 Synthesis different catalysts on opposite ends of CNTs 111

F.2.4 Characterization 112

F.2.5 Kinetic measurements 112

F.3 Results 113

F.3.1 Reaction of pure furfural over Ru/TiO_2 113

E.3.2 Role of water for furfural conversion to cyclopentanone (CPNO) 115

F.3.3 Active sites responsible for the conversion Ru/TiO_2 and Pd/TiO_2 117

F.4 Conclusions 124

REFERENCES 125

List of Tables

Table 1. Rate expression for each potential rate-determined step. 63

Table 2. Oxygen vacancy titration measures the CO or O_2 uptake at a low temperature over 0.05 wt% Pt/MoO_3..... 78

Table 3. Rate of products normalized per exposed metal, support, or metal-support perimeter. 119

Table 4. Yield of products for reactions feeding different possible intermediates for the ring rearrangement. 121

Table S1. Binding energies of Mo (3d) doublet for Mo^{4+}, Mo^{5+}, and Mo^{6+} and Pt (4f) doublet for Pt^0 as determined by XPS characterization…….. 149

Table S2. External Mass transfer limitation test. Conditions for experimental test for external mass transfer limitation..... 152

Table S3. Oxygen chemisorption uptake and hydrogen bronzes using Pt/MoO_3 with different loadings of Pt. 165

Table S4. Binding energies of Mo 3d doublet for $Mo^{4+,}$ Mo^{5+}, and Mo^{6+} as determined by XPS characterization. 168

Table S5. Weight percentages of all deposited metals on Pt/CNT/MoO_3 and Pt/MoO_3/CNT. 170

List of Figures

Figure 1. Different conversion routes of lignocellulosic biomass to high-value chemicals.[2,3,14,15] 2

Figure 2. Furfural Conversion to various value-added chemicals and biofuels. The green, red, blue, and black arrows indicate hydrogenation, hydrogenolysis, decarbonylation, and ring-opening reactions.[16] 3

Figure 3. Mechanism of the furfural conversion to cyclopentanone.[22,23] 6

Figure 4. GVL ring opening to pentenoic acids and 1-butene via proton-mediated elementary steps.[28] 7

Figure 5. Schematic representation of the molybdenum oxide redox cycle involved in the hydrodeoxygenation of acetone. [33] 9

Figure 6. Different actives sites present on Ru/TiO_2.[41] 10

Figure 7. The selectivity towards acetaldehyde of some oxides with and without platinum.[42] 12

Figure 8. An adapted hydrogen spillover schematic for reducible and no-reducible supports.[64] 13

Figure 9. Activity for HDO of pentanoic acid and product selectivity distribution for PA conversion at different reaction temperatures over MoO_3 26

Figure 10. Comparison of product distribution measured at the same conversion levels with different temperatures for MoO_3... 27

Figure 11. TPR results for MoO_3 and 0.05 wt% Pt/MoO_3 samples. 29

Figure 12. (a-b) STEM characterization of 0.05 wt% Pt/MoO_3, (c-d) FTIR spectra of CO adsorbed at 30ºC on Pt on MoO_3 prepared by incipient wetness impregnation. The

catalyst was pretreated at 150ºC in 10%CO/He for 30 min (c) 1 wt% Pt/MoO_3 and (d) 0.05% Pt/MoO_3.....30

Figure 13. XPS results of MoO_3 and 0.05 wt% Pt/MoO_3. (a) XPS analysis showing the Mo (3d) energy region of MoO_3 calcined, reduced, and 0.05 wt% Pt/MoO_3 composition on MoO_3 and doped catalyst. (b) XPS analysis showing the Pt (4f) regions for three different pre-reaction samples: non-reduced MoO_3, both MoO_3 and 0.05 wt% Pt/MoO_3 (c) Mo oxidation states (%) for MoO_3 and 0.05 wt% Pt/MoO_3. 32

Figure 14. (a) Activity for HDO of pentanoic acid and product selectivity distribution for PA conversion at different reaction temperatures over 0.05 wt% Pt/ MoO_3. (b) Dependence of product selectivity of PA conversion at various W/F using 0.05 wt% Pt/MoO_3 as a catalyst at 350 ºC.....34

Figure 15. Reaction rate and selectivity using different loading of Pt over MoO_3. 35

Figure 16. Rate consumption of PA varying temperature. Comparison of the rate conversion of PA using MoO_3 and 0.05 wt% Pt/MoO_3 in the temperature range 300-400 °C......37

Figure 17. Effect of selectivity to pentanal at different reduction pretreatments over MoO_3. **(a)** different reduction time when the catalyst is pre-reduced at 350 ºC **(b)** Different reduction temperatures when the catalyst is reduced for 1 h.....38

Figure 18. Product distribution at the same conversion levels for MoO_3 (320 °C) and 0.05 wt% Pt/MoO_3 (280 °C).....39

Figure 19. (a) Schematic of PA to PAL reaction over a hydrogen-covered Pt/MoO_3 surface. (b) Activation energy using MoO_3 and 0.05 wt% Pt/ MoO_3 as a catalyst. ……...40

Figure 20. (a) Reaction coordinate for the formation of PAL. (b) Activation energy using MoO_3 as a catalyst at different partial H_2 pressures. 42

Figure 21. (a) Effect of hydrogen suppression in the conversion of PA over MoO_3 in a flow system evaluated at 350ºC. 45

Figure 22. **(a)** Order of reaction with respect to PA over MoO_3. **(b)** Order of reaction with respect to PA using 0.05 wt% Pt/MoO_3 as a catalyst. 53

Figure 23. Order of reaction with respect to PA over MoO_3 at a different mass of catalyst.. 54

Figure 24. Activation energy comparison at a different partial pressure of PA over MoO_3. 55

Figure 25. Possible causes of inhibition at a high partial pressure of PA **(i)** Site competition for adsorbates over metallic Pt cluster on MoO_3, **(ii)** Hinder H_2 dissociation at oxygen vacancies on MoO_3, and **(iii)** H_2 spillover inhibition on MoO_3. 56

Figure 26. (a) Order of reaction with respect to H_2 using MoO_3 as a catalyst at low P_{PA}. **(b)** Order of reaction with respect to H_2 using MoO_3 as a catalyst at high P_{PA}. **(c)** Order of reaction with respect to H_2 over 0.05 wt% Pt/MoO_3 at low P_{PA}. **(d)** Order of reaction with respect to H_2 over 0.05 wt% Pt/MoO_3 at high P_{PA}. 58

Figure 27. Dependence of reaction rate on the partial pressure of water over (a) MoO_3 and (b) 0.05 wt% Pt/MoO_3. 59

Figure 28. Proposed elementary steps for the hydrogenation of PA over promoted MoO_3. (•) denotes metal site, (⊛) oxidized or heal O vacancy, (∅) reduced or empty O vacancy. All rates are represented as quasi-equilibrated steps, which will be decoupled with varying hypothesized kinetically relevant steps below. 62

Figure 29. Proposed mechanism for deoxygenation of carboxylic acid over Pt/MoO_3. 67

Figure 30.. XRD patterns during reduction of MoO_3 and 0.05 wt% Pt/MoO_3 in 100 ml/min of H_2 at different temperatures. (a) MoO_2 and (b) MoO_3 diffraction pattern of unreduced MoO_2 and MoO_3 for comparison. (c) MoO_3 reduced at 400 ºC, (d) MoO_3 reduced at 500 ºC, (e) 0.05 wt% Pt/MoO_3 reduced at 400 ºC, (f) 0.05 wt% Pt/MoO_3 reduced at 500 ºC, (g) 0.05 wt% Pt/MoO_3 oxidized at 350 ºC, (h) 0.05 wt% Pt/MoO_3 oxidized at 500 ºC..... 75

Figure 31. Oxygen (O_2 or O) uptake at different chemisorption temperatures over 0.05 wt% Pt/MoO_3..... 76

Figure 32. Hydrogen molybdenum bronzes formed over 0.05 wt% Pt/MoO_3.. 79

Figure 33. Activation energy for the oxidation of Mo^{5+} to Mo^{6+} species..... 81

Figure 34. Reaction order with respect to oxygen partial pressure (P_{O2}) for the partially reduced 0.05 wt% Pt/MoO_3 catalyst.. 83

Figure 35. Conversion of PA to 5-Nonanone over MoO_3 and 0.05 wt% Pt/MoO_3 treated under different reduction temperatures under H_2 gas. 84

Figure 36. Conversion of PA to PAL over 0.05 wt% Pt/MoO_3 and MoO_3.. 85

Figure 37. Metals and metal oxides deposited on opposing ends of a carbon nanotube. **(a)** Schematic depicting a metal (red) capable of dissociating hydrogen (yellow) onto a carbon nanotube where hydrogen can travel across to a metal oxide (blue). **(b)** SEM image of a nanotube forest with Pd and TiO_2 deposited on opposite ends through metal evaporation and after treatment in hydrogen for 1 h at 400 °C. (Scale bar in b indicates 15 micrometers). **(c–e)** Portions of the top, middle and bottom of the forest, respectively, at increased magnification. (Scale bar indicates from top to bottom 200,

500, and 250 nanometers). **(f–h)** EDS spectra corresponding to the locations indicated in c–e. 96

Figure 38. TPR profiles of CuO/CNT and Pd/CNT/CuO catalysts were performed with a flowing 5% H2/Ar stream at a ramp rate of 5°C/min. 97

Figure 39. Furfural conversion over Pd and TiO_2 catalysts supported on CNTs. T 99

Figure 40. Main reaction pathways for anisole and phenol conversion over MoO_3/ZrO_2. Green arrows—hydrogenolysis, blue arrows—hydrogenation.[157] 101

Figure 41. Anisole conversion over catalysts containing Cu and TiO_2. Sum of quantifiable products (cresol+ phenol) resulting from anisole conversion over Cu and TiO_2 catalysts supported on CNTs.. 102

Figure 42. Carbon nanotube with metal and metal oxide deposited at opposite ends. **(a)** An illustration of a metal (red) capable of dissociating hydrogen (yellow) onto a carbon nanotube where H atoms can travel across to a metal oxide (blue). **(b)** SEM image of a nanotube forest with Pt and MoO_3 deposited on opposite ends via metal evaporation. **(c–e)** Magnified portions of the top, middle, and bottom of the forest, respectively. (Scale bar indicates 1 micrometer for the images c-e) **(f–h)** EDS results corresponding to the locations indicated in c–e. 103

Figure 43. Pentanoic conversion over Pt and MoO_3 catalysts supported on CNTs. 105

Figure 44. (a) Reaction pathway of furfural conversion over Ru/TiO_2. **(b)** Furfural conversion and product yield with W/F over 4.4% Ru/TiO2 at 400 °C. 1 atm, TOS: 30 min. Carbon balance ~ 95% for all reactions. 113

Figure 45. Possible species on the surface during conversion of furfural. This picture was taken from [19] 115

Figure 46. Product distribution for pure furfural and furfural co-fed with water. 4.4% Ru/TiO_2 at 400 °C, 1 atm, and 30 min TOS. Conversion: 36 ± 2%. Carbon balance>94% for all reactions. 116

Figure 47. Product distribution for pure furfural and furfural co-fed with water. 4.4% Ru/TiO_2 at 400 °C, 1 atm, and 30 min TOS. Conversion: 36 ± 2%. Carbon balance>94% for all reactions. Product Yield for water/furfural (12:1 molar ratio) feed mixture over TiO_2, Ru/SiO_2, Ru/CNT, and Ru/TiO_2 catalysts W/F = 1.85h (TiO_2) and 0.13h (Ru/SiO_2 and Ru/TiO_2) and 0.39h(Ru/CNT) Conversion = 10% (TiO_2); 25%(5.3% Ru/SiO_2); 38% (4.4% Ru/TiO_2) and 37% (1% Ru/CNT) T = 400 °C, P = 1 atm, TOS = 30 mins. Carbon balance ~ 94% for all reactions..... 118

Figure 48. FAL conversion over Pd and TiO_2 catalysts supported on CNTs at controlled separations distances along the nanotube surface..... 122

Figure S1. Molar fraction of PAL and POL vs temperature..... 148

Figure S2. TGA-TPR profiles for **a)** MoO_3 and **b)** 0.05% Pt/MoO_3..... 149

Figure S3. Comparison of product distribution measured at the same conversion levels with different temperatures for 0.05% Pt/MoO_3.. 150

Figure S4. Order of reaction with respect to PA over MoO_3..... 150

Figure S5. (a) Adsorption of PA on MoO_3 defect site through hydroxyl group oxygen. **(b)** Adsorption of PA on MoO_3 defect site through carbonyl-group oxygen..... 151

Figure S6. Transition state for the conversion of PA to PAL over MoO_3 defect site through hydroxyl group (-OH) at an oxygen vacancy. 151

Figure S7. Product yield for the conversion of PA over MoO_3 using a micro-pulse reactor.. 152

Figure S8. Flow diagram for pulse system. 153

Figure S9. STEM characterization of 0.05% Pt/MoO_3..... 154

Figure S10. TEM particle size distribution of 0.05% Pt/MoO_3 catalyst pre-reduced at 400 ºC for 1 h before imaging. 155

Figure S11. Comparison of the rate conversion of PA by using MoO_3 and MoO_2 as a catalyst. 155

Figure S12. DFT calculated reaction profile for PA with the carbonyl group adsorbed at an oxygen vacancy.. 156

Figure S13. (a) Rate vs. time on stream comparison of pentanoic acid over MoO_3 and 0.05% Pt/MoO_3. **(b)** Deactivation profile for MoO_3 and 0.05% Pt/MoO_3. 156

Figure S14. Reaction order with respect to PA over MoO_3 at 320 °C. 157

Figure S15. Conversion of PA over MoO_3 without H_2 pre-treatment. 157

Figure S16. Propose elementary steps for the hydrogenation of PA over promoted MoO_3……...158

Figure S17. Oxygen chemisorption at different temperatures over 0.05 wt% Pt/MoO_3. .. 163

Figure S18. Oxygen chemisorption over 0.05 wt% Pt/MoO_3 after different reduction temperatures..... 163

Figure S 19. MS signal spectrum for oxygen chemisorption over MoO_3. 164

Figure S20. MS signal spectrum for oxygen chemisorption over 0.05% Pt/MoO_3..... 164

Figure S21. SEM with EDX of a Pd/CNT/CuO forest after treatment in hydrogen for 1 hour at 400 °C. 166

Figure S22. Reaction feeding furfural over physical mixture Pd/CNT and TiO_2/CNT catalyst. 167

Figure S23. Furfural conversion (estimated based on disappearance of furfural) over Pd and TiO2 catalysts supported on CNTs……. 167

Figure S24. XPS results for (a) calcined MoO_3/CNT, and (b) MoO_3. 169

Figure S25. Proposed reaction mechanism for the furan ring rearrangement to cyclopentanone. 171

ABSTRACT

The pressing need to address environmental issues has led to a growing demand for cleaner and sustainable energy sources, such as biomass. Lignocellulosic biomass-derived bio-oil offers great potential for producing renewable chemicals and fuels. However, the complex nature of this mixture, characterized by a high oxygen content, makes it unstable and undesirable. Therefore, catalytic upgrading is required to improve its properties and remove unwanted components. In this dissertation, the author will utilize various model compounds to investigate the deoxygenation of biomass on highly active reducible metal oxides like MoO_3 and TiO_2.

The first part of the dissertation focuses on investigating the selective activation of renewable carboxylic acids using promoted molybdenum oxide (MoO_3) to form alcohols and aldehydes. This study used a combination of reaction kinetics, temperature programming reduction (TPR), and X-Ray photoelectron spectroscopy (XPS) to gain insights into the underlying mechanism. The findings suggest that the activity for HDO reaction scales with the concentration of Mo^{5+} species. Meanwhile, this study explores the effect of adding a small amount of Pt (0.05 wt%.) on the rate of selective deoxygenation. The outcomes demonstrate that adding Pt clusters results in a substantial decrease of 32 kJ/mol in activation energy required for the HDO reaction. Moreover, a kinetic study is performed to enlighten the understanding of the selective deoxygenation of carboxylic acid on promoted MoO_3 at mild temperatures, indicating that incorporating Pt clusters over MoO_3 shifts the reaction order with respect to hydrogen from 1 to 0.5 at a low partial pressure of pentanoic acid (PA). The inhibition effect of PA and its possible causes are discussed for both MoO_3 and 0.05 wt% Pt/MoO_3 catalysts.

Furthermore, the rapid dynamic changes in MoO_3 upon reduction and under reaction conditions were also investigated. A catalytic kinetic model is developed for redox chemistry on MoO_3, which considers the formation of hydrogen bronzes, phase transition, oxidation states, oxygen vacancies, hydrogen splitting and spillover, and oxygen mobility throughout the oxide. A micro-pulse reactor was employed to quantify the number of hydrogen bronzes and oxygen vacancies created after various pretreatments. The effect of hydrogen bronzes on MoO_3 for the deoxygenation of pentanoic acid is also investigated.

In the second part of this dissertation, carbon nanotubes were utilized to investigate the location of the active sites involved in the three different chemistries, including furfural, pentanoic acid, and anisole conversion. This novel catalyst was synthesized by depositing two different metals on different ends of the nanotube to decouple if the active sites were created either by promotor effects or short-range interactions between the two components in the bifunctional catalyst system. In all cases, a rapid hydrogen spillover observed across the nanotubes from one metal to another is considered.

Through the end of this dissertation, the conversion of furfural to cyclopentanone is studied, focusing on the role of water, the active sites involved, and the reaction mechanism over various catalyst supports. The study reveals that the selectivity for ring rearrangement versus C-O cleavage over Ru and Pd catalysts supported on TiO_2 can be adjusted by controlling the partial pressure of water. Additionally, the location of the active site and crucial kinetic pathways for this rearrangement reaction are discussed by utilizing the ability to synthesize carbon nanotubes with different properties.

CHAPTER I

A. Introduction

Among the renewable energy technologies available nowadays, lignocellulosic biomass is widely recognized as a promising renewable carbon source to produce fuels and commodity chemicals.[1–3] Biomass has the potential to contribute to the growing global energy demand and mitigate the global warming issues related to burning fossil fuels. When biomass is burned, it releases carbon dioxide (CO_2) into the atmosphere, just like fossil fuels. However, the carbon in biomass is part of a closed carbon cycle, where the carbon released during combustion is balanced by the carbon absorbed by new plant growth.[4,5] Thus, biomass can contribute significantly to a low-carbon energy system when produced sustainably and combined with other renewable resources and energy efficiency measures.

Lignocellulosic biomass is a type of biomass comprising cellulose, hemicellulose, and lignin, with varying proportions of each component depending on the source of the biomass. Sugars constitute over 50% of lignocellulosic biomass and can be converted into valuable platform molecules, such as hydroxymethylfurfural, levulinic acid, and furfural, through dehydration in aqueous solutions. These based compounds possess significant potential to produce high-value chemicals, fuels, and polymers.[1–3,6,7] Levulinic acid (LA), for instance, can be obtained from fructose by hydrolyzing hydroxymethylfurfural (HMF) under acidic aqueous conditions, as is illustrated in **Figure 1**. Moreover, LA in an aqueous-phase solution can be transformed into γ-valerolactone (GVL), which can undergo ring opening to produce a mixture of unsaturated carboxylic acids [6–11] or ketonic decarboxylation to generate large symmetrical ketones. [12,13]

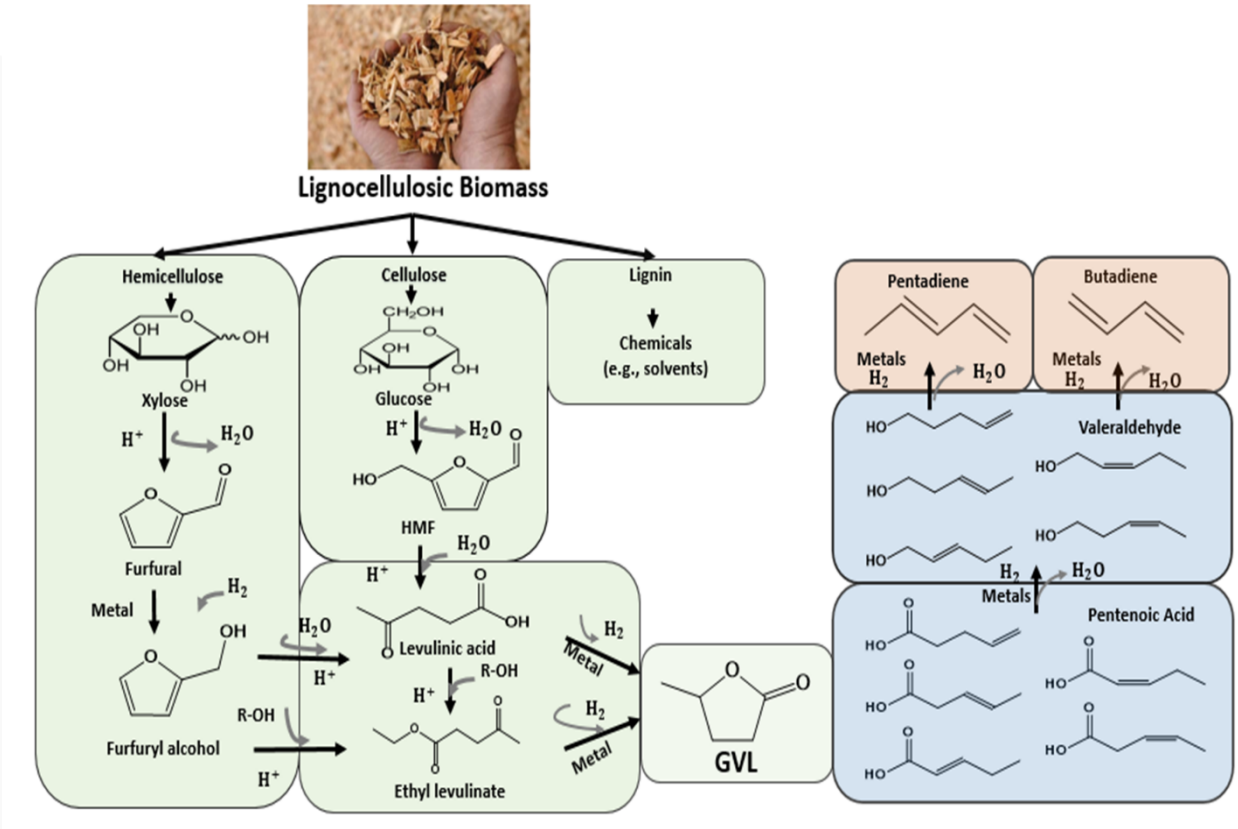


Figure 1. Different conversion routes of lignocellulosic biomass to high-value chemicals.[2,3,14,15]

Pentanoic acid, furfural, and anisole are common examples of oxygenated compounds derived from biomass. Pentanoic acid deoxygenation is challenging due to the stability of its carboxyl group, while furfural is a highly reactive compound that can lead to polymerization reactions. This dissertation aims to investigate the catalytic conversion of these oxygenated compounds over metal oxides such as TiO_2 and MoO_3 and determine the active site responsible for their conversion. In addition, kinetic studies will also be conducted to gain insights into the underlying mechanism governing the deoxygenation reactions. This chapter provides crucial background information necessary to understand better the research conducted in this dissertation.

A.1.1 Furfural upgrading

Furfural (FAL) is a particularly attractive building block compound derived from lignocellulosic biomass. However, one of the main challenges associated with FAL as a feedstock for catalytic upgrading processes is that the number of carbons in a FAL molecule is too low after deoxygenation to be blended with gasoline as a fuel. Additionally, furfural is highly reactive and thermally unstable, which can lead to rapid polymerization and humin (carbon-based macromolecular substance, polymer-like) formation. Therefore, the possibility of converting FAL in the dilute vapor phase before condensing in the liquid phase can significantly increase yields and improve the characteristics of the final product. **Figure 2** illustrates different pathways for upgrading furfural into more stable and valuable products.[16]

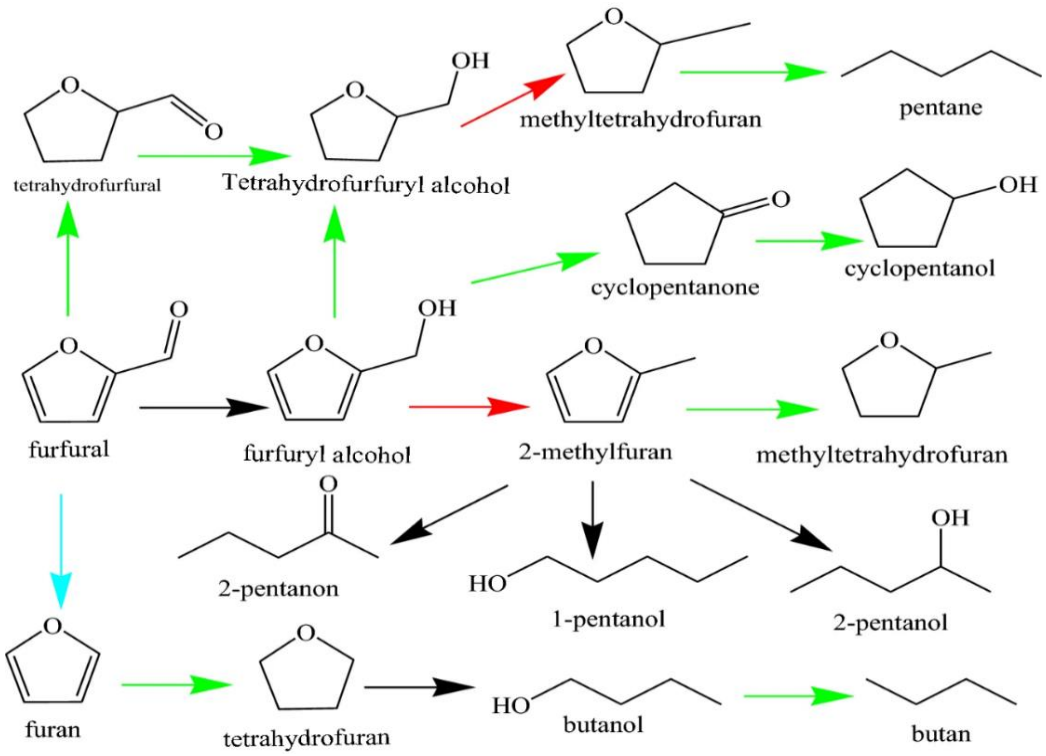


Figure 2. Furfural Conversion to various value-added chemicals and biofuels. The green, red, blue, and black arrows indicate hydrogenation, hydrogenolysis, decarbonylation, and ring-opening reactions.[16]

A.1.1.1 Hydrogenation of furfural to furfuryl alcohol (FOL)

Hydrogenation of furfural to furfuryl alcohol (FOL) is one of the key pathways for the catalytic upgrading of furfural. FOL is a high-value chemical with a wide range of industrial applications, including as a solvent, a flavor and fragrance intermediate, and a monomer for producing resins and polymers. Copper chromium catalysts are commercially available for this chemistry; however, their low efficiency and high toxicity have limited their use. Sitthisa et al. demonstrated that Cu, Pd, and Ni metals supported on SiO_2 were all active for the hydrodeoxygenation of furfural to FOL. However, Cu showed the highest selectivity towards FOL formation compared to Pd and Ni. They showed that the weak interaction of furfural with the Cu surface enables facile hydrogenation of the C=O bond while avoiding over-hydrogenation of the ring.[17,18]

A.1.1.2 Furfural to methylfuran

Methylfuran (2MF) is a desirable molecule for fuel production, as it has high octane number and low water solubility, making it a good candidate for blending with gasoline. Additionally, it has applications in the production of perfume intermediates, fine chemicals, and medicine. 2MF can be produced through two main pathways: hydrogenation of FAL to FOL, followed by further hydrogenolysis of the C-O bond of FOL, or direct decarbonylation of FAL. Resasco et al. have shown that combining metals with oxophilic sites, such as Ni-Fe alloys, can facilitate the selective cleavage of the C-O bond of furfuryl alcohol, leading to the production of 2MF. The oxophilic nature of the Fe sites makes the di-bonded η2(C, O)-aldehyde more stable on the surface, which weakens the C-O bond of the FOL and facilitates its hydrogenolysis.[19]

A.1.1.3 Furfural decarbonylation to Furan (FUR)

Furan is widely used as a starting material for the synthesis of a variety of chemicals and materials, including pharmaceuticals, agrochemicals, polymers, and resins. Furan can be produced from the decarbonylation of furfural. This reaction is typically carried out under high-temperature and high-pressure conditions in the presence of a metal catalyst, such as copper, nickel, palladium, or platinum. Wang et al. synthesized a core-shell Pd@Si-MFI catalyst that demonstrated high selectivity toward furan (98.7%). This catalyst combines the advantages of highly dispersed metal particles and zeolite's microporous properties. In contrast, Pd/Si-MFI showed lower selectivity towards furan than core-shell Pd@Si-MFI, which could be attributed to the aggregation of Pd nanoparticles and a lack of confined space for the catalytic reaction.[20]

A.1.1.4 Ring rearrangement of furfural to 2-cyclopentenone and cyclopentanone

The ring rearrangement of furfural is a common transformation that involves the conversion of FAL into 2-cyclopentenone (2CPNE) and/or cyclopentanone (CPNO). This reaction is important because both 2CPNE and CPNO are valuable building blocks for the synthesis of various organic compounds, including pharmaceuticals and natural products. Currently, furfural is converted to 2CPNE and CPNO in the aqueous phase via the Piancatelli mechanism, a desired reaction since it does not reduce the number of carbons in the molecule. However, before FAL conversion in the liquid phase to 2CPNE/CPNO, a humin condensation reaction can occur, promoting polymerization reactions.

Numerous studies have investigated Cu-based catalysts for their ability to convert FAL into 2CPNE/CNPO. These catalysts have demonstrated a high FAL conversion yield, typically 60-80%. Other studies have also shown promising results with Pd-Cu and Ni-

Cu/SBA-15 bimetallic catalysts.[21] Additionally, Hronec et al. demonstrated that the presence of furfural in water inhibited the formation of THFA, and instead, CPNO conversion is favored over Ni-Fe/SBA-15 at reaction temperatures of 140-190 ºC.[22]

The conversion of FAL to CPNO typically proceeds through several steps.[22,23] Initially, furfural is hydrogenated over metallic Pd sites to form furfuryl alcohol. The furan ring in FOL is then attacked by a water molecule, forming the FAL oxycation intermediate. This specie undergoes a Piancatelli rearrangement to form 4-hydroxy-cyclopentenone, which loses a water molecule through dehydration. The resulting 2CPNE intermediate is hydrogenated in the final step, producing CPNO. **Figure 3** illustrates the proposed mechanism.[24–27]

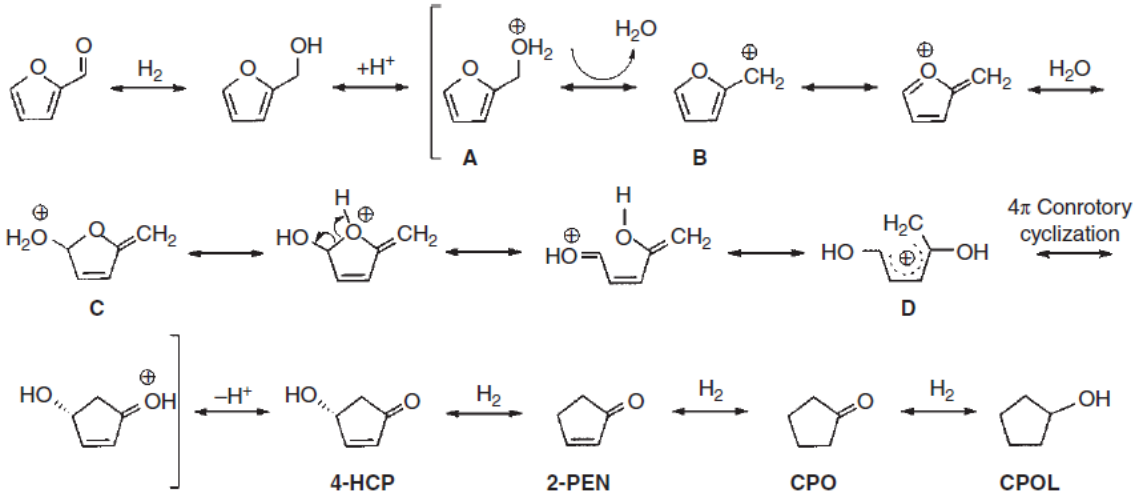


Figure 3. Mechanism of the furfural conversion to cyclopentanone.[22,23]

A.1.2 Ring opening of γ-valerolactone (GVL) to produce pentenoic acids

The conversion of γ-valerolactone (GVL) to pentenoic acids through ring-opening is a critical process in biomass valorization facilitated by heterogeneous acid catalysts. This reaction pathway enables the production of a range of chemicals and fuels. This platform molecule has significant potential for sustainable development as it can serve as the building

blocks for a wide range of products. The ring-opening can occur on bifunctional catalysts such as Pt/SiO_2 on H-ZSM-5, which have both acidic and hydrogenation properties.

Figure 4 shows the proposed mechanism for the GVL ring opening to pentanoic acids and 1-butene.[14] Bonds et al. conducted a microkinetic analysis of the ring-opening of GVL to produce pentenoic acids, which proceed via proton-mediated elementary steps on the surface of Bronsted sites. These steps, including ring-opening, hydride shift, deprotonation, and decarboxylation, occur simultaneously and lead to the formation of the final products. The formation of a carbenium ion intermediate in the C4 position during the GVL ring opening is followed by the conversion of the intermediate into various isomers of pentenoic acids through hydride shifts. Further deprotonation of these isomers produces stable pentenoic acid isomers.[28]

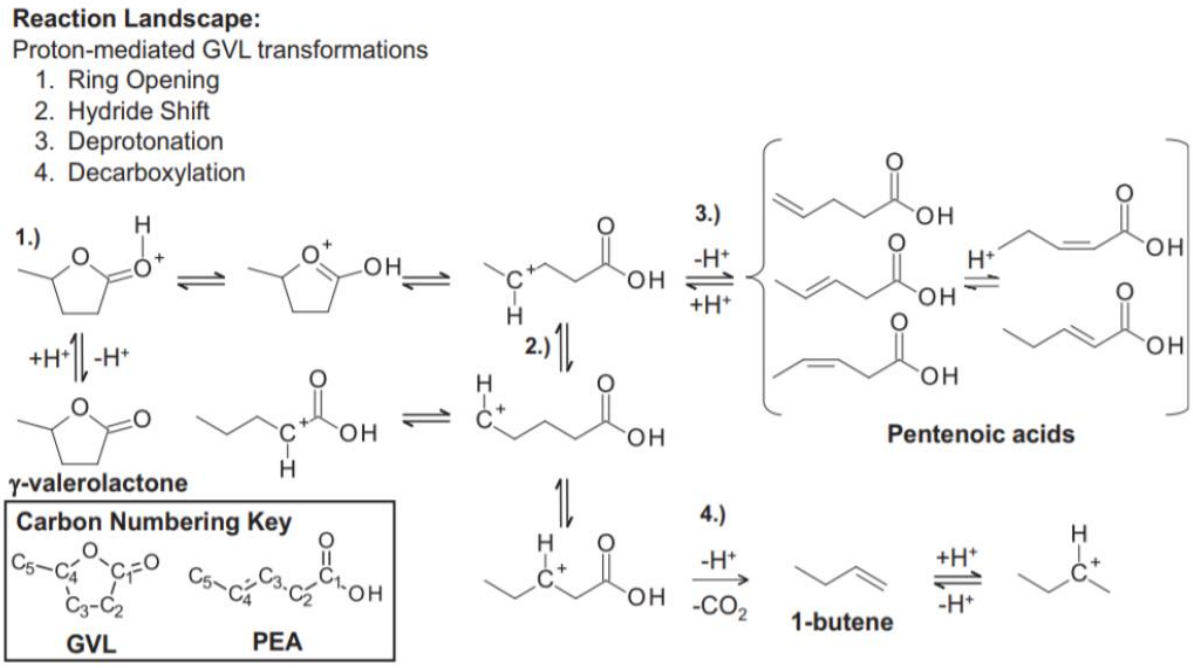


Figure 4. GVL ring opening to pentenoic acids and 1-butene via proton-mediated elementary steps.[28]

A.1.3 Selective HDO: A promising technique for upgrading biomass

The high oxygen content of lignocellulosic biomass has presented a significant challenge for developing efficient and sustainable processes for producing transportation fuels.[2,15] Therefore, biomass upgrading into tailor-made fuels involves oxygen removal to lower the energy density and stability of the resulting fuels.[13] To address this challenge, hydrodeoxygenation (HDO) is an attractive catalytic route for selectively removing oxygen from biomass-derived oxygenated compounds without perturbing other chemical functionalities.[29] The efficiency of the HDO process can be affected by several factors, including the specific metal oxide catalyst used, the reaction conditions (e.g., temperature, pressure, etc.), and the composition and structure of the biomass feedstock.[30,31]

HDO process involves a range of reactions, including hydrogenation, hydrogenolysis, dehydration, decarbonylation, decarboxylation, and hydrocracking.[32] However, the type of reactions involved in HDO depends on the catalyst used to carry out these reactions. Noble metals are excellent catalysts for HDO, but their use requires high H_2 pressures promoting C=C bond hydrogenation, C-C breaking, ring opening, and other undesirable reactions. On the other hand, metal-oxide catalysts have received much attention since they are active and selective for C-O cleavage without further hydrogenation/hydrocracking reaction.[5] Besides, metal oxides offer several advantages over noble metal catalysts, including lower cost, greater abundance, and higher stability under reaction conditions. Some of the most widely studied metal oxide catalysts for HDO include molybdenum oxide (MoO_3),[33–35] tungsten oxide (WO_3),[36] titanium oxide (TiO_2),[37–41] and iron oxide (Fe_2O_3).[42,43]

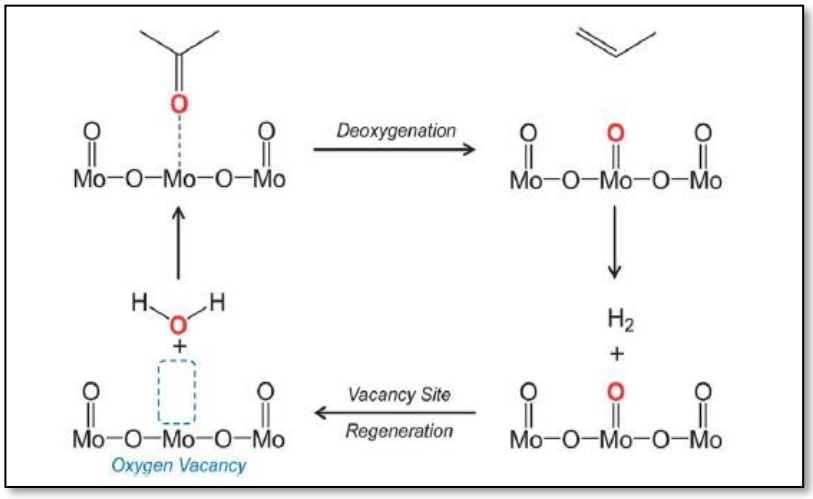


Figure 5. Schematic representation of the molybdenum oxide redox cycle involved in the hydrodeoxygenation of acetone. [33]

Prasomsri et al. have demonstrated that MoO_3 is an active and selective catalyst for converting biomass-derived compounds (ketones, aldehydes, and aromatic compounds) without promoting undesired reactions.[33–35,44,45] **Figure 5** shows the proposed mechanism of deoxygenation of acetone to propylene via the reverse Mar-van Krevelen mechanism,[33] where the oxygen atom from the reactants is abstracted by the lattice terminal oxygen vacancy, restoring the initial surface structure.[33,34,42,46]

Typically, reducible metal oxides are combined with other metals to increase the activity and selectivity of HDO. Adding noble metals to reducible supports can increase their reducibility and ability to form active sites. Vlachos et al. have demonstrated that doping TiO_2 with an ultralow loading of Pt increases the conversion of FOL to 2MF by two orders of magnitude compared to pure TiO_2.[47]

A.1.4 Active sites on reducible metal oxides

Oxygen vacancies are well accepted as the active sites for metal oxides, which can interact with oxygen-containing functional groups to facilitate C=O breaking.[48–53] The

surface properties of metal oxides are highly dynamic and strongly influenced by the specific environment, such as gas phase composition, pressure, and temperature. Shetty et al. showed that HDO of acetone to propylene occurs through an oxygen vacancy over MoO_3, as described in **Figure 5**.[33,34,54.] After each catalytic cycle, these active sites are regenerated with H_2 to produce water. Thus, an effective catalyst for HDO should have a balanced rate between C-O bond scission and oxygen vacancy regeneration to achieve high efficiency.

The addition of noble metal on reducible support can promote the formation of several catalytically active sites that can play various roles in catalyzing reactions.[55] The specific role of the metal in supported metal oxides depends on factors such as the nature of the metal, the metal-support interaction, and the specific reaction being catalyzed. **Figure 6** describes the possible active sites created by a metal and a reducible metal oxide interaction, mainly classified as short- and long-range metal interactions.

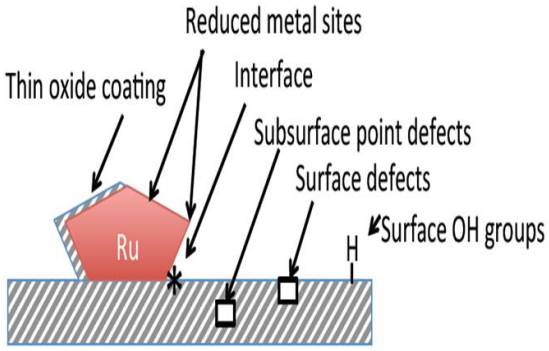


Figure 6. Different actives sites present on Ru/TiO_2.[41]

A.1.4.1 Short-range interactions

These interactions can occur between the two metals that are in proximity to each other and can lead to changes in the electronic and geometric properties of the active sites. Several studies have shown that catalytic activity can be enhanced due to the creation of highly active sites at the interface. Omotoso et al. demonstrated the critical role of active sites

created at the Ru/TiO_2 interface for the selective deoxygenation of m-cresol to toluene by changing metal loading, particle size, and support phases.[41] Similar study was conducted for the HDO reaction of phenol over a $Pd\text{-}Nb_2O_5/SiO_2$ catalyst, where different loading of niobium was incorporated to evaluate the role of the active sites at the interface. As a result, Telles et al. showed that the active sites located in the perimeter of $Pd\text{-}Nb_2O_5$ are responsible for activating the C-O bond.[56]

Another significant short-range type of interaction is the decoration of a thin film of oxide layer on the metal particle due to the strong metal support interaction (SMSI), which can decrease or increase the catalytic activity in some specific cases. Polo-Garzon et al. revealed that the synergistic effect on 2-propanol conversion over Pd/TiO_2 promotes catalyst deactivation due to the overcoating of Pd sites with the TiO_x layer during the rising reaction temperature.[57] In contrast, a promotional effect has been observed on the methanol synthesis from the hydrogenation of carbon dioxide over Pd/CeO_2 reduced at a high temperature.[58]

A.1.4.2 Long-range interactions

This type of metal interaction can be facilitated by hydrogen spillover, which promotes the formation of oxygen vacancies or defects on the oxide surface. To promote this interaction, it is beneficial to use a combination of a noble metal that can dissociate H_2 and metal oxide that can transport H species across its surface. The constant H supply promotes this interaction, enhancing the activity, selectivity, and stability of metal oxides for HDO chemistry.[59,60] For example, Pt over TiO_2 can promote the formation of actives sites on the support, increasing the conversion rate of FOL to 2MF.[47] Pham et al. have shown similar enhancements by incorporating Ru clusters over TiO_2. Ru clusters promoted the formation of Ti^{3+}, active sites for the ketonization of acetic acid over Ru/TiO_2.[13,37]

Ponec et al. conducted a series of studies related to the deoxygenation of carboxylic acid on metal oxide catalysts, and they found that the most effective metal supports for this process are those with intermediate metal-oxygen bond strength, which can be operated under the partially reduced surface, as indicated in **Figure 7**. [42,46,61] In addition, they studied the promoter effect of incorporating noble metal to increase reducibility of the metal oxides surface. **Figure 7** illustrates the effect of Pt as a promoter on the selectivity towards acetaldehyde of various oxides with and without Pt.[62] Less reducible oxides, such as TiO_2 and ZrO_2, highly increase the activity for deoxygenation with the addition of Pt clusters.[42] This suggests that the incorporation of noble metals can improve the reducibility of metal oxide surfaces, thereby increasing their activity for deoxygenation reactions.

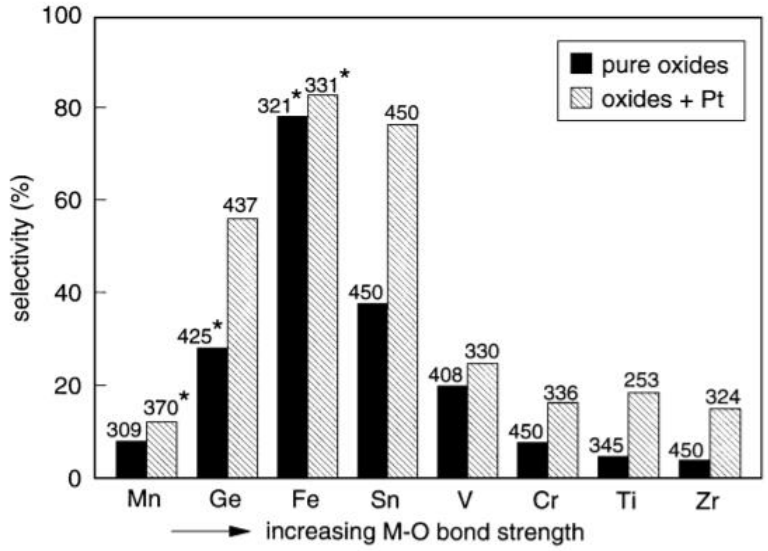


Figure 7. The selectivity towards acetaldehyde of some oxides with and without platinum.[42]

Surface OH groups are another type of long support interaction. These surface OH groups can also be involved in hydrogen bonding with reactants or intermediates, promoting the formation of crucial reaction intermediates or facilitating the transfer of protons or

electrons during the reaction cycle. Therefore, the presence of OH groups can contribute to reducing the activation barrier of rotational motions across the support.[63]

A.1.5 Hydrogen spillover

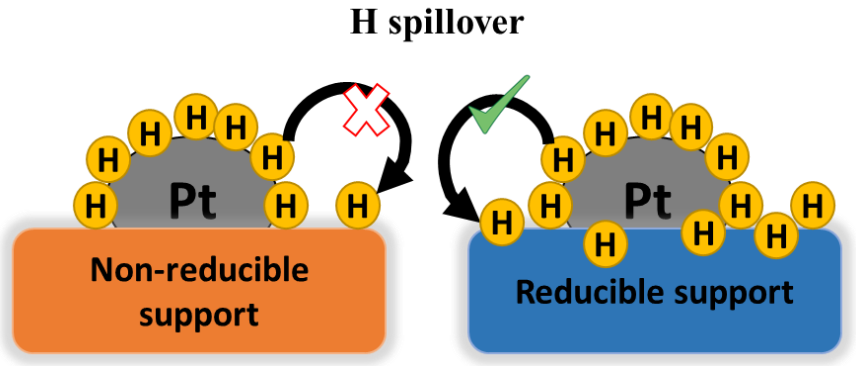


Figure 8. An adapted hydrogen spillover schematic for reducible and no-reducible supports.[64]

Hydrogen spillover is the surface migration of activated hydrogen atoms from a metal particle, on which H_2 is dissociated, to a nearby support material, such as an oxide.[65] This can lead to changes in the properties of the support material, including changes in its redox properties, acidity/basicity, and catalytic activity.[64] The interaction between the metal and support can affect the hydrogen binding energy on the metal surface, modifying its ability to migrate to the support, as described in **Figure 8**. Prins et al. have provided compelling evidence that hydrogen spillover can occur over reducible metal oxides, while non-reducible metal oxides pose significant energetic barriers to this process.[59,66,67] The possibility of hydrogen spillover on non-reducible oxides, such as Al_2O_3, is controversial, with some studies suggesting its presence.[68] However, hydrogen spillover on Al_2O_3 is only observed in the presence of carbonaceous deposits[69], structural defects [59] or OH groups[59,60,68,70], which can act as anchoring sites for hydrogen atoms, promoting their migration and facilitating the spillover process. Overall, two main conditions are required to observe hydrogen spillover

over a support, (i) the presence of metal capable of dissociating H_2; (ii) the presence of support capable of accepting active H species and transferring them through the support.[60]

A.1.5.1 Hydrogen spillover to reducible supports

The migration of hydrogen atoms from the metal surface to the oxide surface is facilitated by defects or oxygen vacancies in the oxide lattice, which serve as diffusion channels for the hydrogen atoms. The hydrogen spillover effect has been observed on a variety of metal oxide catalysts, including TiO_2, WO_3, MoO_3, and CeO_2.[59,60,67]

In a computational study, Chen et al. investigated the hydrogen spillover effect over Pt/MoO_3, where H atoms migrate from the metal clusters (Pt) into the support as a proton and electron with an activation energy of 36 kJ/mol. The desorbed H atom from the Pt cluster diffuses onto terminal oxygen to form an O-H bond at the substrate. The interaction between a hydrogen atom and the terminal oxygen (Ot) is electrostatically repulsive at the beginning of the process. However, when the H atom donates the electrons from its H-1s orbital to the O-2p orbital, it becomes a proton with a charge of +0.96. As a result, the oxygen atoms gain extra electrons, leading to the transition from repulsive O-H interactions to attractive proton-oxygen interactions along the migration pathway. This strong O-H bond interaction also changes the bond strength of Mo-O from 1.67 to 1.88 Å. [48,71–73]

Computational studies have revealed that the energy required for H species to hop into the terminal oxygen located within the surface layer is around 40-60 kJ/mol, which is higher than the activation energy of 6-12 kJ/mol associated with the diffusion of H atoms into the bulk of MoO_3.[48,71,73] Therefore, the migration of the proton and electron in the bulk of MoO_3 is easier than on the surface, which promote the formation of hydrogen bronzes ($HxMoO_3$) due to the extensive hydrogen bonding network in the crystalline lattice. The

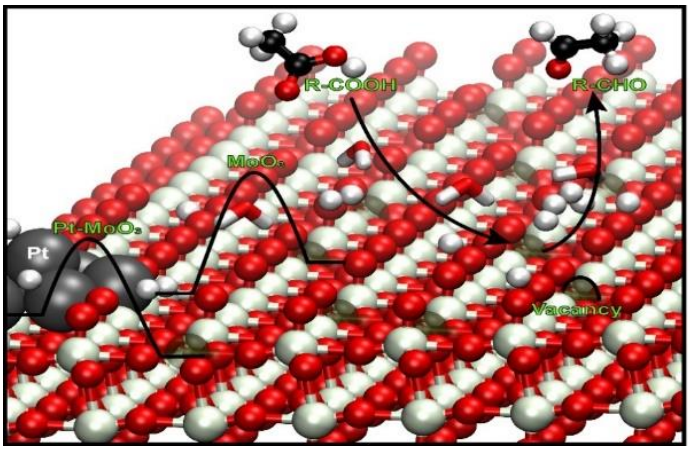
migration of H protons can also be facilitated through a hydrogen shuttle in the presence of water or alcohol. Similar observations have been made for WO_3.[74,75]

A.1.5.2 Hydrogen spillover to carbon nanotubes

Hydrogen spillover on carbon nanotubes offers a promising avenue for developing more efficient and cost-effective hydrogen storage and fuel cell technologies. The flux of H atoms generated in the metal site (Pt) flows onto the carbon-based material and continues diffusing throughout the substrate. Copper et al. have calculated that the binding energy of C-H is 80-140 kJ/mol on graphitic carbon materials, which indicates that the H_2 molecule cannot dissociate over carbon nanotubes materials since 435 kJ/mol is needed to break the H_2 bond.[76] Several studies have indicated that the mechanistic spillover phenomenon on a nanotube can occur both through chemisorption and physisorption. However, Chen et al. have concluded that the most feasible process for hydrogen spillover is through physisorption since the diffusion of chemisorbed H atoms requires C-H bond breaking, increasing the activation energy for H atom diffusion onto carbon nanotubes.[77] Hydrogen spillover is facile by the decoration of the carbon substrate with oxygen functionalities, leading to a faster H diffusion.[78]

CHAPTER II

B. Selective reduction of carboxylic acids to aldehydes over MoO_3 catalysts



Mallikharjuna R. Komarneni conducted the X-ray photoelectron spectroscopy (XPS) analysis, while Justin Marlowe and Dr. Phillip Christopher contributed to the analysis of CO-FTIR. Andrew D. D'Amico analyzed BET and chemisorption experiments, and Reda Bababrik, Taha Salavati-fard, and Dr. Bin Wang contributed to the DFT studies. The findings were published in ACS Catalysis in 2021.

B.1 Introduction

The reduction of carboxylic acids to form alcohols and aldehydes is a highly desirable process for producing fuels and commodity chemicals. One of the most well-known examples of this chemistry is the selective conversion of acetic acid to form ethanol, an essential commodity feedstock used as an additive in the food and fuel industry.[61,79] Another example is the selective deoxygenation of long-chain fatty acids and triglycerides, with the potential

to produce surfactants.[80] Carboxylic acids containing five carbon atoms, such as levulinic acid and pentanoic acid, are particularly interesting feedstocks for producing commodity chemicals obtained from renewable organic materials.

The most traditional chemical pathways for upgrading carboxylic acids into more desirable products are decarboxylation/decarbonylation reactions to produce non-oxygenated hydrocarbons (alkanes and alkenes) and coupling reactions to form ketones.[9–11,14] However, the low reactivity of carboxylic acids compared to the high reactivity of alkenes (at reaction conditions) often leads to rapid oligomerization, ultimately resulting in coke formation and subsequent catalyst deactivation. Furthermore, the production of shorter-length hydrocarbon chains and CO_2/CO as a byproduct is one of the main drawbacks of carboxylic acid upgrading via decarboxylation/ decarbonylation. An alternative pathway is carboxylic acid reduction via selective hydrodeoxygenation (HDO), preserving C-C bonds without disturbing other chemical functionalities.

Several catalysts have been proposed to deoxygenate carboxylic acids to produce aldehydes and alcohols. However, most of them rely on noble metals that are highly active for hydrogenation/dehydrogenation reactions, requiring high hydrogen pressures to limit rapid coke formation and shifting product distributions to fully saturated analogs.[81,82] Therefore, there is a need to develop an efficient and selective heterogeneous catalyst for carboxylic acid hydrodeoxygenation chemistry while minimizing side reactions such as coke formation, cracking reactions, and double bond saturation associated with most metals.[29,42,46]

As an alternative to high-pressure metal catalysts, highly oxophilic materials can reduce carboxylic acids to aldehydes. Even though these catalysts also favor coupling reactions via ketonization, fine-tuning surface conditions could inhibit these side reactions.[42,46] The

reduction with highly oxophilic supports carries the advantage of selective activation of the acid functional group without disturbances to other functional groups or shortening the hydrocarbon chain length. These two features are particularly important to forming multifunctional products from carboxylic acids (e.g., C-5).

Recently, Prasomsri et al. showed that molybdenum oxide (MoO_3) could perform hydrodeoxygenation selectively on aldehydes and alcohols, forming unsaturated products at low H_2 pressures.[33–35,44,45] The reaction was proposed to occur at the surface via a reverse Mars-van Krevelen-type mechanism, where the oxygen atom from the reactants is abstracted by the lattice terminal oxygen vacancy, restoring the initial surface structure. Hydrogen was used as a reducing agent to regenerate the oxygen vacancies, removing oxygen as H_2O.[33,45,83]

Although partially reduced MoO_3 has been proven to selectively deoxygenate ketones and alcohols via HDO,[33,34] reducing more challenging molecules such as long carbon chain carboxylic acids, to the best of our knowledge, has not yet been explored. Since MoO_3 demonstrates low relative rates for the hydrogenation of carbon-carbon double bonds, the possibility for selective conversion of unsaturated acids to highly valuable dienes could exist if selective acid deoxygenation chemistry over these catalysts was established. The intriguing affinity to selectively cleave C-O bonds over MoO_3 surfaces without subsequent hydrogenation of formed products makes this an excellent material to explore for selective acid reduction.

Here we report the promising activity of the MoO_3 catalyst for the selective conversion of pentanoic acid (PA) to pentanaldehyde (PAL) under atmospheric hydrogen pressure. The reducibility of MoO_3 is known to require high temperatures; therefore, the addition of very low loadings (0.05wt%) of Pt metal clusters to promote H_2 dissociation and spillover is

explored to promote enhanced deoxygenation while exploring consequential impacts on product selectivity.[84] We reveal that this low loading facilitates low-temperature activity of the catalyst while minimizing undesirable side reactions that may occur on the metal directly.

The results reported here demonstrated that MoO_3 and Pt/MoO_3 are promising catalysts for the selective reduction of carboxylic acids to aldehydes, exhibiting tradeoffs between rate and selectivity as temperature increases. X-ray photoelectron spectroscopy (XPS) was used to investigate the distribution of different oxidation states on the surface during the partial reduction of MoO_3 and 0.05 wt% Pt/MoO_3 catalysts to identify the active species responsible for the selective conversion. These were complemented with density functional theory (DFT) computational analysis that illustrates the complex transition state involved and the critical importance of surface hydrogen coverage on net reaction rates.

B.2 Experimental section

B.2.1 Chemical and catalyst materials

Pentanoic acid (99%, Sigma-Aldrich) was fed without further purification. H_2 (99.999%, Airgas), He (99.999%, Airgas), N_2 (99.998%, Airgas), and air (Ultra zero, Airgas) were used in the reaction experiments and characterization techniques. Commercial molybdenum (VI) oxide, MoO_3 (>99.5 wt%), was purchased from Alfa Aesar. The catalyst was mixed with acid-washed glass beads (50-70 US sieve, Sigma).

B.2.2. Catalyst synthesis

Supported 0.05% Pt over MoO_3 catalyst was prepared by incipient wetness impregnation method. For a batch of 10 g of supported catalyst, a 2 mL aqueous solution with 10 mg of tetraammineplatinum (II) nitrate (99.99%, 50% Pt, Alfa Aesar) was added dropwise to the support. After completing the previous step, the sample dried at 80 °C for 12 h and

calcined at 600 ℃ (ramp rate 10 ℃/min) under airflow (100 mL/min). Commercial MoO_3 was calcined under identical conditions. Before catalytic testing, the catalyst powders were pelletized and sieved to yield pellet sizes from 90 to 125 um (120-170 US sieve).

B.2.3 Kinetic measurements

The catalytic reaction experiments were conducted at atmospheric pressure in a vapor-phase packed-bed flow reactor system. A quartz tube of 0.25 inches OD was used as a reactor, placed in a vertical tube furnace (Thermcraft Inc., 1200W/115V). The reactor tube was connected to an inlet gas line at the top and an outlet gas line at the bottom. The MoO_3 catalyst bed was mixed with inert, acid-washed glass beads, packed between two layers of quartz wool inside the reactor, and situated in the furnace center. The catalyst was reduced by flowing 100 SCCM of H_2 through a quartz tube for 1 hour at 400 ℃. The liquid reactant was fed into the reactor via a syringe pump (KD Scientific) and vaporized (at 92-100 ℃) before entering the reactor. Pentanoic acid was mixed with heptane to avoid corrosion in the syringe and needle. The vaporized reactant was mixed with H_2 or H_2/He gas at the inlet of the reactor.

Each reaction experiment was conducted at 280-400 ℃ and atmospheric pressure. The outlet stream of the reactor was heated up to 250 ℃ to prevent any condensation of effluents. The products were quantified via an online gas chromatography (GC) system equipped with a flame ionization detector (FID), Agilent 6890, using an HP-INNOWAX column (Agilent, 60 m × 0.32 mm ID × 0.5 μm). The injection port and FID detector were heated up to 250 ℃. Product identification was analyzed by using a Gas Chromatography system Shimadzu QP-2010 GC-MS. The standard compound of each product was used to

determine the retention time, and they were quantified using relative response factors estimated based on the effective carbon number (ECN).

The reactions were run without external mass transfer limitations, demonstrated by a common experimental test, doubling the reactant flow rate and the catalyst mass while keeping partial pressure constant. This test allows higher velocity at the external surface while maintaining a constant contact time between the catalyst and reactant. Thus, if changes in conversion are observed, the apparent rate of reaction is affected by the rate of external mass transfer. The conversion should be identical in the absence of any mass transfer limitations (**Table S2**).

B.2.4 Pulse reaction experiments

The role of hydrogen was investigated by a micro-pulse reactor using helium as a carrier gas, as shown in **Figure S8**.[85] The pelletized catalyst (10 mg) was mixed with glass beads, packed in a quartz tube of 0.25 inches OD, and used as a reactor. Before the reaction, the catalyst was reduced by flowing 100 SCCM of H_2 through a quartz tube for 1 h at 400 ℃. The size of the loop was 1 mL. Pentanoic acid was diluted with helium or hydrogen in the sample loop and then sent over the catalyst bed. During the period between continuous pulses, the catalyst was exposed to helium flow. The outlet stream of the reactor was heated up to 250 ℃ to prevent any condensation of effluents. The products were quantified via an online gas chromatography (GC) system equipped with a flame ionization detector (FID), Agilent 6890, using an HP-INNOWAX column (Agilent, 60 m × 0.32 mm ID × 0.5 μm).

For vacancy characterization, the same micro-pulse reactor was connected to an atmospheric pressure gas analyzer (MKS, Cirrus 2) to quantify the oxygen uptake on the oxygen vacancies under similar reaction conditions. The catalyst was pre-reduced by flowing

100 SCCM of H_2 through a quartz tube for 1 h at 400 ℃. To remove all physically adsorbed hydrogen from the surface, the catalyst was exposed to helium gas at 350℃ for 2 hours. A 5 vol% O_2/He was pulsed over the catalyst sample until the oxygen saturation level was reached. The oxygen chemisorption was carried out at 350℃. The size of the loop was 1 mL. The identical procedure was performed for both MoO_3 and 0.05 wt% Pt/MoO_3 catalysts.

B.2.5 Catalyst characterization

B.2.5.1 X-ray photoelectron spectroscopy (XPS)

The surface analysis was conducted on a PHI 5800 ESCA multi-technique system equipped with a standard Aluminum (Al) kα X-ray source (1486.6 eV) and a hemispherical analyzer. The X-ray source was operated at 300 W (15 kV and 20 mA). Survey spectra (0 - 1400 eV) were collected with a pass energy of 187.85 eV. The core-level spectra of C (1s), O (1s), Mo (3d), and Pt (4f) were measured using a pass energy of 58.70 eV. The binding energy values were referenced to C (1s) peak at 284.8 eV. The core-level peaks were analyzed by PHI MultiPak (Version 9.5). All the catalysts were reduced at 400 ℃ under a hydrogen flow (100 mL/min) for 1 hour before XPS analysis. A sample transfer vessel (PHI Model 04-110) was used to transfer the ex-situ reduced samples from a glove bag to the XPS chamber to avoid exposure to air. The samples were mounted on sample stubs using double-sided conductive carbon tape. The surface composition was estimated from the integrated intensities and corrected by atomic sensitivity factors.

B.2.5.2 Temperature-programmed reduction (TPR)

The reduction temperature of the catalysts was measured by using a house-built system. The TPR experiments were carried out in a 0.25-inch quartz tube packed with 50 mg of the catalyst under a 5% v/v H_2 in Argon (Ar) with a total flow rate of 15 SCCM. The

temperature was increased to 1000 ℃ at a flow rate of 10 ℃/min and held at 1000 ℃ for 30 min. Hydrogen consumption was monitored as a function of temperature using an online SRI 110 thermal conductivity detector (TCD). A cold trap that mixes isopropyl alcohol and liquid nitrogen was used to condense the water evolved in the experiment before entering the TCD detector.

In addition, a temperature-programmed reduction was also performed in a Netzsch STA 449F1 equipped with a pin thermocouple and a Netzsch nanobalance. Outlet gases were measured by an Aeölos quadrupole mass spectrometer (QMS 403 C), scanning each mass from 2-20 amu to monitor the evolution of H_2O (m/z =18) and consumption of H_2 (m/z = 2). The temperature ramp used for this analysis ranged from room temperature to 550 ℃ with a rate of 2 ℃/min, and approximately 50 mg of catalyst was used for the analysis.

B.2.5.3 Carbon Monoxide Probe Molecule Infrared Spectroscopy (CO-FTIR)

In-situ DRIFTS experiments were performed in a high-temperature reaction cell (Harrick Scientific) equipped with ZnSe windows. The in-situ cell was mounted inside a Praying Mantis diffuse reflectance accessory (Harrick Scientific) paired with a Thermo Scientific Nicolet iS10 FTIR spectrometer equipped with a HgCdTe (MCT) detector. Spectra were collected in absorbance units with a resolution of 4 cm^{-1} by merging between 64-256 individual scans to minimize spectral noise. Measurements were made while purging the FTIR and Praying Mantis unit with dry N_2 to minimize atmospheric gas interference with the beam path.

In a typical experiment, ~50 mg of catalyst was loaded atop a bed of inert SiO_2 (US Nano, 20-30 nm) to reduce overall catalyst consumption. The catalyst was then oxidized at 250 ˚C for 1 h by ramping at 10 ˚C/min in a pure flow of O_2 (Airgas, 99.999%) at 30 SCCM.

After cooling in O_2 flow to 30 ˚C, the catalyst was purged in Ar (Airgas, 99.999%) at 50 SCCM for 10 minutes, and then a background scan was taken. Then, the catalyst was ramped to 150 ˚C at 10 ˚C/min. Once the catalyst reached 150 ˚C, the atmosphere was switched to 10% CO/Ar (Airgas) at 50 SCCM and held at 150 ˚C for 30 minutes. The catalyst was then cooled down to 30 ˚C in 10% CO/Ar before purging with Ar at 50 SCCM for 10 minutes to collect the final spectrum of adsorbed CO. This pretreatment was found to be highly effective for promoting CO adsorption on the sample as both oxidation in pure O_2 and reduction in pure H_2 led to significant and complete suppression of CO adsorption.

B.2.5.4 Scanning Transmission Electron Microscopy (STEM)

STEM was performed on a JEOL Grand ARM at UC Irvine operated at 300 kV. The STEM was employed to estimate the distribution of Pt particle sizes. A lacey Formvar film with the lacey structure enforced by a heavy carbon coating was utilized to load the sample (Lacey Formvar/Carbon, 300 mesh, Copper approx. grid hole size: 63µm). Dry loading was employed as a loading method, where two silica slides break down the samples and load them directly to the grid. Compressed air was used to remove the excess loose particles.

B.2.5.5 BET Surface Area

The BET surface area was calculated from isotherms measured with Micromeritics ASAP 2020. Approximately 2 grams of each catalyst were pretreated at 400 ˚C in a vacuum for 1.5 h before the adsorption analysis. The isotherms were measured at 77 K using nitrogen as the adsorptive. The BET surface area was calculated using isotherm data in the relative pressure range of $0.05 < P/P_o < 0.3$.

B.2.6 DFT Calculations

The α-MoO_3 surface was modeled using a three-dimensional periodic bulk supercell (4 x 1 x 4) separated by an 18 Å vacuum region. The bottom Y layers of MoO_3 were fixed at their bulk positions, while the top Y layers were fully relaxed. DFT calculations were carried out using the VASP package.[86] The Perdew-Burke-Ernzerhof generalized gradient approximation exchange-correlation potential (PBE-GGA) was used,[87,] and the electron-core interactions were treated in the projector augmented wave (PAW) method.[81,88] Structures were optimized until the atomic forces were smaller than 0.02 eV $Å^{-1}$ with a kinetic cutoff energy of 400 eV. The van der Waals interactions were considered using the DFT-D3 semi-empirical method.[82] Transition state structures and energies were determined using the Climbing Image Nudged Elastic Band[89,90] and dimer methods.[91] The surface Brillouin zone was sampled with a single k point at Gamma. The adsorption energy (E_{ad}) of the adsorbate was calculated using the equation below:

$$E_{ad} = E_{adsorbate-surface} - (E_{adsorbate} + E_{surface}) \quad \text{Eq. 1}$$

B.3 Results

B.3.1 Pentanoic acid conversion over MoO_3 catalysts

Pentanoic acid (PA) conversion over MoO_3 catalysts was evaluated at different temperatures in a fixed bed flow reactor under atmospheric hydrogen pressure. The conversion and product distributions are shown in **Figure 9**. All conversions and rates reported here were obtained after extrapolating rates to an initial time on stream (TOS) to mitigate any effects of catalyst deactivation on reported rates. Under the wide temperature range studied, conversion of PA over MoO_3 exhibits very high selectivity to pentanal (PAL>80%). Moreover, low selectivities to decarbonylation and C-O hydrogenolysis products were observed, even at the

highest conversion levels tested. The competing ketonization reaction to yield 5-nonanone was also detected in small quantities at higher reaction temperatures. Alcohols were not produced at the highest reaction temperatures tested, as confirmed by the thermodynamic analysis carried out using Aspen Plus V12, as described in **Figure S1**. However, rapid dehydration to yield C-5 hydrocarbons would be expected if they were formed in equilibrium quantities. This suggests that subsequent hydrogenation of the generated products is kinetically unfavorable under the wide range of conditions reported here. Given the well-documented potential of MoO_x catalysts for the deoxygenation of aldehydes, this selectivity could potentially arise via inhibition of subsequent aldehyde re-adsorption due to high acid coverages.

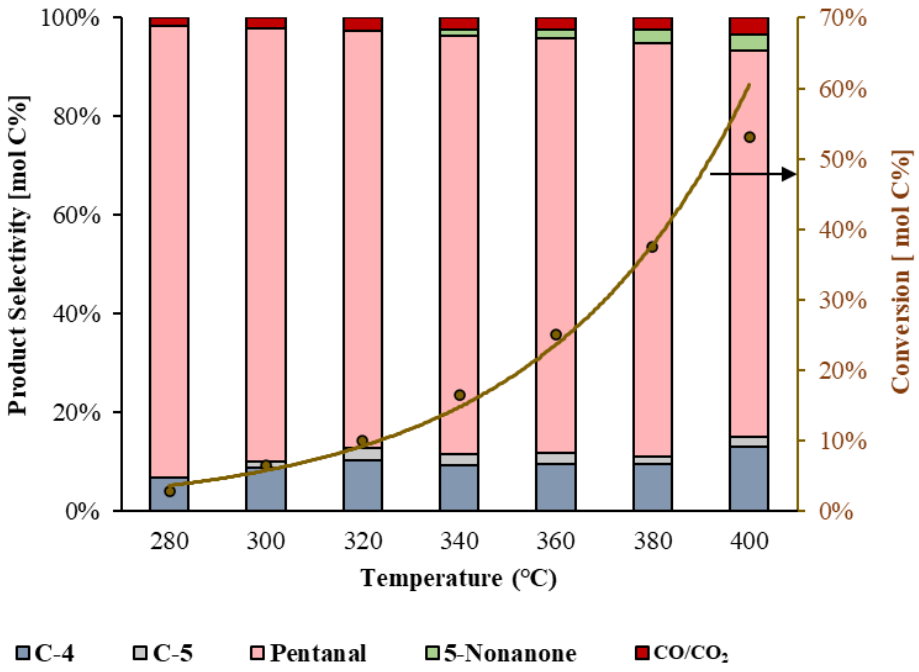


Figure 9. Activity for HDO of pentanoic acid and product selectivity distribution for PA conversion at different reaction temperatures over MoO_3. Reaction conditions: Flow of H_2= 30 mL/min, P_{Total}= 1atm, TOS= 0 min, and W/F= 0.11 g_{cat}/mL·h.

In addition to potential competition with the acid feed to inhibit undesired side reactions such as decarbonylation, inhibition of subsequent reactions due to the presence of

reaction products (e.g., H_2O) also appears to influence this chemistry. The role of product inhibition can be more clearly compared by evaluating product selectivity at iso-conversion levels (**Figure 10**), revealing that decarbonylation selectivity is a more significant function of temperature than depicted at varying conversion levels in **Figure 9**.

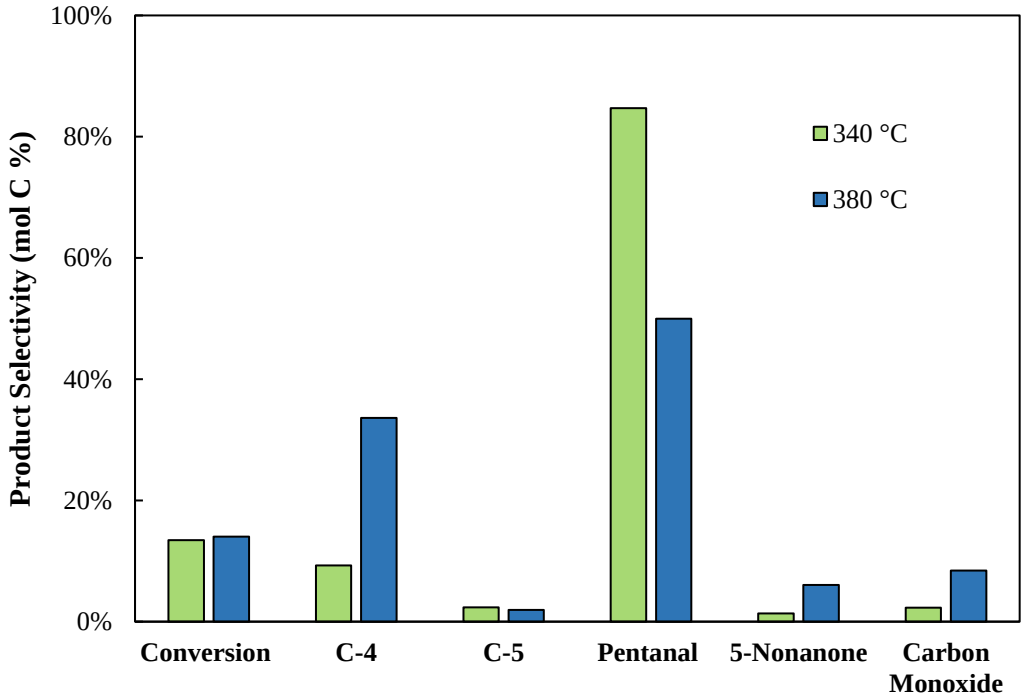


Figure 10. Comparison of product distribution measured at the same conversion levels with different temperatures for MoO_3. Reaction conditions: Conversion: ~ 14%, Flow of H_2 = 30 mL/min, P_{Total} = 1 atm, and TOS = 70 min. The catalyst was previously reduced under H_2 flow (100 mL/min) at 400 °C for 1 h.

Surface oxygen defects have been proposed as active sites for HDO reactions over MoO_x catalysts.[50,53] In this study, we hypothesize that the selective C-O cleavage reactions occur over these defects on the sub-stoichiometric oxide to form Mo-O bonds. These active sites can be regenerated by dissociated hydrogen to produce water. Green et al. showed that the rate-determining step for acetone deoxygenation to propene is the hydrogen dissociation on a stoichiometric surface, with a considerable activation barrier.[54] However, it is noted that reduced oxygen vacancies exhibit metallic character and likely aid in H_2 dissociation once

defects are created. Therefore, promoting MoO_3 with small levels of a noble metal capable of fast H_2 dissociation, such as Pt, should profoundly influence vacancy creation rates.

B.3.2 Influence of metal cluster (Pt) over MoO_3-based catalysts

Adding noble metal clusters onto MoO_3 is expected to facilitate H_2 dissociation, leading to dissociated hydrogen spillover onto the metal oxide support to promote oxygen removal on the oxide surface. Thus, reducible oxides doped with noble metals often provide enhanced catalyst activity.[55] Sermon et al. showed that MoO_3 reduction by molecular hydrogen only occurs at appreciable rates above 400 °C. However, the catalyst reduction can occur at a lower temperature if hydrogen atoms are supplied or created at the surface.[92] A kinetic study of H_2 adsorption over MoO_3 showed minimal hydrogen uptake on the MoO_3 catalyst in the temperature range of 50-300 °C, demonstrating that the hydrogen dissociation rate on MoO_3 is very low under this reduction temperature range. In contrast, the same study concluded that adsorption of H_2 on Pt/MoO_3 was 190 times higher than on MoO_3, which further suggests the positive role of noble metals on hydrogen dissociation and uptake on MoO_3.[93,94]

The temperature-programmed reduction (TPR) spectra of MoO_3 and 0.05 wt% Pt/MoO_3 samples are shown in **Figure 11**. MoO_3 does not show significant hydrogen consumption below 650 °C; only a broad H_2 consumption peak is observed in the 650-900 °C temperature range, attributed to the bulk MoO_3 reduction. In contrast, adding Pt clusters (0.05 wt%) to MoO_3 produces a significant shift in the initial reduction temperature of MoO_3 with considerable uptake at lower temperatures. This significant difference is ascribed to the presence of metallic Pt clusters that can easily dissociate H_2 and enhance the reducibility of MoO_3 by hydrogen spillover. In general, the reduction process of MoO_3 has been reported to be a

two-step reduction mechanism (MoO_3 → MoO_2 → Mo) with the additional formation of Mo_4O_{11} in a parallel reaction ($3MoO_3 + MoO_2 \rightarrow Mo_4O_{11}$).[95]

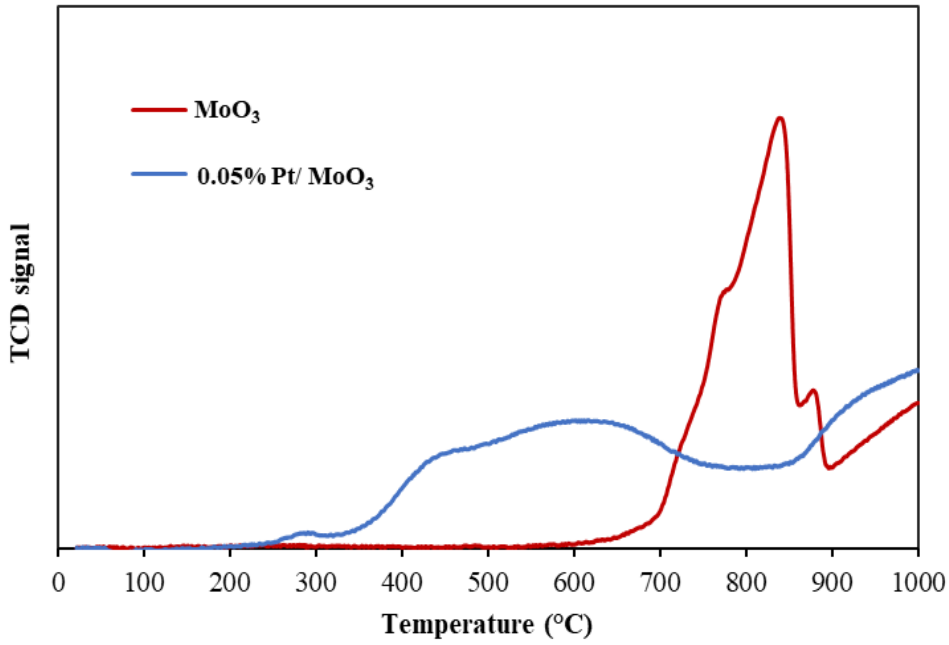


Figure 11. TPR results for MoO_3 and 0.05 wt% Pt/MoO_3 samples.

TGA-TPR was also performed to evaluate the weight loss during the reduction process; the temperature was varied from room temperature up to 550 °C in H_2/Ar flow (**Figure S2**). The weight loss reported represents the water production by MoO_3 during the reduction process. For water formation, dissociated H_2 is adsorbed on MoO_3, creating two hydroxyl species (-OH) with oxygen atoms located at the surface; subsequently, these are recombined to yield one water molecule.[93] For the MoO_3 catalyst, less than 1 wt% weight loss was observed at 400 °C. In contrast, the 0.05 wt% Pt/MoO_3 catalyst exhibited eight times more weight loss at 400 °C than MoO_3. It is important to note that despite small metallic loading, significant differences in MoO_3 reduction are observed upon Pt incorporation.

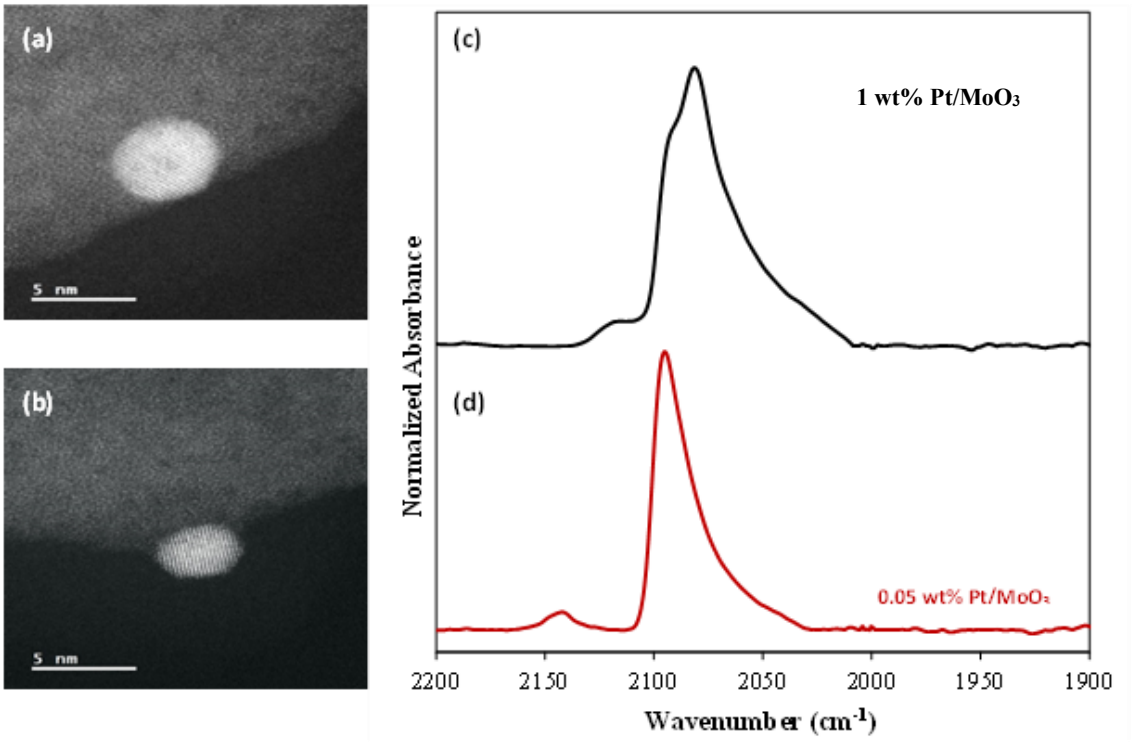


Figure 12. (a-b) STEM characterization of 0.05 wt% Pt/MoO_3, (c-d) FTIR spectra of CO adsorbed at 30ºC on Pt on MoO_3 prepared by incipient wetness impregnation. The catalyst was pretreated at 150ºC in 10%CO/He for 30 min (c) 1 wt% Pt/MoO_3 and (d) 0.05% Pt/MoO_3. Data normalized to maximum peak intensity and offset for clarity.

STEM analysis was performed on a JEOL Grand ARM to characterize the structure of 0.05 wt% Pt/MoO_3. This technique allows us to visualize if the Pt exists as isolated atoms or small metallic clusters (**Figure S9**). Although 0.05 wt% Pt/MoO_3 was synthesized via incipient impregnation, which generally promotes the formation of different cluster sizes, isolated atoms could be expected due to low Pt loading. **Figure 12 (a-b**) reveals that Pt is exhibited as small clusters over MoO_3, with a wide range of particle sizes between 1.6 to 11.3 nm (**Figure S10**).

STEM results were coupled with probe molecule Fourier transform infrared spectroscopy (FTIR) to confirm the presence of Pt as metallic clusters. It has been shown that FTIR using a CO as a probe molecule is a useful characterization technique, especially when coupled with STEM imaging, to characterize the distribution of Pt species (Pt atoms, metallic Pt^0 nanoparticles or clusters, or oxidized Pt clusters) on oxides-supported catalysts.[96] The IR spectra of CO adsorbed to 0.05 wt% and 1wt% Pt/MoO_3 at room temperature following the reduction in CO at 150 ºC are shown in **Figure 12 (c-d)**. These materials were chosen for analysis because they were expected to represent the range of Pt loadings at different structures, such as clusters or single atoms, that could be potentially present. The primary stretch associated with adsorbed CO for both materials was centered between the range of 2080-2095 cm^{-1}. Although there is limited literature on the CO vibrational frequency in Pt/MoO_3 catalyst,[97] we can attribute this feature to CO bound linearly to metallic Pt^0 nanoparticles or clusters based on its vibrational frequency and the fact that CO can reduce Pt even at temperatures (400 K).[98] The slight differences in the peak shape and location between each material could be due to particle size-dependent electron transfer to the support, Pt nanoparticle size, or other effects.

In addition to the primary CO stretching feature, both materials showed a small peak between 2115-2145cm^{-1}, which is more challenging to assign. The location above 2100cm^{-1} indicates CO adsorbed on cationic Pt species (i.e., Pt^{+2}), which may be related to CO adsorption on Pt single atoms or oxidized Pt clusters (e.g., Pt_xO_y).[96] The latter one is more likely due to incomplete Pt reduction. This is evidenced as the relative intensity of this feature with respect to the CO on Pt^0 feature did not change with weight loading, as opposed to what would be expected if the feature was due to CO adsorbed to Pt single atoms. The 2115-2145

cm^{-1} CO stretches make up less than 5% of the total absorbance area of these materials, suggesting the associated adsorption site is a minor contributor to the active Pt species.

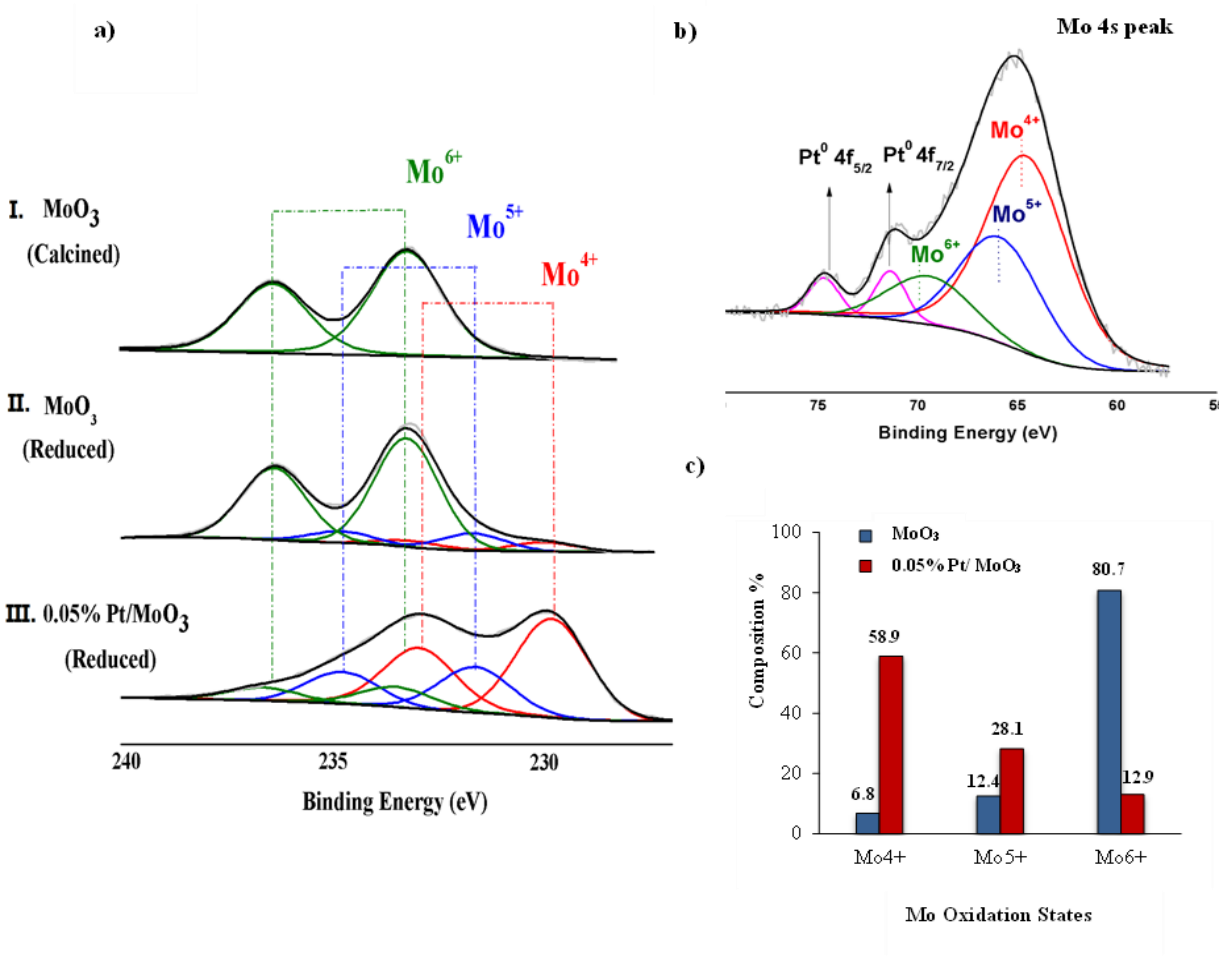


Figure 13. XPS results of MoO_3 and 0.05 wt% Pt/MoO_3. (a) XPS analysis showing the Mo (3d) energy region of MoO_3 calcined, reduced, and 0.05 wt% Pt/MoO_3 composition on MoO_3 and doped catalyst. (b) XPS analysis showing the Pt (4f) regions for three different pre-reaction samples: non-reduced MoO_3, both MoO_3 and 0.05 wt% Pt/MoO_3 (c) Mo oxidation states (%) for MoO_3 and 0.05 wt% Pt/MoO_3.

The nature of active sites during HDO of ketones and alcohols over MoO_3 has been studied by Roman-Leshkov et al. using near-ambient pressure X-ray photoelectron spectroscopy (NAP-XPS)[53]. They showed that during the anisole feed, the transition of the oxidation state over pre-reduced MoO_3 shifted from Mo^{5+} to Mo^{6+}. The presence of Mo^{4+} species was

also observed, which shows that some Mo sites can be over-reduced to Mo^{4+}. However, during the HDO reaction, Mo^{4+} species did not correlate with reaction rates, leading them to conclude that Mo^{4+} species were not involved in this selective HDO reaction. Thus, NAP-XPS characterization indicated that only Mo^{5+} species are responsible for HDO activity over MoO_3.[53] Hence, the effect of oxidation states on MoO_3 and 0.05 wt% Pt/MoO_3 catalyst was investigated using x-ray photoelectron spectroscopy (XPS). **Figure 13 (a-b)** shows the XPS spectra of the Mo 3d, and Pt 4f regions for three distinct samples: non-reduced MoO_3 and both MoO_3 and 0.05 wt% Pt/MoO_3 reduced at 400 °C in H_2. XPS results demonstrate a noticeable shift in the oxidation state of the Mo species after a reduction in atmospheric hydrogen flow at 400 °C for 1 h. Only Mo^{6+} species were identified in the non-reduced sample. Upon comparing the non-reduced MoO_3 with reduced MoO_3, modest amounts of Mo^{4+} and Mo^{5+} were observed. The presence of Mo^{4+} and Mo^{5+} species in reduced samples gives evidence of surface modifications during H_2 reduction.

Furthermore, XPS results show that incorporating Pt clusters leads to a significant enhancement in the reduction of Mo species, with the majority of Mo existing in the Mo^{4+} and Mo^{5+} states. This finding indicates that if the rate of Mo reduction is kinetically relevant in this selective HDO reaction, adding small levels of Pt dopant could accelerate the rate of carboxylic acid reduction. The corresponding binding energies for each characteristic XPS peak identified for the above samples are presented in **Table S1**. These results are also consistent with O_2 uptake measurements, described in the methods section. After reduction at 400 °C followed by dilute oxygen pulses at 350 °C, the MoO_3 catalyst showed adsorption of 405 micromoles per gram of O_2, while the 0.05 wt% Pt/MoO_3 catalyst showed adsorption of 1495 micromoles per gram of O_2. This significant increase in O_2 adsorption on the Pt-doped

catalyst further highlights the increased concentration of vacancies in the MoO_3 lattice after reduction in the presence of Pt.

B.3.3 Catalytic activity for HDO using a promoted MoO_3 catalyst

The promoting effect of small Pt clusters in the HDO conversion of pentanoic acid was investigated under the same reduction and reaction conditions as MoO_3 catalysis. **Figure 14a** shows the product selectivity of PA conversion as a function of temperature. The presence of small Pt clusters exhibits significant changes in the product distribution as a function of temperature. The findings suggest that a higher temperature, 0.05 wt% Pt/MoO_3 enhances the conversion towards decarboxylation (C-4) products. However, the selectivity to PAL over Pt/MoO_3 improves at lower temperatures. This could be due to less nonselective chemistry promoted by the Pt metal at lower temperatures and less-severe over-reduction of the MoOx surface under mild reaction conditions.

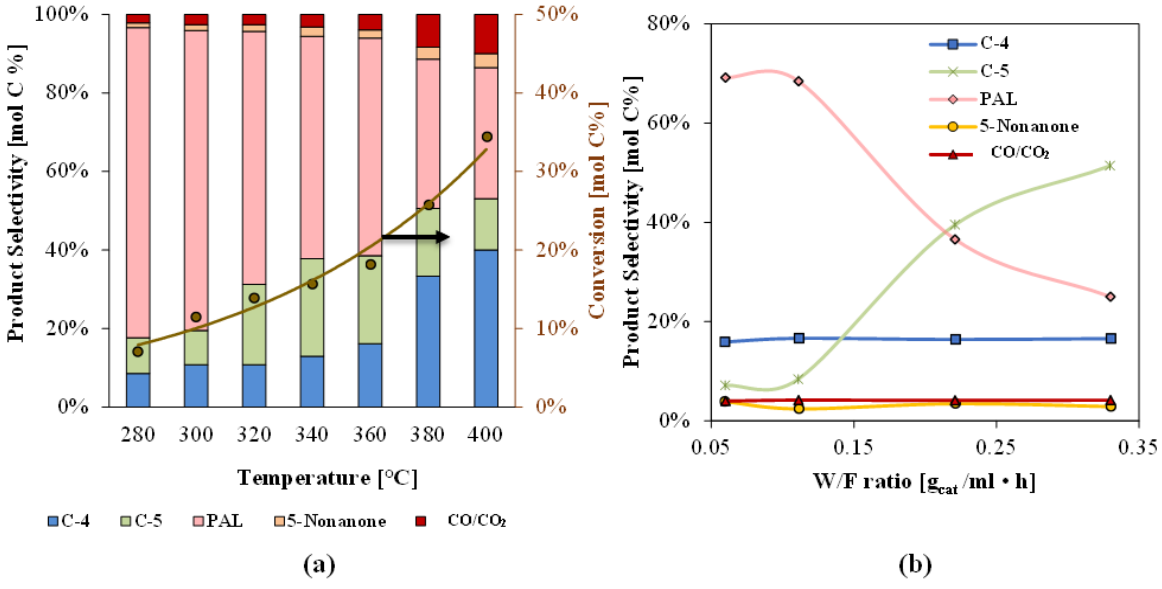


Figure 14. (a) Activity for HDO of pentanoic acid and product selectivity distribution for PA conversion at different reaction temperatures over 0.05 wt% Pt/ MoO_3. (b) Dependence of product selectivity of PA conversion at various W/F using 0.05 wt% Pt/MoO_3 as a catalyst at 350 ºC.

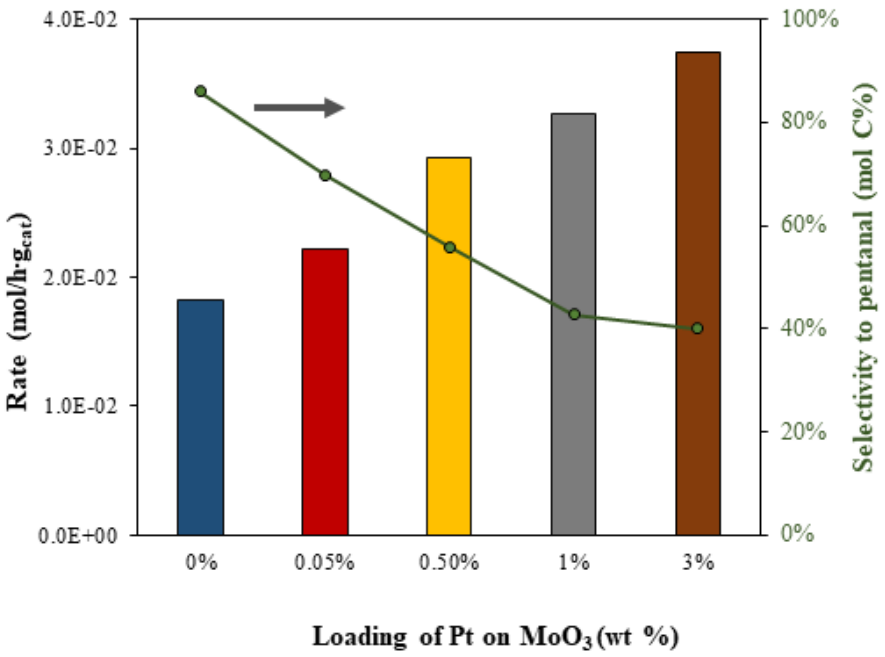


Figure 15. Reaction rate and selectivity using different loading of Pt over MoO_3. Reaction conditions: Flow of H_2 = 30 mL/min, W/F = 0.11 g_{cat}/mL·h, P_{Total} = 1 atm and $T_{reaction}$= 350 °C. The catalyst was previously reduced under H_2 flow (100 mL/min) for all the cases at 400 °C for 1 h.

To understand the temperature dependence of the selectivity on 0.05 wt% Pt/MoO_3, a set of experiments was conducted at different temperatures but at similar conversion levels (**Figure S3**). These experiments confirm that the decarbonylation (C-4) reaction at high temperatures becomes much more prominent, as was expected due to the presence of Pt clusters. The product distribution was also studied at different contact times (W/F); **Figure 14b** shows that at lower W/F, high selectivity to PAL (69%) is observed with low C-5 product selectivity (7%). However, at high contact times, a shift of selectivity is observed, and the dominant product of the reaction became C-5 compounds (51% selectivity). Thus, the pentanal selectivity over 0.05 wt% Pt/MoO_3 was affected when varying the conversion from 3 to 52 % of pentanoic acid is converted to pentanal, which consecutively undergoes HDO reaction to generate C-5 products. **Figure 15** shows the negative impact on aldehyde production at

higher Pt loading on MoO_3, where increasing the Pt loading results in higher rates of decarbonylation/decarboxylation and other side reactions observed in similar deoxygenation reactions involving metals and reducible oxides. [47]

The tradeoff associated with ultra-low Pt loadings (0.05% wt) on pentanoic acid hydrodeoxygenation vs. over-reduction of the surface is shown in **Figure 16**. The rate of PA consumption clearly increases at lower temperatures when a small loading of Pt (0.05 wt%) is added. This increase in activity can be explained by XPS results, where a higher presence of Mo^{4+} (52%) and Mo^{5+}(16%) species was observed after the reduction process (**Figure 13c**). In contrast, at reaction temperatures above 360 °C, the catalytic activity of 0.05% Pt/MoO_3 decreased, suggesting that some undercoordinated sites have been excessively reduced to lower oxidation states (Mo^{4+}). These results indicate that the benefits in deoxygenation rate observed upon the incorporation of small Pt loadings at lower temperatures (<350°C) may be attributed to the production of more Mo^{5+} surface species. These benefits are no longer present at elevated temperatures, where over-reduction of the metal oxide catalyst support (MoO_{3-x}) can occur.

Similar behavior is observed when MoO_3 is over-reduced for longer times or at higher temperatures. **Figure 17a** shows that with a more prolonged reduction time (3h), MoO_3 exhibits a lower selectivity to pentanal. The same trend is observed when the reduction temperature increases to 450 °C. **Figure 17b** shows that the catalyst decreases the overall activity at higher reduction temperatures (400-500 °C). Thus, more severe reduction conditions appear to result in the unavoidable creation of less active Mo^{4+} species.

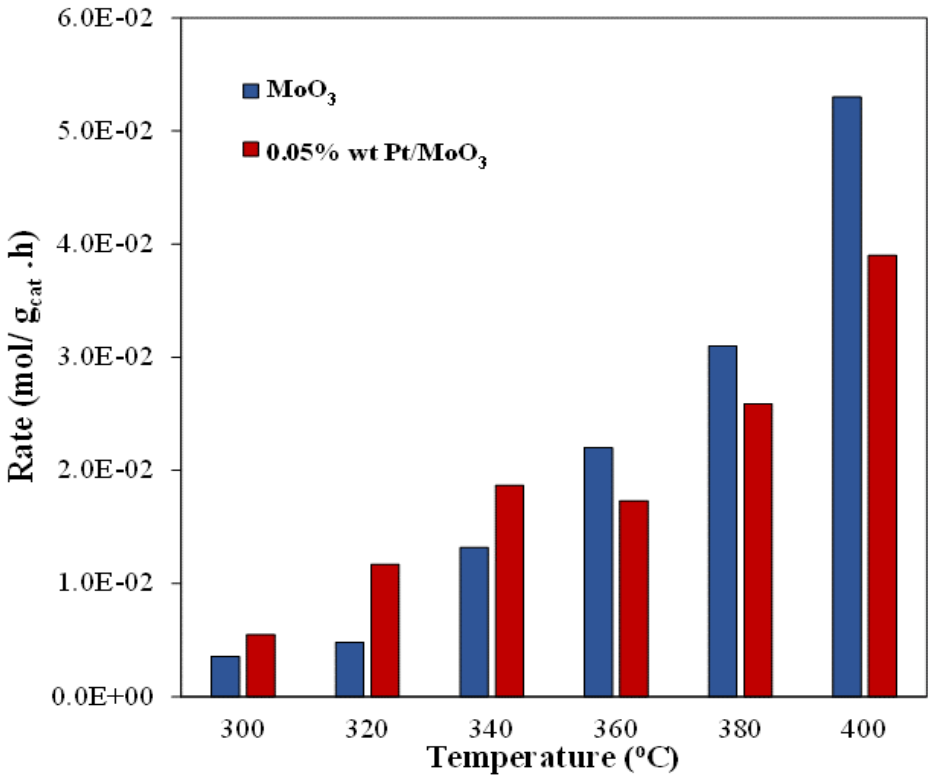


Figure 16. Rate consumption of PA varying temperature. Comparison of the rate conversion of PA using MoO_3 and 0.05 wt% Pt/MoO_3 in the temperature range 300-400 °C. Reaction conditions: Flow of H_2= 30 mL/min, TOS= 0 min, P_{Total}= 1atm, and W/F= 0.11 g_{cat}/mL·h.

The activity of commercial MoO_2 was evaluated under the same reaction conditions as the MoO_3 catalyst to investigate the effect of the total reduction of Mo species from both Mo^{6+} and Mo^{5+} to Mo^{4+} on this hydrodeoxygenation chemistry. A Commercial MoO_2 is prepared by reducing MoO_3 in dry hydrogen at 500 °C. **Figure S11** shows a higher PA conversion rate (mol/h·gcat) for MoO_3 than MoO_2. However, to account for the difference in surface area between MoO_2 and MoO_3, a comparison rate per surface area is also presented in **Figure S11**, which clearly shows the significantly lower catalytic activity of MoO_2 compared to MoO_3 under the same reaction conditions. These results suggest that a partial reduction of Mo species at the surface is necessary to maintain high deoxygenation rates. In contrast, the

formation of MoO_2 during reaction conditions because of over-reduction leads to an inactive phase, consistent with previous proposals.[53]

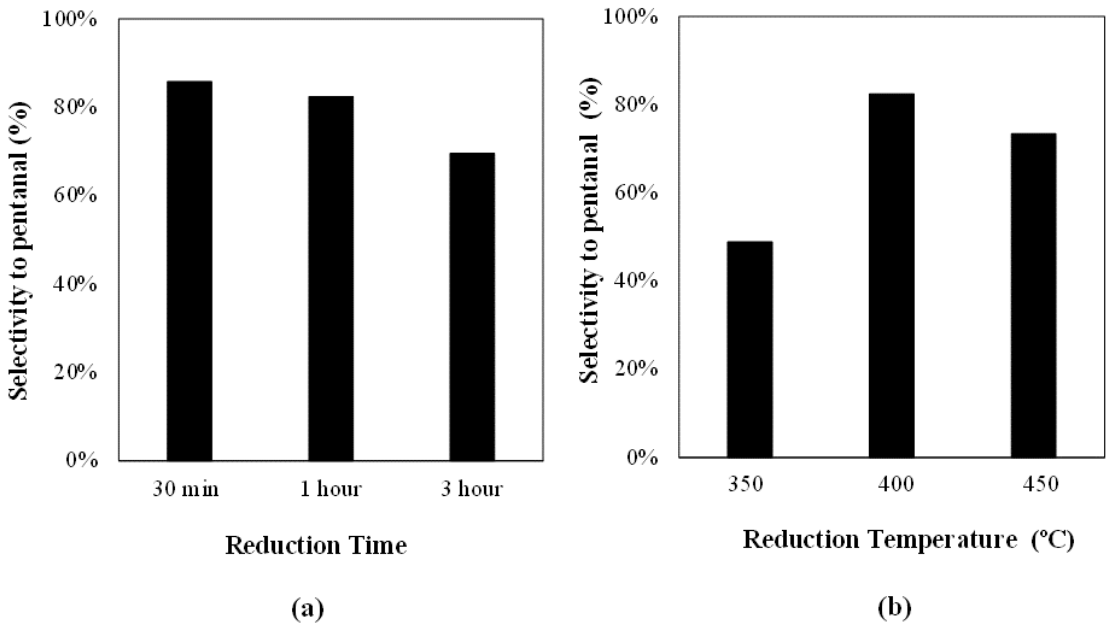


Figure 17. Effect of selectivity to pentanal at different reduction pretreatments over MoO_3. **(a)** different reduction time when the catalyst is pre-reduced at 350 ºC **(b)** Different reduction temperatures when the catalyst is reduced for 1 h. Reaction conditions: P_{Total} = 1 atm, Flow of H_2 = 30 mL/min, $T_{reaction}$ = 350 ºC and W/F = 0.11 g_{cat}/mL·h.

The influence of these species on catalyst stability was investigated at intermediate temperatures (350°C), where the conversion per gram of 0.05wt% Pt/MoO_3 is comparable to the conversion per gram of MoO_3. **Figure S13 (a-b)** shows that both catalysts exhibit similar deactivation trends when evaluated at similar initial conversion levels, with slightly enhanced deactivation rates observed for the Pt-doped catalyst. In contrast, deactivation rates with those observed over MoO_3 under identical temperatures with m-cresol,[34] it is evident that both catalysts in the current study exhibit slightly higher stability as a function of time, indicating lower rates of coke formation for aliphatic acids compared to aromatic oxygenate compounds.

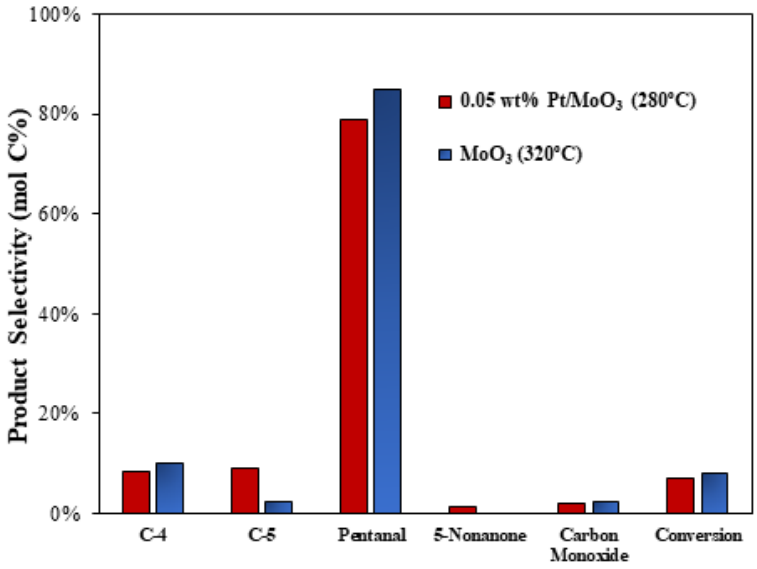


Figure 18. Product distribution at the same conversion levels for MoO_3 (320 °C) and 0.05 wt% Pt/MoO_3 (280 °C). The product distribution was compared at the same conversion levels with different temperatures for both catalysts. Conversion: ~ 9 %. Reaction conditions: Flow of H_2= 30 mL/min, TOS= 0 min, W/F= 0.11 g_{cat}/mL·h, and P_{Total}= 1 atm.

The results presented thus far highlight the relevant role of oxygen vacancies in the HDO reaction of pentanoic acid over MoO_3 and illustrate how the creation of these sites can be accelerated by adding a small amount of metal dopant at mild conditions (<350 °C). To demonstrate the role of Pt in this chemistry at lower temperatures, experiments were carried out over MoO_3 and 0.05 wt% Pt/MoO_3 using the identical catalyst mass but different reaction temperatures to achieve iso-conversion. **Figure 18** reveals that adding 0.05 wt% Pt reduces the temperature required by 40 °C to achieve a similar conversion level (9%) while maintaining high selectivity to pentanal. It is noted that even under these mild conditions, some selectivity losses due to the presence of even trace Pt levels are present, as evidenced by the slightly higher yields to fully deoxygenated products. Nonetheless, this significant shift in the rate at low temperatures highlights the critical role that hydrogen dissociation plays in this reaction. Hence, similar steady-state levels of oxygen vacancies could be obtained at

lower temperatures by tuning the addition of Pt metal. In this regard, we hypothesize that the effect of the Pt clusters increases the concentration of OH groups and reduction rate of MoO_3 catalysts, resulting in enhanced rates of oxygen defect formation and potentially higher H surface coverage under reaction conditions (**Figure 19a**).

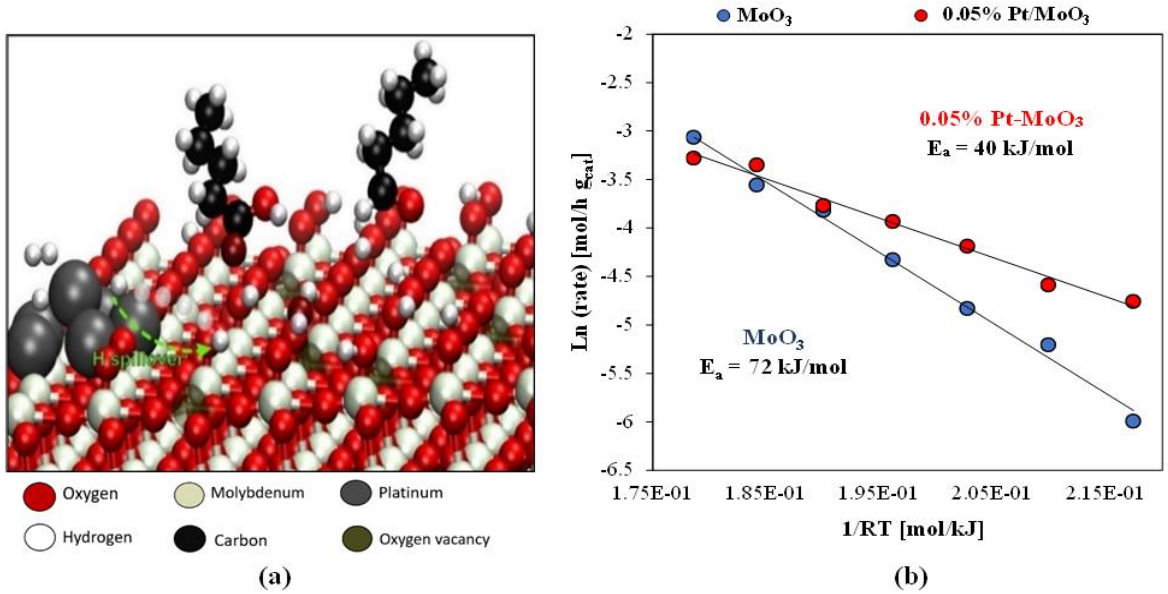


Figure 19. (a) Schematic of PA to PAL reaction over a hydrogen-covered Pt/MoO_3 surface. (b) Activation energy using MoO_3 and 0.05 wt% Pt/ MoO_3 as a catalyst. Reaction conditions: Flow of H_2= 30 mL/min, TOS= 0 min, W/F= 0.11 g_{cat}/mL·h, and P_{Total}= 1 atm.

The energetic barriers for the conversion of PA were measured for both catalysts to provide further evidence of the enhancing effect of metal oxide surface doping with Pt (**Figure 19b**). As a result, the apparent activation energy observed for MoO_3 (72 kJ/mol) is significantly higher than the 0.05 wt% Pt/MoO_3 (40 kJ/mol). Incorporating Pt clusters as a hydrogen dissociation promoter decreased the kinetic barrier by 32 kJ/mol. This suggests that the rate-limiting step could be either the formation/regeneration of oxygen vacancies or a surface reaction with a strong correlation between hydrogen surface coverage on stabilization of kinetically relevant transition states. These apparent activation energies were calculated under a slightly negative-order kinetic regime (-0.19), which is observed due to the high

binding energy of acid over undercoordinated MoO_x sites (**Figure S4**). The inhibition order with respect to acid co-fed suggests that the acid is either impeding the overall rate by negatively impacting hydrogen dissociation, spillover across the surface, or vacancy regeneration.

B.3.4 Density functional theory study for pentanoic acid over MoO_3

Here, we also explored the energetic barriers for the conversion of PA to PAL by performing computational calculations on reduced MoO_3(010). Mei et al. showed that creating oxygen vacancies is more favorable for single-coordinate terminal oxygen than for two-coordinate asymmetric and three-coordinate symmetric bridging oxygen atoms due to the lower formation energy.[50] Therefore, this study considered two adsorption conformation energies of PA on the α-MoO_3 (010) surface with a single-coordinated terminal oxygen vacancy. The first adsorption conformation assumed for the conversion of PA to PAL is through the oxygen atom double bonded to a carbonyl carbon atom (C=O), which results in the high adsorption energy of -104 kJ/mol (**Figure S5a**). The computed adsorption energy for the second configuration, adsorption of PA on a terminal oxygen defect through the oxygen of the hydroxyl group (-OH), is -47 kJ/mol (**Figure S5b**), indicating a much weaker interaction compared to the first configuration.

Green et al. studied the hydrodeoxygenation of acetone to propylene on the α-MoO_3 (010) catalyst. Their results indicate that dissociative hydrogen adsorption is the rate-limiting step in the catalytic cycle (170 kJ/mol).[54] However, as mentioned earlier, the results of our experiments reveal that Pt addition can quickly accelerate the hydrogen dissociation and oxygen vacancy formation/regeneration on MoO_3.

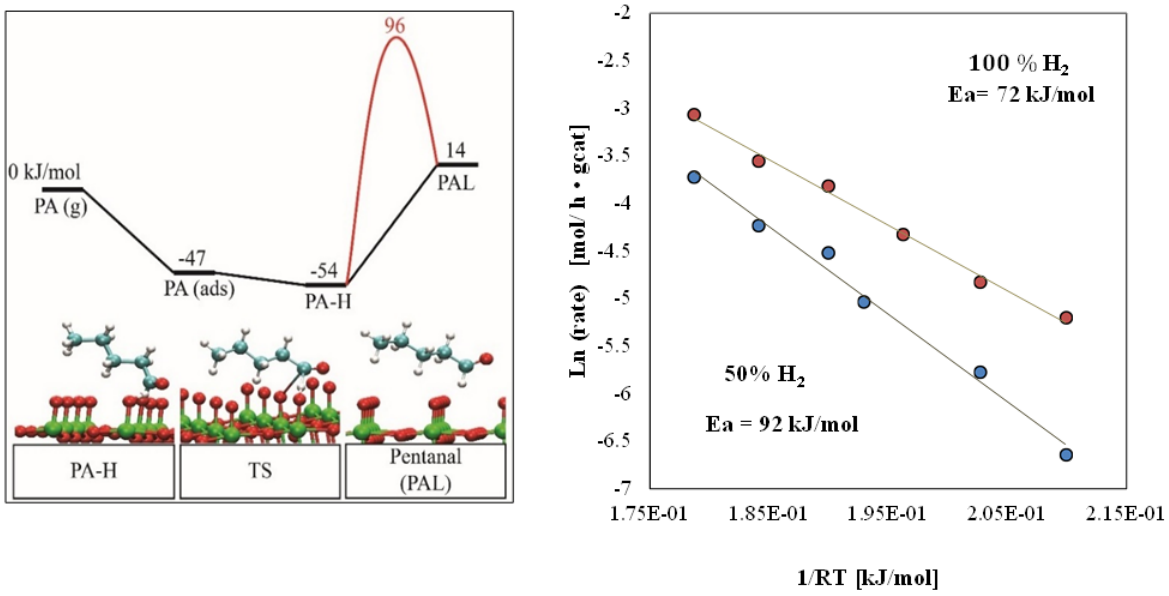


Figure 20. (a) Reaction coordinate for the formation of PAL. (b) Activation energy using MoO_3 as a catalyst at different partial H_2 pressures. For all the cases, the reaction conditions were: P_{Total}= 1 atm, Flow of H_2= 30 mL/min, W/F= 0.11 g_{cat}/mL·h, and TOS= 0 min. The catalyst was previously reduced under H_2 flow (100 mL/min) at 400 ºC. For the case of 50% H_2, the total pressure was balanced with He.

Figure 20a shows the energetic requirements for the elementary steps involved in PAL formation. Following the adsorption of PA on an oxygen defect (Ot) through the hydroxyl group (-OH), a metal carboxylate intermediate (PA-H) is formed after the hydrogen atom abstraction from the hydroxyl group. This step is exothermic with a reaction energy of -7 kJ/mol. The formation of a physisorbed PAL occurs following hydrogen-assisted deoxygenation. This endothermic step has a reaction energy of 60 kJ/mol and an apparent barrier of 96 kJ/mol. At the transition state, the bond lengths for the C-O and O-H bonds are 2.85 and 1.09 Å, respectively, indicating that the C-O bond is broken (**Figure S6**). These results suggest that H addition to carbonyl carbon is energetically demanding. The intermediate, transition and final state geometries are shown in **Figure 20a**. All values presented were

calculated at 0 K on a pristine molybdenum oxide surface and did not account for the entropy, pressure, or coverage effects.

Theoretical calculations show that the formation of PAL over a single oxygen vacancy in the absence of residual O-H groups has a higher apparent barrier (150 kJ/mol) compared to the experimentally observed barrier (72 kJ/mol) in the absence of Pt. It is worth mentioning that reaction conditions and DFT modeled conditions are not the same; therefore, a straight comparison cannot be made. However, we hypothesize that this difference can be explained by hydrogen and hydroxyl groups at the surface under reaction conditions. To further investigate the effect of hydrogen coverage in the catalytic conversion of PA to PAL, a kinetic barrier was experimentally determined when the partial pressure of hydrogen was reduced by 50% (balance with He), maintaining the overall pressure constant. **Figure 20b** shows that the activation energy increases by 20 kJ/mol when the partial pressure of H_2 is decreased by 50%, suggesting that hydrogen coverage plays a significant role in converting PA to PAL over MoO_3.

An alternative mechanism was tested, in which the PA adsorbs through the carbonyl group at an oxygen vacancy, as shown in **Figure S12**, followed by C=O bond cleavage and hydrogen transfer. This proposed mechanism was investigated step-wise, showing a barrier over 300 kJ/mol for the C=O cleavage. Instead, the concerted mechanism appears to be a more feasible pathway for PAL formation; however, the intrinsic activation energy required for this mechanism is 223 kJ/mol, which is significantly higher than the value presented in **Figure 20a**. These results suggest that, although adsorption via the carbonyl group is stronger, PA in this adsorption configuration is likely a spectator due to the high activation barrier.

B.3.5 Role of intermediate hydrogen pulses on acid conversion chemistry

The impact of hydrogen on the rate of PA conversion was further investigated by intermittently switching the carrier gas from H2 to He during a continuous flow reaction. We note that the catalyst was initially reduced at the same conditions mentioned above, so the results obtained over the initial 40 minutes are identical to those reported earlier. As shown in **Figure 21a**, in the absence of hydrogen in the flow system, the catalytic activity of MoO_3 rapidly diminishes to exhibit negligible conversions (<2%). This can be explained by the suppression of vacancy regeneration in the absence of hydrogen and the decline in hydrogen coverage on the surface. However, the catalytic activity is recovered once hydrogen is re-introduced to the reactive system. The results indicate that hydrogen coverage plays a crucial role in the catalytic chemistry of PA conversion, along with the surface changes that occur during the reaction.

A micro-pulse reactor technique was utilized as a tool to investigate the mechanism underlying this dynamic catalytic behavior in greater detail, as shown in **Figure S8**.[85] Small doses of carboxylic acid diluted with hydrogen or helium were introduced to a reduced MoO_3 surface via a sample loop. This unique approach was employed to investigate the initial interactions of reactants with the catalyst surface before significant modifications of the catalyst surface due to coke formation and other effects induced by persistent reactant flow. Thus, this technique decouples the acid conversion from oxygen vacancy formation/regeneration steps.

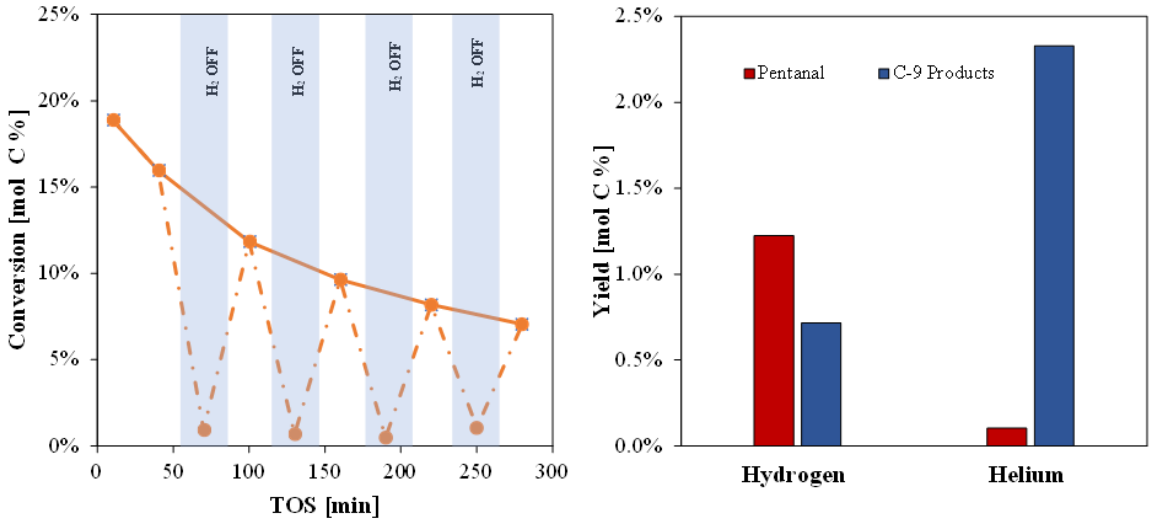


Figure 21. (a) Effect of hydrogen suppression in the conversion of PA over MoO_3 in a flow system evaluated at 350ºC. The reaction conditions were: P_{Total}= 1 atm, Flow of H_2= 30 mL/min, TOS= 0 min, and W/F= 0.11 g_{cat}/mL·h. The catalyst was previously reduced under H_2 flow (100 mL/min) at 400 ºC. (b) Role of the hydrogen for the conversion PA over MoO_3 at 350 ºC, assessed in a micro pulse reactor. The data represented on this graph correspond to the yields after 9 pulses.

The production of PAL is favored only in the presence of hydrogen, as shown in **Figure 21b**, which clearly indicates that existing OH groups on the catalyst surface are necessary for aldehyde formation. In the presence of the inert carrier, this chemistry is less pronounced, instead favoring ketone formation. While it could be proposed that the H atoms removed from the dissociated acid species upon adsorption could ultimately transfer back to form the aldehyde product, we anticipate that it would be entropically favorable for this H atom to migrate along the catalyst surface away from the reactive intermediate. This requires a significant H coverage on the surface to facilitate the removal of formed pentanal products. The small yield of pentanal observed under inert gas could be attributed to the existence of residual H atoms from pretreatment carried out in the hydrogen gas. Supporting this argument is the decline in the activity of pentanal production in an inert gas environment with sequential pulses, as shown in **Figure S7**.

Our findings suggest that carboxylic acid conversion over MoO_3 occurs via a more complex mechanism than a simplified reverse Mars-van Krevelen mechanism, where the PA (-OH) oxygen is adsorbed on the vacancy, healed and subsequently converts the acid to aldehyde. The presence of hydrogen coverage is a residual requirement for this chemistry to occur. As shown above, the protonation of the carbonyl carbon is characterized by high energy demand, as suggested by DFT calculations. A more detailed kinetic model considering the water and CO poisoning effect and hydrogen surface coverage, and the effect of hydrogen on the theoretically computed barrier should provide more insight into this dynamic surface reaction.

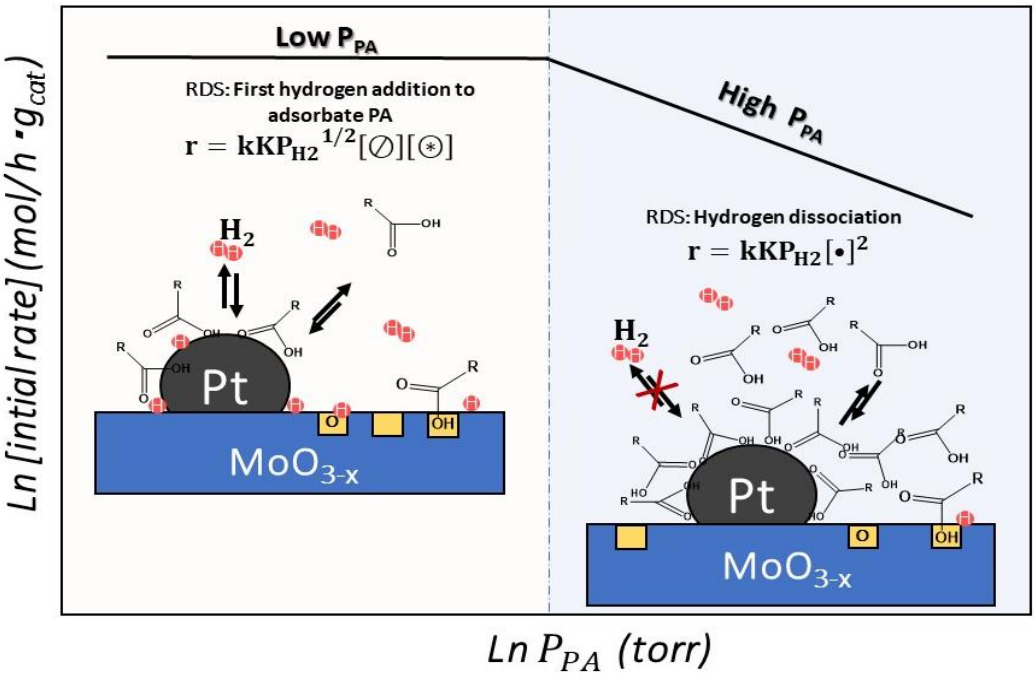
B.4 Conclusions

Here we demonstrate that MoO_3-based catalysts are remarkably selective for the deoxygenation of carboxylic acids to aldehydes. Under mild conditions, (<350 ºC) dissociation of hydrogen and generating undercoordinated sites is slow, with overall deoxygenation rates significantly enhanced upon the addition of trace levels of Pt. The addition of only 0.05 wt% Pt leads to a significant 32 kJ/mol reduction in the activation barrier under low temperatures at the expense of deoxygenation side reactions and activity losses due to over-reduction at more elevated temperatures. DFT results and experimental hydrogen coverage studies reveal that although defects on the surface are essential, continuous coverage of surface H atoms facilitates high rates of selective acid reduction. DFT analysis also indicated that the addition of hydrogen to the carbonyl group is an energetically demanding step over MoO_3. Here, we also showed that the apparent activation energy increased by 20 kJ/mol when the hydrogen partial pressure was reduced by 50%. A micro-pulse reactor was used to decouple the oxygen vacancy formation steps from carboxylic acid conversion, confirming the critical role of

persistent H coverage. A more detail kinetic model will reveal the details about the mechanism of the conversion of PA over promoted MoO_3.

CHAPTER III

C. Revealing the mechanistic details for the selective deoxygenation of carboxylic acids over dynamic MoO_3 catalysts.



The synthesis of the Carbon Nanotubes for identifying the active sites in this study was carried out by Caleb Q. Bavlnka and Ethan Zhang. Dr. Resasco provided insights into this study's analysis and rate-determining step.

C.1 Introduction

The MoO_3 has been proposed as a catalyst for the deoxygenation of ketones and alcohols via a reverse Mars-van Krevelen mechanism. This process involves the removal of an oxygen atom from the oxygenated compound by an oxygen vacancy, followed by re-

establishing the initial surface structure.[99] Similar and related proposals have also been made for other redox catalysts, with varying claims regarding the importance of co-fed hydrogen in the process. Thibodeau et al. have also proposed a closely related deoxygenation mechanism upon the conversion of acrolein over tungsten oxide bronzes, where the persistent presence of hydrogen atoms is required from either surface hydroxyl groups or directly from H species that form the hydrogen bronzes.[100] A radical reverse Mars-van Krevelen mechanism type was proposed by Mironenko and Vlachos for converting furfural to 2-methyl furan over Ru/RuO_2 using 2-propanol as both a solvent and hydrogen donor. In their study, propanol dehydrogenation over metallic Ru sites is essential to sustaining dissolved H_2 concentration and oxygen vacancies.[101]

As mentioned in chapter 2, the persistent presence of hydrogen on the catalyst surface is required to maintain high SDO rates. In this chemistry, hydrogen is typically involved in the formation/regeneration of oxygen vacancies and in the hydrogenation of PA to yield PAL. Our study suggests that complicating factors beyond a simplified MvK-type mechanism, such as the persistent surface coverage of neighboring dissociated H atoms, must be considered. Often, MvK-type mechanisms are modeled as Langmuir-Hinshelwood (LH) type mechanisms when additional complications such as those described above are present. Therefore, utilizing a Langmuir-Hinshelwood framework, it is possible to account for the oxidant and reductant adsorption and dissociation on surface sites, as well as adsorption competition with other reactants and products that could be present in the reaction mixture.[102,103] Although an MvK model can describe the redox chemistry at the surface of the MoO_3 catalyst, cases such as this one, where local H coverage and site competition strongly influence reaction rates,

are better approximated by a Langmuir-Hinshelwood (LH) type modeling framework for the cases outlined here.

To gain more insight into the mechanism type, a kinetic model is developed using Langmuir-Hinshelwood since it closely describes the dynamic redox chemistry that occurs at the surface for both MoO_3 and 0.05 wt% Pt/MoO_3. Herein, we reveal that upon the incorporation of Pt in MoO_3, the rate-limiting step shifts from hydrogen dissociation to the first hydrogen addition to the surface-bound species. The inhibition effect of PA on both catalysts for MoO_3 and 0.05 wt% Pt/MoO_3 catalysts has been investigated in this study. The possible causes of this effect have also been discussed.

C.2 Experimental section

C.2.1 Chemical and catalyst materials

All the gases (H_2 (99.999%), He (99.999%), N_2 (99.998%), Air (Ultra zero), and Ethylene) used for catalyst preparation, reaction, carbon nanotube synthesis, and characterization were purchased from Airgas. Commercial molybdenum (VI) oxide, MoO_3 (>99.5 wt%), was purchased from Alfa Aesar. Acid-washed glass beads (50-70 US sieve, Sigma) were mixed with the catalyst and packed in the reactor. Water (18 MΩ) was obtained from an in-house filtration system and used in this study. Pentanoic acid used in the kinetic measurements was purchased from Sigma Aldrich (CAS No 109-52-4).

For vertical multi-walled carbon nanotubes (CNTs) growth, iron nitrate nonahydrate, cobalt nitrate hexahydrate, aluminum nitrate nonahydrate, and 2-hydroxyethyl cellulose (Mw ~ 1,300,000) were used. Tungsten (1 mm, 99.94%), molybdenum (0.75 mm, 99.95%), and platinum (0.025 mm, 99.00%) wires were used for metal deposition. Aluminum conductive tape (single adhesive surface, 12.7 mm W x 16.4 m L, Ted Pella Inc.) was used to remove

CNTs from the silicon wafers. The silicon wafers used as a base for growing CNTs were purchased from Wafer World, Inc (SKU:1186). Cleaning of these wafers required isopropanol, ethanol, and acetone.

C.2.2 Catalyst synthesis

The promoted molybdenum oxide (0.05 wt% Pt/MoO_3) catalysts were prepared by the incipient wetness impregnation method by using tetraammineplatinum (II) nitrate ($[Pt(NH_3)_4](NO_3)_2$, 99.99%, 50% Pt, Alfa Aesar) as a Pt precursor solution. For each batch, 10 g of MoO_3 was used, and 2 ml aqueous solution with 10 mg of Pt precursor was added dropwise to the support. Once the impregnation step had been completed, the sample was dried at 80 ℃ for 12 h and calcined at 600 ℃ (ramp rate ten ℃/min) for three hours by flowing air (100 mL/min). Commercial MoO_3 was calcined under identical conditions. Before catalytic testing, the catalyst powders were pelletized and sieved to yield pellet sizes from 90 to 125 um (120-170 US sieve).

C.2.3 Kinetic measurements.

The catalytic testing occurred in a gas-phase packed bed reactor under atmospheric pressure conditions, using H_2 or H_2/He as a carrier gas. Catalyst particles were mixed with glass beads (Sigma Aldrich, 212-300 μm) and packed between two layers of quartz wool inside a quartz reactor (0.25” OD). The reactor tube was placed in the center of a vertical furnace (Thermcraft Inc., 1200W/115V). All catalysts were pretreated in situ in hydrogen (100 SCCM) at 400 ℃ for 1 hour. After reduction, the samples were cooled to the reaction temperature (300-400 ℃). Pentanoic acid, mixed with heptane to prevent corrosion, was used as a feed. The reactants were injected using a syringe pump (KD Scientific) and vaporized (92-100 ℃) before entering the reactor. To prevent any product condensation, the outlet

stream was kept at 250 ℃. A gas chromatograph (GC), equipped with a flame ionization detector (FID) and HP-INNOWAX column (Agilent, 60 m × 0.32 mm ID × 0.5 μm), was connected to the reactor for product quantification. The same conditions mentioned above were used for experiments with the carbon nanotube samples, Pt/CNT/MoO_3 and Pt/MoO_3/CNT.

C.2.4 Catalyst characterization

C.2.4.1 Scanning electron microscopy (SEM).

The samples were analyzed using a Thermo Quattro S field-emission environmental scanning electron microscope (FE-ESEM) with an accelerating voltage of 10 kV for imaging and 15 kV when performing energy-dispersive X-ray spectroscopy.

C.2.4.2 X-ray photoelectron spectroscopy (XPS).

The AXIS-supra with a dual anode Al/Ag (2984.2 eV) monochromatic X-ray source was used to perform XPS analysis on the carbon nanotube samples.

C.3 Results

C.3.1 Inhibition effect of pentanoic acid (PA)

An inhibition effect is observed in the deoxygenation of PA over MoO_3 at a high partial pressure of PA (> 3.0 Torr)[51]. To determine if this effect remains present under a lower partial pressure of PA, the pressure was reduced (< 3.0 Torr) at a temperature of 350°C, as shown in **Figure 22a**. Notably, reducing the partial pressure of PA changed the reaction order from inhibition (-0.24) to a zero-order (0th) regime with respect to PA. For 0.05 wt% Pt/MoO_3, the reaction order of PA shows a shift to zero-order dependence at a lower partial pressure of PA, as indicated in **Figure 22b**. This could lead to the interpretation that the surface is saturated with PA or that the rate is independent of PA at lower PA partial

pressures. This observed zero-order dependence also indicates that internal mass transfer limitations are not present in the system. This is because the correlation of measured apparent reaction order η' ($\eta_{Apparent}$) and the true reaction order η (η_{True}), ($2\eta' = (1+\eta)$), suggests that if the internal mass transfer were present in the system, the minimum observed reaction order would be equal to or higher than 0.5.[104]

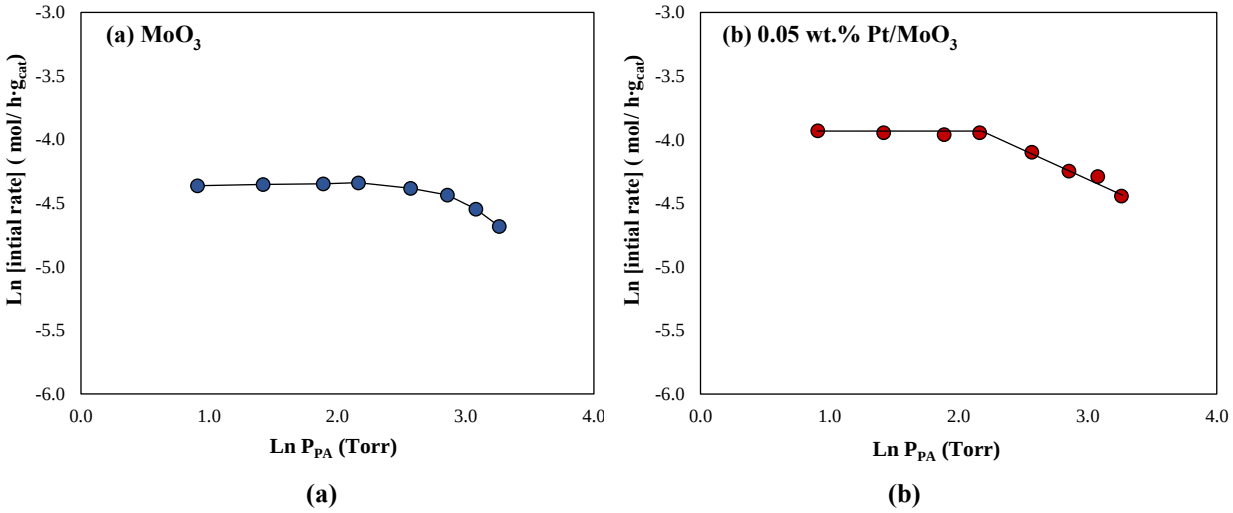


Figure 22. **(a)** Order of reaction with respect to PA over MoO_3. **(b)** Order of reaction with respect to PA using 0.05 wt% Pt/MoO_3 as a catalyst. Reaction conditions: Flow of H_2 = 30 mL/min, $T_{reaction}$ =350 °C, P_{Total} = 760 Torr, and TOS = 0 min. The flow of PA varied from 0.03 to 0.3 mol/h. The catalyst was previously reduced under H_2 flow (100 mL/min) at 400 °C for 1 h for all cases.

In order to confirm that this zeroth order-dependence observed at low partial pressures of PA is not an artifact of the reaction products present at various conversion levels, the catalyst mass was reduced by 50%, and the rates were again measured at low partial pressures of PA (1.0 to 3.0 Torr). As a result, **Figure 23** shows that the reaction rate remains unchanged while the conversion is reduced by 50%, as expected. Thus, the constant rates observed at a low PA partial pressure confirm the true zeroth order regime.

The reaction order with respect to PA was also investigated on the 0.05 wt% Pt/MoO_3 catalyst. **Figure 22 (a-b)** indicates higher reaction rates for the conversion of PA over 0.05 wt% Pt/MoO_3 than MoO_3 under similar conditions. Although 0.05 wt% Pt/MoO_3 initially showed a higher conversion rate, it appears that 0.05 wt% Pt/MoO_3 is less resistant to carboxylic acid inhibition than MoO_3. This is evidenced by the inhibition behavior being reached more quickly on 0.05 wt% Pt/MoO_3 than on MoO_3. We hypothesize that this fast inhibition is due to the strong adsorption of the carboxylic acid onto the metal sites (Pt), rapidly decreases the hydrogen coverage while hindering the regeneration of oxygen vacancies and conversion of PA. Thus, the catalyst surface of 0.05 wt% Pt/MoO_3 at high coverage of PA resembles the surface dynamics of MoO_3, where H_2 dissociation would likely be the rate-limiting step. In all cases, the rates were found by extrapolating to the initial time of stream (TOS) to eliminate the influence of catalyst deactivation.

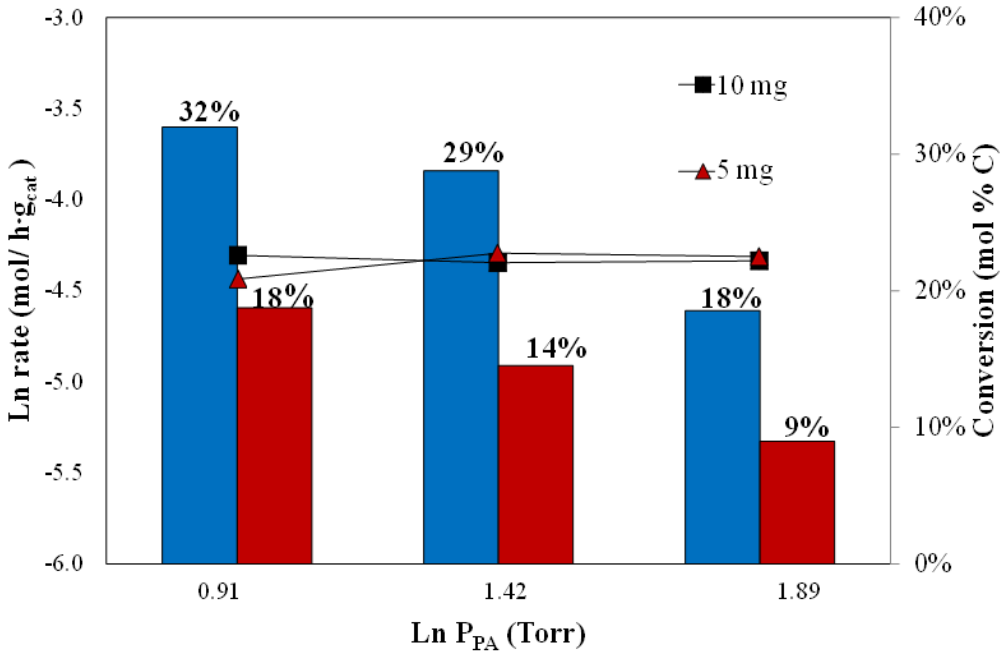


Figure 23. Order of reaction with respect to PA over MoO_3 at a different mass of catalyst. Reaction conditions: Flow of H_2 = 30 mL/min, Treaction =350 °C, P_{Total} = 760 Torr, and TOS = 0 min. The catalyst was previously reduced under H_2 flow (100 mL/min) at 400 °C for 1 h for all cases.

The strong adsorption of PA over an oxygen vacancy might cause the inhibition effect observed at a high partial of PA over both MoO_3 and 0.05 wt% Pt/MoO_3. As previously reported, DFT calculations of the PA adsorption over MoO_3 indicate that the adsorption of PA through carbonyl-group oxygen (C=O) at a defect site is 57 kJ/mol stronger than the adsorption through the hydroxyl group (-OH).[51] Although the adsorption through the C=O group is stronger, the activation energy to produce the aldehyde is significantly higher than that through the hydroxyl group, suggesting that the carboxylic acids adsorbed via the C=O group are only present as spectator species. Hence, we hypothesize that these strongly binding species are responsible for the inhibition behavior observed at 350°C.

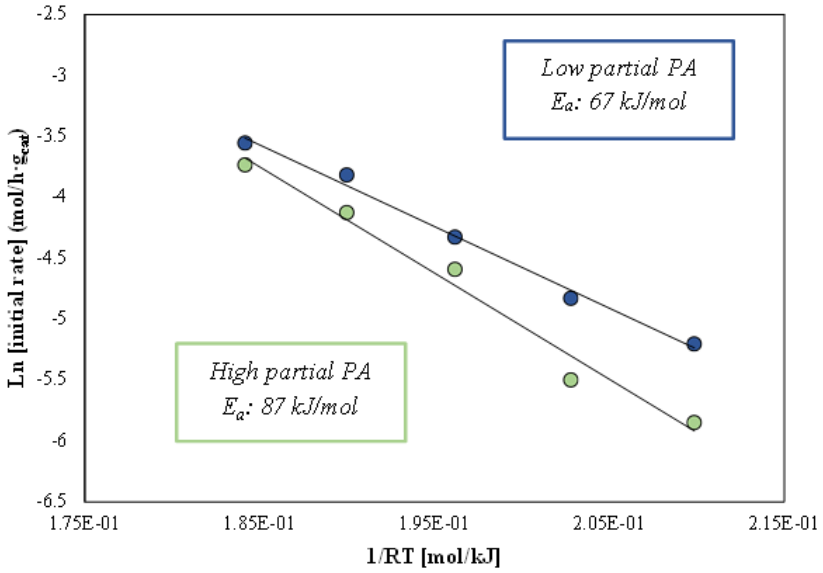


Figure 24. Activation energy comparison at a different partial pressure of PA over MoO_3. Reaction conditions: P_{Total}= 760 Torr, Flow of H_2= 30 mL/min, and TOS= 0 min. The catalyst was previously reduced under H_2 flow (100 mL/min) at 400 ºC.

Consistent with this inhibiting behavior of acid is the increase in activation energy observed as the PA partial pressure increases. As shown in **Figure 24**, an increase in the partial pressure of PA by 2.5 times results in a 20 kJ/mol increase in the activation energy.

This result supports the hypothesis that hydrogen dissociation is limiting at a high partial pressure of PA due to the strong inhibition by PA.

Figure 25 illustrates three possible explanations for the inhibition behavior observed at a high partial pressure of PA. Here, we hypothesize that the strong adsorption of carboxylic acids suppresses the surface reaction by either:

I. Site competition over Pt metal sites between carboxylic acid (PA) and hydrogen (H_2) hinders H_2 dissociation.

II. Site competition between PA and H_2 on oxygen vacancies hinders hydrogen dissociation over this uncoordinated Mo species.[54]

III. Hindrance of hydrogen dissociation and spillover due to the high coverage of carboxylic acids.

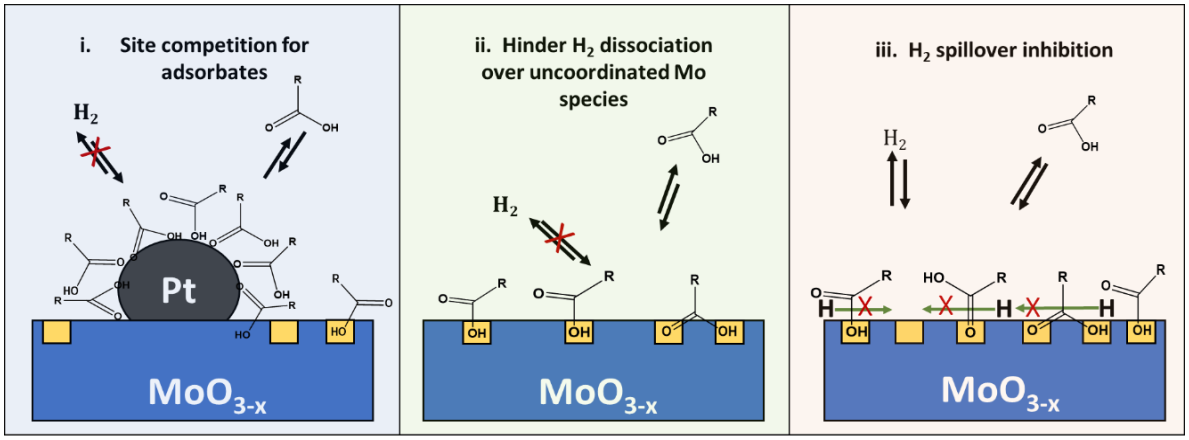


Figure 25. Possible causes of inhibition at a high partial pressure of PA **(i)** Site competition for adsorbates over metallic Pt cluster on MoO_3, **(ii)** Hinder H_2 dissociation at oxygen vacancies on MoO_3, and **(iii)** H_2 spillover inhibition on MoO_3.

For all three cases, hydrogen dissociation and spillover are limited due to the high partial pressures of PA. Consequently, the limitations of hydrogen dissociation/spillover decrease the rate of formation and generation of oxygen vacancies, which explains the decrease

in the rate of conversion of PA, even in the presence of Pt clusters. In contrast, at lower coverage of PA, the surface reaction is less limited by hydrogen dissociation and spillover, as indicated by the shift in reaction order regime; more details will be discussed in **Sections C.3.2** and **C.3.5**.

C.3.2 H_2 effect on reaction order

Hydrogen plays an important role in HDO since it helps to form oxygen vacancies, enabling the catalyst surface to maintain redox chemistry. To further investigate the kinetic relevance of hydrogen in this chemistry, the reaction order with respect to H_2 was studied at a low and high partial pressure of PA for MoO_3 at 350°C. **Figure 26 (a-b)** shows that regardless of the partial pressure of PA, the reaction order with respect to H_2 remains first-order. As shown in **Figure S14**, the same first-order in H_2 is observed at a lower temperature (320°C).

Moreover, the reaction order with respect to H_2 was also investigated over the 0.05 wt% Pt/MoO_3 catalyst. As shown in **Figure 26 (c-d)**, we observed a change in the H_2 reaction order from 0.5 to 1.0 as the partial pressure of PA increased. This shift in the H_2 reaction order caused by the changes in the surface coverage of PA suggests that either hydrogen and PA compete for the same sites or that hydrogen is involved in the rate-limiting step. Here, we hypothesize that at high partial pressures of PA, the surface dynamics of 0.05 wt% Pt/MoO_3 behave similarly to MoO_3 since the strong inhibition effect of PA hinders hydrogen dissociation, as described above in **Section C.3.1**.

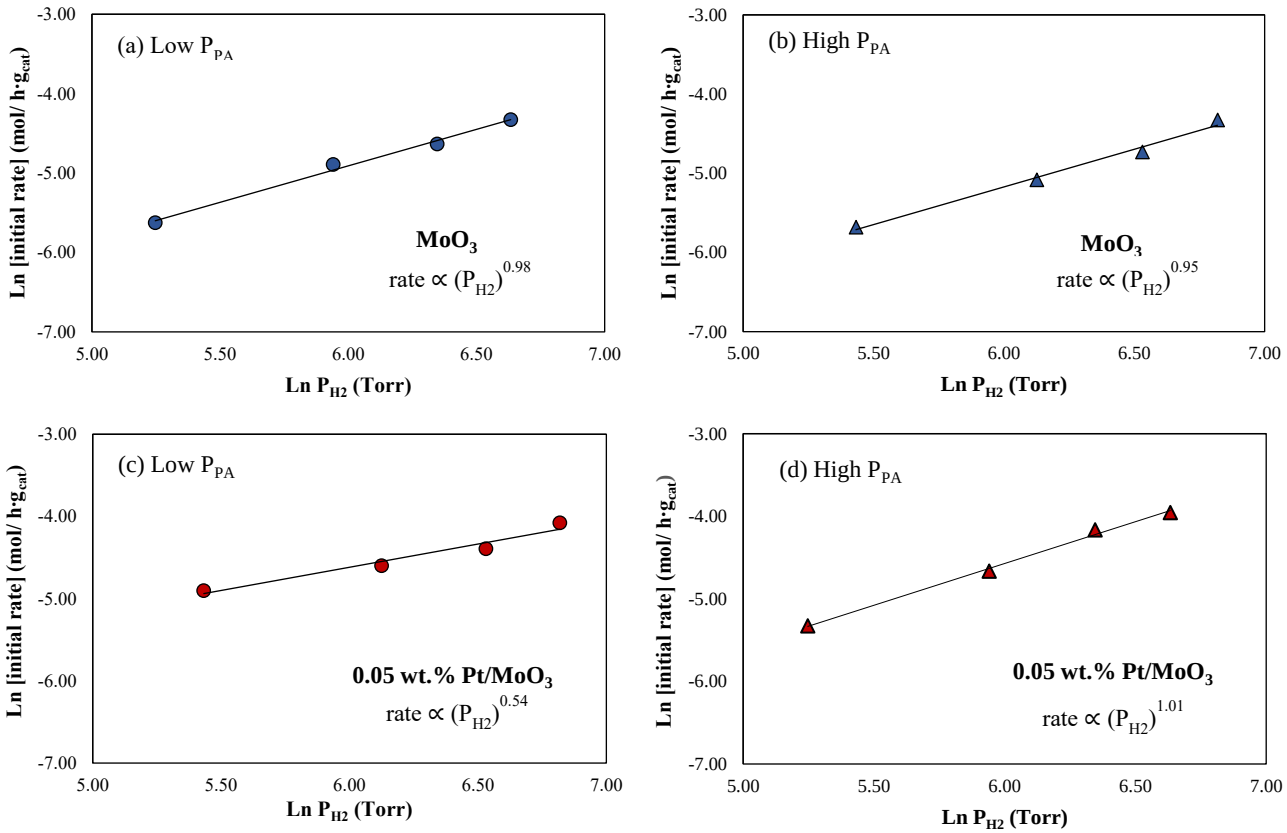


Figure 26. (a) Order of reaction with respect to H_2 using MoO_3 as a catalyst at low P_{PA}. **(b)** Order of reaction with respect to H_2 using MoO_3 as a catalyst at high P_{PA}. **(c)** Order of reaction with respect to H_2 over 0.05 wt% Pt/MoO_3 at low P_{PA}. **(d)** Order of reaction with respect to H_2 over 0.05 wt% Pt/MoO_3 at high P_{PA}. Reaction conditions: P_{Total} = 760 Torr (H_2 pressure was varied and balanced with He to maintain the same total pressure), W/F = 0.11 g_{cat}/mL·h, $T_{reaction}$: 350°C, and TOS = 0 min.

C.3.3 Water inhibition

Water is a by-product of oxygen vacancy formation. Similarly, the reverse reaction may occur, where water strongly adsorbs on an existing oxygen vacancy. Bluhm et al. have performed DFT calculations indicating that water can adsorb strongly on MoO_{3-x} surfaces. Reported energies for water adsorption on an oxygen vacancy is -130 kJ/mol. Water dissociation to form OH groups and effectively heal an oxygen vacancy is also energetically favored, with an adsorption energy of -77 kJ/mol.[49] This strong heat of adsorption of water over surface defects might explain the inhibition observed when water is co-fed with acid, as shown

in **Figure 27,** where the presence of water results in the suppression of deoxygenation activity. A similar inhibiting effect is observed in both catalysts, MoO_3 and 0.05 wt% Pt/MoO_3.

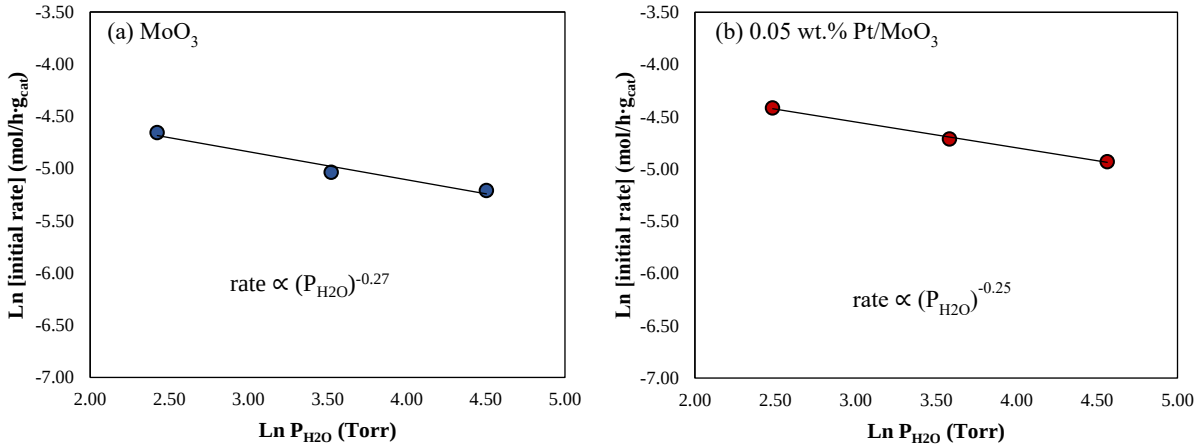


Figure 27. Dependence of reaction rate on the partial pressure of water over (a) MoO_3 and (b) 0.05 wt% Pt/MoO_3. Reaction conditions: Flow of H_2 = 30 mL/min, P_{Total} = 760 Torr, TOS = 0 min, and W/F = 0.11 g_{cat}/mL·h.

C.3.4 Site requirements for deoxygenation of carboxylic acids

Oxygen vacancies have been proposed as the active sites for the HDO of several biomass-derived compounds over MoO_3.[34] Roman-Leshkov and co-workers have provided insights into the state of the surface during the deoxygenation of anisole over MoO_3 by NAP-XPS data, which indicate that the undercoordinated species are responsible for C-O bond activation. Their study suggests that Mo^{5+} species are active in this chemistry, while Mo^{4+} species do not seem to be involved in the deoxygenation of anisole.[53]

To assess the importance of oxygen vacancies on the deoxygenation of PA to PAL, we used a micro-pulse reactor to study the initial interaction of reactants with the surface before surface modification (e.g., phase changes, overreduction, carbon deposition, carboxylic acid saturation/inhibition). **Figure S15** confirms that the initial formation of oxygen vacancies during the reduction pretreatment is essential for the deoxygenation reaction;

pentanal formation is suppressed in the absence of these vacancies, even when hydrogen is added to each pulse.

Metal dopants are frequently incorporated to facilitate the formation of oxygen vacancies over metal oxides and increase rates. Using high-dispersion Ni metal deposition into MoO_3/SiO_2, Yang et al. showed an enhancement of m-cresol HDO selectivity. Their study suggests that the synergistic cooperation between Ni and MoO_x species is important to achieve high activity and selectivity.[105] Similar findings were reported by Rachmady et al. in the conversion of acetic acid in Pt/FeO_3, where the promoted catalyst showed improved activity and selectivity toward acetaldehyde[43]. However, the interaction of a reducible metal oxide with a hydrogen promoter metal can be complex due to the formation of multiple surface features that one might assign as active sites.[41,106] These prospective active sites can be categorized as short and long-range interactions. Short-range interactions involve the active sites located in proximity to the metal particle and its modifications around the interface. Long-range interactions, often referred to as promoter effects, are the active sites found on the support itself (surface defects, subsurface defects, or surface OH groups) created by the hydrogen spillover from the hydrogen promoter metal to the reducible oxide support.[107,108]

To determine the role of Pt on MoO_3, we use vertical multi-walled carbon nanotubes (CNT) as hydrogen highways to evaluate the kinetic relevance of short and long-range interactions. A similar approach has been used to discern the active site for the furfural conversion to methyl furan on Pd/TiO_2 and anisole deoxygenation on Cu/TiO_2.[109] To achieve this, Pt and MoO_3 were deposited on opposing ends of carbon nanotube forests of a controlled length. This allowed H atoms to migrate from Pt metal clusters to the MoO_3 surface and partially reduce the surface of MoO_3 without being in physical contact. As a result, Pt over MoO_3 does

not create a highly active interface; instead, it only promotes oxygen vacancies. The next chapter will discuss this technique in more detail and its use for identifying active sites involved in this chemistry.

C.3.5 Elementary steps and reaction mechanism

To develop a mathematical expression for the deoxygenation of the PA mechanism, we consider two distinct active sites: an oxygen vacancy and a metallic active site. The active metal sites include undercoordinated Mo species created during the reduction process and Pt clusters on the 0.05 wt% Pt/MoO_3 catalyst. No other active sites were considered since a significant kinetic contribution due to distinct active sites located in the metal-support interface was ruled out in **Section E.3.4**.

The sequence of elementary steps proposed for this chemistry involves H_2 dissociation on the metal site **[1]**, followed by H migration from metal sites to the MoO_3 surface **[2]**. When H spills over onto reducible oxides, it migrates in proton/electron pairs, following parallel but different paths.[59] Oxygen vacancy formation/regeneration is considered by combining two OH to yield one water molecule on the oxygen vacancy and an oxidized vacancy site, as described in step **[3]**. PA is assumed to adsorb dissociatively over metal sites and oxygen vacancies, as described in steps **[4]** and **[5]**. After PA is adsorbed strongly on an oxygen vacancy without hydrogen abstraction, as shown in step **[6]**[13], one hydrogen atom is added to the adsorbed PA species **[7]**. These steps are highly dependent on H coverage.[51] To yield pentanal, the first hydrogenation is followed by a second hydrogen addition to the adsorbed species to produce pentanal in the gas phase and an adsorbed water molecule **[8]**. As described in steps **[9]** and **[10]**, water and pentanal may compete for oxygen vacancies, modifying the surface coverage of kinetically relevant intermediates. The sequence of proposed

elementary steps proposed is described in **Figure 28**. The apparent activation energy required for this chemistry to occur affected by both PA and H_2 partial pressure, as described above in **Sections C.3.1** and **C.3.2**.

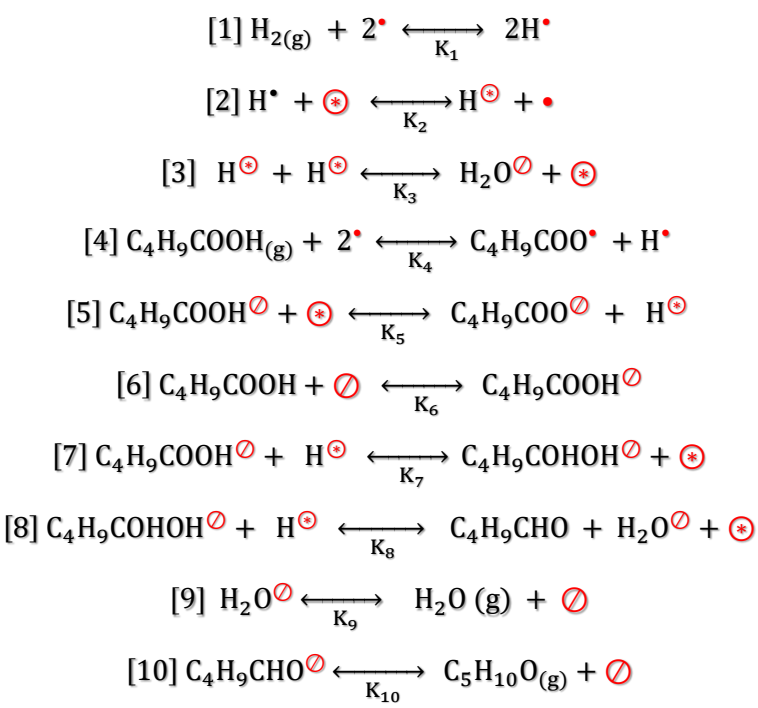


Figure 28. Proposed elementary steps for the hydrogenation of PA over promoted MoO_3. (•) denotes metal site, (⊛) oxidized or heal O vacancy, (∅) reduced or empty O vacancy. All rates are represented as quasi-equilibrated steps, which will be decoupled with varying hypothesized kinetically relevant steps below.

Several elementary steps were considered as potential rate-limiting for this chemistry. The rate expression for each possible rate-determining step considered for the deoxygenation of PA is shown in **Table 1**. Detailed mathematical expressions for each case are shown in the supplementary information **Section S1.** In **equations 8** and **9**, k_i is the intrinsic rate constant for the corresponding elementary step described in **Figure 28**; K_i represents the equilibrium constant for step i; $[\oslash]_0$ is the total number of oxygen vacancies; $[\bullet]_0$ is the total number of metallic sites available at the surface and $[\circledast]$ are the oxidized oxygen vacancy sites, which are considered constant.

RDS	Rate Expression
Hydrogen dissociation	$r_1 = k_1 K_1 P_{H2} [\bullet]^2$
Oxygen vacancy formation/ regeneration	$r_3 = k_3 K_1 K_2^2 P_{H2} [\circledast]^2$
First hydrogen addition to PA species	$r_7 = k_7 {K_1}^{0.5} K_6 K_2 P_{PA} {P_{H2}}^{0.5} [\oslash][\circledast]$
Second hydrogen addition to PA species	$r_8 = k_8 K_1 K_2^2 K_6 K_7 P_{PA} P_{H2} [\circledast][\oslash]$

Table 1. Rate expression for each potential rate-determined step.

Where [•] corresponds to metal balance sites. $[\bullet]_0$ represents the density of all adsorption sites (vacant and occupied) on a catalyst surface.

$$[\bullet]_0 = [\bullet] + [H^\bullet] + [C_4H_9COO^\bullet] \quad \text{Eq. 2}$$

$$[\bullet] = \frac{[\bullet]_0}{(1 + K_1^{1/2} P_{H2}^{1/2} + K_4 P_{PA} / K_1^{1/2} P_{H2}^{1/2})} \quad \text{Eq. 3}$$

Expression for $[\oslash]$ can be obtained by site balance of the oxygen vacancies as follows:

$$[\oslash]_0 = [\oslash] + [C_4H_9COO^{\oslash}] + [C_4H_9COOH^{\oslash}] + [C_4H_9COHOH^{\oslash}] + [H_2O^{\oslash}] + [C_4H_9CHO^{\oslash}] \quad \text{Eq. 4}$$

Since $[C_4H_9COOH^{\oslash}]$ is the only significant surface intermediate on the oxygen vacancies, the following expression gives a balance of $[\oslash]$ sites:

$$[\oslash]_0 = [\oslash] + [C_4H_9COOH^{\oslash}] \quad \text{Eq. 5}$$

Where $[C_4H_9COOH^{\oslash}]$ is obtained by the adsorption constant related to step 5:

$$[\oslash]_0 = [\oslash] + K_6 P_{PA} [\oslash] \quad \text{Eq. 6}$$

$$[\oslash] = \frac{[\oslash]_0}{(1 + K_6 P_{PA})} \quad \text{Eq. 7}$$

In a computational study, Shetty et al. reported that hydrogen dissociation shows the highest barrier for the overall reaction in the HDO of acetone to propylene over a pristine MoO_3 catalyst (164 kJ/mol).[54] Typically, hydrogen dissociation occurs through homolytic

bond breaking without prior surface activation, which can explain the high energy barrier for hydrogen splitting on MoO_3.[110] However, a real catalyst contains defects, including oxygen vacancies, which can reduce the activation energy for H_2 dissociation. Despite this, this step could still limit the deoxygenation of PA on MoO_3. Thus, the rate expression depicted in **Eq. 8** was determined by considering H_2 dissociation as the rate-limiting step (**RDS1, step 1**), which shows a first-order dependence on hydrogen pressure, consistent with the experimental results for MoO_3 in **Figure 26 (a-b)**. Here, we consider other potential rate-determining steps in addition to H_2 dissociation that also exhibit a first-order dependence with respect to hydrogen pressure, such as oxygen vacancy formation, as we have previously indicated as a possibility,[51] or the second H atom addition to the adsorbed PA species, as shown in **Table 1**. Due to the strong dependence of this reaction on a persistent presence of hydrogen on the catalyst surface, and not simply defects, we had previously speculated that hydrogen addition to the carbonyl carbon could be an important rate-determining step over unpromoted Mo catalysts as well. However, the reaction order suggests that the prior step of hydrogen dissociation is the more likely RDS. The lack of kinetic relevance associated with the oxygen vacancies formation over MoO_3 lies in DFT calculations. Once H atoms are formed, they can diffuse over the surface easily (~38-60 kJ/mol) and form an oxygen vacancy with a total activation energy of 22 kJ/mol.[110] This value is much lower than the barriers we observe experimentally.

$$r_1 = \frac{k_1 K_1 P_{H2} [\bullet]_0}{(1 + K_1^{\frac{1}{2}} P_{H2}^{\frac{1}{2}} + K_3 P_{PA} / K_1^{\frac{1}{2}} P_{H2}^{\frac{1}{2}})^2} \quad \text{Eq. 8}$$

Since Pt clusters promote H_2 dissociation, a different rate-limiting step is considered for 0.05 wt% Pt/MoO_3. **Figure 26c** shows that the reaction order with respect to hydrogen is

between 0.5 and 0.6. Two rate-determining steps could result in a 0.5 dependence on hydrogen, the addition of the first H atom to the adsorbed PA species, or hydrogen spillover on MoO_3, according to **Table 1**. As hydrogen dissociative over the Pt cluster, H atoms tend to form -OH groups at the surface with low energy barriers (~38-60 kJ/mol),[110] favoring hydrogen spillover over the MoO_3 surface. In **Section E.3.4**, we show that hydrogen spillover is not likely to be the rate-determining step of this reaction since Pt-MoO_3 that are in direct contact (Pt/MoO_3/CNT) show similar rates as Pt-MoO_3 separated by carbon nanotubes (Pt/CNT/MoO_3). Therefore, the rate expression described by **Eq. 9** assumes that the hydrogen addition to an adsorbed PA is the rate-limiting step (**RDS2, step 7**). Our experimental results are in agreement with the experimental data at low partial pressures of PA for 0.05 wt% Pt/MoO_3 shown in **Figure 26c**. Thus, the presence of Pt in this catalyst serves as a source for accelerating hydrogen activation to maintain the constant hydrogen supply at the surface, lowering the energy barrier and enhancing the PA conversion rate, as described in **Section C.3.2**. Rachmady et al. have shown similar H_2 dependence on the hydrogenation of acetic acid at the interfacial sites of Pt/TiO_2.[43,111]

$$r_7 = \frac{k_7 K_1^{\frac{1}{2}} K_6 K_2 P_{PA} P_{H2}^{\frac{1}{2}} [\circledast]_0 [\varnothing]_0}{(1 + K_6 P_{PA})} \qquad \text{Eq. 9}$$

Our experimental results reveal that upon the incorporation of Pt, the reaction order with respect to H_2 shifts from 1 to 0.5 at a low partial pressure of PA, as shown in **Figure 26 (a, c)**. This change in reaction order is due to the change in hydrogen coverage at the surface. Therefore, this reaction is highly dependent on the local hydrogen concentration since more H atoms will participate in the hydrogenation of the carboxylic acid. Furthermore, incorporating Pt clusters on MoO_3 not only enhances the rate of hydrogen dissociation but may also

promote the formation of hydrogen bronzes (H_xMoO_3). These H species diffuse into the support and intercalate into the structure by forming -OH bonds with the oxide. [112] Kosydar et al. have shown that the selectivity towards C=O hydrogenation increase with $Pt/HxWO_3$ than $Pt/HxMoO_3$ in the conversion of cinnamaldehyde and furfural since H species are more mobile and form weaker H-bonding in the W-O-H than in Mo-O-H .[113] Similar observations have been made in the selective hydrogenation of acrolein to allyl alcohol, where Pt/H_xMoO_3 can easily activate aldehyde oxygen atoms and promote hydrogen addition.[114]

Overall, the kinetic model framework presented here demonstrates that a Langmuir Hinshelwood-type reaction mechanism describes the deoxygenation of PA over promoted $Pt\text{-}MoO_3$, with orders matching those observed experimentally. As the concentration of PA increases over the catalyst, the results suggest that the RDS shifts from r7 at low PA concentrations in the presence of a metal capable of maintaining a high H coverage on the surface. At high concentrations of PA, the RDS shifts to r1, with a negative order dependence on increasing PA at significant PA coverages. This suggests that the concentration of PA not only influences hydrogen coverage but also modifies the RDS. **Figure 29** shows the proposed mechanism for the deoxygenation of carboxylic acid over promoted $Pt\text{-}MoO_3$ catalyst. A similar mechanism has been previously used to explain the hydrogenation of acetic acid in the interfacial region of Pt/TiO_2. However, in that case, it was considered unlikely for

spillover to carry out this chemistry on vacancies far from the Pt metal particle, which is proposed in the current study.[43,111]

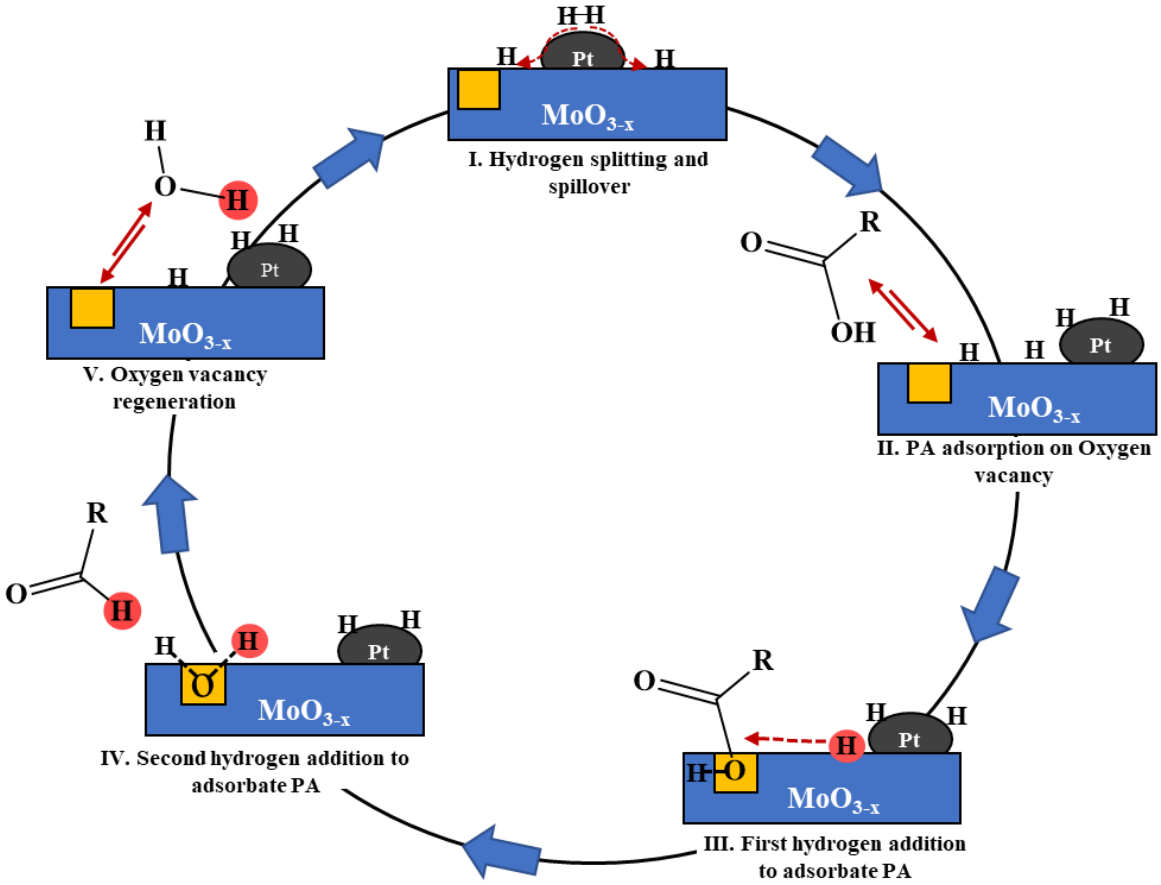


Figure 29. Proposed mechanism for deoxygenation of carboxylic acid over Pt/MoO_3.

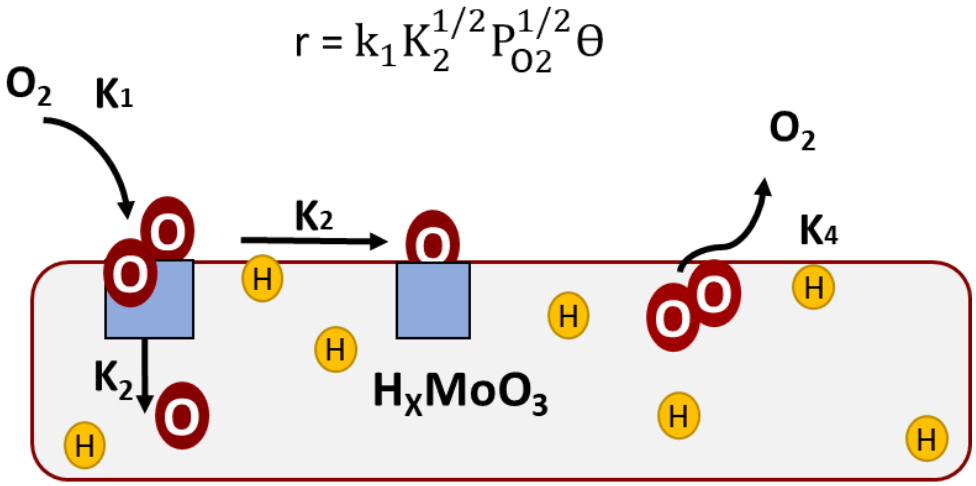
C.4 Conclusions

The mechanistic details of pentanoic acid conversion on promoted MoO_3 give evidence that the deoxygenation of PA takes place primarily at the metal oxide surface, specifically on oxygen vacancies, rather than on highly active sites located at the interface. Our results suggest that the role of Pt is to maintain the high hydrogen concentration at the surface. This study shows that a Langmuir-Hinshelwood-type mechanism can describe the conversion of pentanoic acid over both MoO_3 and 0.05 wt% Pt/MoO_3, assuming two types of active sites,

metal sites that activate H_2 and oxygen vacancies that enable the deoxygenation of PA. The RDS of the reaction shifts with the partial pressure of acid and H_2 coverage from hydrogen addition to the adsorbed acid species to hydrogen splitting. Overall, this study provides a mechanistic understanding of the deoxygenation of PA on dynamic MoO_3 catalysts in the presence and absence of small amounts of metal promoters.

CHAPTER IV

D. Quantifying the influence of surface and subsurface H on selective C-O bond scission rates over MoO_3-x catalysts.



The X-ray diffraction (XRD) experiments for all samples analyzed in this chapter were conducted by Ismaeel.

D.1 Introduction

Molybdenum oxide (MoO_3) is a transition metal oxide with unique properties, such as its capacity to undergo oxygen vacancy formation, significantly affecting its electronic properties.[115–117] When an O atom is removed, two electrons are left, leading to the formation of two different configurations. The first configuration is the grounded-state, which comprises two Mo^{5+} centers, $Mo^{5+}(\square)-O-Mo^{5+}(=O)$, where an oxygen vacancy is formed, and both neighboring cations have a 5+ character. However, these Mo^{5+} centers can be disproportionated, with one center oxidized to Mo^{6+} and the other reduced to Mo^{4+}, leading to a metastable state with a Mo^{4+} (□) center. These configurations are separated by an energy

difference of 0.2 eV.[118] The capability of the Mo center to reach different oxidation states can have implications for HDO chemistry.

Several studies have shown that MoO_3 is a very effective catalyst for deoxygenating biomass-derived compounds.[33–35,44,45,51,53,54] However, its poor activity for hydrogen dissociation limits its overall catalytic performance for selective HDO. For instance, Green et al. showed that hydrogen activation is the rate-limiting step in the overall reaction of acetone deoxygenation over a pristine α-MoO_3.[54] Therefore, reducible metal oxides are often combined with noble metals, such as Pd and Pt, which enhance the formation of defects or oxygen vacancies. In our recent study, we demonstrated that the addition of 0.05 wt% Pt significantly enhanced the formation of oxygen vacancies, improving deoxygenation rates.[51] This combination of MoO_3 with noble metals like Pd or Pt induces the formation of hydrogen bronzes in which H species can be intercalated into the MoO_3 structure.[95,112,119,120]

Metal oxides such as MoO_3, WO_3, and Nb_2O_5 have the ability to form hydrogen bronzes, which enhances the potential to use these materials as hydrogen storage, hydrogenation catalysts, and hydrogen sensors.[48,84,117,121–123] Chen et al. found that hydrogen bronzes on Nb_2O_5 exist in two distinct states: a proton bound to oxygen ions or highly mobile H species.[123] Computational studies have shown that the migration of H protons and electrons on MoO_3 is easier than in the surface due to the presence of hydrogen bonding of the proton with oxygen anions, favoring the formation of hydrogen bronzes on Pt/MoO_3.[72,73,124]

In this study, we introduce a new approach for quantifying hydrogen molybdenum bronzes that involves monitoring the evolution of water during O_2 chemisorption experiments. We also explore the stability of these bronzes at different temperatures and evaluate the impact of varying Pt loadings on their formation.

The extent of reduction or defect density in MoO_3 can significantly affect its HDO activity. Prolonged exposure to high temperatures and reduction conditions can lead to the formation of MoO_2, an inactive phase for HDO conversion.[53,125] Hence, identifying the number of active sites and their respective oxidation states is crucial to optimize the properties of MoO_3 for deoxygenation chemistry. Probing chemisorption of oxygenated compounds (NO_2, O_2, CO) is a well-established method for accurately quantifying the concentration of oxygen vacancies in the surface and bulk of reducible metal oxides.[126–129] Oxidation of MoO_3 at high temperatures through oxygen chemisorption typically quantifies the oxygen uptake, which correlates to the number of oxygen vacancies located at both the surface and bulk. Therefore, one of the aims of this study is to decouple the oxygen vacancy located in the top layer by titrating these active sites utilizing CO and O_2 as probe molecules at low temperatures (≤50 ºC). Measuring the amount of oxygen uptake at different reduction and chemisorption temperatures using oxygen chemisorption can also provide valuable information on the existence of hydrogen bronzes in the structure and the concentration of oxygen vacancies that play a role in HDO chemistry.

Besides, this study also estimates the activation energy associated with the oxidation of Mo^{4+} and Mo^{5+} to Mo^{6+} species. The proposed rate-determining step for the oxidation of these species is also discussed. This study will also provide the role of the number of oxygen vacancies, hydrogen bronzes, and oxidation states in the deoxygenation and ketonization of pentanoic acid over MoO_3 and 0.05 wt% Pt/MoO_3. Overall, this approach can also be extended to characterize other reducible metal oxides, providing valuable insights into their properties and potential applications in the fields such as energy storage and catalysis. Thus, this study shed light on the potential of MoO_3 as an O_2 and H_2 storage material.

D.2 Experimental section

D.2.1 Chemical and catalysts materials

All the gases (H_2 (99.999%), He (99.999%), N_2 (99.998%), Air (Ultra zero), O_2 (5 vol% O_2/He, UHP), CO (5 vol% O_2/He, UHP) used for catalyst preparation, reaction, and chemisorption experiments were purchased from Airgas. Commercial molybdenum (VI) oxide, MoO_3 (>99.5 wt%), was purchased from Alfa Aesar. Acid-washed glass beads (50-70 US sieve, Sigma) were mixed with the catalyst and packed in the reactor. The pentanoic acid used as a reactant in the kinetic measurements of HDO was purchased from Sigma Aldrich (CAS No 109-52-4).

D.2.2 Catalyst synthesis

The incipient wetness impregnation method was employed to prepare a supported catalyst comprising 0.05% Pt over MoO_3. In brief, a 2 ml aqueous solution containing 10 mg of tetraammineplatinum (II) nitrate (99.99%, 50% Pt, Alfa Aesar) was gradually added to 10 g of the support material. The resulting mixture was dried for 12 hours at 80℃, followed by calcination at 600℃ (ramp rate 10℃/min) for 3 hours under an airflow of 100 mL/min. Commercial MoO_3 was subjected to the same calcination conditions. The catalyst was pelletized and sieved to obtain pellets with sizes ranging from 90-125 µm.

D.2.3 Oxygen chemisorption experiments

A pulse reactor, constructed in-house, was employed to perform oxygen chemisorption studies over 0.05 wt% Pt/MoO_3 and MoO_3 at atmospheric pressure. A reactor packed with glass beads (150 mg) and 50 mg of pelletized catalyst into a quartz tube with an outer diameter of 0.25 inches was used for catalytic testing. The catalyst was reduced in situ before each chemisorption experiment by flowing 100 SCCM of H_2 for 1 hour at 400 ℃. The loaded

sample was pretreated under He gas for 30 minutes to remove all physically adsorbed hydrogen from the catalyst's surface. After, the catalyst sample was exposed to several oxygen pulses (5 vol% O_2/He) until saturation was achieved by using a loop size of 1 mL. In this study, different reduction and chemisorption temperatures were utilized. In the case of CO titration, the sample loop was filled with CO (5 vol% CO/He) diluted with He, which was then injected through the catalyst bed instead of pulsing O_2.

D.2.4 Kinetic measurements

The effect of hydrogen molybdenum bronzes on the conversion of pentanoic acid (PA) to pentanal was investigated using a micro-pulse reactor. A sample loop containing the PA was diluted with either helium or hydrogen and then passed over the catalyst bed. During the intervals between continuous pulses, the catalyst was exposed to helium flow. The outlet stream of the reactor was heated to 250 ℃ to prevent any condensation of effluents. The products were analyzed using an online gas chromatography (GC) system equipped with a flame ionization detector (FID), specifically an Agilent 6890 with an HP-INNOWAX column (Agilent, 60 m × 0.32 mm ID × 0.5 μm).

D.2.5 Catalyst characterization

D.2.5.1 Powder X-ray diffraction (XRD)

The XRD analyses were conducted at the School of Geology and Geophysics at the University of Oklahoma using a Rigaku Ultima IV diffractometer equipped with Cu-K-alpha radiation (40 kV, 44 mA). The diffraction angle range 2Θ was varied from 5-70º. MDI Jade2010 software was employed for data analysis, using ICDD (International Centre for Diffraction Data) PDF4+ database as a reference.

D.3 Results

D.3.1 Partial reduction of MoO_3

Several studies have investigated the reduction process of MoO_3 to MoO_2 in a wide range of temperatures (300-550 °C).[119,120,125,130] Ressler et al. investigated the elucidating phase composition of MoO_3 during reduction conditions. Their results indicate that in reaction temperatures below 425°C, the reduction of MoO_3 to MoO_2 occurs through a single step without forming any other intermediate phase.[119] While undergoing reduction at temperatures above 500°C results in the formation of a new phase as a Mo_4O_{11}.[95,119,120,125,130–132]

The catalyst reduction treatment under H_2 gas is commonly employed to induce the formation of active sites on the surfaces of reducible metal oxides, thereby enhancing their potential for deoxygenation reactions. During a partial reduction process of MoO_3, the reduction conditions anticipate and influence the formation of small domains of inactive phases for HDO. **Figure 30 (a-f)** shows that the reduction of MoO_3 at 400°C and 500°C does not create significant MoO_2 domains. However, the addition of 0.05 wt% led to a significant increase in the reduction of MoO_3, resulting in the formation of MoO_2 at the same reduction conditions. Moreover, the reduction of both MoO_3 and 0.05 wt% Pt/MoO_3 at 500°C yields small domains of Mo_4O_{11}, as observed in **Figure 30 (d,f)**.[95] Therefore, if the reduction conditions are severe, it can lead to over-reduction, which decreases the number of active sites available for redox chemistry and causes the formation of MoO_2, an active phase for HDO reactions.[51,53]

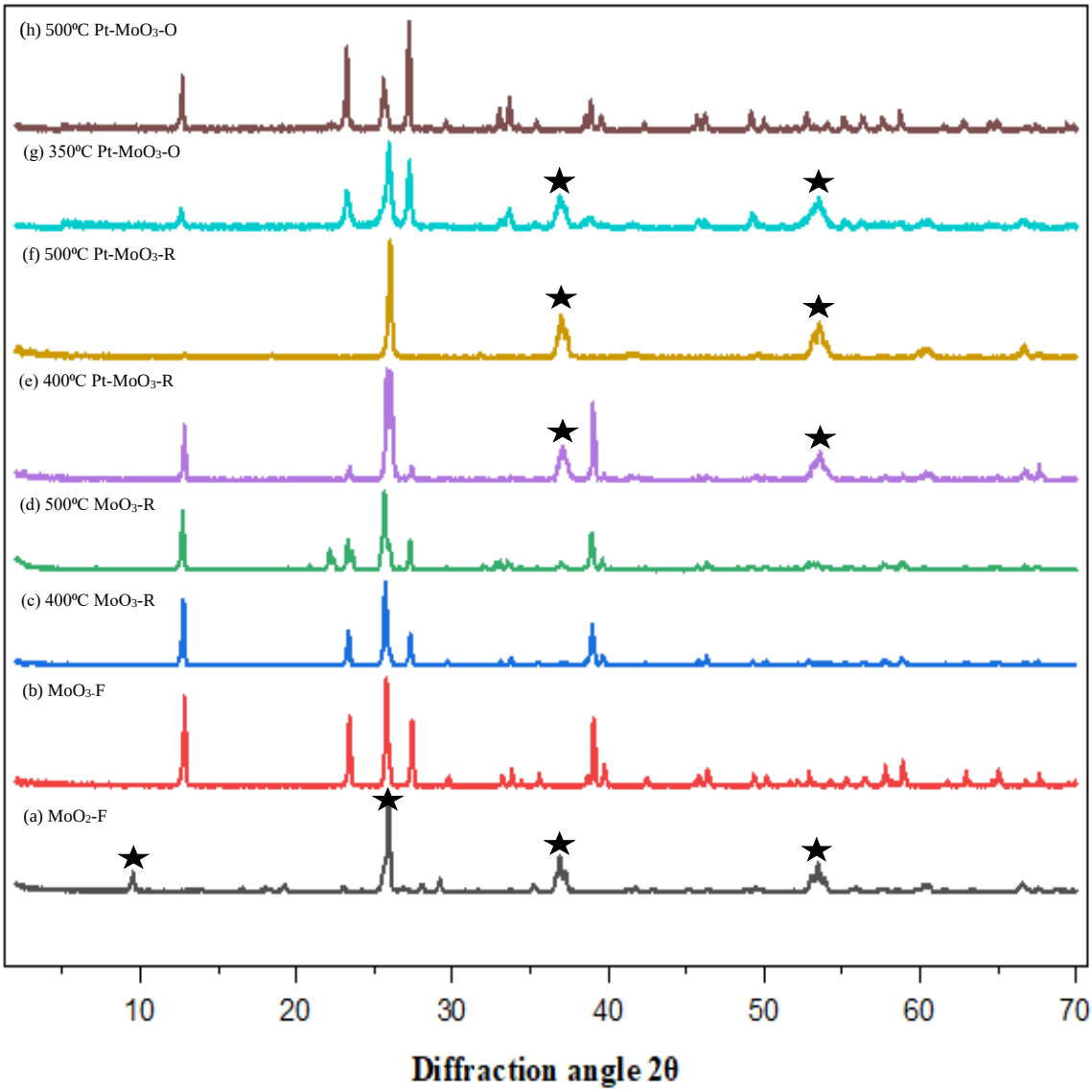


Figure 30. XRD patterns during reduction of MoO_3 and 0.05 wt% Pt/MoO_3 in 100 ml/min of H_2 at different temperatures. (a) MoO_2 and (b) MoO_3 diffraction pattern of fresh MoO_2 and MoO_3 for comparison. (c) MoO_3 reduced at 400 ºC, (d) MoO_3 reduced at 500 ºC, (e) 0.05 wt% Pt/MoO_3 reduced at 400 ºC, (f) 0.05 wt% Pt/MoO_3 reduced at 500 ºC, (g) 0.05 wt% Pt/MoO_3 oxidized at 350 ºC, (h) 0.05 wt% Pt/MoO_3 oxidized at 500 ºC. The labeling key used in the figures is as follows: F (Fresh), R (Reduced), and O (Oxidized). MoO_2 is labeled as a star.

D.3.2 Quantification of oxygen vacancies

MoO_3 is a highly dynamic catalyst with a very active surface for deoxygenation reaction.[33–35,44,45,53,54] In **Figure S17**, the increase in O_2 uptake at 500°C can be attributed to the higher temperature needed for the oxidation of MoO_2, which is consistent with similar trends observed at different reduction temperatures, as shown in **Figure S18**. However, at 350°C, the uptake of O_2 decreased at higher reduction temperatures due to an increase in the formation of MoO_2. **Figure 30 (g-h)** shows the XRD patterns after oxidation at different chemisorption temperatures. These results confirm that the small domains of MoO_2 are only fully oxidized to MoO_3 at 500°C.

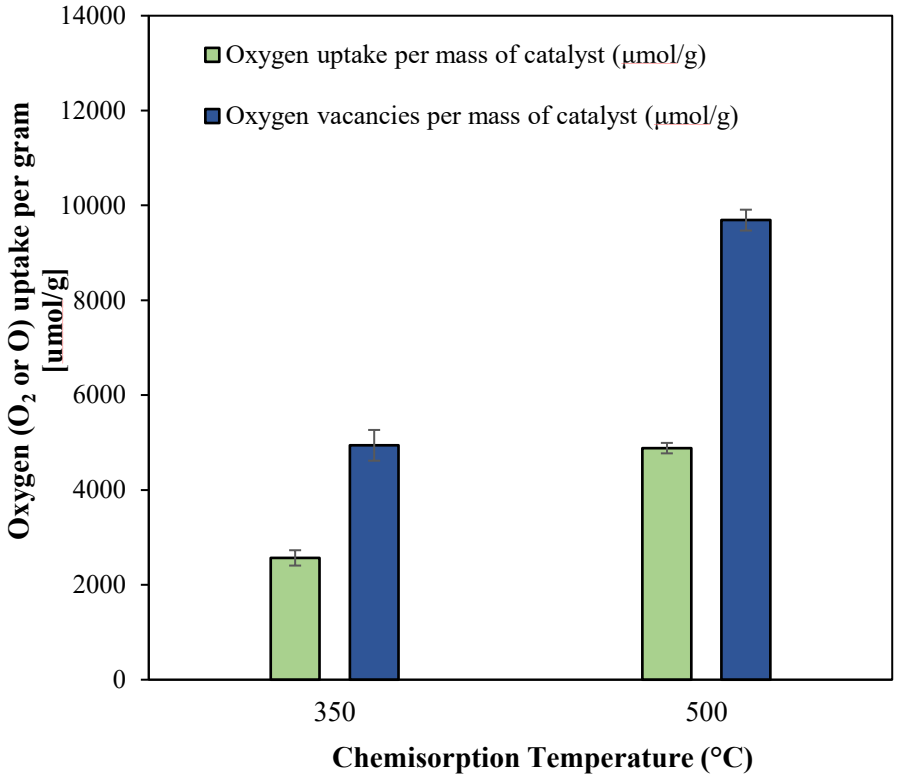


Figure 31. Oxygen (O_2 or O) uptake at different chemisorption temperatures over 0.05 wt% Pt/MoO_3. Reaction conditions: W_{cat} = 50 mg and $T_{chemisorption}$ = 350-500 °C. The catalyst was previously reduced under H_2 flow (100 ml/min) at 400 °C. Pretreatment under He gas for 1 hour.

Hence, taking advantage of the different re-oxidation temperatures, we conducted oxygen chemisorption at 350°C and 500°C, as illustrated in **Figure 31**. These experiments enabled us to isolate and quantify the number of sites created under reduction conditions. For instance, at 350°C, Mo^{5+} will be oxidized to Mo^{6+} species. While at 500°C, both Mo^{4+} and Mo^{5+} species will be fully oxidized to Mo^{6+}, restoring the starving oxygen surface.[131] By calculating the difference in oxygen uptake between 500°C and 350°C, we can determine the quantity of Mo^{4+} species present. After reduction at 400°C, the 0.05 wt% Pt/MoO_3 catalyst exhibited 47% and 53% of titratable Mo^{4+} and Mo^{5+} species, respectively. In this study, the oxygen molecules are considered to be adsorbed and split on the surface, leading to the titration of two oxygen vacancies per molecule.

The extent of oxygen uptake can be influenced by the temperature at which chemisorption occurs. At mild temperatures, oxygen uptake may be related to surface and bulk oxidation, making it challenging to determine the precise number of oxygen vacancies involved in surface reactions. Since only the active sites at the first layer are involved in deoxygenation reactions, the number of active sites at the surface was determined by measuring oxygen uptake at 50°C. Based on **Table 2**, it can be inferred that a relatively small amount of water is produced at 50°C because only a few highly active sites are capable of O_2 dissociation at this temperature. Therefore, the number of active sites present at the first layer is equivalent to the observed O_2 uptake at this temperature since no further diffusion of oxygen atoms to lower layers is expected at 50°C. At this low temperature, it can be assumed that one molecule of O_2 will titrate one oxygen vacancy on the catalyst's surface rather than two oxygen vacancies, as expected at higher temperatures.

CO titration has also been a widely utilized probe molecule for studying oxygen vacancies in metal oxides, such as TiO_2, in addition to O_2.[133,134.] Therefore, CO titration was used to quantify oxygen vacancies and confirm their number on the surface of MoO_3. CO is not expected to bind over-reduced sites (Mo^{4+}, MoO_2), only in the sites capable of redox chemistry. [135] Remarkably, the results obtained using both probe molecules, CO and O_2, were nearly identical, which suggests that the number of oxygen vacancies determined using CO is reliable. Furthermore, these findings indicate that the CO and O_2 probe molecules are equally effective in detecting the presence and quantity of oxygen vacancies on the surface of reducible metal oxides.

Oxygen uptake as measured by O_2 and CO titration	**CO titration (30ºC)**	**O_2 titration (50ºC)**
CO or O_2 uptake per mass of catalyst (μmol/g)	76	78
Produced water per mass of catalyst (μmol/g)	0	20
Hydrogen atoms per mass of catalyst (μmol/g)	0	40

Table 2. Oxygen vacancy titration measures the CO or O_2 uptake at a low temperature over 0.05 wt% Pt/MoO_3. Reaction conditions: W_{cat} = 60 mg and $T_{chemisorption}$= 350°C for CO and 50°C for O_2. The catalyst was previously reduced under H_2 flow (100 ml/min) at 400 °C. Pretreatment under He gas for 1 hour.

D.3.3 Quantification of hydrogen molybdenum bronzes

MoO_3 is known for being a poor catalyst for hydrogen dissociation. Green et al. showed that in the deoxygenation of acetone to propylene over pristine MoO_3, H_2 dissociation is the rate-limiting step in the overall reaction.[54] To enhance the reduction of MoO_3, it is often combined with noble metals to promote oxygen vacancies. Crossley et al. demonstrated that the incorporation of 0.05 wt% Pt drastically increases the formation of oxygen vacancies by facilitating hydrogen dissociation.[51] As a result, the high concentration of H atoms on the

surface promotes the formation of metastable hydrogen molybdenum bronzes (H_xMoO_3), in which H atoms are incorporated into the MoO_3 structure with minor changes in the lattice parameters. The hydrogen's ambivalent character and small atomic diameter facilitate this process.[136] Moreover, Chen et al. showed that the activation energy for the diffusion of H species into the bulk of Mo ranges from 6-12 kJ/mol. This low activation energy is attributed to the abundant hydrogen bonding of the proton with oxygen molecules in the oxide lattice, which promotes the diffusion of H species within the structure.[48]

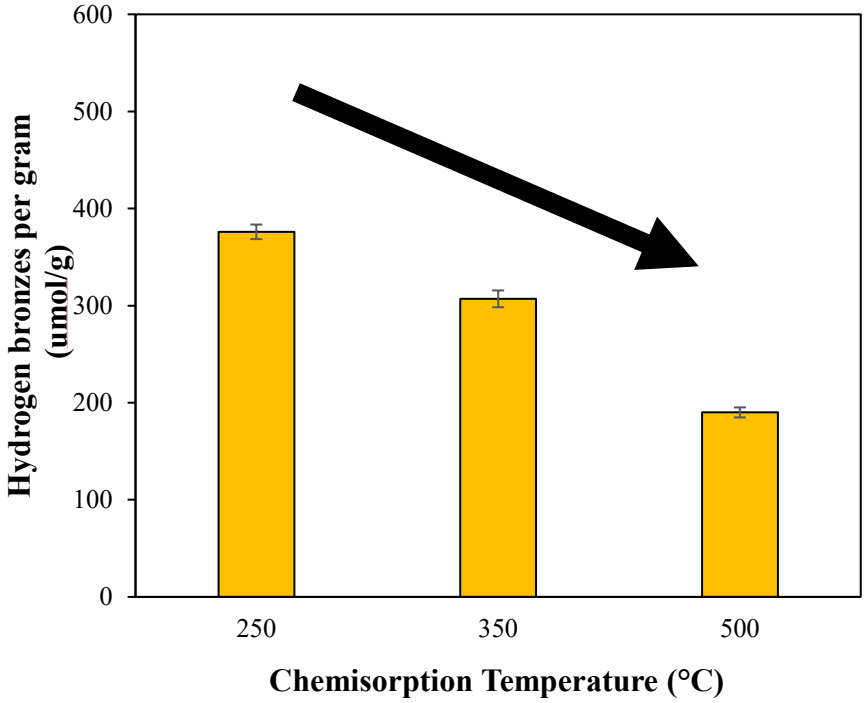


Figure 32. Hydrogen molybdenum bronzes formed over 0.05 wt% Pt/MoO_3. Reaction conditions: W_{cat} = 50 mg and $T_{chemisorption}$ = 250-500 °C. The catalyst was previously reduced under H_2 flow (100 ml/min) at 400 °C. Pretreatment under He gas for 1 hour.

The XRD data shown in **Figure 30** does not exhibit a characteristic peak for hydrogen molybdenum bronzes ($HxMoO_3$) as a third phase in the Pt/MoO_3 and MoO_3 samples, which suggests that either these compounds are not produced significantly under the given reduction

conditions, or the peak is not visible due to overlapping or poor resolution from the instrument. However, water evolution was observed during oxygen titration experiments on Pt/MoO_3, attributed to hydrogen molybdenum bronzes, as is shown in **Figure S20**. In contrast, water evolution is not observed for MoO_3 alone in similar pretreatment and oxidation conditions, as illustrated in **Figure S19**. Low H atoms concentration is expected in MoO_3 due to the poor activity for dissociating hydrogen molecules.[54]

Here, we use oxygen chemisorption experiments to quantify the concentration of H species intercalated into the structure of MoO_3 under reduction conditions by measuring the evolution of water. **Figure 32** shows that the concentration of hydrogen molybdenum bronzes is higher at a lower chemisorption temperature. This may be attributed to the higher stability of hydrogen bronzes at lower temperatures. Sotani et al. showed similar findings, indicating that the number of hydrogen molybdenum bronzes decreases to a lower hydrogen content by heating due to the combination of H species to form H_2. Even during the heating step, intercalated hydrogen atoms in catalyst support can react with the oxygen lattice at higher temperatures, forming oxygen vacancies. The quantity of water participating in the reaction was deducted from the overall oxygen uptake to determine the net amount of oxygen uptake. This technique can be used for the quantification of hydrogen bronzes in other metal oxides such as WO_3 and V_2O_5.[137]

This study evaluated the effect of different loadings of Pt on the formation of hydrogen bronzes. **Table S3** reveals that the number of hydrogen bronzes decreases at higher Pt loadings, likely due to the promoted formation of MoO_2. In addition, higher loading decreases the number of oxygen atoms on the bulk, potentially limiting the diffusion of H into the structure.

D.3.4 Oxidation kinetics of partially reduced MoO_3-x

The activation energy for the oxidation of Mo^{5+} to Mo^{6+} was determined by calculating the energy barrier over a temperature range of 310°C to 380°C. Since the oxidation rate is directly proportional to the conversion of the pulse, plotting the natural logarithm of the oxidation conversion as a function of inverse temperature is equivalent to the activation energy. **Section S2** provides details on how the rate and conversion were calculated. The calculation of the oxidation rate was based on considering a fixed number of oxygen uptakes per catalyst. This approach ensured that the catalyst's oxidation degree remained constant in the final state and that only the oxidation rate required to reach the final state was measured. Besides, all catalysts underwent identical reduction treatment to ensure they were in the same initial state for each experiment.

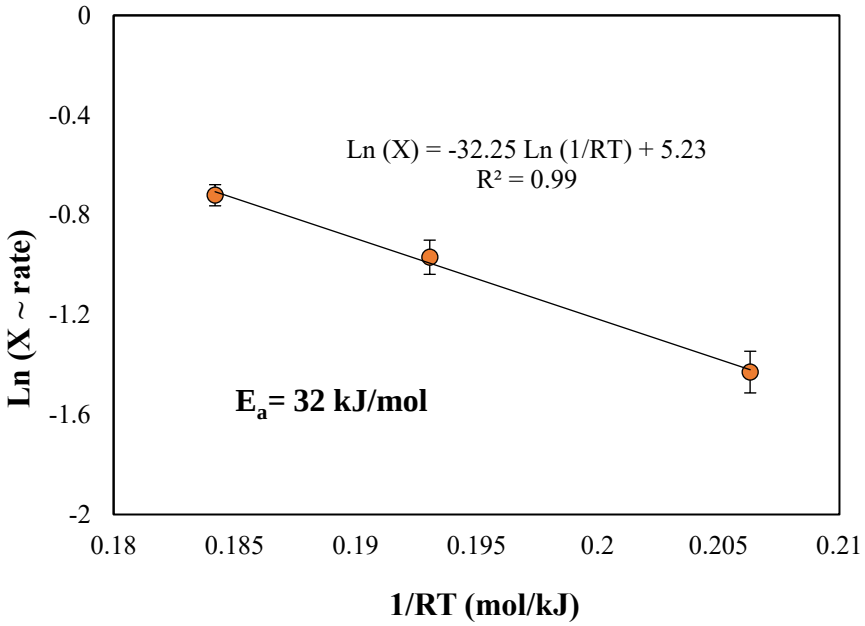


Figure 33. Activation energy for the oxidation of Mo^{5+} to Mo^{6+} species. Reaction conditions: W_{cat} = 50 mg and $T_{chemisorption}$ = 310-380 °C. The catalyst was previously reduced under H_2 flow (100 ml/min) at 400 °C. Pretreatment under He gas for 30 min.

According to **Figure 33**, the activation energy required for the oxidation of Mo^{5+} is approximately 32 kJ/mol. This value can be contrasted with the activation energy of 70 kJ/mol found by Barteau et al. for the oxidation of a partially reduced vanadyl pyrophosphate (VPO) catalyst.[138,139] These activation energy values suggest that the oxidation of Mo^{5+} centers may occur easier than that of VPO. However, it's important to note that the specific conditions of the oxidation process may significantly impact the relative reaction rates

D.3.5 Reaction order with respect to O_2

The oxidation of Mo^{5+} to Mo^{6+} species was identified as the kinetic rate controlling for the oxidation process in the temperature range of 310-380 °C. **Figure 34** shows that the reaction order with respect to the oxygen partial pressure obtained is 0.3. Before each oxidation experiment, the catalyst underwent identical reduction conditions (400 °C for 1 hour under a flow of 100 ml/min) to ensure a uniformly partially reduced surface. To maintain a constant oxidation degree in the final state of the catalyst and measure only the oxidation rate required to reach the final state, a fixed number of oxygen uptakes per catalyst was considered in calculating the oxidation rate.

The sequence of elementary steps that described the oxidation of Mo^{5+} to Mo^{6+} is described as follows:

$$O_2 + 2\,[*] \overset{K_1}{\leftrightarrow} 2O^*$$

$$O^* \overset{K_2}{\leftrightarrow} [O]$$

$$r = \frac{k_1 K_2^{1/2} P_{O2}^{1/2} [\bullet]_0}{(1+K_2^{1/2} P_{O2}^{1/2})} \qquad \text{Eq. 10}$$

The active sites available for O_2 dissociation are denoted by an asterisk [*], and [O] represents the lattice oxygen. The rate expression that follows into half-order is obtained when O lattice migration is considered the rate-limiting step, described in **Eq. 10**. This finding is consistent with the results of Barteau et al., who observed a similar half-order dependence of the oxidation rate with respect to oxygen partial pressure for VPO, where the conversion of adsorbed oxygen into lattice oxygen is considered the rate-limiting step.[138–140] The rate expression indicates in **Eq. 10** suggests that higher partial pressures of O_2 can lead to a reduction in the order dependence, which falls within the range of 0 to 0.5. This finding accounts for the observed 0.3-order dependence with respect to O_2 partial pressure in our study.

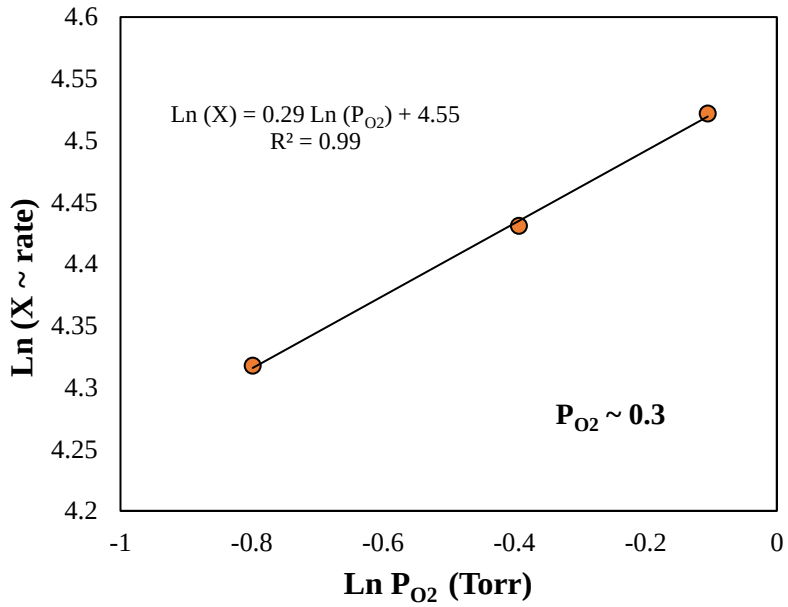


Figure 34. Reaction order with respect to oxygen partial pressure (P_{O2}) for the partially reduced 0.05 wt% Pt/MoO_3 catalyst. Reaction conditions: W_{cat} = 50 mg and $T_{chemisorption}$ = 500-600 °C. The catalyst was previously reduced under H_2 flow (100 ml/min) at 400 °C. Pretreatment under He gas for 1 hour.

D.3.6 The role of hydrogen bronzes in the deoxygenation of PA

The modification of the catalyst surface through reduction can have a direct effect on the deoxygenation of oxygenated compounds derived from biomass. In this study, we aim to

assess how the presence of hydrogen bronzes and the reduction conditions affect the deoxygenation of pentanoic acid (PA) to produce pentanal and the ketonization process to yield 5-nonanone over Pt/MoO_3 and MoO_3 catalysts. Although both catalysts are reduced under the same conditions, the surface of the catalyst is not reduced to the same extent due to the presence of Pt clusters. Our recent study indicated that the number of Mo^{4+} and Mo^{5+} species is higher by 52% and 16%, respectively, when it is reduced at 400 °C in the presence of Pt.

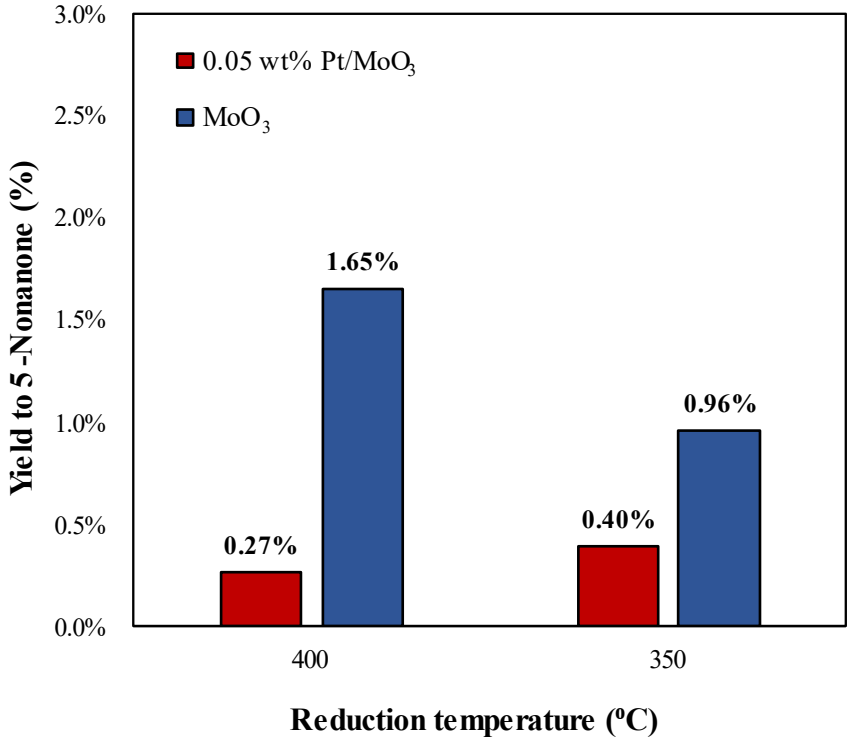


Figure 35. Conversion of PA to 5-Nonanone over MoO_3 and 0.05 wt% Pt/MoO_3 treated under different reduction temperatures under H_2 gas. Instead, an inert gas (He) was used to conduct the reaction. Reaction conditions: W_{cat}= 10 mg and $T_{reaction}$= 350 °C. Before injecting PA, the catalyst was pretreated under He for 30 min to remover hydrogen present at the surface.

Numerous studies have been conducted on the ketonization reaction of carboxylic acids using reducible metal oxides. It is well-established that the oxygen vacancies or exposed cations on the surface of the metal oxide serve as the active site for this reaction. The

rate of ketonization is proportional to the number of oxygen vacancies or exposed cations. However, these active sites are not consumed during the reaction.[13,37,109] **Figure 35** shows that ketonization rate over MoO_3 and 0.05 wt% Pt/MoO_3 at different reduction temperatures. At 350°C, promoted MoO_3 catalyst is expected to exhibit a higher number of oxygen vacancies compared to pure MoO_3 due to the presence of Pt clusters. However, at higher reduction temperatures (beyond 350°C), the Pt clusters may lead to overreduction, resulting in a reduction in the number of sites that facilitate ketonization. The reaction was conducted under an inert (He) gas atmosphere, which means that the absence of hydrogen does not hinder the conversion rates as occurred with the conversion of PA to PAL.[51]

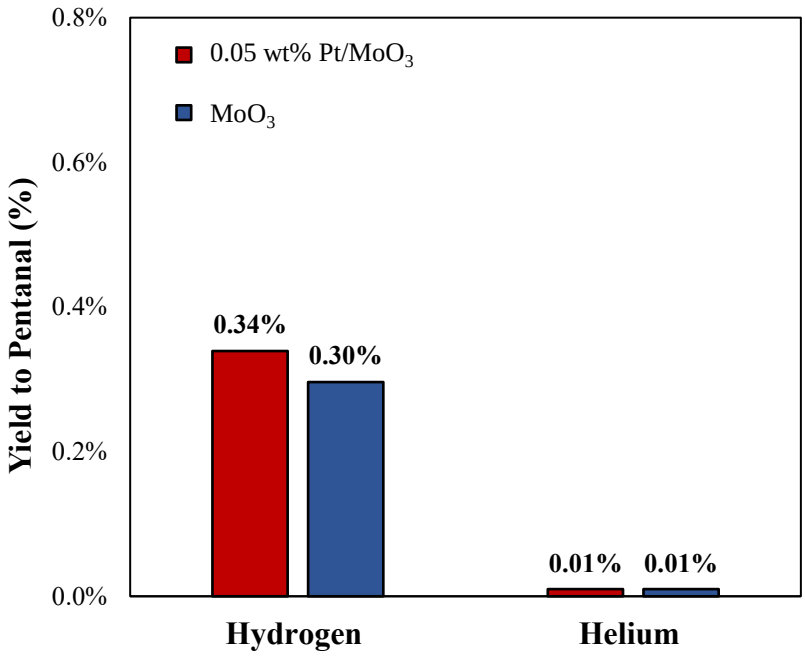


Figure 36. Conversion of PA to PAL over 0.05 wt% Pt/MoO_3 and MoO_3. Reaction conditions: W_{cat}=10 mg and $T_{reaction}$= 350 °C. The catalyst was previously reduced under H_2 flow (100 ml/min) at 350°C.

A similar analysis was carried out for the HDO of PA to yield pentanal (PAL). In our recent study for the selective deoxygenation of PA over MoO_3, we showed the presence of

hydrogen is necessary to obtain PAL.[51] Here, we evaluated the role of Pt on MoO_3 and the effect of hydrogen bronzes in the HDO. Our results indicate that PAL is exclusively produced when the reaction is carried out in the presence of H_2 for both catalysts, while no PAL is observed in the presence of an inert gas, as illustrated in **Figure 36**. These results lead us to conclude that hydrogen bronzes do not act as the source of H atoms to produce PAL but rather modify the electronic properties of the support to facilitate PA conversion over Pt/MoO_3.

D.4 Conclusions

The results of this study demonstrate that utilizing a combination of different methods, such as oxygen vacancy titration at varying temperatures, assessment of the reduction levels of the catalysts, analysis of the oxidation process, measurement of the activation energy over different temperature ranges, and quantification of the role of hydrogen bronzes, can offer valuable insights into the catalytic activity involved in the conversion of PA to PAL and 5-Nonanone. Additionally, this study introduces an experimental technique for quantifying hydrogen bronzes by monitoring water evolution and provides a quantification method for oxygen vacancies on Pt/MoO_3, including the conditions necessary for decoupling the number of oxygen vacancies in the top layer and in bulk, which can also be applied to other reducible metal oxides. These findings also enlighten the use of MoO_3 as a storage material for H_2 and O_2.

D.5 Future work

As I conclude this project, I have identified aspects for future research that could advance our understanding of this topic.

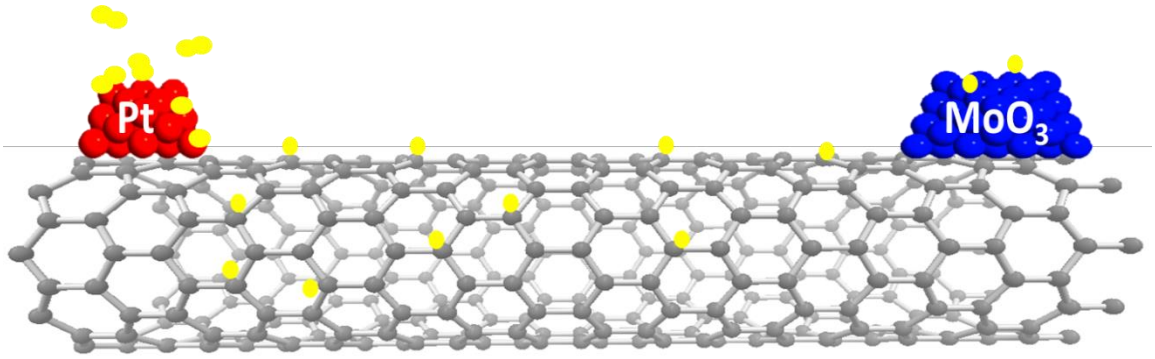
Firstly, I propose a more detailed investigation into the behavior of the O_2 molecule at 50 ºC, specifically whether it splits on the oxygen vacancies. To achieve this, I plan to measure the heat adsorption at 50 ºC and 350 ºC and explore if there is a difference between them. I will correlate these findings with the adsorption energy related to O_2 splitting or adsorption as a molecule. Additionally, I would use IR spectroscopy to identify if the oxygen adsorbed as a molecule or has split. Similar approaches I would use for the CO binding in MoO_3 support.

Secondly, I intend to utilize TGA to calculate the activation energy related to the oxidation of MoO_3 more precisely, enabling me to compare the results with those obtained using a micro-pulse reactor.

Lastly, I propose a more comprehensive XRD analysis to verify the presence of hydrogen bronzes on MoO_3 and Pt/MoO_3. To achieve more accurate results and better understand the analysis, I plan to repeat the XRD analysis. This will involve taking additional measurements to confirm the initial findings. By repeating the analysis, I can verify the results and potentially identify any discrepancies that may have been missed during the initial analysis. This will ensure that the data is reliable and can be used as a basis for further research in the future. These investigations and extra experiments can potentially expand our understanding of the topic.

CHAPTER V

E. Use of carbon nanotubes hydrogen highways to identify active sites over bifunctional catalysts.



Leidy Valeria Herrera carried out the kinetic measurements for the conversion of furfural over Pd/TiO_2; Lawrence Barret synthesized the carbon nanotubes samples (Cu/CNT/TiO_2 and Cu/ TiO_2/CNT) used to identify the sites responsible for anisole conversion and the TPR experiments; Caleb Q. Bavlnka and Tianhao E. Zhang synthesized the carbon nanotubes samples (Pt/CNT/MoO_3 and Pt/MoO_3/CNT) used to identify the sites responsible for pentanoic acid conversion.

E.1 Introduction

Metals deposited on oxide supports exhibit promising activity for numerous reactions, including C-C cleavage, C-O cleavage, and C-O oxidation. While examples of superior catalytic activity and selectivity when combining two different catalytically active substances are abundant, the fundamental cause of this enhanced performance is often not well understood, and there may be conflicting findings in the literature. Many of these active oxide supports are also reducible oxides, with OH groups and oxygen vacancies present on their

surface under reaction conditions. The interaction between a reducible metal oxide and a metal capable of hydrogen dissociation, such as Pd or Pt, can be complex and create multiple potential catalytically active sites under reduction conditions. Generally, these active sites can be separated into two general categories, short-range interactions, and long-range interactions. Short-range interactions are in proximity to the metal particle and include the highly reducible interface along the perimeter of the metal, electronic perturbations to the exposed metal surface due to interaction with the support, as well as thin oxide films forming over the metal surface.[41,106–108]Surface defects, subsurface defects, and surface OH groups that are created due to spillover from the metal nanoparticle to the support can be considered long-range interactions, or promoter effects, as the primary active sites are found on the support itself.[141,142]

Understanding the nature of these active sites, their location and their role in the reaction mechanism is crucial for developing efficient and selective metal oxide-based catalysts. Various methods have been applied to determine the active sites responsible for the activity observed over these catalysts. One approach is to change the particle size of the metal supported on the oxide, which changes the perimeter of the metal oxide interface.[41,106–108] By systematically modifying the perimeter and particle size, correlations with the observed rate can be developed between perimeter sites and sites on the metal with various coordination. Lack of direct correlation with perimeter or metal surface is often correlated with promoter effects. However, the metal oxide interface can change due to strong metal support interaction involving decoration or encapsulation of the metal particle by the reducible oxide support.[108,143–145] Spectroscopic techniques are also used to propose active sites,[108,] however, the possibility of observable vibrations from spectator species that are often difficult to

distinguish from catalytically relevant intermediates complicates this approach. This leads to much speculation about the location of the active site, often without any direct proof.

This study employs vertically grown carbon nanotubes to segregate between the direct catalytic interactions and the promoter effects in a catalytic reaction. The carbon nanotubes act as a physical separator between the catalyst and the promoter, thereby preventing them from directly interacting with each other. Utilizing a conductive bridge of carbon nanotubes as hydrogen highways, the selective deposition of metal and oxide catalysts at precise distances allows for the accurate separation of the catalyst and promoter. This separation enables a more precise determination of their individual contributions to the overall reaction, leading to a better understanding of the catalytic system's design and optimization. We use this technique to identify the active site in three different catalytic reactions. The reaction includes furfural conversion over Pd/TiO_2, anisole over Cu/TiO_2, and pentanoic acid deoxygenation over Pt/MoO_3.

E.2 Experimental

E.2.1 Chemicals and catalysts materials

All the gases (H_2 (99.999%), He (99.999%), N_2 (99.998%), Air (Ultra zero), and Ethylene used for catalyst preparation, reaction, carbon nanotube synthesis, and characterization were purchased from Airgas.

Chemicals used for multi-walled carbon nanotubes growth were iron nitrate nonahydrate, cobalt nitrate hexahydrate, aluminum nitrate nonahydrate, and 2-hydroxyethyl cellulose (Mw ~ 1,300,000)). All the chemicals used were purchased from Sigma Aldrich. Tungsten (1 mm, 99.94%), molybdenum (0.75 mm, 99.95%), platinum (0.025 mm, 99.00%), Pd (0.5 mm, 99.95%), Ti (0.25 mm,99.95%), Cu (0.1 mm, 99.95%) wires were used for metal

deposition. Aluminum conductive tape (single adhesive surface, 12.7 mm W x 16.4 m L, Ted Pella Inc.) was used to remove CNTs from the silicon wafers. The silicon wafers used as a base for growing vertical multi-walled carbon nanotubes were purchased from Wafer World, Inc (SKU:1186). Cleaning of these wafers required isopropanol, ethanol, and acetone. Water (18 MΩ) was obtained from an in-house filtration system and used in this study.

E.2.2 Catalyst synthesis

E.2.2.1 Vertical multi-walled carbon nanotube growth

A catalyst solution was spin-coated on silicon wafers for growing vertically aligned carbon nanotubes (CNTs). Silicon wafers were cut into 23 mm x 23 mm square pieces using a diamond scribe. The wafers were calcined in a horizontal furnace under continuous airflow (150 SCCM) at 600 °C for two hours. Then, the wafers were ultrasonically washed in subsequent acetone, ethanol, and isopropanol solutions for 45 minutes each to ensure a clean surface for spin coating. A catalyst solution consisted of 1.11 wt% iron nitrate nonahydrate, 0.39 wt% cobalt nitrate hexahydrate, 1.23 wt% aluminum nitrate nonahydrate, and 0.74 wt% 2-hydroxyethyl cellulose, all with respect to water. One milliliter of catalyst solution was spin-coated on each silicon wafer in a two-step process ten seconds at 500 rpm, followed by 30 seconds at 2000 rpm. The silicon wafers were dried overnight and calcined the following day at 450 °C under continuous airflow (150 SCCM) for one hour.

In order to synthesize carbon nanotubes on silicon wafers, the samples were balanced on top of one another in a one-inch quartz-diameter tube, ensuring each catalyst surface was accessible to flowing gas. The vertical reactor was heated to 650 °C at 10 °C min^{-1} under hydrogen flow (200 SCCM) and maintained at 650 °C for 30 min to ensure reduction of the catalyst. Then, nitrogen (370 SCCM) was flowed through the reactor tube and heated to the

reaction temperature of 675 °C at 10 °C min^{-1}. The system was held at 675°C for 30 minutes under nitrogen flow. Carbon nanotube synthesis occurred as ethylene (200 SCCM) was mixed for 20 minutes with the flowing nitrogen. After CNT synthesis, nitrogen was fed into the reactor until the system was cooled. To weaken the interaction between the CNTs and the silicon wafer, the sample was calcined in air (150 SCCM) at 480 °C for 2 hours. This allowed for future controllable removal of the CNTS from the silicon wafer.

E.2.2.2 Depositing different catalysts on opposite ends of CNTs

A custom-built vacuum evaporator was used for depositing the different metals onto CNTs. To synthesize Pt/CNT/MoO_3 catalyst, Pt and Mo were deposited on opposite ends of the CNTs, which was achieved by adding Pt metal to the exposed end of the CNTs on the silicon wafer. Aluminum tape was then used to remove the CNTs from the silicon wafer. This flipped the orientation of the CNTs, causing the exposed end of the forest to be free of any Pt. Thus, CNTs on aluminum tape were returned to the evaporator, and Mo was evaporated on the other end of the CNTs. The edges of the aluminum tape containing the CNTs samples were removed with a razor blade to prevent contamination from excess metal not deposited on the CNTs. The synthesized (Pt/CNT/MoO_3) samples were submerged in acetone for 45 seconds. This process removed CNTs from the adhesive tape. The solution was then filtered to obtain the synthesized sample. The sample was calcined in air (150 SCCM) at 350°C for one hour to remove adhesive residue from the tape. Weight percentages of all deposited metals can be found in **Table S5**. The same procedure was conducted for Pd/CNT/TiO_2 and Cu/CNT/TiO_2 catalysts.

E.2.3 Characterization

E.2.3.1 Scanning electron microscopy (SEM)

E.2.3.1.1 Pd/CNT/TiO_2 and Cu/CNT/TiO_2

SEM of the catalyst was performed using a Zeis Neon 40 EsB scanning electron microscope operating at an accelerating voltage of 5 kV for imaging and 10 kV when performing energy-dispersive X-ray spectroscopy.

E.2.3.1.2 Pt/CNT/MoO_3

The samples were analyzed using a Thermo Quattro S field-emission environmental scanning electron microscope (FE-ESEM) with an accelerating voltage of 5 kV for imaging and 15 kV when performing energy-dispersive X-ray spectroscopy.

E.2.3.2 X-ray photoelectron spectroscopy (XPS) for Pt/CNT/MoO_3 and Pt/MoO_3/CNT

The AXIS-supra with a dual anode Al/Ag (2984.2 eV) monochromatic X-ray source was used to perform XPS analysis on the carbon nanotube samples. This was used to confirm the final oxidation state of the metals after calcination and previous reactions. For the case of MoO_3, it is crucial to fully oxidize the catalyst before reaction to minimum the catalyst surface of commercial MoO_3.

E.2.3.3 Inductively coupled plasma mass spectrometry (ICP-MS) for Pt/CNT/MoO_3 and Pt/MoO_3/CNT

A PerkinElmer NexION2000 inductively coupled plasma (ICP)-MS with laser ablation was used to analyze the Pt content on the synthesized CNTs catalysts. The appropriate internal standards and dilution factors were selected based on a preliminary semiquantitative analysis. The samples were digested using the dry ashing method combined with acid extraction. Because multi-walled carbon nanotubes decompose above 500 °C, the catalyst samples

(10-20 mg) were placed in a furnace at 700 °C for 2 hours. The ashes from each sample were diluted with 2% HCl solution at room temperature and further diluted with ionized water before ICP-MS analysis.

EDS was used to confirm the presence of palladium, copper, and titanium for the loading metal of the other synthesized catalysts in this chapter.

E.2.4 Kinetic measurements

The catalytic testing occurred in a gas-phase packed bed reactor under atmospheric pressure conditions, using H_2 or H_2/He as a carrier gas. Catalyst particles were mixed with glass beads (Sigma Aldrich, 212-300 μm) and packed between two layers of quartz wool inside a quartz reactor (0.25" OD). The reactor tube was placed in the center of a vertical furnace (Thermcraft Inc., 1200W/115V). All catalysts were pretreated in situ in hydrogen (100 SCCM) at 400 ℃ for 1 hour. After reduction, the samples were cooled to the reaction temperature. The reactants were injected using a syringe pump (KD Scientific) and vaporized before entering the reactor. To prevent any product condensation, the outlet stream was also heated up to 250 ℃. A gas chromatography (GC), equipped with a flame ionization detector (FID) and HP-INNOWAX column (Agilent, 60 m × 0.32 mm ID × 0.5 μm), was connected to the reactor for product quantification. Product identification was confirmed using a Shimadzu QP-2010 GC-MS, and standards were used to quantify the various products in the flame ionization detector.

Anisole, distilled furfural (obtained from Sigma Aldrich; distilled and stored at -15 ℃), distilled water (H_2O was obtained from an in-house filtration system), and pentanoic acid was introduced to the reactor at a flow rate of 0.16 ml/h for anisole, 0.1 ml/h for furfural,

0.25 ml/h for distilled water, and 0.05 ml/h for pentanoic acid. The catalyst mass and other relevant conditions are described in the caption of each graph.

E.3 Discussion

Lawrence Barret and Nick Briggs conducted the SEM and EDX analysis for Pd/CNT/TiO_2.

Selective deposition of metal oxides at a specific distance along the length of a nanotube was accomplished through the use of vertically grown carbon nanotube forests. A schematic illustrating the desired material obtained with this approach is shown in **Figure 37a**. The unique novelty of this technique is that it eliminates the direct contact of the metal nanoparticle with the oxide support while maintaining the formation and regeneration of prospective active sites on the oxide. Promoter effects of the metal on the active support (e.g., TiO_2) are still possible in this scenario since carbon nanotubes are known to facilitate the spillover of dissociated hydrogen from the metal.[146–150]

Energy-dispersive X-ray spectroscopy (EDS) was used to verify that the metal oxides in consideration were not in contact. **Figure 37 (b-e)** shows EDS spectra taken at various positions along the length of the nanotube forest where Pd metal was deposited on one end of the forest and TiO_2 on the other. Catalyst particles are known to sinter and migrate at various rates depending on the catalyst support.[151,152] To ensure that migration is insufficient to induce significant physical contact, EDS spectra were taken after treating them under 1 h at 400 °C in hydrogen. This analysis confirmed that the Pd and TiO_2 did not migrate across the length of the nanotube and that the two catalysts did not come into contact. In all cases, it was observed that Pd, Cu, or TiO_2 did not penetrate the forest beyond a depth of five microns. Similar analyses were conducted for Pt/CNT/MoO_3.

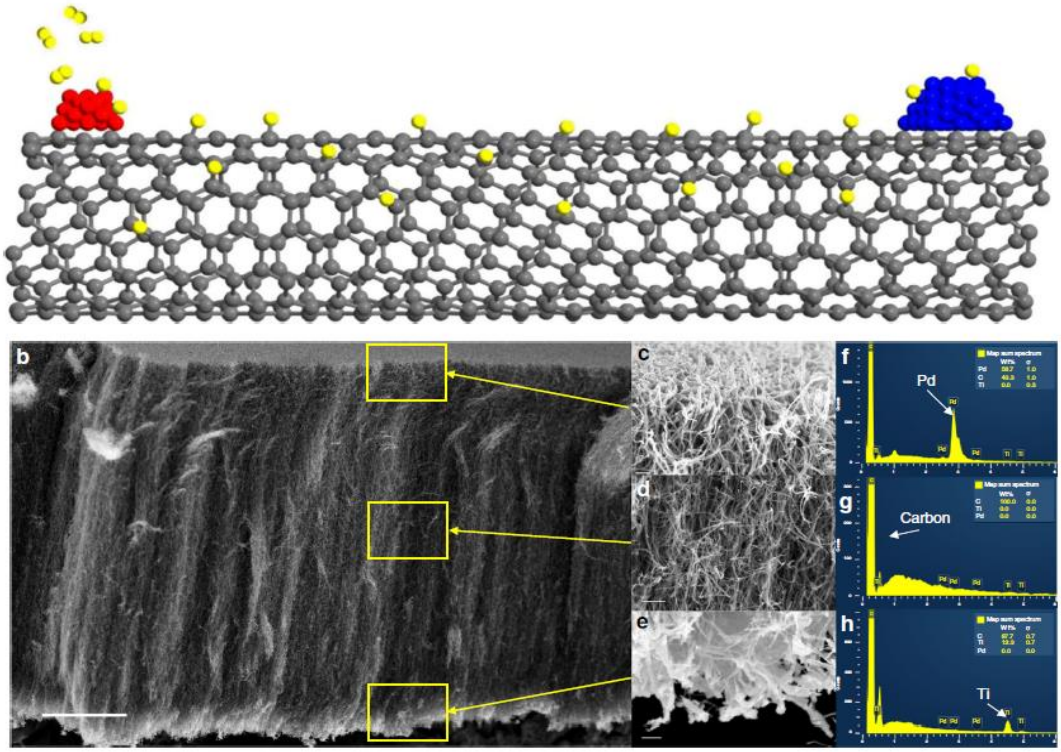


Figure 37. Metals and metal oxides are deposited on opposing ends of a carbon nanotube. **(a)** Schematic depicting a metal (red) capable of dissociating hydrogen (yellow) onto a carbon nanotube where hydrogen can travel across to a metal oxide (blue). **(b)** SEM image of a nanotube forest with Pd and TiO_2 deposited on opposite ends through metal evaporation and after treatment in hydrogen for 1 h at 400 °C. (Scale bar in b indicates 15 micrometers). **(c–e)** Portions of the forest's top, middle and bottom, respectively, at increased magnification. (Scale bar indicates from top to bottom 200, 500, and 250 nanometers). **(f–h)** EDS spectra corresponding to the locations indicated in c–e.

E.3.1 Evidence for hydrogen spillover

Lawrence Barret carried out TPR experiments.

Temperature-programmed reduction (TPR) is used to validate this approach for discerning promoter effects from direct contact between the metal and the support in these catalysts. Before conducting catalytic runs, simple shifts in the reduction profile of a CuO catalyst supported on a carbon nanotube were conducted in the presence or absence of physically separated Pd on the same nanotube. Pd is well known to reduce and dissociate hydrogen at

temperatures well below those required for dissociation on Cu. Pd catalysts can be reduced to 100°C or even at room temperature, while CuO typically requires above 200°C to be reduced in pure hydrogen.[38]**Error! Bookmark not defined.** **Figure 38** compares the TPR profile of Pd and CuO, which are spatially separated on carbon nanotubes (Pd/CNT/CuO), with CuO that is deposited on carbon nanotubes alone (CuO/CNT). **Figure S21** displays **the** EDS results of this catalyst after high-temperature reduction, indicating the absence of any direct contact between Pd and Cu.

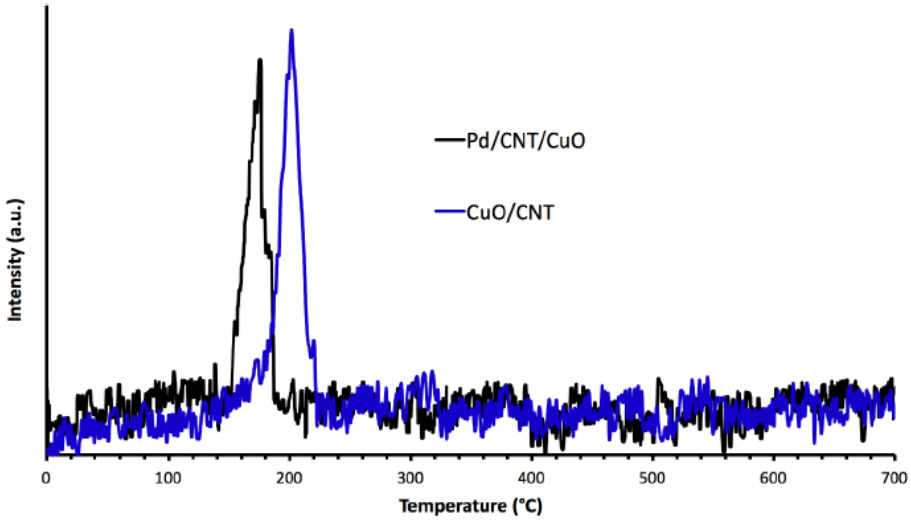


Figure 38. TPR profiles of CuO/CNT and Pd/CNT/CuO catalysts were performed with a flowing 5% H2/Ar stream at a ramp rate of 5°C/min.

As can be seen in **Figure 38**, the reduction temperature for CuO is lowered by 30°C when Pd is present on the same carbon nanotube. Pd is reduced during equilibration of the TPR system at room temperature. Therefore, this reduction temperature shift is associated with CuO and indicates that dissociated hydrogen from the Pd is spilling over onto the carbon nanotubes and reaching the CuO, causing the CuO to reduce at a lower temperature than normal. Comparable shifts in reduction temperature have been observed when Pd and CuO are in direct contact in the absence of the carbon nanotube bridge.[38] This illustrates that

hydrogen can travel along the length of the carbon nanotube to reach the oxide and facilitate its reduction.

Once we had established the effectiveness of this innovative catalyst in isolating the metal from the support and facilitating hydrogen dissociation, we proceeded to explore its potential applications in distinguishing the active sites responsible for the deoxygenation of furfural, anisole, and pentanoic acid using bifunctional catalysts.

E.3.2 Furfural conversion over Pd/TiO_2: Metal-support interfaces sites

Leidy Valeria Herrera carried out the kinetic measurements for the conversion of furfural over Pd/TiO_2.

Cleavage of oxygen from carbonyl-containing species has been proposed over reducible oxide catalysts via a reverse Mars-van Krevelen mechanism.[33] Specifically, over TiO_2, the selective conversion of FAL to form methylfuran (2MF) has been proposed to occur over oxygen vacancies on the surface of TiO_2 that are produced by hydrogen spillover from the metal.[153] Other groups have proposed that the enhanced activity for methylfuran production is due to the metal Pd-TiO_2 interface based on rate and selectivity shifts observed after coating Pd with a porous TiO_2 film.[154] The selective deoxygenation of furfural has been the subject of many recent research articles due to its high presence in biomass-derived streams.[13,19,154,155]

Since defects are present on the TiO_2 surface at a steady state when the Pd and TiO_2 catalysts are separated on a nanotube bridge, the role of direct contact between the TiO_2 and the Pd nanoparticle may be investigated. **Figure 39** shows that Pd on nanotubes alone (Pd/CNT) yields similar rates and selectivity to FUR vs. 2MF when compared with Pd and TiO_2 deposited on opposite ends of carbon nanotubes (Pd/CNT/TiO_2). Similar behavior is

observed across a physical mixture of Pd/CNT and TiO_2/CNT, as can be seen in **Figure S22**. The small quantities of light compounds observed due to ring opening and CO-hydrogenation products do not exhibit a trend. In contrast, selectivity for 2MF increased significantly when Pd is deposited on the same side as TiO_2 on the carbon nanotubes (Pd/TiO_2/CNT). It should be noted that furfural conversions were comparable overall catalysts (X~ 3%), and similar deactivation profiles with respect to furfural conversion were observed over all of the Pd containing catalysts, as can be seen in **Figure S23**. These results suggest that active sites for 2MF production are due to direct contact between the Pd and the TiO_2, as opposed to longer-range defects, as some have claimed.[153] Thus, furfural deoxygenation over TiO_2-supported catalysts occurs through C–O cleavage at the site interface rather than promoter effects.

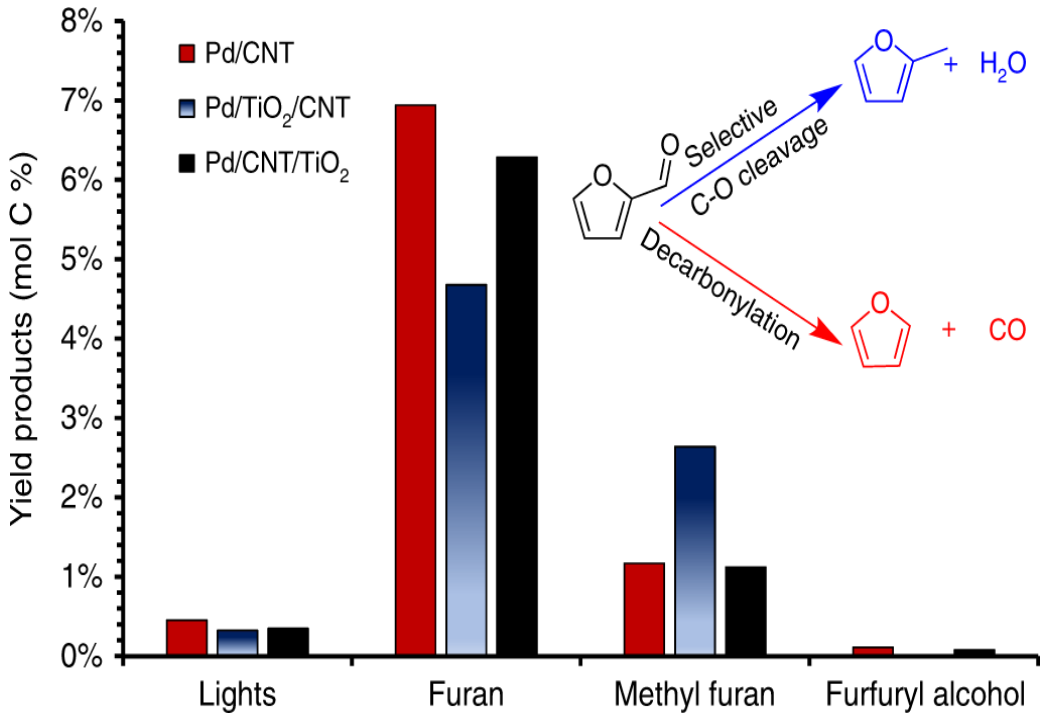


Figure 39. Furfural conversion over Pd and TiO_2 catalysts supported on CNTs. T = 400 ºC, P = 1 atm, under flowing H_2, 30 min time on stream (TOS). The "lights" represent the sum of ring-opening products and products

resulting from the hydrogenation of CO found in low abundance. The inset to the upper right indicates the two primary competing reaction pathways to form furan or methylfuran.

E.3.3 The promoting effect of Cu on anisole conversion over TiO_2 catalysts

Lawrence Barret synthesized the carbon nanotubes samples (Cu/CNT/TiO_2 and Cu/TiO_2/CNT) used to identify the sites responsible for this chemistry.

Rios-Escobedo et al. have proposed possible reaction pathways for the conversion of anisole over Ni/TiO_2, where anisole is converted through transalkylation to cresol or via dealkylation to phenol. The resulting product may then undergo further reactions.[156] Similar pathways are expected for the anisole conversion over Cu/TiO_2. Omotoso et al. have demonstrated that the active sites located at the interface of Ru/TiO_2 are important for the deoxygenation of guaiacol due to the synergistic effect between Ru and TiO_2.[40] Here, we investigate the influence of promoter effects vs. sites located at the metal/support interface for the conversion of anisole over Cu/TiO_2. The main reaction pathways for guaiacol, anisole, and phenol are described in **Figure 40.** Three different Cu-TiO_2 catalysts were prepared: one with the metal subsequently deposited on the same side of the nanotube as the oxide (Cu/TiO_2/CNT), one with the two catalytic materials separated on the same nanotube (Cu/CNT/TiO_2), and a physical mixture of Cu supported on nanotubes (Cu/CNT) with TiO_2 supported on nanotubes (TiO_2/CNT).

Figure 41 shows the results for the three tested catalysts under steady-state conditions. In the cases where spillover from the copper to the titania is possible through direct contact or the carbon nanotube bridge, cresol and phenol are observed as products. This likely results from an initial C–O cleavage to form surface methyl groups on the TiO_2 surface, followed by subsequent alkylation of phenolic species to form cresol or interaction with hydrogen to form lights and phenol. A small amount of unquantifiable lights was also produced,

containing methane and methanol produced in conjunction with phenol. It is clear from **Figure 41** that anisole conversion products are only prevalent over catalysts whose population of Ti^{3+} sites is maintained by the presence of a metal on the same nanotube.

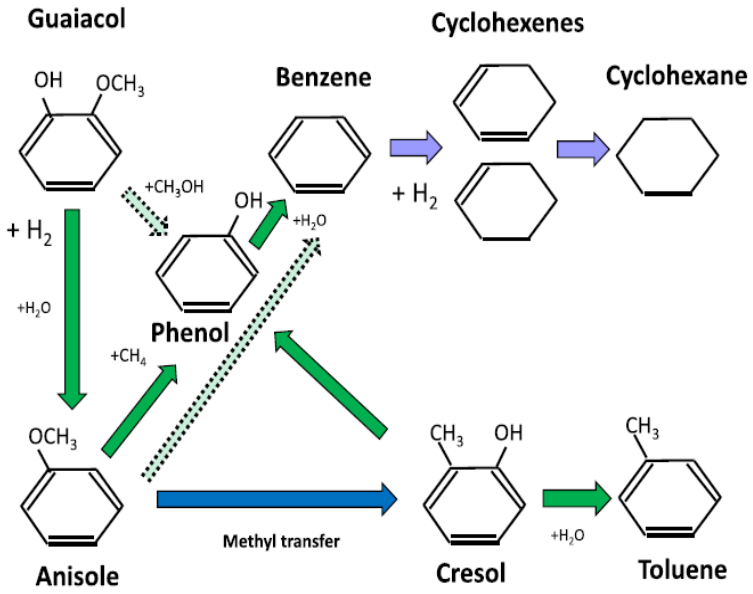


Figure 40. Main reaction pathways for anisole and phenol conversion over MoO_3/ZrO_2. Green arrows—hydrogenolysis, blue arrows—hydrogenation.[157]

Interestingly, in the case of copper and titania separated on different ends of the same nanotube, the yield of products is much higher than in the case where Cu is sequentially deposited over Ti. This decrease is caused by the copper covering a portion of the titanium, diminishing the number of exposed Ti^{3+} sites. This demonstrates that not only does hydrogen spillover across the nanotube, but spillover rates are sufficient to maintain the population of Ti^{3+} sites necessary for sustained activity. This example shows that this experimental technique can also be applied to investigate promoter effects.

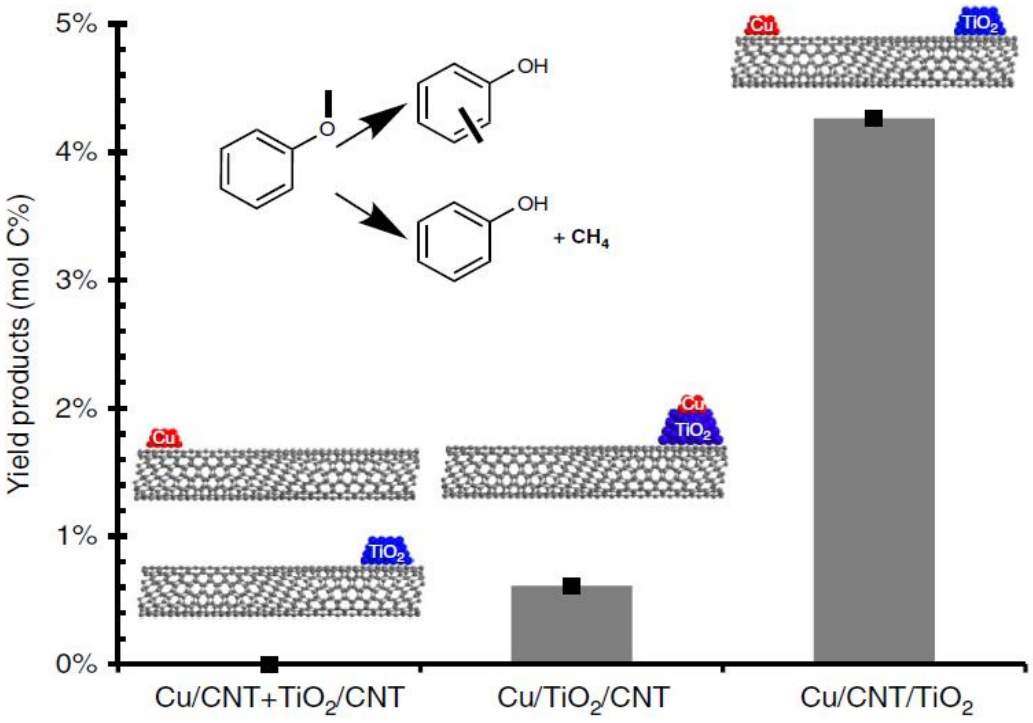


Figure 41. Anisole conversion over catalysts containing Cu and TiO_2. Sum of quantifiable products (cresol+ phenol) resulting from anisole conversion over Cu and TiO_2 catalysts supported on CNTs. T = 400 °C, P = 1 atm, under an H_2 flow, 100 min TOS. The inset in the upper left indicates the main conversion products from anisole under these conditions to generate cresol or phenol.

E.3.4 Promoter effect in the deoxygenation of pentanoic acid over Pt/MoO_3

Caleb Q. Bavlnka and Tianhao E. Zhang synthesized the carbon nanotube samples (Pt/CNT/MoO_3 and Pt/MoO_3/CNT) used to identify the sites responsible for this chemistry.

Oxygen vacancies have been proposed as the active sites for the HDO of biomass-derived compounds over MoO_3.[34] Roman-Leshkov and co-workers have provided insights into the surface's nature during the anisole deoxygenation over MoO_3 by NAP-XPS, which elucidate that the undercoordinated species are responsible for C-O bond activation. Their study suggests that Mo^{5+} species are active in this chemistry, while Mo^{4+} species do not seem to be involved in the deoxygenation of anisole.[53]

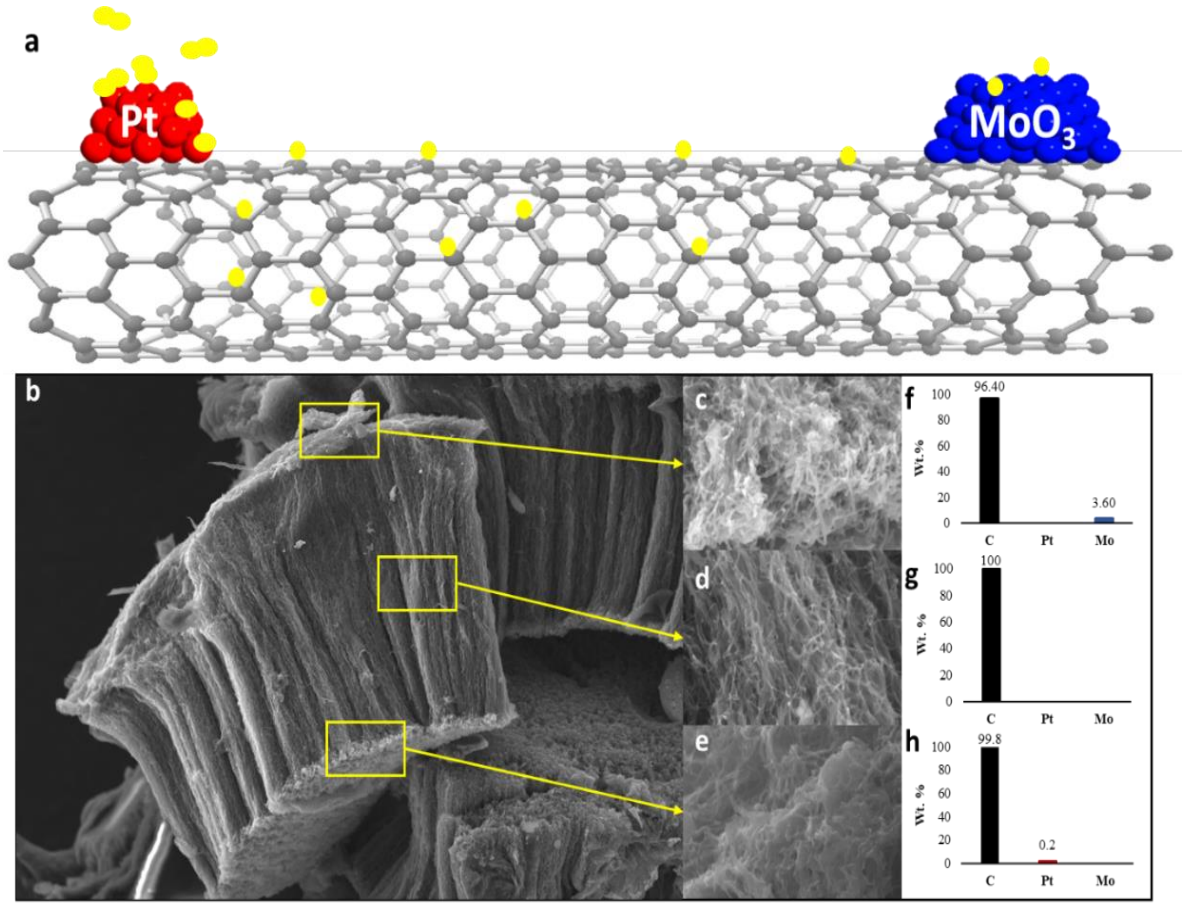


Figure 42. Carbon nanotube with metal and metal oxide deposited at opposite ends. **(a)** An illustration of a metal (red) is capable of dissociating hydrogen (yellow) onto a carbon nanotube where H atoms can travel across to a metal oxide (blue). **(b)** SEM image of a nanotube forest with Pt and MoO_3 deposited on opposite ends via metal evaporation. **(c–e)** Magnified portions of the forest's top, middle, and bottom, respectively. (Scale bar indicates 1 micrometer for the images c-e) **(f–h)** EDS results corresponding to the locations indicated in c–e.

As previously mentioned, the incorporation of metal dopants is a common strategy to promote the formation of oxygen vacancies on metal oxides and enhance reaction rates. Yang et al. demonstrated an enhancement of m-cresol HDO selectivity by using high-dispersion Ni metal deposition into MoO_3/SiO_2. Their study suggests that the synergistic cooperation between Ni and MoO_x species is important to achieve high activity and selectivity.[105] Similar findings were reported by Rachmady et al. in the conversion of acetic acid in Pt/FeO_3, where the promoted catalyst showed improved activity and selectivity toward acetaldehyde[43].

However, the interaction of a reducible metal oxide with a hydrogen promoter metal can be complex due to the formation of multiple surface features that one might assign as active sites.[41,106]

To determine the role of Pt on MoO_3, a technique recently developed in our research group utilizes carbon nanotubes (CNT) as hydrogen highways to evaluate the kinetic relevance of short and long-range interactions. To achieve this, Pt and MoO_3 were deposited on opposing ends of carbon nanotube forests of a controlled length. This allowed H atoms to migrate from Pt metal clusters to the MoO_3 surface and partially reduce the surface of MoO_3 without being in physical contact, as illustrated in **Figure 42a**.

Figure 42 (c-e) shows EDS spectra along the nanotube forests with Pt and MoO_3 deposited on opposite ends, which confirms that Pt and MoO_3 are not in direct contact after reduction. Since a high loading of Pt can promote side reactions, the low ratio of Pt/Mo was maintained for all these samples. The weight loadings of Mo were determined through a quartz crystal microbalance. Due to the low amount of Pt present among the CNTs, the weight loadings of Pt were determined with ICP-MS. Catalyst weight loadings can be found in **Table S5**. The oxidation states for these samples were evaluated via XPS in order to verify that the calcination process was sufficient to convert metallic Mo^{0+} into Mo^{6+}. XPS results reported in **Figure S24** indicate that the Mo species were fully oxidized after moderate calcination (400 °C) for 1 hour**.**

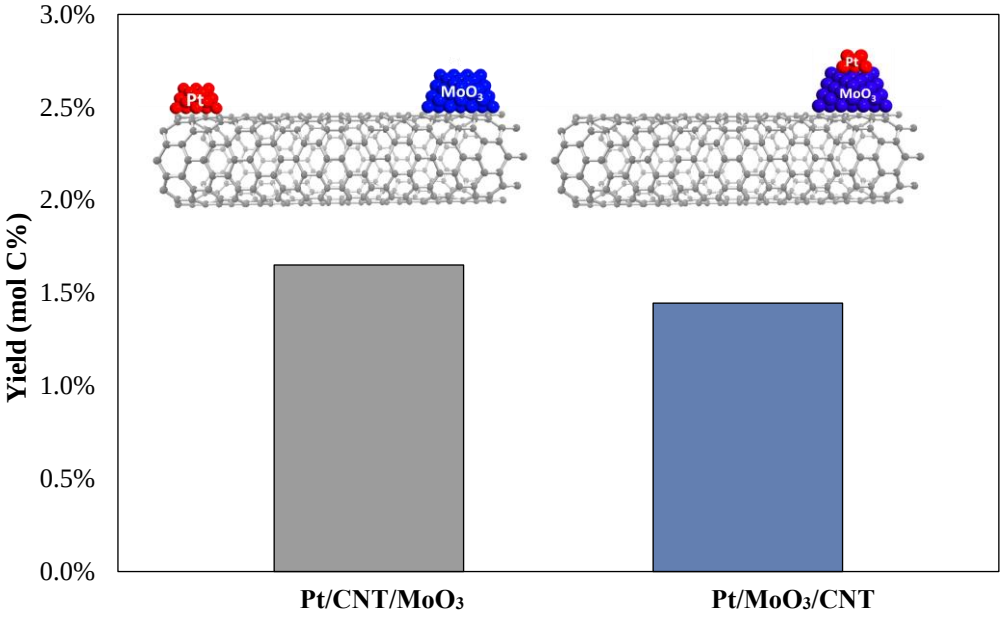


Figure 43. Pentanoic conversion over Pt and MoO_3 catalysts supported on CNTs. Reaction conditions: Flow of H_2 = 30 mL/min, P_{Total} = 760 Torr, TOS = 0 min, and W/F = 0.3 g_{cat}/mL·h. The catalyst was previously calcined in situ for 1 hour at 400 °C and reduced under H_2 flow (100 mL/min) at 400 °C for 1 h.

Here, two different Pt-MoO_3 catalysts were prepared, one with the metals subsequently deposited on the same side of the nanotube forest (Pt/MoO_3/CNT) and another with the two catalytic materials deposited on the opposite ends of the nanotube forests (Pt/CNT/MoO_3). **Figure 43** shows the results for the two catalysts in the deoxygenation of PA. As can be seen, there is no significant difference in the measured rates for the two catalysts. As these rates are very similar, we can infer that the role of Pt is to promote H_2 dissociation, leading to the formation of oxygen vacancies to sustain the SDO activity over the catalyst surface. Thus, we conclude that the sites at the metal/support interface are neither kinetically relevant nor responsible for the selective deoxygenation of PA to PAL when noble metals are incorporated at these low loadings; otherwise, the rate for SDO would be higher

when Pt and MoO_3 are in direct contact. This technique confirms our hypothesis about the promoter effect of Pt clusters over MoO_3 on this chemistry.

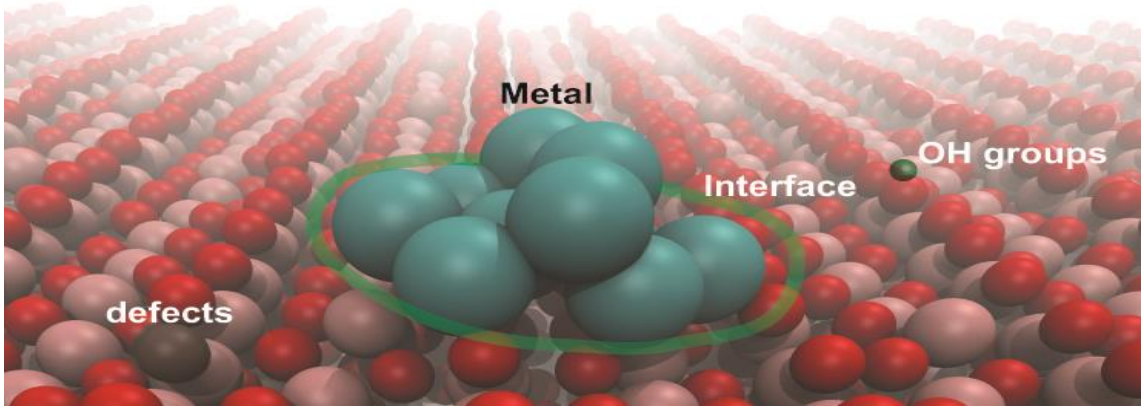
E.5 Conclusions

The experimental approach described in this chapter can be used with a variety of different bifunctional catalysts to isolate the role of sites induced by direct contact from promoter effects. To illustrate the broad-ranging applications of this method, examples are given for both carbonyl group conversion at the metal-support interface as well as carboxylic acid deoxygenation and methoxy group conversion on defects present on the support itself. Here, Our study employed TPR to demonstrate the occurrence of hydrogen spillover via carbon nanotubes from metal sites to less reducible metal oxide. Overall, through this technique, we were able to identify the active sites and draw the following conclusions:

- The conversion of furfural to 2-methylfuran over Pd/TiO_2 occurs at the interface sites.
- Anisole undergoes conversion on the oxygen vacancies or defects located over TiO_2.
- The conversion of pentanoic acid on Pt/MoO_3 occurs in the oxygen vacancies.

CHAPTER VI

F. Vapor-phase ring rearrangement of furfural to cyclic ketone over Ru/TiO_2 catalyst



Leidy Valeria Herrera performed the kinetic measurements over Pd/TiO_2 and Ru/TiO_2; Lawrence Barret synthesized the carbon nanotubes samples ($Pd/CNT/TiO_2$ and $Pd/TiO_2/CNT$) used to identify the sites responsible for this chemistry; Alejandra Gomez measured the kinetic rates of furfural conversion over $Pd/CNT/TiO_2$ and $Pd/TiO_2/CNT$; Dr. Wang performed the DFT studies over Ru/TiO_2. This study was published in Applied Catalysis B: Environmental (2019).

F.1 Introduction

Furanic species are produced from biomass in high abundance via thermal or chemical route. However, the selective conversion of furanics to higher-value products while minimizing side reactions such as the formation of humin remains a challenge. The Piancatelli

ring rearrangement reaction has emerged as a promising solution to convert furanic compounds into cyclic ketones, leading to the production of higher-value products in the liquid phase.[19,155,158,159]

The formation of cyclopentanone (CPNO) and its derivatives from the ring rearrangement of furanic molecules, such as furfural (FAL), is promising for a variety of reasons. CPNO is more stable than FAL and more amenable to long-term storage and transportation than its furanic counterpart. In addition, CPNO can undergo self-aldol condensation reactions to form jet fuel precursors, unlike furfural.[160–162] CPNO is also a valuable specialty chemical, serving as an important intermediate for producing a variety of polymers and pharmaceutical chemicals and a feedstock for jet fuel precursor production.[163,164] The production of the partially unsaturated precursor, 2-cyclopentenone (2CPNE), potentially holds even more value. The market for this chemical has not been studied to the same extent as CPNO due to the difficulty in capturing this intermediate under typical CPNO production conditions. Thus, the ring rearrangement of furfural via the Piancatelli mechanism to form 2CPNE/CPNO is a desired reaction because it does not involve the loss of any carbon, and CPNO can undergo aldol condensation reactions to more valuable products.

Recently studies have shown that the presence of water is necessary for Piancatelli rearrangement to occur, and the reaction rate is enhanced in an acidic environment.[21,158,164,165] In the Piancatelli mechanism, water is suggested to attack the furan ring by nucleophilic attack or by stabilizing the intermediate species on metal surfaces under an aqueous environment. In the absence of water, furfural conversion is mainly to THFA and methyltetrahydrofuran rather than the ring closure products. Unfortunately, the conditions responsible for the

ring rearrangement (acidic aqueous conditions) are also the same conditions responsible for undesirable humin formation.

While a great deal of effort has been dedicated to the transformation of FAL and other furanics in the vapor phase,[166–169] products observed are typically limited to furfuryl alcohol (FOL), 2-methylfuran (2MF), furan (FUR), and cracking products.[170–172] Overall, this study highlights that TiO_2-supported catalysts can facilitate ring rearrangement reactions in the absence of a condensed phase under elevated temperature and atmospheric pressure conditions, even in the presence of water vapor. Our results show that adding water as a co-feed shows a remarkable shifting the selectivity from 2MF to 2CPNE and, subsequently, to CPNO, decreasing excess hydrogenolysis to form light gases. Besides, the role of the metal/support interface and defects on the TiO_2 support in this reaction is discussed.

F.2 Experimental

F.2.1 Chemicals and catalysts materials

All the gases (H_2 (99.999%), He (99.999%), N_2 (99.998%), Air (Ultra zero), and Ethylene) used for catalyst preparation, reaction, carbon nanotube synthesis, and characterization were purchased from Airgas.

Chemicals used for multi-walled carbon nanotubes growth were iron nitrate nonahydrate, cobalt nitrate hexahydrate, aluminum nitrate nonahydrate, and 2-hydroxyethyl cellulose (Mw ~ 1,300,000)). All the chemicals used were purchased from Sigma Aldrich. Tungsten (1 mm, 99.94%), Pd (0.5 mm, 99.95%), Ti (0.25 mm,99.95%), Cu (0.1 mm, 99.95%) wires were used for metal deposition. Aluminum conductive tape (single adhesive surface, 12.7 mm W x 16.4 m L, Ted Pella Inc.) was used to remove CNTs from the silicon wafers. The silicon wafers used as a base for growing vertical multi-walled carbon nanotubes were

purchased from Wafer World, Inc (SKU:1186). To clean the wafers, isopropanol, ethanol, and acetone were used. The water (18 MΩ) used in this study was obtained from an in-house filtration system.

F.2.2 Catalyst synthesis

F.2.2.1 Ru/TiO_2 and Pd/TiO_2

Ru and Pd catalysts were synthesized using the incipient wetness impregnation method with an aqueous solution of hexaaminеruthenium (III) chloride (98% Sigma Aldrich) and palladium (II) nitrate dehydrated, respectively, on the TiO_2 support (Aeroxide P25, 0.25 ml/g pore volume) or SiO_2 support (Hisil-210, 0.96 ml/g pore volume). The catalysts were then dried at room temperature in air for 48 h, at 120 °C for 12 h in an oven before reducing at 400 °C for 2 h in hydrogen flow. The catalysts were pelletized and sieved to yield obtained particle sizes from 250-420 μm.

F.2.2.3 Vertical multi-walled carbon nanotube growth

A catalyst solution was spin-coated on silicon wafers for growing vertically aligned carbon nanotubes (CNTs). Silicon wafers were cut into 23 mm x 23 mm square pieces using a diamond scribe. The wafers were calcined in a horizontal furnace under continuous airflow (150 SCCM) at 600 °C for 2 hours. Then the wafers were ultrasonically washed in subsequent acetone, ethanol, and isopropanol solutions for 45 minutes each to ensure a clean surface for spin coating. A catalyst solution consisted of 1.11 wt% iron nitrate nonahydrate, 0.39 wt% cobalt nitrate hexahydrate, 1.23 wt% aluminum nitrate nonahydrate, and 0.74 wt% 2-hydrox-yethyl cellulose, all with respect to water, was made. One milliliter of catalyst solution was spin-coated on each silicon wafer in a two-step process that consisted of 10 seconds at 500

rpm, followed by 30 seconds at 2000 rpm. The silicon wafers were dried overnight and calcined the following day at 450 °C under continuous air flow (150 SCCM) for 1 hour.

In order to synthesize carbon nanotubes on silicon wafers, the samples were balanced on top of one another in a one-inch quartz-diameter tube, ensuring each catalyst surface was accessible to flowing gas. The vertical reactor was heated to 650 °C at 10 °C min^{-1} under hydrogen flow (200 SCCM) and maintained at 650 °C for 30 min to ensure reduction of the catalyst. Then, nitrogen (370 SCCM) flowed through the reactor tube, then was heated to the reaction temperature of 675 °C at 10 °C min^{-1}. The system was held at 675°C for 30 minutes under nitrogen flow. Carbon nanotube synthesis occurred as ethylene (200 SCCM) was mixed for 20 minutes with the flowing nitrogen. After CNT synthesis, nitrogen was fed into the reactor until the system was cooled. To weaken the interaction between the CNTs and the silicon wafer, the sample was calcined in air (150 SCCM) at 480 °C for 2 hours. This allowed for future controllable removal of the CNTS from the silicon wafer.

F.2.3 Synthesis of catalysts on opposite ends of CNTs

Palladium and titanium were deposited on the surface of the wafer by thermal evaporation in our previously described homebuilt evaporator system. In order to deposit metals on opposing ends, the sample was manipulated by using aluminum tape containing a carbon adhesive after Pd incorporation. Ti was then evaporated on the opposing end of the nanotube forest. The carbon residue was removed by soaking the sample in isopropanol to dissolve the adhesive. The sample was then calcined at 350 °C to oxidize the Ti to form TiO_2, the oxidation state of which has been confirmed with both TPR and XAS in our prior publication. The Pd/CNT/TiO_2 catalyst contains 0.3 wt% Pd and 0.65 wt% TiO_2, while the Pd/TiO_2/CNT catalyst contains 0.38 wt Pd and 0.64 wt% TiO_2.Weight loadings of Pd and Ti were determined

via a calibrated quartz crystal microbalance. More details about the synthesis of CNTs can be found in **Section E.2.2**.

F.2.4 Characterization

Inductively coupled plasma mass spectrometry (ICP-AES) was utilized to determine Ru content of the synthesized catalysts, since Ru is known to have high mobility during reduction and can form volatile oxides upon calcination which can decrease the total amount of the metal on the catalyst [39]. Ru and Pd particle size distributions were obtained using Transmission Electron Microscopy (TEM, JEOL JEM-2100 model). Before imaging, the catalysts were pre-reduced in hydrogen flow at 400 °C for 1 h and cooled down to room temperature in nitrogen before dispersion in isopropanol and sonication to obtain a uniform suspension. A few drops of the suspension were dispersed on carbon-coated copper TEM grids.

F.2.5 Kinetic measurements

The catalytic testing occurred in a gas-phase packed bed reactor under atmospheric pressure conditions, using H_2 or H_2/He as a carrier gas. Catalyst particles were mixed with glass beads (Sigma Aldrich, 212-300 μm) and packed between two layers of quartz wool inside a quartz reactor (0.25” OD). The reactor tube was placed in the center of a vertical furnace (Thermcraft Inc., 1200W/115V). All catalysts were pretreated in situ in hydrogen (100 SCCM) at 400 ℃ for 1 hour. After reduction, the samples were cooled to the reaction temperature. The reactants were injected using a syringe pump (KD Scientific) and vaporized before entering the reactor. To prevent any product condensation, the outlet stream was also heated up to 250 ℃. A gas chromatography (GC), equipped with a flame ionization detector (FID) and HP-INNOWAX column (Agilent, 60 m × 0.32 mm ID × 0.5 μm), was connected to the reactor for product quantification. Product identification was confirmed using a

Shimadzu QP-2010 GC-MS, and standards were used to quantify the various products in the flame ionization detector. Distilled furfural (obtained from Sigma Aldrich; distilled and stored at -15 ℃) and distilled water (H_2O was obtained from an in-house filtration system) were introduced to the reactor at a flow rate of 0.1 ml/h for furfural and 0.25 ml/h for distilled water. The catalyst mass and other relevant conditions are described in the caption of each graph.

F.3 Results

F.3.1 Reaction of pure furfural over Ru/TiO_2

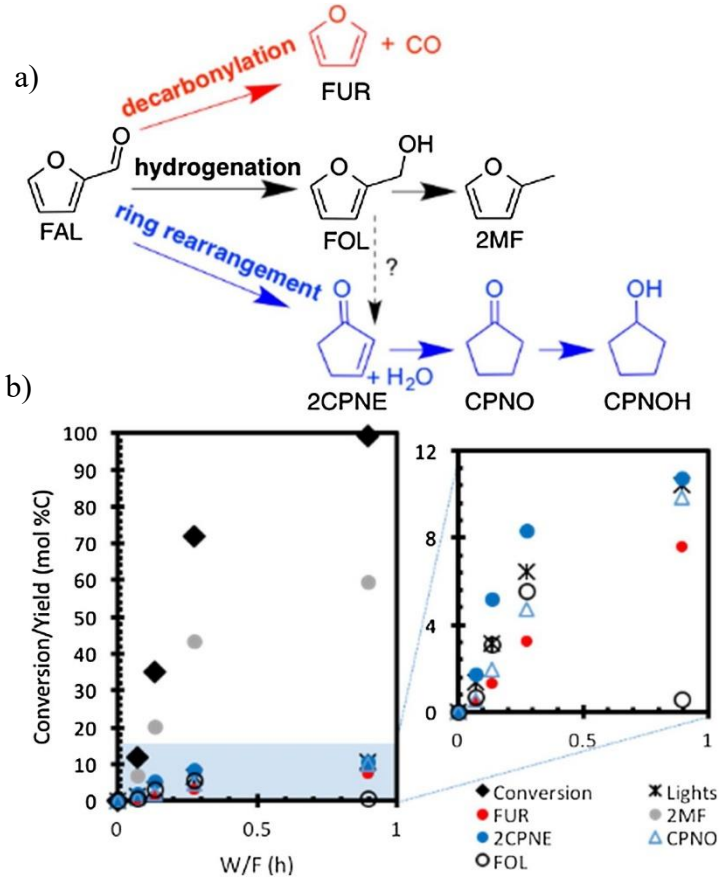


Figure 44. (a) Reaction pathway of furfural conversion over Ru/TiO_2. **(b)** Furfural conversion and product yield with W/F over 4.4% Ru/TiO2 at 400 °C. 1 atm, TOS: 30 min. Carbon balance ~ 95% for all reactions.

Product distributions for furfural conversion over Ru/TiO_2 in the vapor phase are shown in **Figure 44b**. The most abundant product is 2MF (yield = 59.7 % at 0.9 h), which is produced from the hydrogenolysis of the C-O bond of FOL. While it is known that this hydrogenolysis can occur on metal surfaces,[17,19,172] interfacial sites formed as a result of the interaction between Ru and TiO_2 can play an important role in forming 2MF from FOL. Interfacial sites are important in various chemical reactions, including Fischer- Tropsch[107] and alkane hydrogenolysis.[108] All the possible pathways consider for furfural conversion are illustrated in **Figure 44a**.

The unanticipated reaction product observed under these conditions is 2CPNE and CPNO. **Figure 44b** shows that both products appear to increase at higher contact times (W/F, defined as grams of catalyst/grams of furfural fed per hour), while FOL yields pass through a maximum (yield = 5.5 % at 0.3 h). This result implies that FOL is subsequently converted to 2MF or 2CPNE/CPNO at higher W/F values. FOL can be formed from direct hydrogenation of the carbonyl C-O bond of FAL on surface metal. This reaction has been shown to occur over various metal catalysts such as Pt, Pd, Cu, and Ni in the liquid and gas phases, with different metals exhibiting varying activity and selectivity towards the reaction products.[18,19,165,173] FAL can adsorb on the metal surface in either an η1 or η2 mode. The O atom in the carbonyl group of FAL can adsorb on top of the Ru surface in an η1 configuration, which is commonly observed over Cu catalysts.[18] Moreover, FAL can adsorb on metal surfaces with both C and O atoms binding to the surface in a η2 mode, as is illustrated in **Figure 45**.[17,174,175] Besides, the metal-oxygen bond of the η2 intermediate could break to form a surface acyl species at higher temperatures, which is a precursor to decarbonylation to produce FUR. Catalysts with oxophilic sites have been shown to stabilize the metal-oxygen bond

more strongly and hinder the formation of surface acyl species,[19] leading to decreased selectivity to decarbonylation products. This may be occurring at the Ru/TiO_2 interface in this case.

The unexpected formation of 2CPNE and the subsequent hydrogenation of the olefin to form CPNO represent the most interesting products observed here. From **Figure 44b**, the yield of these products increases steadily as the W/F increases, with the H_2O partial pressure also increasing along the reactor bed due to the in-situ water generated from 2MF production.

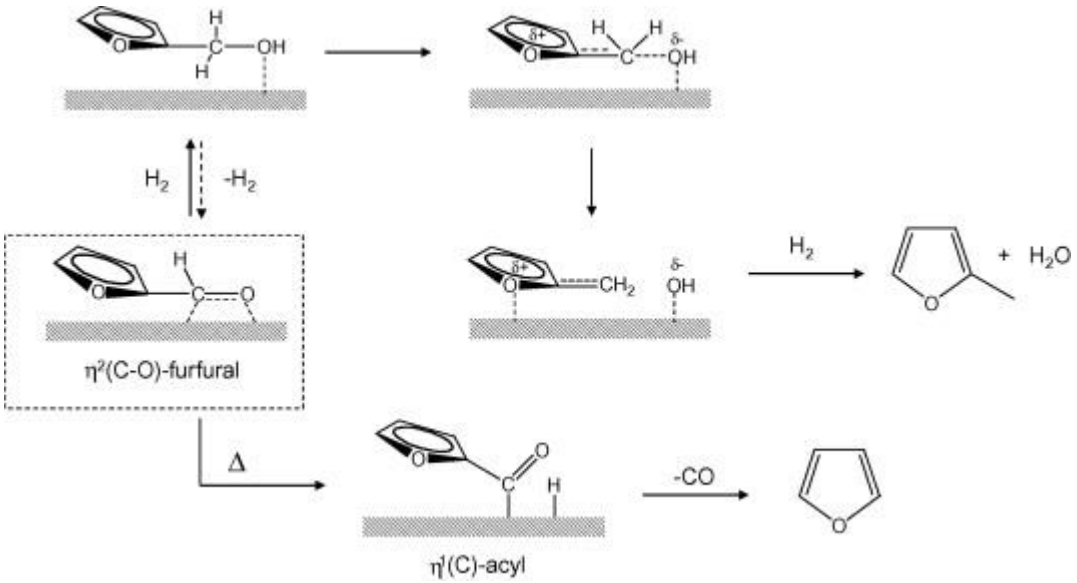


Figure 45. Possible species on the surface during conversion of furfural. This picture was taken from [19]

E.3.2 Role of water for furfural conversion to cyclopentanone (CPNO)

The presence of water in the FAL conversion to CPNO have a significant impact on the product distribution and selectivity in the liquid phase. Jia et al. have shown that the presence of methanol/water solution over NiFe/SBA-15 catalyst inhibits the formation of tetrahydrofurfuryl alcohol (THFA) and shift the selectivity towards CPNO.[22] Similarly,

Hronec et al. demonstrated that the formation of THFA can drastically affect the formation of CPNO from FAL over Pd-Cu/C catalyst . [21,165,169]

The aim of this study is to explore the role of water on the conversion of FAL to 2CPNE/CPNO in vapor phase. It should be noted that even though the water was not introduced as a reactant in the results presented in **Figure 44b**, CPNO/2CPNE products were still observed. However, water can be produced in situ through the hydrogenolysis of FOL to form 2MF.

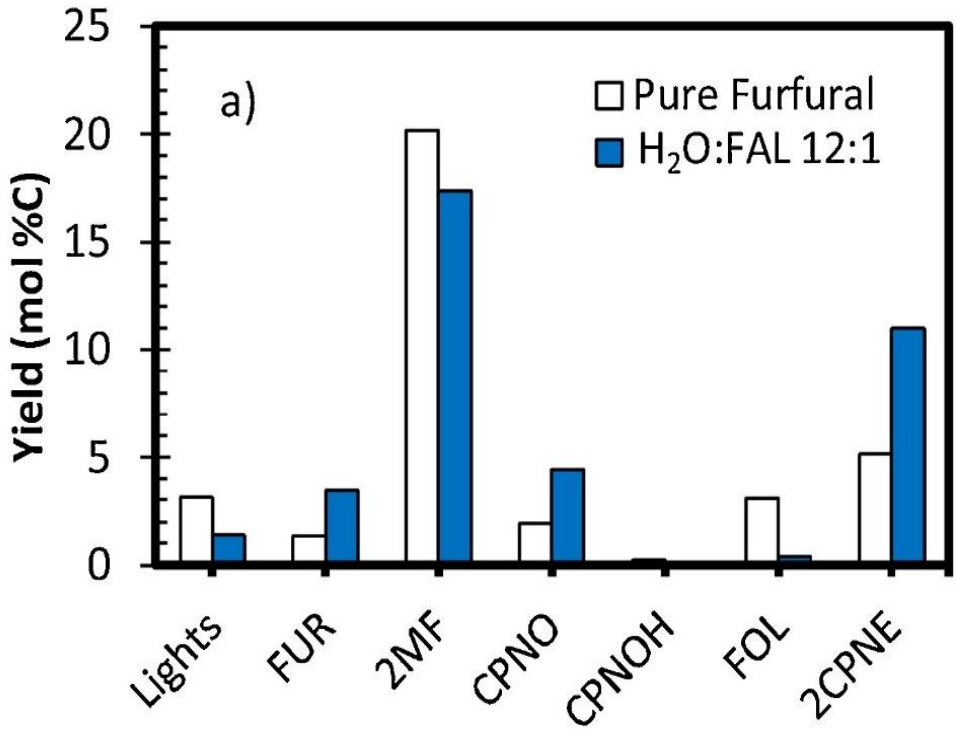


Figure 46. Product distribution for pure furfural and furfural co-fed with water. 4.4% Ru/TiO_2 at 400 °C, 1 atm, and 30 min TOS. Conversion: 36 ± 2%. Carbon balance>94% for all reactions.

To assess the possible involvement of gas phase water in the ring rearrangement, furfural was co-fed with excess water in a molar ratio of 12:1; the results are presented in **Figure 46**. With the introduction of water, the sum of the CPNO/2CPNE products (yield = 16 %) is similar to the yield of 2MF (yield = 17 %). Thus, comparing this result with the values

obtained without water in the feed, CPNO/2CPNE (yield = 7 %), 2MF (yield = 20 %), an enhancement in the rate of the ring rearrangement reaction is clearly observed upon the introduction of water to the system. The role of the support in this reaction will be discussed in the following section.

F.3.3 Active sites responsible for the conversion of furfural over Ru/TiO_2 and Pd/TiO_2

TiO_2-supported catalysts have been shown to exhibit several possible types of active sites for the selective cleavage of C-O bonds, ranging from the creation of new sites at the metal support perimeter to the presence of defects or promoter effects on the support.[40] The introduction of reducible oxide TiO_2 as a support has been found to result in increased rates of C-O cleavage for the conversion of phenolic compounds. This effect was attributed to the synergistic effect between Ru and TiO_2. While it was unclear if these sites were around the perimeter of the Ru metal or defects on the TiO_2 support far away from the metal, further studies showed that defect sites on the TiO_2 support are the active sites for the initial transalkylation step of guaiacol conversion. However, this may not be applicable in the case of C-O bond cleavage reactions, such as the conversion of cresol to toluene.[39]

To investigate the importance of active sites on the support in the ring rearrangement of furfural to 2CPNE/CPNO, pure Ru catalysts (supported on SiO_2 and CNT) catalyst with no metal loading were compared with Ru/TiO_2. The results obtained from feeding a water/furfural (12:1 molar ratio) mixture over these catalysts are presented in **Figure 47**. It has been proposed that Ru metal clusters can assist in the splitting of water, resulting in the formation of OH groups decorating the metal surface. These OH groups decorating the metal surface could potentially play a role in enhancing the catalytic activity of the metal surface in this reaction.[176] **Figure 47** shows the variation in product selectivity observed over pure

Ru catalysts on inert supports (Ru/SiO_2 and Ru/CNT) and Ru/TiO_2. The results show that there are several noticeable observations: i) CPNO and 2CPNE are only observed over Ru and Pd catalysts supported on TiO_2; ii) An enhancement in FAL conversion to 2MF, which is also a valuable product, is observed when compared to Ru-supported on the other tested supports. iii) Decarbonylation and C-C hydrogenolysis rates are suppressed on Ru/TiO_2 when compared to other supported Ru catalysts.

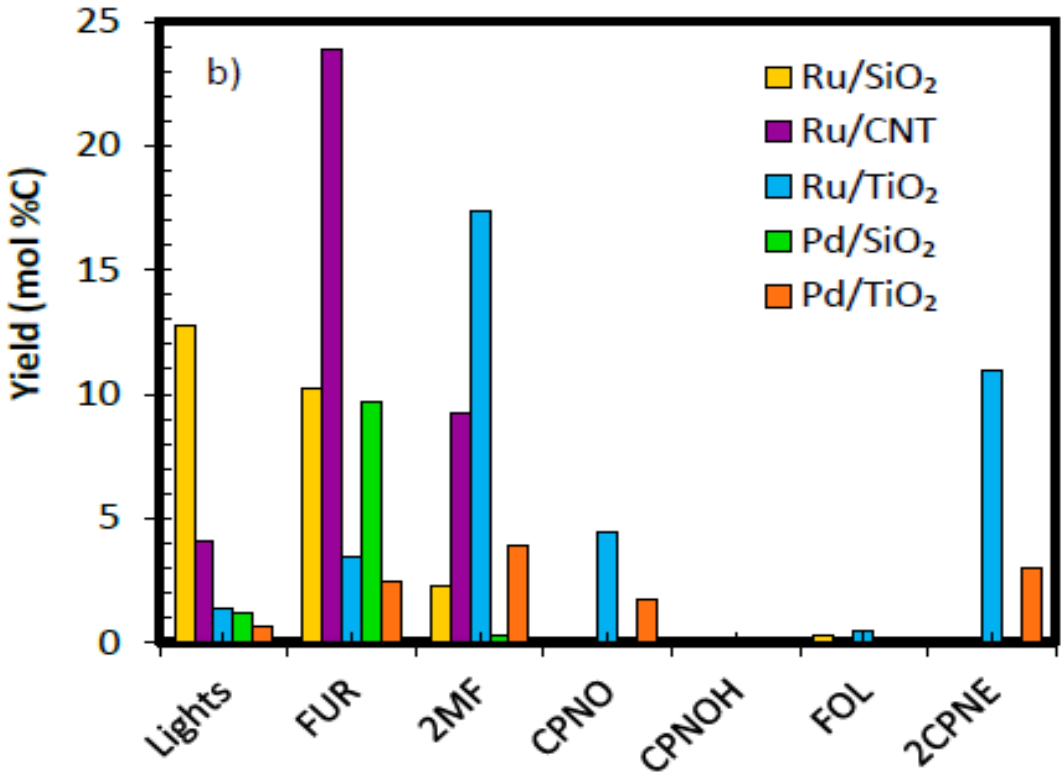


Figure 47. Product distribution for pure furfural and furfural co-fed with water. 4.4% Ru/TiO_2 at 400 °C, 1 atm, and 30 min TOS. Conversion: 36 ± 2%. Carbon balance>94% for all reactions. Product Yield for water/furfural (12:1 molar ratio) feed mixture over TiO_2, Ru/SiO_2, Ru/CNT, and Ru/TiO_2 catalysts W/F = 1.85h (TiO_2) and 0.13h (Ru/SiO_2 and Ru/TiO_2) and 0.39h(Ru/CNT) Conversion = 10% (TiO_2); 25%(5.3% Ru/SiO_2); 38% (4.4% Ru/TiO_2) and 37% (1% Ru/CNT) T = 400 °C, P = 1 atm, TOS = 30 mins. Carbon balance ~ 94% for all reactions.

Catalyst	Conversion (%)	Rate product/exposed metal (mol/m^2 h)			Rate product/per TiO_2 (mol/m^2 h)	Rate product/per perimeter (mol/m h)
		FUR	LIGHTS	2CPNE+CPNO	2CPNE+CPNO	2CPNE+CPNO
Ru/SiO_2	25	$1.23*10^{-03}$	$2.53*10^{-03}$	----------	----------	----------
Ru/CNT	37	$5.55*10^{-03}$	$9.51*10^{-04}$	----------	----------	----------
Ru/TiO_2	38	$4.42*10^{-04}$	$1.78*10^{-04}$	$1.95*10^{-03}$	$1.96*10^{-04}$	$3.52*10^{-12}$
Pd/SiO_2	11	$4.98*10^{-03}$	$6.02*10^{-04}$	----------	----------	----------
Pd/TiO_2	12	$6.22*10^{-04}$	$1.57*10^{-04}$	$1.21*10^{-03}$	$5.96*10^{-05}$	$1.03*10^{-12}$
TiO_2	10	----------	----------	----------	$5.14*10^{-06}$	

Table 3. Rate of products normalized per exposed metal, support, or metal-support perimeter. All reactions were carried out using a feed mixture of water and FAL in a 12:1 molar ratio. W/F=0.13h (Pd/SiO_2 and Pd/TiO_2), Conversion=11.12% (1%Pd/SiO_2) and 12.05% (1% Pd/TiO_2); W/F=1.85 h (TiO_2) and 0.13 h (Ru/SiO_2 and Ru/TiO_2) and 0.39 h (Ru/CNT) Conversion=10% (TiO_2); 25% (5.3% Ru/SiO_2); 38% (4.4% Ru/TiO_2) and 37% (1% Ru/CNT). T=400 °C, P=1 atm, TOS=30 min.

When TiO_2 is used as a support, desired products (CPNO/2CPNE and 2MF) are formed due to defects in TiO_2 or sites around the perimeter of metal particles. Therefore, the same reaction was conducted over pure TiO_2 without the Ru metal to understand this further. As seen in **Table 3**, when passing FAL and water over TiO_2 alone, some 2CPNE/CPNO is observed, but due to the lack of a metal that promotes the dissociation of hydrogen, nearly an order of magnitude higher TiO_2 catalyst amount is necessary to achieve the same level of conversion as with metal supported TiO_2 catalysts. If sites at the metal/support interface are directly involved in the ring rearrangement reaction, one would anticipate significant shifts in reaction rate with the carbon-metal and carbon-oxygen bond strength should play an important role in this reaction. To further probe the role of the metal, the FAL reactions with water were carried out over Pd supported on TiO_2, with Pd forming much weaker bonds with both carbon and oxygen than Ru.[177,178] The role of Pd in opening the furanic ring at interfacial sites is anticipated to be very different. Barteau et al. reported indistinguishable isothermal

reduction profiles when Pd and Ru were added to a TiO_2 support in similar quantities.[179] This implies that the different behavior between these two catalysts likely involves the direct interaction of the metal with the furanic species, as opposed to a simple shift in the number of defects on the TiO_2 support at a steady state. As shown in **Figure 47**, the production of CPNO/2CPNE over Pd/TiO_2 is clearly lower than observed for Ru/TiO_2, but it is still present.

For the ring rearrangement reaction in an aqueous phase, it is generally accepted that the role of the metal is to hydrogenate the FAL to form FOL, with subsequent ring rearrangement reactions in the acidic aqueous phase to form CPNO precursors such as unsaturated hydroxycyclopentanones or ring-opened intermediates, as is described in **Figure S25**.[21,180,181] Hronec et al. have proposed that the metal could play the additional role of conversion of these active intermediates that are produced in the acidic aqueous phase to limit side products produced from polymerization/humin formation. Overall, low hydrogen concentration or less active catalyst toward hydrogenation can promote the formation of oligomers and polymers.[21]

Rates of 2CPNE/CPNO production when feeding intermediate products (FOL and 2MF) can be used to determine the kinetic relevance of pathways involving these intermediates. **Table 4** shows that feeding 2MF did not result in the production of CPNO/2CPNE, indicating that it is not a relevant intermediate in this reaction. Surprisingly, when FOL is fed, the yield of CPNO/2CPNE is lower than was observed when FAL was fed over Pd/TiO_2. This indicates that FAL itself can undergo CPNO/2CPNE the furanic rearrangement prior to desorbing from the surface, and the role of the metal is not only to supply hydrogen to create defects and yield alcohol intermediates that react on the TiO_2 support. These results suggest that the active site for this reaction lies at the interface of the metal and the TiO_2 support. To

gain further proof of the interface as the active site, FAL was co-fed with water over a physical mixture composed of Ru/SiO_2 and TiO_2 as is seen in **Table 4**. As a result, no significant yields to ring rearrangement products were observed at the tested W/F when the physical mixture was used. It should be noted that while some yield to these products is expected over the TiO_2 used in the physical mixture, the rate is sufficiently low to not observe significant quantities under the conditions tested.

Catalyst	Entry	Yield Products (%)				
		2CPNE	CPNO	2MF	Lights	FUR
Pd/TiO_2	2MF	--------	--------	--------	0.59	--------
	FOL	2.42	0.12	7.72	0.95	--------
	FAL	2.96	1.72	3.94	0.61	2.42
Ru/TiO_2	FAL	6.82	1.69	5.98	1.40	3.47

Table 4. Yield of products for reactions feeding different possible intermediates for the ring rearrangement. Reaction conditions: water/2MF: 12:1 (W/F= 0.13 h, Pd/TiO_2, Conversion= 9.15%); water/FOL:12:1 (W/F= 0.13 h, Pd/TiO_2, Conversion= 21.8%); water/FAL:12:1 (W/F= 0.13 h, Pd/TiO_2, Conversion= 13.05%), and water/FAL:12:1 (W/F= 0.13 h, Ru/TiO_2, Conversion= 38%), T= 400 °C, P= 1 atm, TOS= 30 min.

To further investigate the role of the metal/support interface and defects on the TiO_2 support, we carried out the reactions by separating Pd from TiO_2 by a controlled distance on opposing ends of the carbon nanotube forest ($Pd/CNT/TiO_2$). As discussed in **Section E.3**, hydrogen spillover leads to the formation of Ti^{3+} sites over TiO_2.[109] Here, we applied the same technique discussed in chapter V, which can differentiate between sites at the metal-support interface and traditional promoter effects, allowing us to study these phenomena more closely.

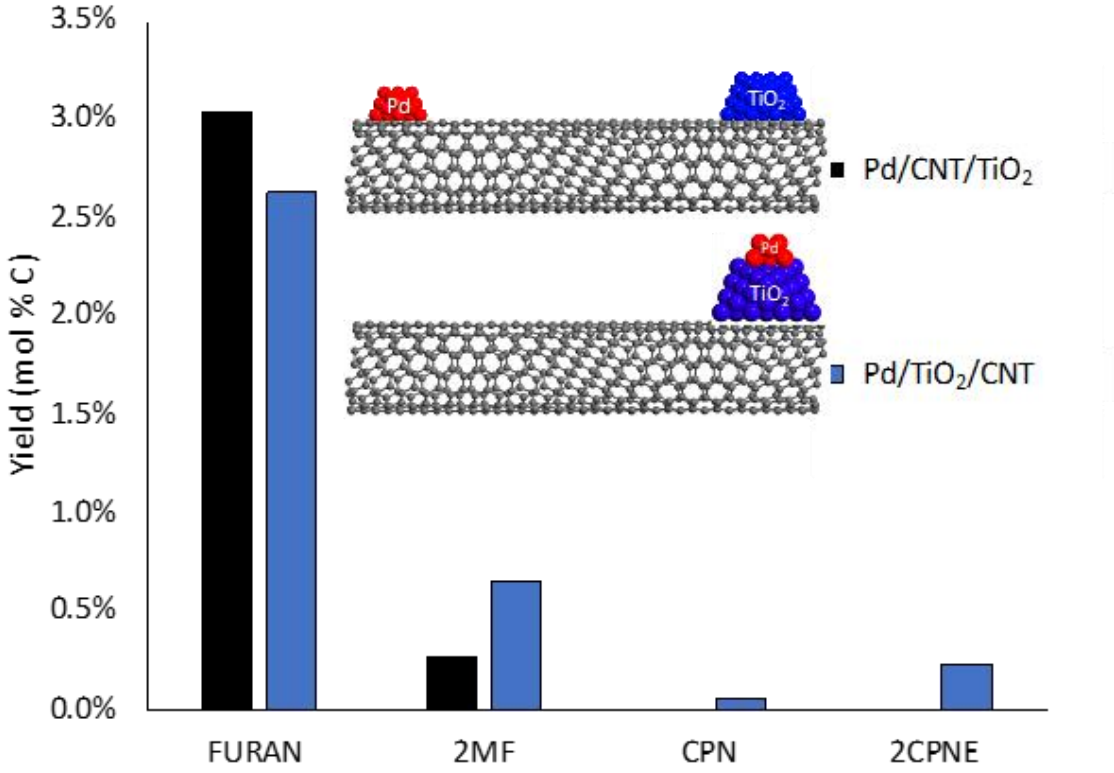


Figure 48. FAL conversion over Pd and TiO_2 catalysts supported on CNTs at controlled separations distances along the nanotube surface. The Pd/CNT/TiO_2 catalyst contains 0.3 wt% Pd and 0.65 wt% TiO_2. The Pd/TiO_2/CNT catalyst contains 0.38 wt Pd and 0.64 wt% TiO_2. T=400 °C, P=1 atm, under flowing H_2, 30 min TOS. 5 mg of catalyst was used in both cases. Water was co-fed at a molar ratio of 12:1 with respect to FAL.

As depicted in **Figure 48**, the results suggest that the production of 2MF and 2CPNE/CPNO occurs at the interface between the metal and the support. In contrast, CPNO or 2CPNE were not observed when the Pd and TiO_2 were not in physical contact, as in the case of Pd/CNT/TiO_2. This result supports the prior argument that FOL is not an intermediate equilibrated with the vapor phase, and this ring rearrangement chemistry occurs at the metal-support interface. The role of the interface for the enhanced selectivity to form 2MF and 2CPNE/CPNO is intriguing, as we anticipate these two transformations will occur through very different binding configurations. The production of 2MF at the metal support interface

likely results from the furan ring interacting with the edge of the metal particle, where the oxygen interacts with a defect on the support, similar to the case of cresol deoxygenation.[41] Ring rearrangement, on the other hand, requires the interaction of the furanic ring with the support as well as a water molecule, with the oxygen likely binding to the edge of the metal particle. We anticipate that these two binding modes may be influenced by surface coverage and could be in competition with one another under reaction conditions.

To gain a further understanding of the conversion of FAL to 2CPNE/CPNO, Dr. Wang conducted computational studies. As a result, DFT studies indicate that FOL binds 0.3 eV weaker than FAL at the interface, which helps to explain why ring rearrangement rates and selectivities are greater when FAL is fed to the system as opposed to when FOL is fed to the system. FAL binds strongly to sites near the interface, modifying the nature of the C–O bond while allowing a strong interaction of this surface intermediate with the TiO_2 surface. Here we hypothesized two possible options for how the ring rearrangement of FAL occurs at the Pd/TiO_2 interface. These options are a) the furan ring of the surface-bound intermediate interacts with an exposed Ti cation directly, making the surface intermediate amenable to attack from vapor-phase water to facilitate ring opening a rearrangement, or b) water interacts with the surface of the TiO_2 support to facilitate the protonation of the furanic ring and subsequent ring opening. One possible explanation that supports the latter option is the enhanced protonation ability of a water molecule that has adsorbed in an oxygen vacancy site near the surface of the metal particle. In a prior study, we had discussed the potential of these activated water molecules as responsible for the deoxygenation of cresol at the Ru/TiO_2 interface.[41]

F.4 Conclusions

Here we reveal the conditions required to selectively convert furfural to unsaturated cyclic ketones in the absence of a condensed aqueous phase. Conversion of furfural in the vapor phase at 400 °C results in a number of reactions including hydrogenation, decarbonylation, and hydrogenolysis to form products such as furfuryl alcohol, furan and 2-methylfuran. In the absence of co-fed water, minor selectivity to the carbon efficient reaction of furfural to cyclopentanone and 2-cyclopentenone was also observed. The selectivity for these reactions significantly increased as water vapor was introduced, resulting in shifts in product selectivity from 2-methylfuran to cyclopentanone and 2-cyclopentenone. The support plays an important role in determining the product distribution as pure Ru catalysts produced mainly light gases and furan under these conditions when compared with Ru/TiO_2. Experiments feeding various intermediates indicate that the vapor phase reaction does not proceed through an alcohol intermediate that desorbs from the catalyst surface. Experiments over Pd supported catalysts imply that carbon-metal and oxygen-metal bond strength at the metal/support interface likely plays an important role in this reaction.

REFERENCES

(1) Climent, M. J.; Corma, A.; Iborra, S. Conversion of Biomass Platform Molecules into Fuel Additives and Liquid Hydrocarbon Fuels. *Green Chemistry* **2014**, *16* (2), 516–547. https://doi.org/10.1039/C3GC41492B.

(2) Huber, G. W.; Iborra, S.; Corma, A. Synthesis of Transportation Fuels from Biomass: Chemistry, Catalysts, and Engineering. *Chem Rev* **2006**, *106* (9), 4044–4098. https://doi.org/10.1021/cr068360d.

(3) Chheda, J. N.; Huber, G. W.; Dumesic, J. A. Liquid-Phase Catalytic Processing of Biomass-Derived Oxygenated Hydrocarbons to Fuels and Chemicals. *Angewandte Chemie International Edition* **2007**, *46* (38), 7164–7183. https://doi.org/https://doi.org/10.1002/anie.200604274.

(4) Alonso, D. M.; Hakim, S. H.; Zhou, S.; Won, W.; Hosseinaei, O.; Tao, J.; Garcia-Negron, V.; Motagamwala, A. H.; Mellmer, M. A.; Huang, K.; Houtman, C. J.; Labbé, N.; Harper, D. P.; Maravelias, C. T.; Runge, T.; Dumesic, J. A. Increasing the Revenue from Lignocellulosic Biomass: Maximizing Feedstock Utilization. *Sci Adv* **2017**, *3* (5). https://doi.org/10.1126/SCIADV.1603301/SUPPL_FILE/1603301_SM.PDF.

(5) Komandur, J.; Mohanty, K. Fast Pyrolysis of Biomass and Hydrodeoxygenation of Bio-Oil for the Sustainable Production of Hydrocarbon Biofuels. *Hydrocarbon Biorefinery: Sustainable Processing of Biomass for Hydrocarbon Biofuels* **2022**, 47–76. https://doi.org/10.1016/B978-0-12-823306-1.00003-0.

(6) Serrano-Ruiz, J. C.; Pineda, A.; Balu, A. M.; Luque, R.; Campelo, J. M.; Romero, A. A.; Ramos-Fernández, J. M. Catalytic Transformations of Biomass-Derived Acids into Advanced Biofuels. *Catal Today* **2012**, *195*, 162–168.

(7) Serrano-Ruiz, J. C.; Dumesic, J. A. Catalytic Routes for the Conversion of Biomass into Liquid Hydrocarbon Transportation Fuels. *Energy Environ Sci* **2011**, *4* (1), 83–99. https://doi.org/10.1039/C0EE00436G.

(8) Wright, W. R. H.; Palkovits, R. Development of Heterogeneous Catalysts for the Conversion of Levulinic Acid to γ-Valerolactone. *ChemSusChem* **2012**, *5* (9), 1657–1667. https://doi.org/https://doi.org/10.1002/cssc.201200111.

(9) Alonso, D. M.; Wettstein, S. G.; Dumesic, J. A. Gamma-Valerolactone, a Sustainable Platform Molecule Derived from Lignocellulosic Biomass. *Green Chem.* **2013**, *15* (3), 584–595. https://doi.org/10.1039/C3GC37065H.

(10) Bond, J. Q.; Martin Alonso, D.; West, R. M.; Dumesic, J. A. γ-Valerolactone Ring-Opening and Decarboxylation over SiO2/Al2O3 in the Presence of Water. *Langmuir* **2010**, *26* (21), 16291–16298. https://doi.org/10.1021/la101424a.

(11) Bond, J. Q.; Alonso, D. M.; Wang, D.; West, R. M.; Dumesic, J. A. Integrated Catalytic Conversion of Gamma-Valerolactone to Liquid Alkenes for Transportation Fuels. *Science (1979)* **2010**, *327* (5969), 1110–1114. https://doi.org/10.1126/science.1184362.

(12) Serrano-Ruiz, J. C.; Wang, D.; Dumesic, J. A. Catalytic Upgrading of Levulinic Acid to 5-Nonanone. *Green Chem.* **2010**, *12* (4), 574–577. https://doi.org/10.1039/B923907C.

(13) Pham, T. N.; Sooknoi, T.; Crossley, S. P.; Resasco, D. E. Ketonization of Carboxylic Acids: Mechanisms, Catalysts, and Implications for Biomass Conversion. *ACS Catal* **2013**, *3* (11), 2456–2473. https://doi.org/10.1021/cs400501h.

(14) Bond, J. Q.; Wang, D.; Alonso, D. M.; Dumesic, J. A. Interconversion between γ-Valerolactone and Pentenoic Acid Combined with Decarboxylation to Form Butene over Silica/Alumina. *J Catal* **2011**, *281* (2), 290–299. https://doi.org/10.1016/J.JCAT.2011.05.011.

(15) Alonso, D. M.; Bond, J. Q.; Dumesic, J. A. Catalytic Conversion of Biomass to Biofuels. *Green Chemistry* **2010**, *12* (9), 1493–1513. https://doi.org/10.1039/C004654J.

(16) Moravvej, Z.; Farshchi Tabrizi, F.; Rahimpour, M. R. Vapor Phase Conversion of Furfural to Valuable Biofuel and Chemicals Over Alumina-Supported Catalysts:

Screening Catalysts. *Top Catal* **2021**, *1*, 1–14. https://doi.org/10.1007/S11244-021-01470-9/SCHEMES/1.

(17) Sitthisa, S.; Resasco, D. E. Hydrodeoxygenation of Furfural Over Supported Metal Catalysts: A Comparative Study of Cu, Pd and Ni. *Catal Letters* **2011**, *141* (6), 784–791. https://doi.org/10.1007/s10562-011-0581-7.

(18) Sitthisa, S.; Sooknoi, T.; Ma, Y.; Balbuena, P. B.; Resasco, D. E. Kinetics and Mechanism of Hydrogenation of Furfural on Cu/SiO2 Catalysts. *J Catal* **2011**, *277* (1). https://doi.org/10.1016/j.jcat.2010.10.005.

(19) Sitthisa, S.; An, W.; Resasco, D. E. Selective Conversion of Furfural to Methylfuran over Silica-Supported NiFe Bimetallic Catalysts. *J Catal* **2011**, *284* (1). https://doi.org/10.1016/j.jcat.2011.09.005.

(20) Wang, C.; Wang, L.; Zhang, J.; Wang, H.; Lewis, J. P.; Xiao, F. S. Product Selectivity Controlled by Zeolite Crystals in Biomass Hydrogenation over a Palladium Catalyst. *J Am Chem Soc* **2016**, *138* (25), 7880–7883. https://doi.org/10.1021/JACS.6B04951/SUPPL_FILE/JA6B04951_SI_001.PDF.

(21) Hronec, M.; Fulajtárová, K.; Vávra, I.; Soták, T.; Dobročka, E.; Mičušík, M. Carbon Supported Pd-Cu Catalysts for Highly Selective Rearrangement of Furfural to Cyclopentanone. *Appl Catal B* **2016**, *181*. https://doi.org/10.1016/j.apcatb.2015.07.046.

(22) Jia, P.; Lan, X.; Li, X.; Wang, T. Highly Selective Hydrogenation of Furfural to Cyclopentanone over a NiFe Bimetallic Catalyst in a Methanol/Water Solution with a Solvent Effect. *ACS Sustain Chem Eng* **2019**, *7* (18), 15221–15229. https://doi.org/10.1021/ACSSUSCHEMENG.9B02112/ASSET/IMAGES/LARGE/SC9B02112_0009.JPEG.

(23) Bui, T. V.; Crossley, S.; Resasco, D. E. C□C Coupling for Biomass-Derived Furanics Upgrading to Chemicals and Fuels. *Chemicals and Fuels from Bio-Based Building Blocks* **2016**, 431–494. https://doi.org/10.1002/9783527698202.CH17.

(24) Hronec, M.; Fulajtárova, K.; Mičušik, M. Influence of Furanic Polymers on Selectivity of Furfural Rearrangement to Cyclopentanone. *Appl Catal A Gen* **2013**, *468*, 426–431. https://doi.org/10.1016/J.APCATA.2013.08.052.

(25) Hronec, M.; Fulajtarová, K. Selective Transformation of Furfural to Cyclopentanone. *Catal Commun* **2012**, *24*, 100–104. https://doi.org/10.1016/J.CATCOM.2012.03.020.

(26) Hronec, M.; Fulajtárová, K.; Vávra, I.; Soták, T.; Dobročka, E.; Mičušík, M. Carbon Supported Pd–Cu Catalysts for Highly Selective Rearrangement of Furfural to Cyclopentanone. *Appl Catal B* **2016**, *181*, 210–219. https://doi.org/10.1016/J.APCATB.2015.07.046.

(27) Date, N. S.; Kondawar, S. E.; Chikate, R. C.; Rode, C. V. Single-Pot Reductive Rearrangement of Furfural to Cyclopentanone over Silica-Supported Pd Catalysts. *ACS Omega* **2018**, *3* (8), 9860–9871. https://doi.org/10.1021/ACSOMEGA.8B00980/ASSET/IMAGES/MEDIUM/AO-2018-00980X_M003.GIF.

(28) Bond, J. Q.; Jungong, C. S.; Chatzidimitriou, A. Microkinetic Analysis of Ring Opening and Decarboxylation of γ-Valerolactone over Silica Alumina. *J Catal* **2016**, *344*, 640–656. https://doi.org/10.1016/J.JCAT.2016.10.021.

(29) Kim, S.; Kwon, E. E.; Kim, Y. T.; Jung, S.; Kim, H. J.; Huber, G. W.; Lee, J. Recent Advances in Hydrodeoxygenation of Biomass-Derived Oxygenates over Heterogeneous Catalysts. *Green Chem.* **2019**, *21* (14), 3715–3743. https://doi.org/10.1039/C9GC01210A.

(30) Komandur, J.; Mohanty, K. Fast Pyrolysis of Biomass and Hydrodeoxygenation of Bio-Oil for the Sustainable Production of Hydrocarbon Biofuels. *Hydrocarbon Biorefinery: Sustainable Processing of Biomass for Hydrocarbon Biofuels* **2022**, 47–76. https://doi.org/10.1016/B978-0-12-823306-1.00003-0.

(31) Ramanathan, A.; Begum, K. M. M. S.; Pereira, A. O.; Cohen, C. Pyrolysis of Waste Biomass: Toward Sustainable Development. *A Thermo-Economic Approach to Energy From Waste* **2022**, 1–34. https://doi.org/10.1016/B978-0-12-824357-2.00005-X.

(32) Kumar, P.; Khan, M. A.; Hu, J.; Kibria, M. G. Single-Atom Catalysts for Biomass-Derived Drop-in Chemicals. *Advanced Catalysis for Drop-in Chemicals* **2022**, 63–100. https://doi.org/10.1016/B978-0-12-823827-1.00009-2.

(33) Prasomsri, T.; Nimmanwudipong, T.; Román-Leshkov, Y. Effective Hydrodeoxygenation of Biomass-Derived Oxygenates into Unsaturated Hydrocarbons by MoO3 Using Low H2 Pressures. *Energy Environ. Sci.* **2013**, *6* (6), 1732–1738. https://doi.org/10.1039/C3EE24360E.

(34) Prasomsri, T.; Shetty, M.; Murugappan, K.; Román-Leshkov, Y. Insights into the Catalytic Activity and Surface Modification of MoO3 during the Hydrodeoxygenation of Lignin-Derived Model Compounds into Aromatic Hydrocarbons under Low Hydrogen Pressures. *Energy Environ. Sci.* **2014**, *7* (8), 2660–2669. https://doi.org/10.1039/C4EE00890A.

(35) Shetty, M.; Murugappan, K.; Prasomsri, T.; Green, W.; Roman-Leshkov, Y. Reactivity and Stability Investigation of Supported Molybdenum Oxide Catalysts for the Hydrodeoxygenation (HDO) of m-Cresol. *J Catal* **2015**, *331*, 86–97. https://doi.org/10.1016/j.jcat.2015.07.034.

(36) Echeandia, S.; Arias, P. L.; Barrio, V. L.; Pawelec, B.; Fierro, J. L. G. Synergy Effect in the HDO of Phenol over Ni–W Catalysts Supported on Active Carbon: Effect of Tungsten Precursors. *Appl Catal B* **2010**, *101* (1–2), 1–12. https://doi.org/10.1016/J.APCATB.2010.08.018.

(37) Pham, T. N.; Shi, D.; Resasco, D. E. Kinetics and Mechanism of Ketonization of Acetic Acid on Ru/TiO2 Catalyst. In *Topics in Catalysis*; 2014; Vol. 57. https://doi.org/10.1007/s11244-013-0227-7.

(38) Sitthisa, S.; Pham, T.; Prasomsri, T.; Sooknoi, T.; Mallinson, R. G.; Resasco, D. E. Conversion of Furfural and 2-Methylpentanal on Pd/SiO2 and Pd-Cu/SiO2 Catalysts. *J Catal* **2011**, *280* (1). https://doi.org/10.1016/j.jcat.2011.02.006.

(39) Omotoso, T.; Boonyasuwat, S.; Crossley, S. P. Understanding the Role of TiO2 Crystal Structure on the Enhanced Activity and Stability of Ru/TiO2 Catalysts for the

Conversion of Lignin-Derived Oxygenates. *Green Chemistry* **2014**, *16* (2). https://doi.org/10.1039/c3gc41377b.

(40) Boonyasuwat, S.; Omotoso, T.; Resasco, D. E.; Crossley, S. P. Conversion of Guaiacol over Supported Ru Catalysts. *Catal Letters* **2013**, *143* (8). https://doi.org/10.1007/s10562-013-1033-3.

(41) Omotoso, T. O.; Baek, B.; Grabow, L. C.; Crossley, S. P. Experimental and First-Principles Evidence for Interfacial Activity of Ru/TiO2 for the Direct Conversion of m-Cresol to Toluene. *ChemCatChem* **2017**, *9* (14). https://doi.org/10.1002/cctc.201700157.

(42) Pestman, R.; Koster, R. M.; Pieterse, J. A. Z.; Ponec, V. Reactions of Carboxylic Acids on Oxides: 1. Selective Hydrogenation of Acetic Acid to Acetaldehyde. *J Catal* **1997**, *168* (2), 255–264. https://doi.org/https://doi.org/10.1006/jcat.1997.1623.

(43) Rachmady, W.; Vannice, M. A. Acetic Acid Hydrogenation over Supported Platinum Catalysts. *J Catal* **2000**, *192* (2). https://doi.org/10.1006/jcat.2000.2863.

(44) Shetty, M.; Murugappan, K.; Prasomsri, T.; Green, W.; Roman-Leshkov, Y. Reactivity and Stability Investigation of Supported Molybdenum Oxide Catalysts for the Hydrodeoxygenation (HDO) of m-Cresol. *J Catal* **2015**, *331*, 86–97. https://doi.org/10.1016/j.jcat.2015.07.034.

(45) Shetty, M.; Murugappan, K.; Prasomsri, T.; Green, W.; Roman-Leshkov, Y. Reactivity and Stability Investigation of Supported Molybdenum Oxide Catalysts for the Hydrodeoxygenation (HDO) of m-Cresol. *J Catal* **2015**, *331*, 86–97. https://doi.org/10.1016/j.jcat.2015.07.034.

(46) Pestman, R.; Duijne, A.; Pieterse, J.; Ponec, V. The Formation of Ketones and Aldehydes from Carboxylic Acids, Structure-Activity Relationship for Two Competitive Reactions. *Journal of Molecular Catalysis A-chemical - J MOL CATAL A-CHEM* **1995**, *103*, 175–180. https://doi.org/10.1016/1381-1169(95)00138-7.

(47) Fu, J.; Lym, J.; Zheng, W.; Alexopoulos, K.; Mironenko, A. v; Li, N.; Boscoboinik, J. A.; Su, D.; Weber, R. T.; Vlachos, D. G. C–O Bond Activation Using Ultralow

Loading of Noble Metal Catalysts on Moderately Reducible Oxides. *Nat Catal* **2020**, *3* (5), 446–453. https://doi.org/10.1038/s41929-020-0445-x.

(48) Chen, L.; Cooper, A. C.; Pez, G. P.; Cheng, H. On the Mechanisms of Hydrogen Spillover in MoO3. *Journal of Physical Chemistry C* **2008**, *112* (6), 1755–1758. https://doi.org/10.1021/jp7119137.

(49) Head, A. R.; Gattinoni, C.; Trotochaud, L.; Yu, Y.; Karslloğlu, O.; Pletincx, S.; Eichhorn, B.; Bluhm, H. Water (Non-)Interaction with MoO3. *Journal of Physical Chemistry C* **2019**, *123* (27). https://doi.org/10.1021/acs.jpcc.9b03822.

(50) Mei, D.; Karim, A. M.; Wang, Y. Density Functional Theory Study of Acetaldehyde Hydrodeoxygenation on MoO3. *The Journal of Physical Chemistry C* **2011**, *115* (16), 8155–8164. https://doi.org/10.1021/jp200011j.

(51) Gomez, L. A.; Bababrik, R.; Komarneni, M. R.; Marlowe, J.; Salavati-fard, T.; D'Amico, A. D.; Wang, B.; Christopher, P.; Crossley, S. P. Selective Reduction of Carboxylic Acids to Aldehydes with Promoted MoO3 Catalysts. *ACS Catal* **2022**, *12* (11), 6313–6324. https://doi.org/10.1021/acscatal.2c01350.

(52) Ranga, C.; Lødeng, R.; Alexiadis, V. I.; Rajkhowa, T.; Bjørkan, H.; Chytil, S.; Svenum, I. H.; Walmsley, J.; Detavernier, C.; Poelman, H.; van der Voort, P.; Thybaut, J. W. Effect of Composition and Preparation of Supported MoO3 Catalysts for Anisole Hydrodeoxygenation. *Chemical Engineering Journal* **2018**, *335*. https://doi.org/10.1016/j.cej.2017.10.090.

(53) Murugappan, K.; Anderson, E.; Teschner, D.; Jones, T.; Skorupska, K.; Roman-Leshkov, Y. Operando NAP-XPS Unveils Differences in MoO3 and Mo2C during Hydrodeoxygenation. *Nat Catal* **2018**, *1*. https://doi.org/10.1038/s41929-018-0171-9.

(54) Shetty, M.; Buesser, B.; Román-Leshkov, Y.; Green, W. H. Computational Investigation on Hydrodeoxygenation (HDO) of Acetone to Propylene on α-MoO3 (010) Surface. *The Journal of Physical Chemistry C* **2017**, *121* (33), 17848–17855. https://doi.org/10.1021/acs.jpcc.7b02942.

(55) Ruiz Puigdollers, A.; Schlexer, P.; Tosoni, S.; Pacchioni, G. Increasing Oxide Reducibility: The Role of Metal/Oxide Interfaces in the Formation of Oxygen Vacancies. *ACS Catal* **2017**, *7* (10), 6493–6513. https://doi.org/10.1021/acscatal.7b01913.

(56) Teles, C. A.; Rabelo-Neto, R. C.; Duong, N.; Quiroz, J.; Camargo, P. H. C.; Jacobs, G.; Resasco, D. E.; Noronha, F. B. Role of the Metal-Support Interface in the Hydrodeoxygenation Reaction of Phenol. *Appl Catal B* **2020**, *277*, 119238. https://doi.org/10.1016/j.apcatb.2020.119238.

(57) Polo-Garzon, F.; Blum, T. F.; Bao, Z.; Wang, K.; Fung, V.; Huang, Z.; Bickel, E. E.; Jiang, D. E.; Chi, M.; Wu, Z. In Situ Strong Metal-Support Interaction (SMSI) Affects Catalytic Alcohol Conversion. *ACS Catal* **2021**, *11* (4), 1938–1945. https://doi.org/10.1021/acscatal.0c05324.

(58) Tsubaki, N.; Fujimoto, K. Promotional SMSI Effect on Supported Palladium Catalysts for Methanol Synthesis. *Top Catal* **2003**, *22* (3–4), 325–335. https://doi.org/10.1023/A:1023548608733.

(59) Prins, R. Hydrogen Spillover. Facts and Fiction. *Chem Rev* **2012**, *112* (5), 2714–2738. https://doi.org/ 10.1021/cr200346z.

(60) Shen, H.; Li, H.; Yang, Z.; Li, C. Magic of Hydrogen Spillover: Understanding and Application. *Green Energy & Environment* **2022**, *7* (6), 1161–1198. https://doi.org/10.1016/J.GEE.2022.01.013.

(61) Pei, Z.-F.; Ponec, V. On the Intermediates of the Acetic Acid Reactions on Oxides: An IR Study. *Appl Surf Sci* **1996**, *103* (2), 171–182. https://doi.org/https://doi.org/10.1016/0169-4332(96)00453-9.

(62) Grootendorst, E. J.; Pestman, R.; Koster, R. M.; Ponec, V. Selective Reduction of Acetic Acid to Acetaldehyde on Iron Oxides. *J Catal* **1994**, *148* (1), 261–269. https://doi.org/10.1006/JCAT.1994.1207.

(63) Li, S. C.; Wang, J. G.; Jacobson, P.; Gong, X. Q.; Selloni, A.; Diebold, U. Correlation between Bonding Geometry and Band Gap States at Organic-Inorganic Interfaces:

Catechol on Rutile TiO 2(110). *J Am Chem Soc* **2009**, *131* (3), 980–984. https://doi.org/ 10.1021/ja803595u.

(64) Sihag, A.; Xie, Z. L.; Thang, H. V.; Kuo, C. L.; Tseng, F. G.; Dyer, M. S.; Chen, H. Y. T. DFT Insights into Comparative Hydrogen Adsorption and Hydrogen Spillover Mechanisms of Pt4/Graphene and Pt4/Anatase (101) Surfaces. *Journal of Physical Chemistry C* **2019**, *123* (42), 25618–25627. https://doi.org/ 10.1021/acs.jpcc.9b04419.

(65) Boudart, M.; Vannice, M. A.; Benson, J. E. Adlineation, Portholes and Spillover. *Zeitschrift fur Physikalische Chemie* **1969**, *64* (1–4), 171–177. https://doi.org/ 10.1524/zpch.1969.64.1_4.171.

(66) Karim, W.; Spreafico, C.; Kleibert, A.; Gobrecht, J.; Vandevondele, J.; Ekinci, Y.; Van Bokhoven, J. A. Catalyst Support Effects on Hydrogen Spillover. *Nature 2017 541:7635* **2017**, *541* (7635), 68–71. https://doi.org/10.1038/nature20782.

(67) Prins, R.; Palfi, V. K.; Reiher, M. Hydrogen Spillover to Nonreducible Supports. *Journal of Physical Chemistry C* **2012**, *116* (27), 14274–14283. https://doi.org/10.1021/JP212274Y.

(68) Karim, W.; Spreafico, C.; Kleibert, A.; Gobrecht, J.; Vandevondele, J.; Ekinci, Y.; Van Bokhoven, J. A. Catalyst Support Effects on Hydrogen Spillover. *Nature 2017 541:7635* **2017**, *541* (7635), 68–71. https://doi.org/10.1038/nature20782.

(69) Prins, R.; Palfi, V. K.; Reiher, M. Hydrogen Spillover to Nonreducible Supports. *Journal of Physical Chemistry C* **2012**, *116* (27), 14274–14283. https://doi.org/ 10.1021/jp212274y.

(70) Tan, M.; Yang, Y.; Yang, Y.; Chen, J.; Zhang, Z.; Fu, G.; Lin, J.; Wan, S.; Wang, S.; Wang, Y. Hydrogen Spillover Assisted by Oxygenate Molecules over Nonreducible Oxides. *Nature Communications 2022 13:1* **2022**, *13* (1), 1–8. https://doi.org/10.1038/s41467-022-29045-6.

(71) Wang, T.; Zhang, Q.; Li, B.; Chen, H.; Chen, L. Density Functional Study of Hydrogen Spillover on Direct Pd-Doped Metal-Organic Frameworks IRMOF-1. *Int J*

Hydrogen Energy **2012**, *37* (6), 5081–5089. https://doi.org/10.1016/J.IJHYDENE.2011.12.065.

(72) Corti, G.; Zhan, Y.; Wang, L.; Chen, L.; Pez, G.; Cooper, A. C.; Cheng, H. A Mechanistic Study of Hydrogen Spillover in MoO3 and Carbon-Based Graphitic Materials. *Journal of Physics: Condensed Matter* **2008**, *20* (6), 064223. https://doi.org/10.1088/0953-8984/20/6/064223.

(73) Sha, X.; Chen, L.; Cooper, A. C.; Pez, G. P.; Cheng, H. Hydrogen Absorption and Diffusion in Bulk α-MoO3. *Journal of Physical Chemistry C* **2009**, *113* (26), 11399–11407. https://doi.org/10.1021/jp9017212.

(74) Levy, R. B.; Boudart, M. Platinum-like Behavior of Tungsten Carbide in Surface Catalysis. *Science* **1973**, *181* (4099), 547–549. https://doi.org/10.1126/SCIENCE.181.4099.547.

(75) Schlatter, J. C.; Boudart, M. Hydrogenation of Ethylene on Supported Platinum. *J Catal* **1972**, *24* (3), 482–492. https://doi.org/10.1016/0021-9517(72)90132-7.

(76) Chen, L.; Cooper, A. C.; Pez, G. P.; Cheng, H. Mechanistic Study on Hydrogen Spillover onto Graphitic Carbon Materials. *Journal of Physical Chemistry C* **2007**, *111* (51), 18995–19000. https://doi.org/10.1021/JP074920G.

(77) Chen, L.; Cooper, A. C.; Pez, G. P.; Cheng, H. Mechanistic Study on Hydrogen Spillover onto Graphitic Carbon Materials. *Journal of Physical Chemistry C* **2007**, *111* (51), 18995–19000. https://doi.org/ 10.1021/jp074920g

(78) Psofogiannakis, G. M.; Froudakis, G. E. DFT Study of Hydrogen Storage by Spillover on Graphite with Oxygen Surface Groups. *J Am Chem Soc* **2009**, *131* (42), 15133–15135. https://doi.org/10.1021/JA906159P.

(79) Zhang, M.; Yao, R.; Jiang, H.; Li, G.; Chen, Y. Insights into the Mechanism of Acetic Acid Hydrogenation to Ethanol on Cu(111) Surface. *Appl Surf Sci* **2017**, *412*, 342–349. https://doi.org/https://doi.org/10.1016/j.apsusc.2017.03.222.

(80) Chiappero, M.; Do, P. T. M.; Crossley, S.; Lobban, L. L.; Resasco, D. E. Direct Conversion of Triglycerides to Olefins and Paraffins over Noble Metal Supported Catalysts. *Fuel* **2011**, *90* (3), 1155–1165. https://doi.org/https://doi.org/10.1016/j.fuel.2010.10.025.

(81) Kresse, G.; Joubert, D. From Ultrasoft Pseudopotentials to the Projector Augmented-Wave Method. *Phys. Rev. B* **1999**, *59*, 1758. https://doi.org/10.1103/PhysRevB.59.1758.

(82) Grimme, S.; Antony, J.; Ehrlich, S.; Krieg, H. A Consistent and Accurate Ab Initio Parametrization of Density Functional Dispersion Correction (DFT-D) for the 94 Elements H-Pu. *J Chem Phys* **2010**, *132* (15), 154104. https://doi.org/10.1063/1.3382344.

(83) Prasomsri, T.; Shetty, M.; Murugappan, K.; Román-Leshkov, Y. Insights into the Catalytic Activity and Surface Modification of MoO3 during the Hydrodeoxygenation of Lignin-Derived Model Compounds into Aromatic Hydrocarbons under Low Hydrogen Pressures. *Energy Environ. Sci.* **2014**, *7* (8), 2660–2669. https://doi.org/10.1039/C4EE00890A.

(84) Cheng, H.; Chen, L.; Cooper, A. C.; Sha, X.; Pez, G. P. Hydrogen Spillover in the Context of Hydrogen Storage Using Solid-State Materials. *Energy Environ. Sci.* **2008**, *1* (3), 338–354. https://doi.org/10.1039/B807618A.

(85) Deshpande, A.; Krishnaswamy, S.; Ponnani, K. Pulsed Micro-Reactor: An Alternative to Estimating Kinetic Parameters of Non-Catalytic Gas–Solid Reactions. *Chemical Engineering Research and Design* **2016**, *117*. https://doi.org/10.1016/j.cherd.2016.10.044.

(86) Kresse, G.; Furthmüller, J. Efficient Iterative Schemes for Ab Initio Total-Energy Calculations Using a Plane-Wave Basis Set. *Phys Rev B* **1996**, *54*, 11169. https://doi.org/10.1103/PhysRevB.54.11169.

(87) Perdew, J. P.; Burke, K.; Ernzerhof, M. Generalized Gradient Approximation Made Simple [Phys. Rev. Lett. 77, 3865 (1996)]. *Phys Rev Lett* **1997**, *78*, 1396.

(88) P. E. Blöchl. Projector Augmented-Wave Method. *Phys. Rev. B* **1994**, *50*, 17953–17979.

(89) Henkelman, G.; Uberuaga, B. P.; Jónsson, H. A Climbing Image Nudged Elastic Band Method for Finding Saddle Points and Minimum Energy Paths. *J Chem Phys* **2000**, *113* (22), 9901–9904. https://doi.org/10.1063/1.1329672.

(90) Henkelman, G.; Jónsson, H. Improved Tangent Estimate in the Nudged Elastic Band Method for Finding Minimum Energy Paths and Saddle Points. *J Chem Phys* **2000**, *113* (22), 9978–9985. https://doi.org/10.1063/1.1323224.

(91) Henkelman, G.; Jónsson, H. A Dimer Method for Finding Saddle Points on High Dimensional Potential Surfaces Using Only First Derivatives. *J Chem Phys* **1999**, *111* (15), 7010–7022. https://doi.org/10.1063/1.480097.

(92) Sermon, P. A.; Bond, G. C. Studies of Hydrogen Spillover. Part 1.—Study of the Rate, Extent and Products of Hydrogen Spillover from Platinum to the Trioxides of Tungsten and Molybdenum. *J. Chem. Soc., Faraday Trans. 1* **1976**, *72* (0), 730–744. https://doi.org/10.1039/F19767200730.

(93) Matsuda, T.; Uchijima, F.; Sakagami, H.; Takahashi, N. H2-Reduction of Pt/MoO3 to MoOx with a Large Surface Area and Its Catalytic Activities for the Conversions of Heptane and Propan-2-Ol. *Phys. Chem. Chem. Phys.* **2001**, *3* (19), 4430–4436. https://doi.org/10.1039/B105680H.

(94) Triwahyono, S.; Jalil, A. A.; Timmiati, S. N.; Ruslan, N. N. B.; Hattori, H. Kinetics Study of Hydrogen Adsorption over Pt/MoO3. *Applied Catalysis A-general* **2010**, *372*, 103–107.

(95) Ressler, T.; Jentoft, R.; Wienold, J.; Günter, M.; Timpe, O. In Situ XAS and XRD Studies on the Formation of Mo Suboxides during Reduction of MoO3. *Journal of Physical Chemistry B - J PHYS CHEM B* **2000**, *104*, 6360–6370. https://doi.org/10.1021/jp000690t.

(96) DeRita, L.; Dai, S.; Lopez-Zepeda, K.; Pham, N.; Graham, G. W.; Pan, X.; Christopher, P. Catalyst Architecture for Stable Single Atom Dispersion Enables Site-Specific

Spectroscopic and Reactivity Measurements of CO Adsorbed to Pt Atoms, Oxidized Pt Clusters, and Metallic Pt Clusters on TiO2. *J Am Chem Soc* **2017**, *139* (40), 14150–14165. https://doi.org/10.1021/jacs.7b07093.

(97) Zhou, S.; Yang, Y.; Yin, P.; Ren, Z.; Wang, L.; Wei, M. Metal–Support Synergistic Catalysis in Pt/MoO3–x Nanorods toward Ammonia Borane Hydrolysis with Efficient Hydrogen Generation. *ACS Appl Mater Interfaces* **2022**, *14* (4), 5275–5286. https://doi.org/10.1021/acsami.1c20736.

(98) Bazin, P.; Saur, O.; Marie, O.; Daturi, M.; Lavalley, J. C.; le Govic, A. M.; Harlé, V.; Blanchard, G. On the Reducibility of Sulfated Pt/CeXZr1−XO2 Solids: A Coupled Thermogravimetric FT-IR Study Using CO as the Reducing Agent. *Appl Catal B* **2012**, *119–120*, 207–216. https://doi.org/https://doi.org/10.1016/j.apcatb.2012.02.037.

(99) Mars, P.; van Krevelen, D. W. Oxidations Carried out by Means of Vanadium Oxide Catalysts. *Chem Eng Sci* **1954**, *3*. https://doi.org/10.1016/S0009-2509(54)80005-4.

(100) Thibodeau, T. J.; Canney, A. S.; Desisto, W. J.; Wheeler, M. C.; Amar, F. G.; Frederick, B. G. Composition of Tungsten Oxide Bronzes Active for Hydrodeoxygenation. *Appl Catal A Gen* **2010**, *388* (1–2). https://doi.org/10.1016/j.apcata.2010.08.025.

(101) Mironenko, A. v.; Vlachos, D. G. Conjugation-Driven "Reverse Mars-van Krevelen"-Type Radical Mechanism for Low-Temperature C-O Bond Activation. *J Am Chem Soc* **2016**, *138* (26). https://doi.org/10.1021/jacs.6b02871.

(102) Doornkamp, C.; Ponec, V. The Universal Character of the Mars and Van Krevelen Mechanism. *J Mol Catal A Chem* **2000**, *162* (1–2). https://doi.org/10.1016/S1381-1169(00)00319-8.

(103) Vannice, M. A. An Analysis of the Mars-van Krevelen Rate Expression. *Catal Today* **2007**, *123* (1–4). https://doi.org/10.1016/j.cattod.2007.02.002.

(104) Fogler, H. S. *Elements of Chemical Reaction Engineering*; Prentice Hall, Ed.; Pearson Education, Inc, 2016.

(105) Yang, F.; Libretto, N. J.; Komarneni, M. R.; Zhou, W.; Miller, J. T.; Zhu, X.; Resasco, D. E. Enhancement of M-Cresol Hydrodeoxygenation Selectivity on Ni Catalysts by Surface Decoration of MoOx Species. *ACS Catal* **2019**, *9* (9). https://doi.org/10.1021/acscatal.9b01285.

(106) Cargnello, M.; Doan-Nguyen, V. V. T.; Gordon, T. R.; Diaz, R. E.; Stach, E. A.; Gorte, R. J.; Fornasiero, P.; Murray, C. B. Control of Metal Nanocrystal Size Reveals Metal-Support Interface Role for Ceria Catalysts. *Science (1979)* **2013**, *341* (6147). https://doi.org/10.1126/science.1240148.

(107) Komaya, T.; Bell, A. T.; Weng-Sieh, Z.; Gronsky, R.; Engelke, F.; King, T. S.; Pruski, M. Effects of Dispersion and Metal-Metal Oxide Interactions on Fischer-Tropsch Synthesis over Ru/TiO2 and TiO2-Promoted Ru/SiO2. *J Catal* **1994**, *150* (2). https://doi.org/10.1006/jcat.1994.1358.

(108) Resasco, D. E.; Haller, G. L. A Model of Metal-Oxide Support Interaction for Rh on TiO2. *J Catal* **1983**, *82* (2). https://doi.org/10.1016/0021-9517(83)90194-X.

(109) Briggs, N. M.; Barrett, L.; Wegener, E. C.; Herrera, L. V; Gomez, L. A.; Miller, J. T.; Crossley, S. P. Identification of Active Sites on Supported Metal Catalysts with Carbon Nanotube Hydrogen Highways. *Nat Commun* **2018**, *9* (1), 3827. https://doi.org/10.1038/s41467-018-06100-9.

(110) Rellán-Piñeiro, M.; López, N. A Coupled Density Functional Theory-Microkinetic Modeling for the Hydrodeoxygenation of Glycerol to Propylene on MoO3. *ACS Sustain Chem Eng* **2018**, *6* (12). https://doi.org/10.1021/acssuschemeng.8b02933.

(111) Rachmady, W.; Vannice, M. A. Acetic Acid Reduction by H2 over Supported Pt Catalysts: A DRIFTS and TPD/TPR Study. *J Catal* **2002**, *207* (2), 317–330. https://doi.org/10.1006/JCAT.2002.3556.

(112) Noh, H.; Wang, D.; Luo, S.; Flanagan, T. B.; Balasubramaniam, R.; Sakamoto, Y. Hydrogen Bronze Formation within Pd/MoO3 Composites. *Journal of Physical Chemistry B* **2004**, *108* (1). https://doi.org/10.1021/jp0307506.

(113) Kosydar, R.; Kołodziej, M.; Lalik, E.; Gurgul, J.; Mordarski, G.; Drelinkiewicz, A. The Role of Hydrogen Bronzes in the Hydrogenation of Polyfunctional Reagents: Cinnamaldehyde, Furfural and 5-Hydroxymethylfurfural over Pd/HxWO3 and Pd/HxMoO3 Catalysts. *Int J Hydrogen Energy* **2022**, *47* (4). https://doi.org/10.1016/j.ijhydene.2021.10.162.

(114) Hoang-Van, C.; Zegaoui, O. Studies of High Surface Area Pt/MoO3 and Pt/WO3 Catalysts for Selective Hydrogenation Reactions. II. Reactions of Acrolein and Allyl Alcohol. *Appl Catal A Gen* **1997**, *164* (1–2). https://doi.org/10.1016/S0926-860X(97)00160-9.

(115) Tokarz-Sobieraj, R.; Hermann, K.; Witko, M.; Blume, A.; Mestl, G.; Schlögl, R. Properties of Oxygen Sites at the MoO3(0 1 0) Surface: Density Functional Theory Cluster Studies and Photoemission Experiments. *Surf Sci* **2001**, *489* (1–3), 107–125. https://doi.org/10.1016/S0039-6028(01)01169-4.

(116) Kashfi-Sadabad, R.; Yazdani, S.; Huan, T. D.; Cai, Z.; Pettes, M. T. Role of Oxygen Vacancy Defects in the Electrocatalytic Activity of Substoichiometric Molybdenum Oxide. *Journal of Physical Chemistry C* **2018**, *122* (32), 18212–18222. https://doi.org/10.1021/acs.jpcc.8b03536.

(117) Borgschulte, A.; Sambalova, O.; Delmelle, R.; Jenatsch, S.; Hany, R.; Nüesch, F. Hydrogen Reduction of Molybdenum Oxide at Room Temperature. *Sci Rep* **2017**, *7*. https://doi.org/10.1038/SREP40761.

(118) Rellán-Piñeiro, M.; López, N. One Oxygen Vacancy, Two Charge States: Characterization of Reduced α-MoO3(010) through Theoretical Methods. *Journal of Physical Chemistry Letters* **2018**, *9* (10), 2568–2573. https://doi.org/10.1021/acs.jpclett.8b00536.

(119) Ressler, T.; Jentoft, R. E.; Wienold, J.; Günter, M. M.; Timpe, O. In Situ XAS and XRD Studies on the Formation of Mo Suboxides during Reduction of MoO3. *Journal of Physical Chemistry B* **2000**, *104* (27), 6360–6370. https://doi.org/10.1021/jp000690t.

(120) Ressler, T.; Wienold, J.; Jentoft, R. E. Formation of Bronzes during Temperature-Programmed Reduction of MoO3 with Hydrogen—an in Situ XRD and XAFS Study. *Solid State Ion* **2001**, *141–142*, 243–251. https://doi.org/10.1016/S0167-2738(01)00747-0.

(121) Miu, E. V.; McKone, J. R.; Mpourmpakis, G. The Sensitivity of Metal Oxide Electrocatalysis to Bulk Hydrogen Intercalation: Hydrogen Evolution on Tungsten Oxide. *J Am Chem Soc* **2022**, *144* (14), 6420–6433. https://doi.org/ 10.1021/jacs.2c00825.

(122) Kosydar, R.; Kołodziej, M.; Lalik, E.; Gurgul, J.; Mordarski, G.; Drelinkiewicz, A. The Role of Hydrogen Bronzes in the Hydrogenation of Polyfunctional Reagents: Cinnamaldehyde, Furfural and 5-Hydroxymethylfurfural over Pd/HxWO3 and Pd/HxMoO3 Catalysts. *Int J Hydrogen Energy* **2022**, *47* (4), 2347–2365. https://doi.org/ 10.1016/j.ijhydene.2021.10.162.

(123) Chen, W. P.; He, K. F.; Wang, Y.; Chan, H. L. W.; Yan, Z. Highly Mobile and Reactive State of Hydrogen in Metal Oxide Semiconductors at Room Temperature. *Scientific Reports 2013 3:1* **2013**, *3* (1), 1–5. https://doi.org/10.1038/srep03149.

(124) Chen, L.; Cooper, A. C.; Pez, G. P.; Cheng, H. On the Mechanisms of Hydrogen Spillover in MoO3. *Journal of Physical Chemistry C* **2008**, *112* (6), 1755–1758. https://doi.org/ 10.1021/jp7119137.

(125) Dang, J.; Zhang, G. H.; Chou, K. C.; Reddy, R. G.; He, Y.; Sun, Y. Kinetics and Mechanism of Hydrogen Reduction of MoO3 to MoO2. *Int J Refract Metals Hard Mater* **2013**, *41*, 216–223. https://doi.org/10.1016/J.IJRMHM.2013.04.002.

(126) Baumgarten, R.; Naumann d'Alnoncourt, R.; Lohr, S.; Gioria, E.; Frei, E.; Fako, E.; De, S.; Boscagli, C.; Drieß, M.; Schunk, S.; Rosowski, F. Quantification and Tuning of Surface Oxygen Vacancies for the Hydrogenation of CO2 on Indium Oxide Catalysts. *Chem Ing Tech* **2022**, *94* (11), 1765–1775. https://doi.org/10.1002/CITE.202200085.

(127) Ciftyurek, E.; Li, Z.; Schierbaum, K. Adsorbed Oxygen Ions and Oxygen Vacancies: Their Concentration and Distribution in Metal Oxide Chemical Sensors and

Influencing Role in Sensitivity and Sensing Mechanisms. *Sensors 2023, Vol. 23, Page 29* **2022**, *23* (1), 29. https://doi.org/10.3390/S23010029.

(128) Millet, M. M.; Frei, E.; Algara-Siller, G.; Schlögl, R.; Tarasov, A. Surface Titration of Supported Ni Catalysts by O2-Pulse Thermal Analysis. *Appl Catal A Gen* **2018**, *566*, 155–163. https://doi.org/10.1016/J.APCATA.2018.08.023.

(129) Linsebigler, A.; Lu, G.; Yates, J. T. CO Chemisorption on TiO2(110): Oxygen Vacancy Site Influence on CO Adsorption. *J Chem Phys* **1998**, *103* (21), 9438. https://doi.org/10.1063/1.470005.

(130) Wang, L.; Zhang, G. H.; Chou, K. C. Mechanism and Kinetic Study of Hydrogen Reduction of Ultra-Fine Spherical MoO3 to MoO2. *Int J Refract Metals Hard Mater* **2016**, *54*, 342–350. https://doi.org/10.1016/J.IJRMHM.2015.09.003.

(131) Wang, L.; Zhang, G. H.; Chou, K. C. Study on Oxidation Mechanism and Kinetics of MoO2 to MoO3 in Air Atmosphere. *Int J Refract Metals Hard Mater* **2016**, *57*, 115–124. https://doi.org/10.1016/J.IJRMHM.2016.03.001.

(132) Wang, L.; Zhang, G. H.; Chou, K. C. Study on Oxidation Mechanism and Kinetics of MoO2 to MoO3 in Air Atmosphere. *Int J Refract Metals Hard Mater* **2016**, *57*, 115–124. https://doi.org/10.1016/J.IJRMHM.2016.03.001.

(133) Linsebigler, A.; Lu, G.; Yates, J. T. CO Chemisorption on TiO2(110): Oxygen Vacancy Site Influence on CO Adsorption. *J Chem Phys* **1998**, *103* (21), 9438. https://doi.org/10.1063/1.470005.

(134) He, H.; Dai, H. X.; Au, C. T. Defective Structure, Oxygen Mobility, Oxygen Storage Capacity, and Redox Properties of RE-Based (RE = Ce, Pr) Solid Solutions. *Catal Today* **2004**, *90* (3–4), 245–254. https://doi.org/10.1016/J.CATTOD.2004.04.033.

(135) Zhu, J.; Uslamin, E. A.; Kosinov, N.; Hensen, E. J. M. Tuning the Reactivity of Molybdenum (Oxy)Carbide Catalysts by the Carburization Degree: CO 2 Reduction and Anisole Hydrodeoxygenation. *Catal Sci Technol* **2020**, *10* (11), 3635–3645. https://doi.org/10.1039/D0CY00484G.

(136) Birtill, J. J.; Dickens, P. G. Thermochemistry of Hydrogen Molybdenum Bronze Phases HxMoO3. *J Solid State Chem* **1979**, *29* (3), 367–372. https://doi.org/10.1016/0022-4596(79)90193-2.

(137) Ayyappan, S.; Rao, C. N. R. A Simple Method of Hydrogen Insertion in Transition Metal Oxides to Obtain Bronzes. *Mater Res Bull* **1995**, *30* (8), 947–951. https://doi.org/10.1016/0025-5408(95)00088-7.

(138) Wang, D.; Barteau, M. A. Kinetics of Butane Oxidation by a Vanadyl Pyrophosphate Catalyst. *J Catal* **2001**, *197* (1), 17–25. https://doi.org/10.1006/JCAT.2000.3061.

(139) Wang, D.; Barteau, M. A. Oxidation Kinetics of Partially Reduced Vanadyl Pyrophosphate Catalyst. *Appl Catal A Gen* **2002**, *223* (1–2), 205–214. https://doi.org/10.1016/S0926-860X(01)00753-0.

(140) Wang, D.; Kung, H. H.; Barteau, M. A. Identification of Vanadium Species Involved in Sequential Redox Operation of VPO Catalysts. *Appl Catal A Gen* **2000**, *201* (2), 203–213. https://doi.org/10.1016/S0926-860X(00)00439-7.

(141) Kennedy, G.; Baker, L. R.; Somorjai, G. A. Selective Amplification of C□O Bond Hydrogenation on Pt/TiO 2 : Catalytic Reaction and Sum-Frequency Generation Vibrational Spectroscopy Studies of Crotonaldehyde Hydrogenation . *Angewandte Chemie* **2014**, *126* (13). https://doi.org/10.1002/ange.201400081.

(142) Poenitzsch, V. Z.; Slinker, K. A.; Miles, D. W.; Miller, M. A.; Wei, R.; Coulter, K. E.; Gardner, S. H. Freestanding Foils of Nanotube Arrays Fused with Metals. *J Mater Sci* **2014**, *49* (20), 7080–7086. https://doi.org/10.1007/s10853-014-8414-x.

(143) Zhao, E. W.; Zheng, H.; Ludden, K.; Xin, Y.; Hagelin-Weaver, H. E.; Bowers, C. R. Strong Metal-Support Interactions Enhance the Pairwise Selectivity of Parahydrogen Addition over Ir/TiO2. *ACS Catal* **2016**, *6* (2). https://doi.org/10.1021/acscatal.5b02632.

(144) Tauster, S. J.; Fung, S. C.; Garten, R. L. Strong Metal-Support Interactions. Group 8 Noble Metals Supported On Titanium Dioxide. *Chemischer Informationsdienst* **1978**, *9* (16). https://doi.org/10.1002/chin.197816029.

(145) Haller, G. L.; Resasco, D. E. Metal–Support Interaction: Group VIII Metals and Reducible Oxides. *Advances in Catalysis* **1989**, *36* (C). https://doi.org/10.1016/S0360-0564(08)60018-8.

(146) Chen, L.; Cooper, A. C.; Pez, G. P.; Cheng, H. Mechanistic Study on Hydrogen Spillover onto Graphitic Carbon Materials. *Journal of Physical Chemistry C* **2007**, *111* (51). https://doi.org/10.1021/jp074920g.

(147) Chen, L.; Pez, G.; Cooper, A. C.; Cheng, H. A Mechanistic Study of Hydrogen Spillover in MoO3 and Carbon-Based Graphitic Materials. *Journal of Physics Condensed Matter* **2008**, *20* (6). https://doi.org/10.1088/0953-8984/20/6/064223.

(148) Psofogiannakis, G. M.; Froudakis, G. E. DFT Study of Hydrogen Storage by Spillover on Graphite with Oxygen Surface Groups. *J Am Chem Soc* **2009**, *131* (42). https://doi.org/10.1021/ja906159p.

(149) Wang, L.; Yang, F. H.; Yang, R. T.; Miller, M. A. Effect of Surface Oxygen Groups in Carbons on Hydrogen Storage by Spillover. *Ind Eng Chem Res* **2009**, *48* (6). https://doi.org/10.1021/ie8014507.

(150) Bhowmick, R.; Rajasekaran, S.; Friebel, D.; Beasley, C.; Jiao, L.; Ogasawara, H.; Dai, H.; Clemens, B.; Nilsson, A. Hydrogen Spillover in Pt-Single-Walled Carbon Nanotube Composites: Formation of Stable C-H Bonds. *J Am Chem Soc* **2011**, *133* (14). https://doi.org/10.1021/ja200403m.

(151) Campbell, C. T.; Parker, S. C.; Starr, D. E. The Effect of Size-Dependent Nanoparticle Energetics on Catalyst Sintering. *Science (1979)* **2002**, *298* (5594). https://doi.org/10.1126/science.1075094.

(152) Dai, Y.; Lim, B.; Yang, Y.; Cobley, C. M.; Li, W.; Cho, E. C.; Grayson, B.; Fanson, P. T.; Campbell, C. T.; Sun, Y.; Xia, Y. A Sinter-Resistant Catalytic System Based on Platinum Nanoparticles Supported on TiO2 Nanofibers and Covered by Porous Silica. *Angewandte Chemie - International Edition* **2010**, *49* (44). https://doi.org/10.1002/anie.201001839.

(153) Baker, L. R.; Kennedy, G.; van Spronsen, M.; Hervier, A.; Cai, X.; Chen, S.; Wang, L. W.; Somorjai, G. A. Furfuraldehyde Hydrogenation on Titanium Oxide-Supported Platinum Nanoparticles Studied by Sum Frequency Generation Vibrational Spectroscopy: Acid-Base Catalysis Explains the Molecular Origin of Strong Metal-Support Interactions. *J Am Chem Soc* **2012**, *134* (34). https://doi.org/10.1021/ja306079h.

(154) Zhang, J.; Wang, B.; Nikolla, E.; Medlin, J. W. Directing Reaction Pathways through Controlled Reactant Binding at Pd–TiO2 Interfaces. *Angewandte Chemie - International Edition* **2017**, *56* (23). https://doi.org/10.1002/anie.201703669.

(155) Williams, C. L.; Chang, C. C.; Do, P.; Nikbin, N.; Caratzoulas, S.; Vlachos, D. G.; Lobo, R. F.; Fan, W.; Dauenhauer, P. J. Cycloaddition of Biomass-Derived Furans for Catalytic Production of Renewable p -Xylene. *ACS Catal* **2012**, *2* (6). https://doi.org/10.1021/cs300011a.

(156) Rios-Escobedo, R.; Ortiz-Santos, E.; Colín-Luna, J. A.; Díaz de León, J. N.; del Angel, P.; Escobar, J.; de los Reyes, J. A. Anisole Hydrodeoxygenation: A Comparative Study of Ni/TiO2-ZrO2 and Commercial TiO2 Supported Ni and NiRu Catalysts. *Top Catal* **2022**, *65* (13), 1448–1461. https://doi.org/10.1007/s11244-022-01662-x.

(157) Lødeng, R.; Ranga, C.; Rajkhowa, T.; Alexiadis, V. I.; Bjørkan, H.; Chytil, S.; Svenum, I. H.; Walmsley, J.; Thybaut, J. W. Hydrodeoxygenation of Phenolics in Liquid Phase over Supported MoO3 and Carburized Analogues. *Biomass Convers Biorefin* **2017**, *7* (3), 343–359. https://doi.org/10.1007/S13399-017-0252-Z/METRICS.

(158) Piutti, C.; Quartieri, F. The Piancatelli Rearrangement: New Applications for an Intriguing Reaction. *Molecules*. 2013. https://doi.org/10.3390/molecules181012290.

(159) Gumidyala, A.; Wang, B.; Crossley, S. Direct Carbon-Carbon Coupling of Furanics with Acetic Acid over Brønsted Zeolites. *Sci Adv* **2016**, *2* (9). https://doi.org/10.1126/sciadv.1601072.

(160) Hronec, M.; Fulajtárova, K.; Liptaj, T.; Štolcová, M.; Prónayová, N.; Soták, T. Cyclopentanone: A Raw Material for Production of C15 and C17 Fuel Precursors. *Biomass Bioenergy* **2014**, *63*, 291–299. https://doi.org/10.1016/J.BIOMBIOE.2014.02.025.

(161) Bui, T. v.; Crossley, S.; Resasco, D. E. C□C Coupling for Biomass-Derived Furanics Upgrading to Chemicals and Fuels. In *Chemicals and Fuels from Bio-Based Building Blocks*; 2016. https://doi.org/10.1002/9783527698202.ch17.

(162) Kawabata, T.; Kato, M.; Mizugaki, T.; Ebitani, K.; Kaneda, K. Monomeric Metal Aqua Complexes in the Interlayer Space of Montmorillonites as Strong Lewis Acid Catalysts for Heterogeneous Carbon-Carbon Bond-Forming Reactions. *Chemistry - A European Journal* **2005**, *11* (1). https://doi.org/10.1002/chem.200400672.

(163) Fischer, J.; Hölderich, W. F. Baeyer-Villiger-Oxidation of Cyclopentanone with Aqueous Hydrogen Peroxide by Acid Heterogeneous Catalysis. *Appl Catal A Gen* **1999**, *180* (1–2). https://doi.org/10.1016/S0926-860X(98)00378-0.

(164) Yang, Y.; Du, Z.; Huang, Y.; Lu, F.; Wang, F.; Gao, J.; Xu, J. Conversion of Furfural into Cyclopentanone over Ni-Cu Bimetallic Catalysts. *Green Chemistry* **2013**, *15* (7). https://doi.org/10.1039/c3gc37133f.

(165) Hronec, M.; Fulajtarová, K.; Liptaj, T. Effect of Catalyst and Solvent on the Furan Ring Rearrangement to Cyclopentanone. *Appl Catal A Gen* **2012**, *437–438*. https://doi.org/10.1016/j.apcata.2012.06.018.

(166) Nielsen, E. R. Vapor Phase Oxidation of Furfural. *Ind Eng Chem* **1949**, *41* (2). https://doi.org/10.1021/ie50470a026.

(167) Milas, N. A.; Walsh, W. L. Catalytic Oxidations. I. Oxidations in the Furan Series. *J Am Chem Soc* **1935**, *57* (8). https://doi.org/10.1021/ja01311a001.

(168) Badovskaya, L. A.; Povarova, L. v. Oxidation of Furans (Review). *Chem Heterocycl Compd (N Y)* **2009**, *45* (9). https://doi.org/10.1007/s10593-009-0390-8.

(169) Hronec, M.; Fulajtarová, K. Selective Transformation of Furfural to Cyclopentanone. *Catal Commun* **2012**, *24*. https://doi.org/10.1016/j.catcom.2012.03.020.

(170) Zhu, Y. L.; Xiang, H. W.; Li, Y. W.; Jiao, H.; Wu, G. S.; Zhong, B.; Guo, G. Q. A New Strategy for the Efficient Synthesis of 2-Methylfuran and γ-Butyrolactone. *New Journal of Chemistry* **2003**, *27* (2). https://doi.org/10.1039/b208849p.

(171) Zheng, H. Y.; Zhu, Y. L.; Teng, B. T.; Bai, Z. Q.; Zhang, C. H.; Xiang, H. W.; Li, Y. W. Towards Understanding the Reaction Pathway in Vapour Phase Hydrogenation of Furfural to 2-Methylfuran. *J Mol Catal A Chem* **2006**, *246* (1–2). https://doi.org/10.1016/j.molcata.2005.10.003.

(172) Kijeński, J.; Winiarek, P.; Paryjczak, T.; Lewicki, A.; Mikolajska, A. Platinum Deposited on Monolayer Supports in Selective Hydrogenation of Furfural to Furfuryl Alcohol. *Appl Catal A Gen* **2002**, *233* (1–2). https://doi.org/10.1016/S0926-860X(02)00140-0.

(173) Scholz, D.; Aellig, C.; Hermans, I. Catalytic Transfer Hydrogenation/Hydrogenolysis for Reductive Upgrading of Furfural and 5-(Hydroxymethyl)Furfural. *ChemSusChem* **2014**, *7* (1). https://doi.org/10.1002/cssc.201300774.

(174) Davis, J. L.; Barteau, M. A. Polymerization and Decarbonylation Reactions of Aldehydes on the Pd(111) Surface. *J Am Chem Soc* **1989**, *111* (5). https://doi.org/10.1021/ja00187a035.

(175) Shekhar, R.; Barteau, M. A.; Plank, R. v.; Vohs, J. M. Adsorption and Reaction of Aldehydes on Pd Surfaces. *Journal of Physical Chemistry B* **1997**, *101* (40). https://doi.org/10.1021/jp971077l.

(176) Jiang, J.; Kucernak, A. Electrooxidation of Small Organic Molecules on Mesoporous Precious Metal Catalysts: II: CO and Methanol on Platinum–Ruthenium Alloy. *Journal of Electroanalytical Chemistry* **2003**, *543* (2), 187–199. https://doi.org/10.1016/S0022-0728(03)00046-9.

(177) Zhang, W.; Zhu, Y.; Niu, S.; Li, Y. A Study of Furfural Decarbonylation on K-Doped Pd/Al2O 3 Catalysts. *J Mol Catal A Chem* **2011**, *335* (1–2). https://doi.org/10.1016/j.molcata.2010.11.016.

(178) Tan, Q.; Wang, G.; Nie, L.; Dinse, A.; Buda, C.; Shabaker, J.; Resasco, D. E. Different Product Distributions and Mechanistic Aspects of the Hydrodeoxygenation of M-Cresol over Platinum and Ruthenium Catalysts. *ACS Catal* **2015**, *5* (11). https://doi.org/10.1021/acscatal.5b00765.

(179) Rekoske, J. E.; Barteau, M. A. Isothermal Reduction Kinetics of Titanium Dioxide-Based Materials. *Journal of Physical Chemistry B* **1997**, *101* (7). https://doi.org/10.1021/jp9620025.

(180) Wang, S.; Vorotnikov, V.; Vlachos, D. G. A DFT Study of Furan Hydrogenation and Ring Opening on Pd(111). *Green Chemistry* **2014**, *16* (2). https://doi.org/10.1039/c3gc41183d.

(181) Tumuluru, J. S.; Sokhansanj, S.; Hess, J. R.; Wright, C. T.; Boardman, R. D. A Review on Biomass Torrefaction Process and Product Properties for Energy Applications. *Industrial Biotechnology*. 2011. https://doi.org/10.1089/ind.2011.7.384.

APPENDIX A1. Supporting information for chapter II: Selective reduction of carboxylic acids to aldehydes over MoO_3 catalysts

SECTION 1. Thermodynamic case of study of Pentanal to pentanol conversion on Hysys

The compositions of pentanal (PAL) and pentanol (POL) were studied using a Gibbs reactor, which will solve for the equilibrium of all reactions (element balance is maintained). This case of study was conducted using a fixed initial concentration of pentanal, and atmospheric constant pressure, while the temperatures was varied over a wide range. The resulting data was then used to generate Figure S1, which illustrates the changes in composition of pentanal and pentanol at equilibrium as the temperature is varied.

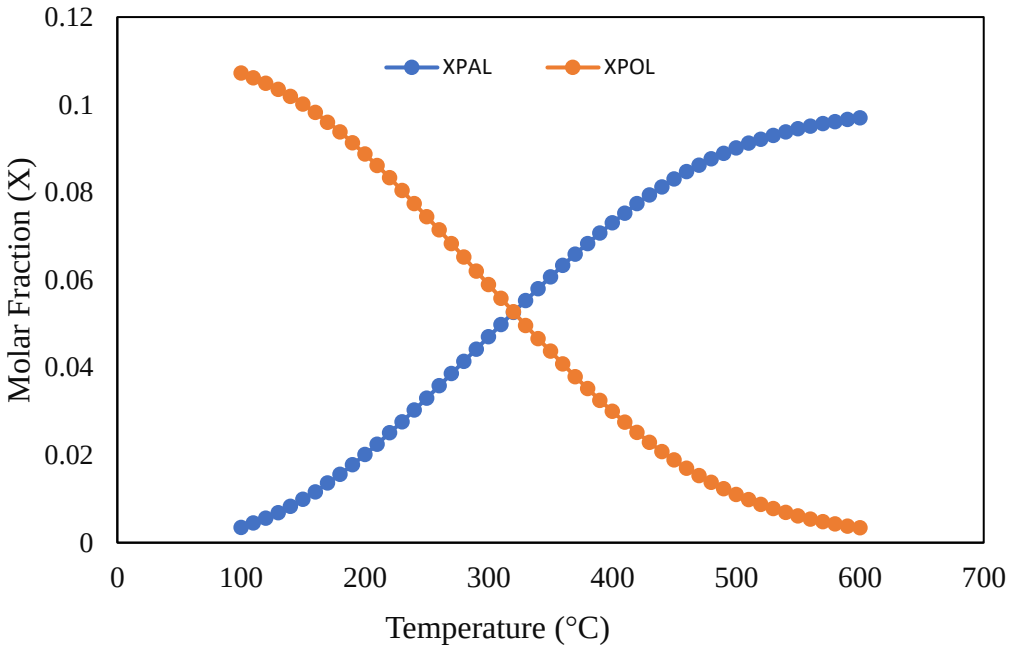


Figure S1. Molar fraction of PAL and POL vs temperature.

Figure S1 demonstrates that an increase in temperature causes a shift in the production of POL towards PAL. Interestingly, during our investigation of the deoxygenation of pentanal (PA) over MoO_3, we did not detect any POL, suggesting that competitive adsorption may be a significant factor in this chemistry. This can be explained by the high coverage of PA on the catalyst surface and its strong adsorption to the oxygen vacancies, which prevents PAL from being reabsorbed and subsequently transformed into POL.

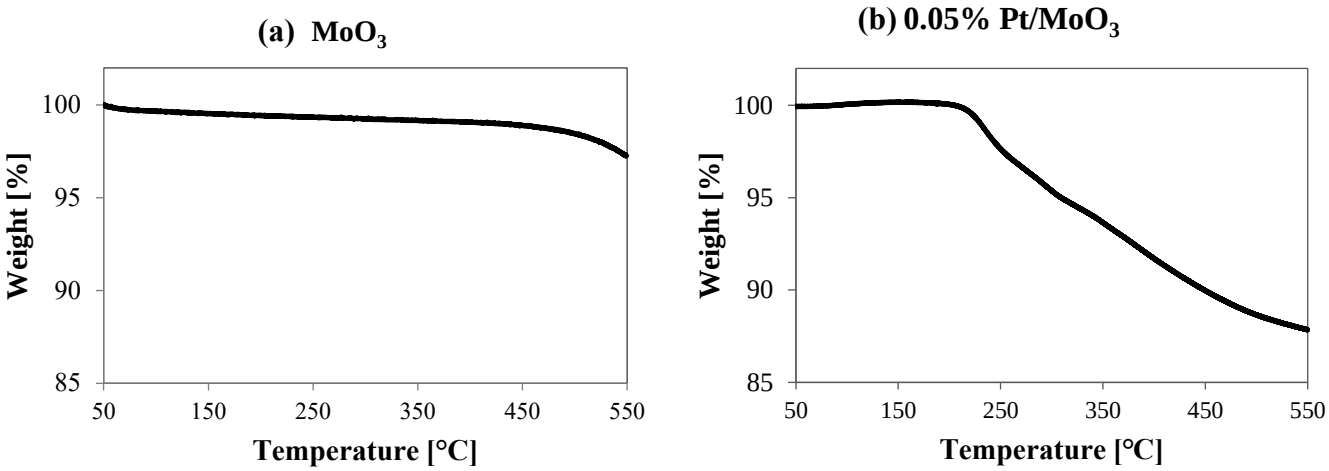


Figure S3. TGA-TPR profiles for **a)** MoO_3 and **b)** 0.05% Pt/MoO_3.

Binding Energies (eV)								
Samples	Mo^{4+}		Mo^{5+}		Mo^{6+}		Pt^0	
*	$Mo3d_{5/2}$	$Mo3d_{3/2}$	$Mo3d_{5/2}$	$Mo3d_{3/2}$	$Mo3d_{5/2}$	$Mo3d_{3/2}$	$Pt4f_{7/2}$	$Pt4f_{5/2}$
MoO_3 (Calcined)	--	--	--	--	233.3	236.43	--	--
MoO_3 (Reduced)	230.01	233.14	231.69	234.82	233.26	236.39	--	--
0.05% Pt/MoO_3 (Reduced)	229.84	232.97	231.65	234.78	233.52	236.65	71.39	74.72

Table S1. Binding energies of Mo (3d) doublet for Mo^{4+}, Mo^{5+}, and Mo^{6+} and Pt (4f) doublet for Pt^0 as determined by XPS characterization.

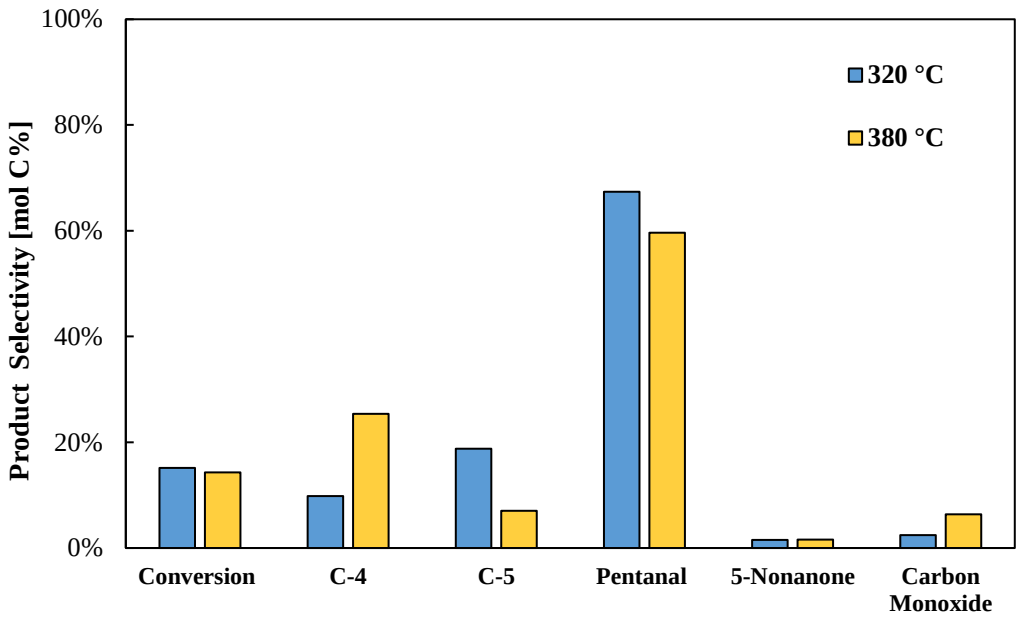


Figure S4. Comparison of product distribution measured at the same conversion levels with different temperatures for 0.05% Pt/MoO_3. Reaction conditions: Conversion: ~ 16%, Flow of H_2 = 30 mL/min, P_{Total} = 1 atm, and TOS = 70 min. The catalyst was previously reduced under H_2 flow (100 mL/min) at 400 °C for 1h.

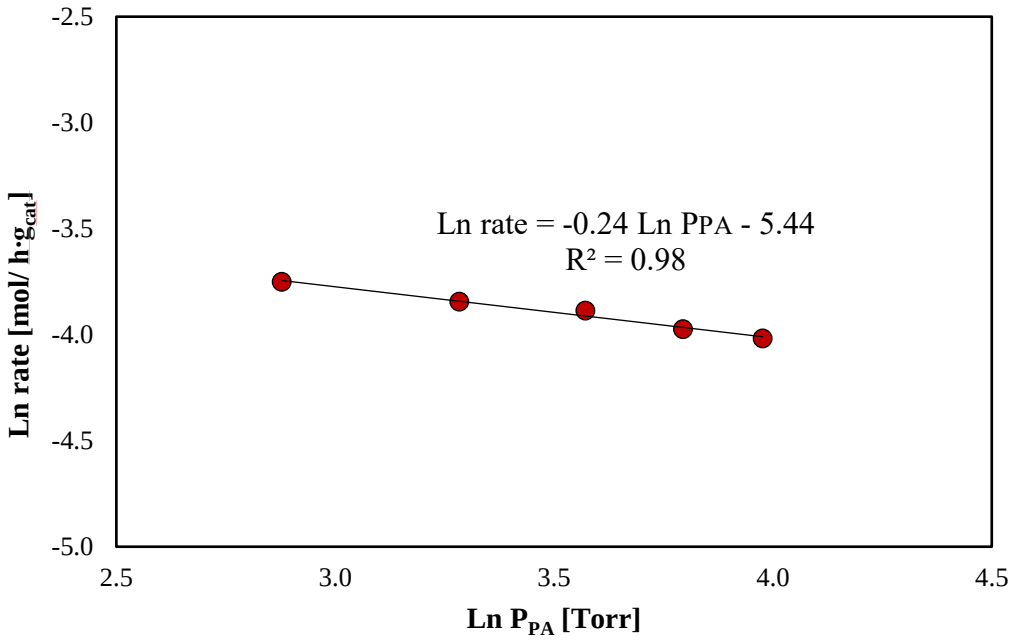


Figure S5. Order of reaction with respect to PA over MoO_3. The flow of H_2 =30 mL/min, P_{Total} = 1 atm, and TOS = 0 min. The flow of PA varied from 0.09 to 0.4 mol/h. The catalyst was previously reduced under H_2 flow (100 mL/min) at 400 °C for 1 h.

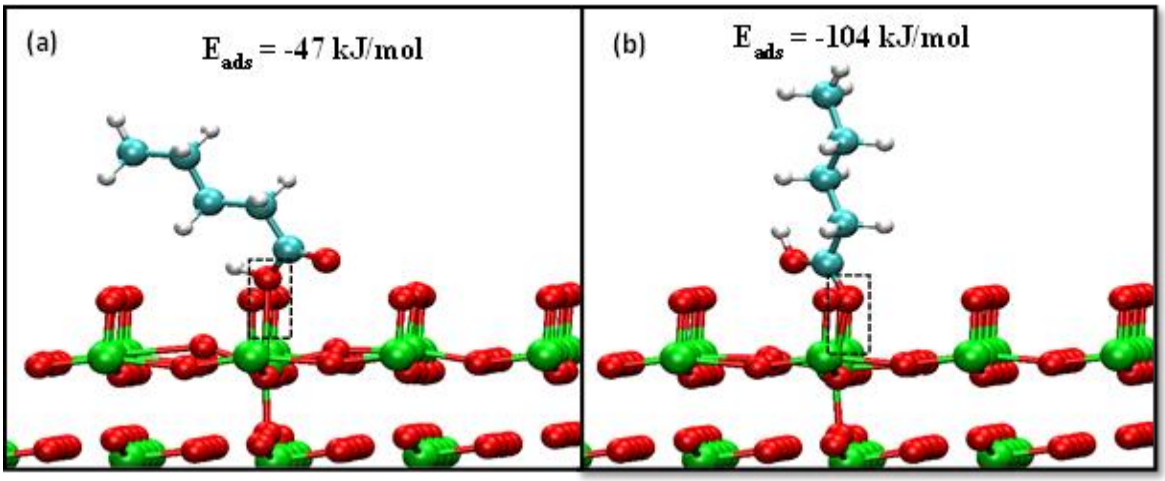


Figure S6. (a) Adsorption of PA on MoO_3 defect site through hydroxyl group oxygen. **(b)** Adsorption of PA on MoO_3 defect site through carbonyl-group oxygen.

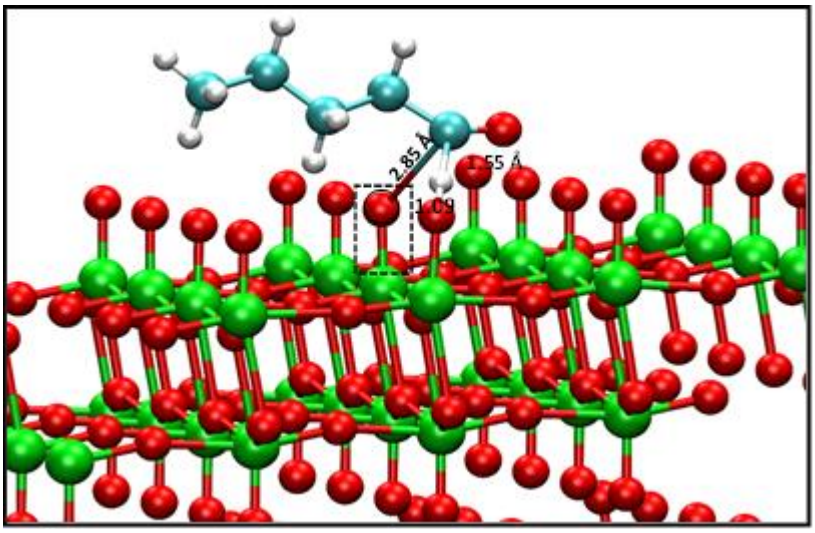


Figure S7. Transition state for the conversion of PA to PAL over MoO_3 defect site through hydroxyl group (-OH) at an oxygen vacancy.

The data reported here are free from external mass transfer limitations. It can be seen from the data in Table S2 that the conversion does not change when the linear velocity is doubled at the same residence time. This experiment showed that external mass transfer limitations do not affect the apparent rate.

$$W_A = K_c\,(C_{Ab} - C_{As}); \qquad K_c \propto \left(\frac{D_{AB}^{2/3}}{v^{1/6}}\right)\left(\frac{v^{1/2}}{d_p^{1/2}}\right)$$

	Reaction 1	Reaction 2
Temperature reaction (°C)	350	350
Mass of catalyst (mg)	10	20
Flow of H_2 (mL/min)	30	60
Flow of PA (mL/h)	0.1	0.2
Conversion (%)	**17**	**17**

Table S2. External Mass transfer limitation test. Conditions for experimental test for external mass transfer limitation.

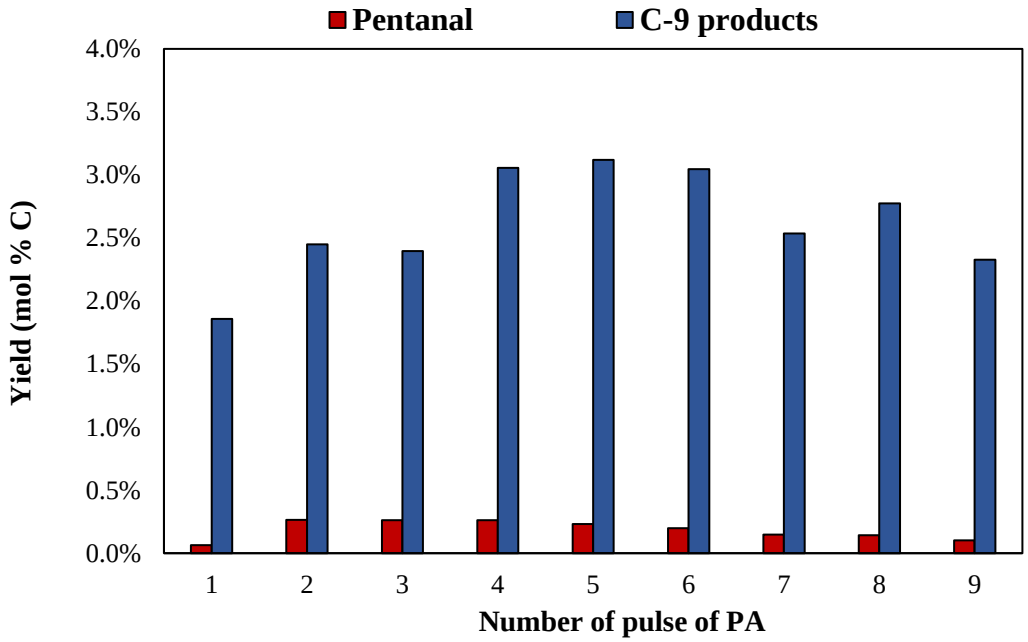


Figure S8. Product yield for the conversion of PA over MoO_3 using a micro-pulse reactor. The reaction was carried out at 350 ºC. The catalyst was previously reduced under H_2 flow (100 mL/min) at 400 °C for 1 h.

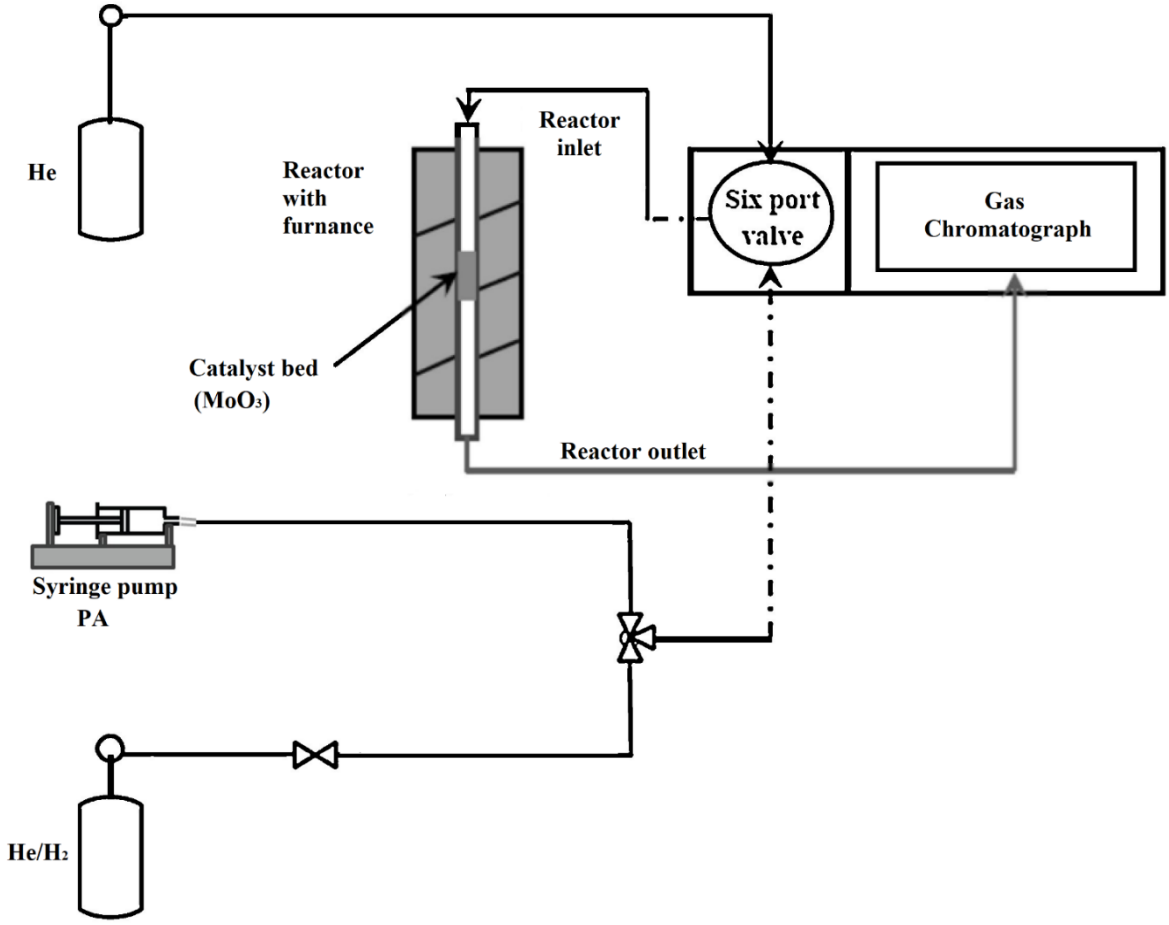


Figure S9. Flow diagram for pulse system.

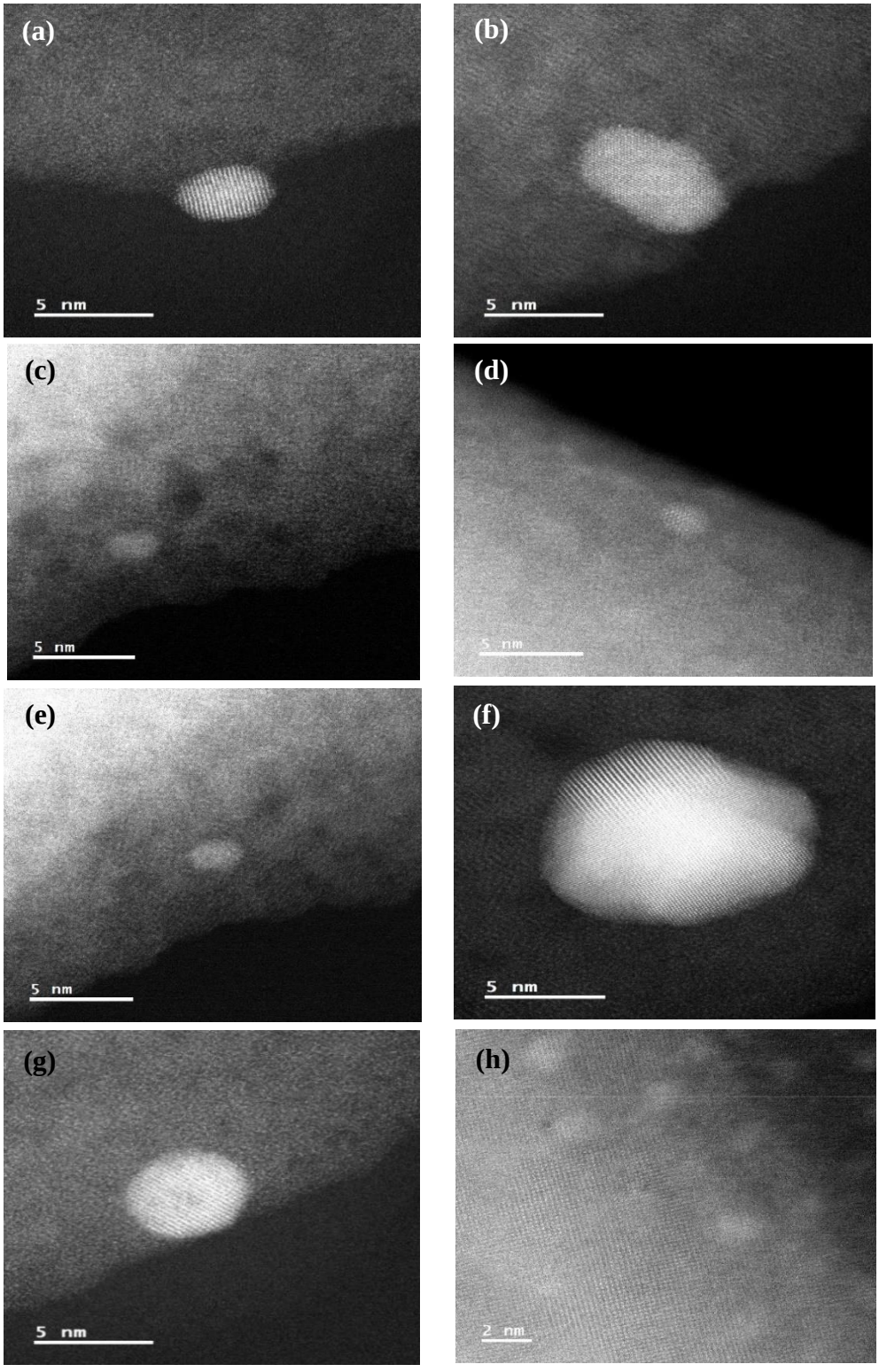


Figure S10. STEM characterization of 0.05% Pt/MoO_3.

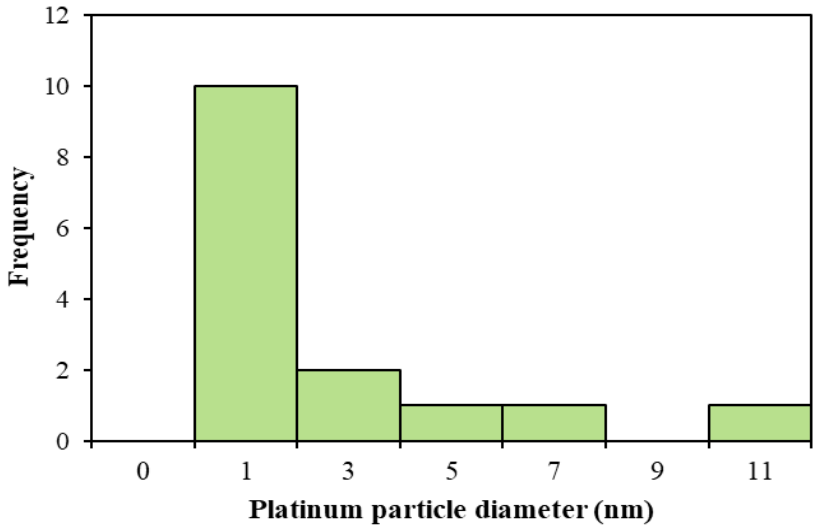


Figure S11. TEM particle size distribution of 0.05% Pt/MoO_3 catalyst pre-reduced at 400 ºC for 1 h before imaging.

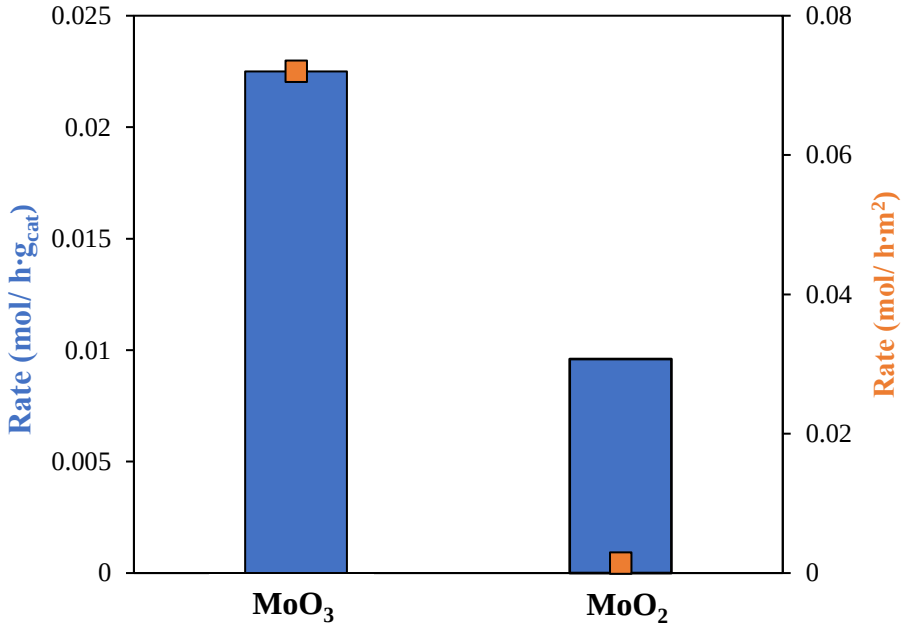


Figure S12. Comparison of the rate conversion of PA by using MoO_3 and MoO_2 as a catalyst. The rate is reported on mol/h·g_{cat} and mol/h·m^2. Blue bars represent the rate normalized per mass; orange symbols represent the rate normalized per BET surface area. Reaction conditions: Flow of H_2 = 30 mL/min, P_{Total} = 1 atm, and W/F = 0.11 g_{cat}/mL·h. The catalyst was previously reduced under H_2 flow (100 mL/min) at 400 °C for 1 h.

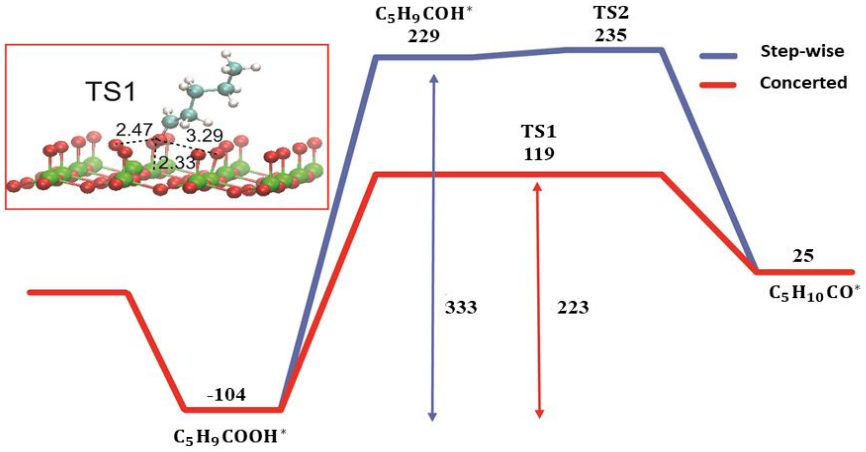


Figure S13. DFT calculated reaction profile for PA with the carbonyl group adsorbed at an oxygen vacancy. The values of energy are in kJ/mol. The inset shows the transition state structure along with the concerted reaction mechanism, which is kinetically more favorable than the step-wise mechanism. The bond distances are shown in the unit of Angstrom.

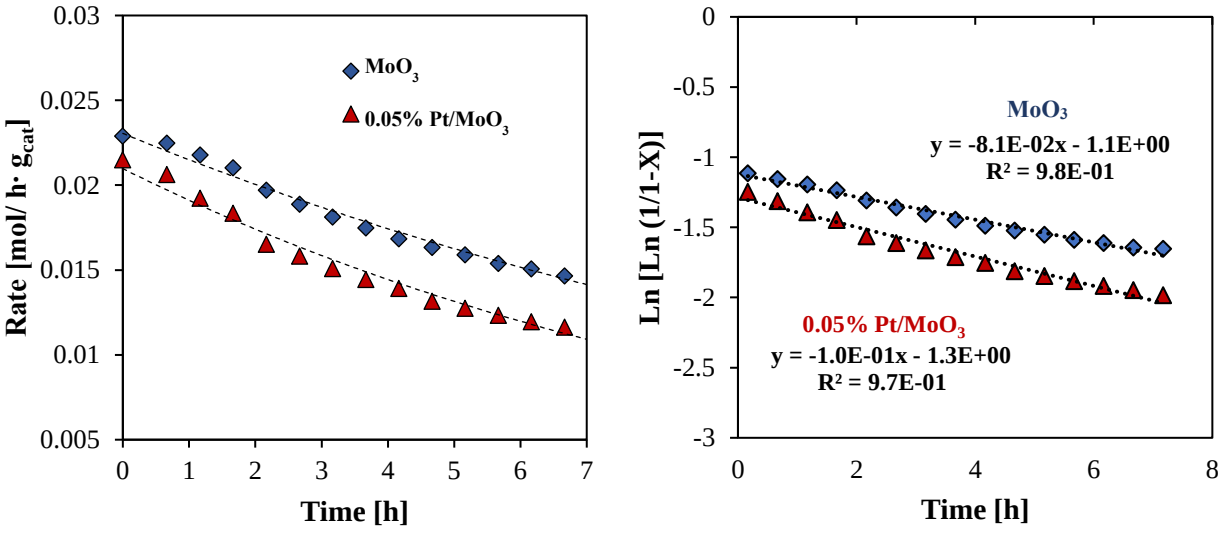


Figure S14. (a) Rate vs. time on stream comparison of pentanoic acid over MoO_3 and 0.05% Pt/MoO_3. **(b)** Deactivation profile for MoO_3 and 0.05% Pt/MoO_3. Reaction conditions: Flow of H_2 = 30 mL/min, P_{Total} = 1 atm, W/F= 0.11 g_{cat}/mL·h and $T_{reaction}$ = 350 °C. The catalyst was previously reduced under H_2 flow (100 mL/min) at 400 °C for 1 h. These catalysts were studied for a period of 8 h and under similar conversion rates (~25%).

APPENDIX A2. Supporting information for chapter III: Revealing the mechanistic details for the selective deoxygenation of carboxylic acids over dynamic MoO_3 catalysts.

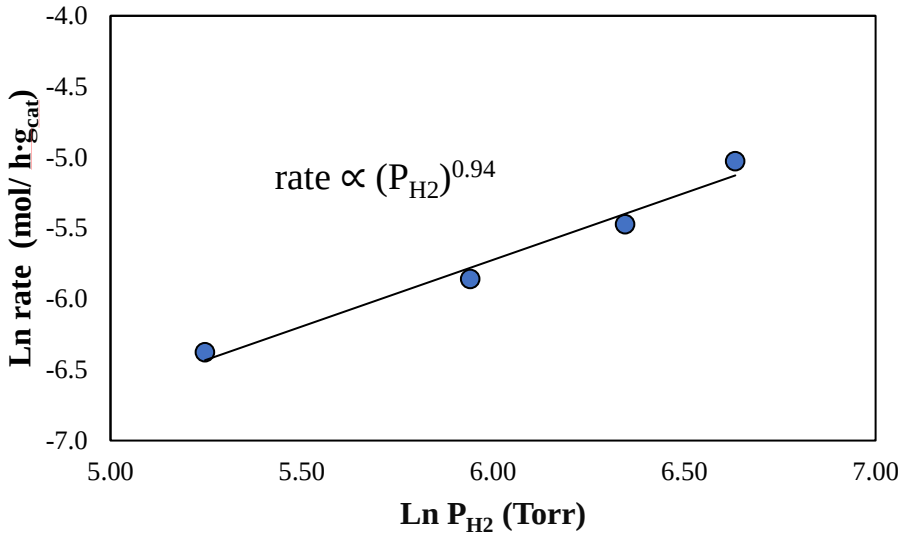


Figure S15. Reaction order with respect to PA over MoO_3 at 320 °C. Reaction conditions: Flow of H_2 = 30 mL/min, W/F = 0.11 g_{cat}/mL·h and P_{Total} = 760 Torr, and TOS = 0 min. The catalyst was previously reduced under H_2 flow (100 mL/min) at 400 °C for 1 h for all cases.

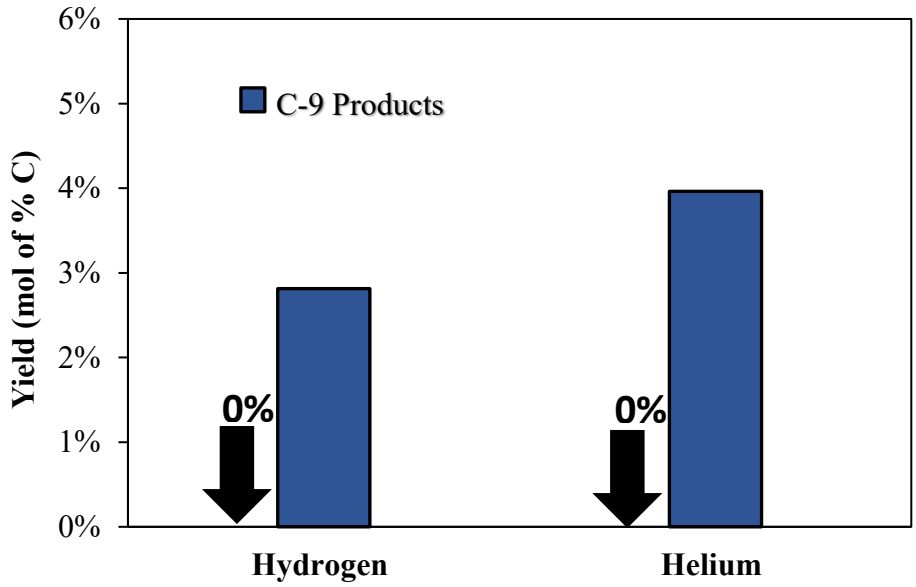


Figure S16. Conversion of PA over MoO_3 without H_2 pre-treatment. Hydrogen or helium gas is mixed with PA and introduced in each pulse by using a six-port valve. Reaction conditions: Flow of H_2 = 30 mL/min, and $T_{reaction}$: 350 °C.

Section S1. Proposed sequence of elementary steps and derived rate expression

[1] $H_{2(g)} + 2^{\bullet} \underset{K_1}{\longleftrightarrow} 2H^{\bullet}$

[2] $H^{\bullet} + \circledast \underset{K_2}{\longleftrightarrow} H^{\circledast} + \bullet$

[3] $H^{\circledast} + H^{\circledast} \underset{K_3}{\longleftrightarrow} H_2O^{\oslash} + \circledast$

[4] $C_4H_9COOH_{(g)} + 2^{\bullet} \underset{K_4}{\longleftrightarrow} C_4H_9COO^{\bullet} + H^{\bullet}$

[5] $C_4H_9COOH^{\oslash} + \circledast \underset{K_5}{\longleftrightarrow} C_4H_9COO^{\oslash} + H^{\circledast}$

[6] $C_4H_9COOH + \oslash \underset{K_6}{\longleftrightarrow} C_4H_9COOH^{\oslash}$

[7] $C_4H_9COOH^{\oslash} + H^{\circledast} \underset{K_7}{\longleftrightarrow} C_4H_9COHOH^{\oslash} + \circledast$

[8] $C_4H_9COHOH^{\oslash} + H^{\circledast} \underset{K_8}{\longleftrightarrow} C_4H_9CHO + H_2O^{\oslash} + \circledast$

[9] $H_2O^{\oslash} \underset{K_9}{\longleftrightarrow} H_2O\,(g) + \oslash$

[10] $C_4H_9CHO^{\oslash} \underset{K_{10}}{\longleftrightarrow} C_5H_{10}O_{(g)} + \oslash$

Figure S17. Propose elementary steps for the hydrogenation of PA over promoted MoO_3. (•) denotes metal site, (⊛) oxidized oxygen vacancy, (∅) reduced oxygen vacancy, (→) proposed kinetically relevant step, and (↔) represents a quasi-equilibrated step.

The steady-state approximation is used to derive the rate expression that represents the surface reaction step. All other steps in the proposed catalytic sequence are assumed to be quasi-equilibrated.

Adsorption/Equilibrium constants

$$K_1 = \frac{[H^{\bullet}]^2}{P_{H2}\,[\bullet]^2} \rightarrow [H^{\bullet}] = K_1^{\frac{1}{2}} P_{H2}^{\frac{1}{2}} [\bullet]$$

$$K_2 = \frac{[H^{\circledast}][\bullet]}{[H^{\bullet}][\circledast]} \rightarrow [H^{\circledast}] = \frac{K_2[H^{\bullet}][\circledast]}{[\bullet]}$$

$$K_3 = \frac{[H_2O^{\oslash}][\circledast]}{[H^{\circledast}]^2} \rightarrow [H_2O^{\oslash}] = \frac{K_3[H^{\circledast}]^2}{[\circledast]}$$

$$K_4 = \frac{[C_4H_9COO^{\bullet}][H^{\bullet}]}{P_{PA}[\bullet]^2} \rightarrow [C_4H_9COO^{\bullet}] = \frac{K_4 P_{PA}[\bullet]^2}{[H^{\bullet}]}$$

$$K_6 = \frac{[C_4H_9COOH^{\oslash}]}{P_{PA}[\oslash]} \rightarrow [C_4H_9COOH^{\oslash}] = K_6 P_{PA}[\oslash]$$

$$K_7 = \frac{[C_4H_9COHOH^{\oslash}][\circledast]}{[C_4H_9COOH^{\oslash}][H^{\circledast}]} \rightarrow [C_4H_9COHOH^{\oslash}] = \frac{K_7[C_4H_9COOH^{\oslash}][H^{\circledast}]}{[\circledast]}$$

Different rate expressions and rate limiting steps were considered to determine which mechanism is best represented by the collected data.

Hydrogen dissociation on metal sites (step 1):

$$H_{2(g)} + 2^{\bullet} \xrightarrow[K_1]{} 2H^{\bullet}$$

$$r_1 = k_1 K_1 P_{H2}[\bullet]^2 \qquad \text{Eq. S1}$$

where [•] corresponds to metal balance sites. $[\bullet]_0$ represents the number density of all adsorption sites (vacant and occupied) on a catalyst surface.

$$[\bullet]_0 = [\bullet] + [H^{\bullet}] + [C_4H_9COO^{\bullet}] \qquad \text{Eq. S2}$$

$$[\bullet] = \frac{[\bullet]_0}{(1 + K_1^{1/2}P_{H2}^{1/2} + K_4 P_{PA}/K_1^{1/2}P_{H2}^{1/2})} \qquad \text{Eq. S3}$$

The final rate equation for hydrogen dissociation on metal sites is provided by substituting equation S3 into equation S1:

$$r_1 = \frac{k_1 K_1 P_{H2}[\bullet]_0}{(1 + K_1^{\frac{1}{2}}P_{H2}^{\frac{1}{2}} + K_4 P_{PA}/K_1^{\frac{1}{2}}P_{H2}^{\frac{1}{2}})^2} \qquad \text{Eq. S4}$$

(A) Hydrogen spillover

$$r_2 = k_2[H^{\bullet}][\circledast] \qquad \text{Eq. S5}$$

Substituting $[H^{\bullet}]$ by using the adsorption constant related to hydrogen dissociation, we can obtain the following expression:

$$r_2 = k_2 K_1^{1/2} P_{H2}^{1/2} [\bullet][\circledast] \quad \text{Eq. S6}$$

Where [•] is given by Eq. S3 as follows:

$$r_2 = \frac{k_2 K_1^{1/2} P_{H2}^{1/2} [\circledast][\bullet]_0}{(1 + K_1^{1/2} P_{H2}^{1/2} + K_4 P_{PA}/K_1^{1/2} P_{H2}^{1/2})} \quad \text{Eq. S7}$$

(B) Oxygen vacancy formation/regeneration (Step 3):

$$H^{\circledast} + H^{\circledast} \underset{K_3}{\longleftrightarrow} H_2O^{\varnothing} + \circledast + \varnothing$$

$$r_3 = k_3 [H^{\circledast}]^2 \quad \text{Eq. S8}$$

$$r_3 = \frac{k_3 K_2^2 [H^{\bullet}]^2 [\circledast]^2}{[\bullet]^2} \quad \text{Eq. S9}$$

Replacing the adsorption constant of hydrogen dissociation, $\frac{[H^{\bullet}]^2}{[\bullet]^2} = K_1 P_{H2}$, the final expression will be given by:

$$r_3 = k_3 K_1 K_2^2 P_{H2} [\circledast]^2 \quad \text{Eq. S10}$$

Oxygen on the oxidized vacancy site ($\circledast$) comes from the support (MoO_3), which is present in high concentration and is the dominant oxidized species.

First hydrogen addition to the adsorbed PA over an oxygen vacancy site (Step 7):

$$C_4H_9COOH^{\varnothing} + H^{\circledast} \underset{K_7}{\longleftrightarrow} C_4H_9COHOH^{\varnothing} + \circledast$$

$$r_7 = k_7 [C_4H_9COOH^{\varnothing}][H^{\circledast}] \quad \text{Eq. S11}$$

From the adsorption constants for step (2) and (5), the expression for $[H^{\circledast}]$ and $[C_4H_9COOH^{\circledast}]$ were derived and replace in r_7:

$$r_7 = k_7 K_1^{\frac{1}{2}} K_6 K_2 P_{PA} P_{H2}^{\frac{1}{2}} [\varnothing][\circledast] \quad \text{Eq. S12}$$

Where [•] is described by equation S3, [⊛] oxidized oxygen vacancy is a constant and [∅] are determined by the oxygen vacancies sites balance as follows:

$$[\oslash]_0 = [\oslash] + [C_4H_9COO^{\oslash}] + [C_4H_9COOH^{\oslash}] + [C_4H_9COHOH^{\oslash}] + [H_2O^{\oslash}] + [C_4H_9CHO^{\oslash}] \quad \text{Eq. S13}$$

Since $[C_4H_9COOH^{\oslash}]$ is the predominant surface species on oxygen vacancies, a balance on [∅] sites give the following expression:

$$[\oslash]_0 = [\oslash] + [C_4H_9COOH^{\oslash}] \quad \text{Eq. S14}$$

Where $[C_4H_9COOH^{\oslash}]$ is obtained by the adsorption constant related to step 5:

$$[\oslash]_0 = [\oslash] + K_6P_{PA}[\oslash] \quad \text{Eq. S15}$$

$$[\oslash] = \frac{[\oslash]_0}{(1 + K_6P_{PA})} \quad \text{Eq. S16}$$

Replacing Eq. S16 in S13, we can obtain the final rate expression when the first hydrogenation of adsorbed species is the rate determined step:

$$r_7 = \frac{k_7K_1^{\frac{1}{2}}K_6K_2P_{PA}P_{H2}^{\frac{1}{2}}[\circledast][\oslash]_0}{(1 + K_6P_{PA})} \quad \text{Eq. S17}$$

(C) Second H addition to the adsorbed PA over an oxygen vacancy site (Step 8):

$$C_4H_9COHOH^{\oslash} + H^{\circledast} \underset{K_8}{\longleftrightarrow} C_4H_9CHO + H_2O^{\oslash} + \circledast$$

$$r_8 = k_8[C_4H_9COHOH^{\oslash}][H^{\circledast}] \quad \text{Eq. S18}$$

In Eq. S15, $[H^{\circledast}]$and $[C_4H_9COHOH^{\oslash}]$ are obtained from the adsorption constants related with the step (3) and (7), respectively. The rate expression for the second hydrogen addition can be expressed as:

$$r_8 = k_8K_1K_2^2K_6K_7P_{PA}P_{H2}[\circledast][\oslash] \quad \text{Eq. S19}$$

Substituting the expression for oxygen vacancy concentration sites (∅) given by Eq. S16 into the Eq. S19, we can obtain the final expression for the second hydrogen addition, as follows:

$$r_8 = \frac{k_8 K_1 K_2^2 K_6 K_7 P_{PA} P_{H2} [\circledast][\varnothing]_0}{(1 + K_6 P_{PA})} \qquad \text{Eq. S20}$$

In this case, we will also consider that the oxygen on the oxidized vacancy site (⊛) comes from the support, so it can be considered a constant.

APPENDIX A3. Supporting information for chapter IV: Quantifying the influence of surface and subsurface H on selective C-O bond scission rates over MoO_{3-X} catalysts.

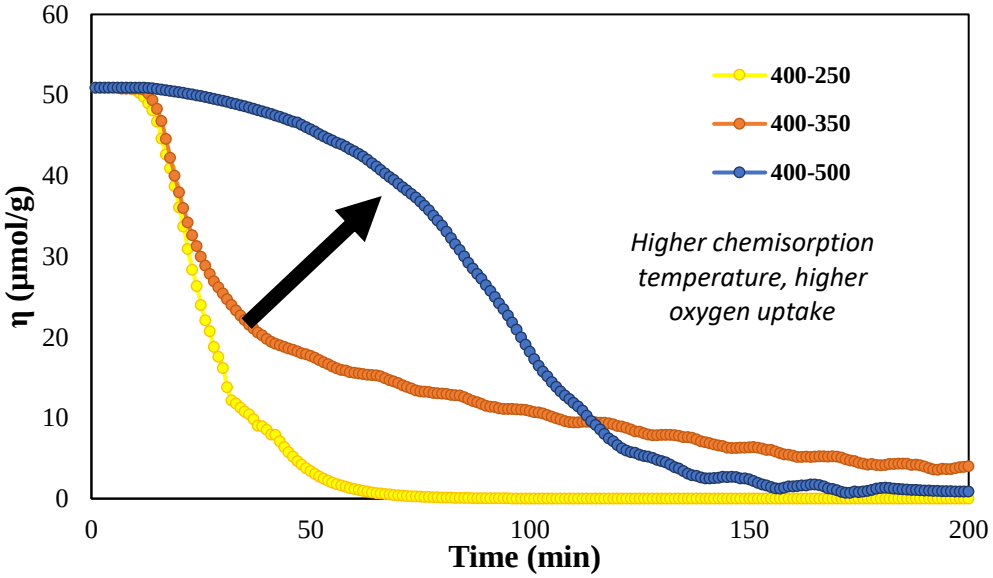


Figure S18. Oxygen chemisorption at different temperatures over 0.05 wt% Pt/MoO_3. Reaction conditions: W_{cat}= 50 mg and $T_{chemisorption}$= 250-500 °C. The catalyst was previously reduced under H_2 flow (100 ml/min) at 400 °C. He pretreatment for 30 mins was used to remove surface hydrogen before O_2 pulse injection.

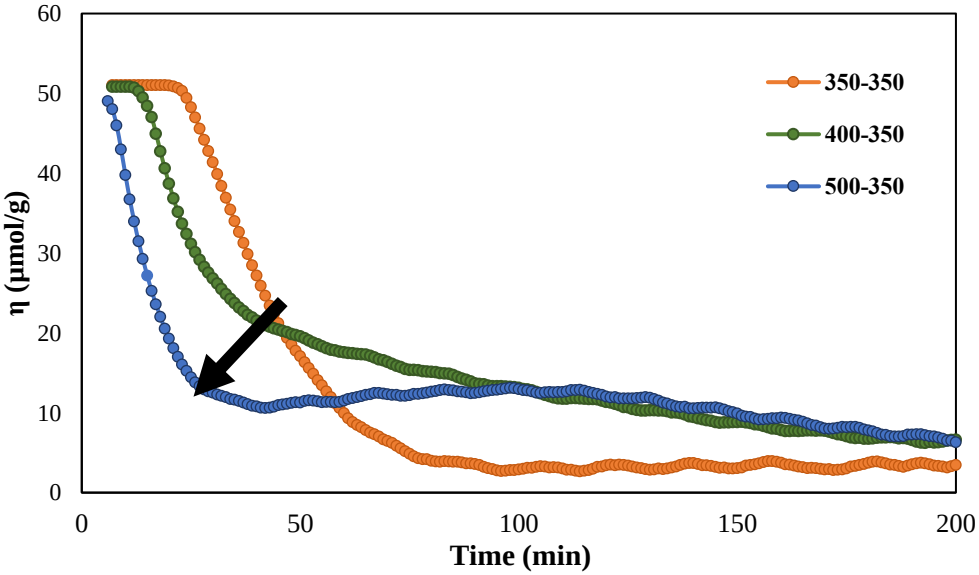


Figure S19. Oxygen chemisorption over 0.05 wt% Pt/MoO_3 after different reduction temperatures. Reaction conditions: W_{cat}= 50 mg and $T_{chemisorption}$= 350 °C. The catalyst was previously reduced under H_2 flow (100 ml/min) at 350-500 °C. He pretreatment for 30 mins was used to remove surface hydrogen before O_2 pulse injection.

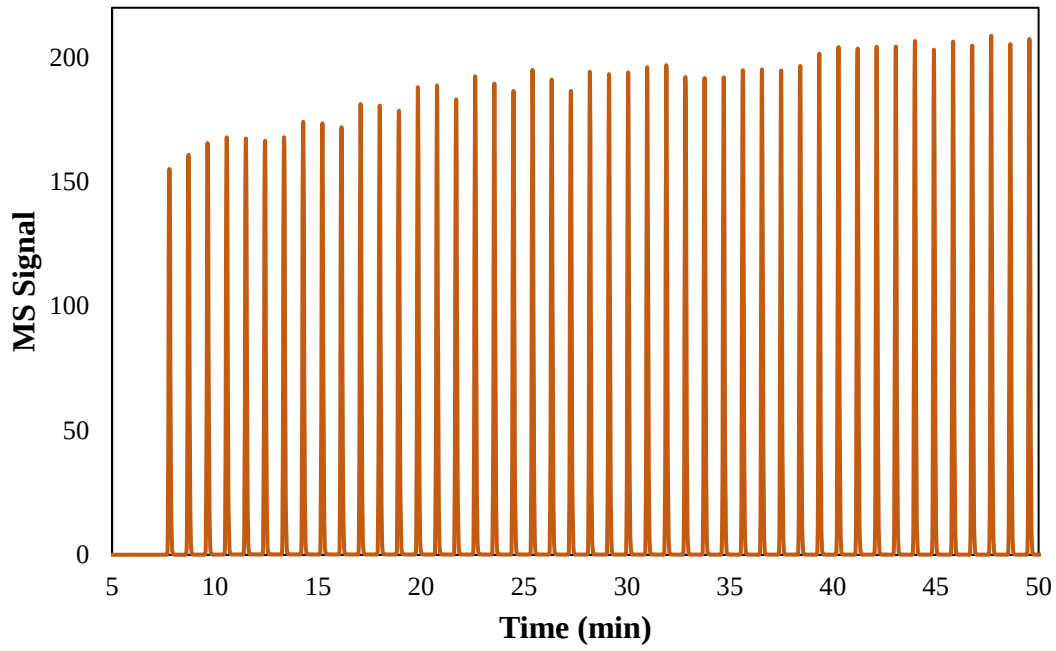


Figure S 20. MS signal spectrum for oxygen chemisorption over MoO_3. Reaction conditions: W_{cat}= 50 mg and $T_{chemisorption}$= 350 °C. The catalyst was previously reduced under H_2 flow (100 ml/min) at 400 °C. He pretreatment for 30 mins was used to remove surface hydrogen before O_2 pulse injection.

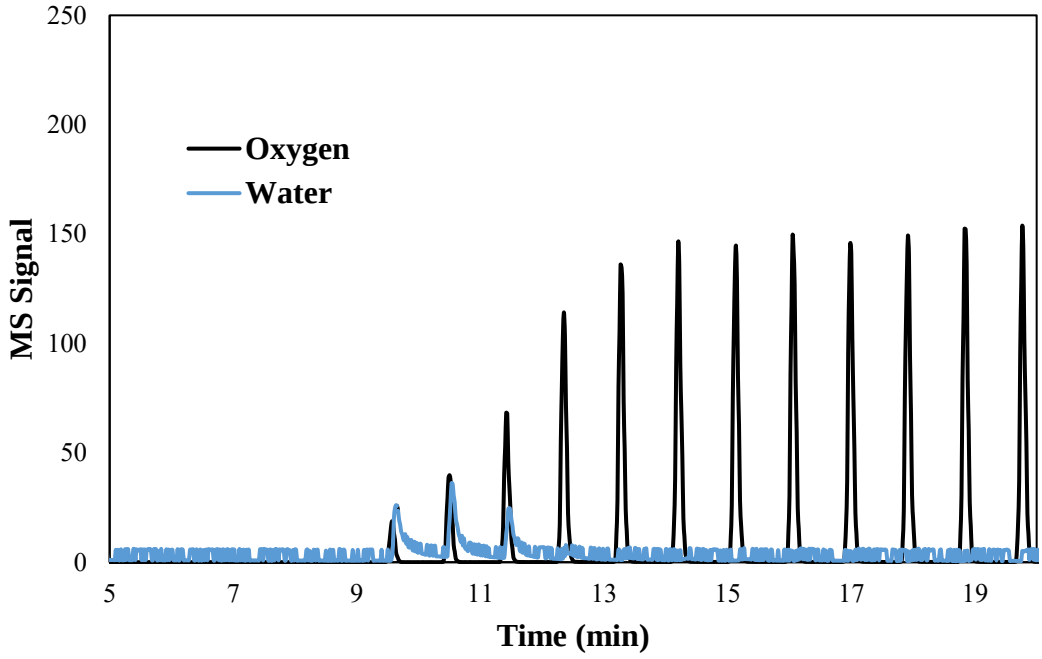


Figure S21. MS signal spectrum for oxygen chemisorption over 0.05% Pt/MoO_3. Reaction conditions: W_{cat}= 50 mg and $T_{chemisorption}$= 350 °C. The catalyst was previously reduced under H_2 flow (100 ml/min) at 400 °C. He pretreatment for 30 mins was used to remove surface hydrogen before O_2 pulse injection.

Different Pt loadings	0.05% wt	1% Pt	3% Pt
Oxygen Uptake per mass of catalyst (μmol/g)	2568	2725	3037
Produced water per mass of catalyst (μmol/g)	153	118	74
Hydrogen atoms per mass of catalyst (μmol/g)	307	236	149

Table S3. Oxygen chemisorption uptake and hydrogen bronzes using Pt/MoO_3 with different loadings of Pt. Reaction conditions: W_{cat}= 50 mg and $T_{chemisorption}$= 350 °C. The catalyst was previously reduced under H_2 flow (100 ml/min) at 400 °C. He pretreatment for 30 mins was used to remove surface hydrogen before O_2 pulse injection.

Section 2

$$\text{Rate} = \frac{X \bullet N_{O2}}{W \bullet \tau}; \quad X: \frac{m_T - m_i}{m_T}$$

X: Conversion/Fractional uptake N_{O2}: Total umole of O_2 in the loop

W: Catalyst weight

τ: Contact time

m_T: Total umoles of O_2 adsorbed/gram

m_i: umoles of O_2 adsorbed/gram at i min

Plot ln(1-X) vs Ln (1/RT)

APPENDIX A4. Supporting information for chapter V: Use of carbon nanotubes hydrogen highways to identify active sites over bifunctional catalysts

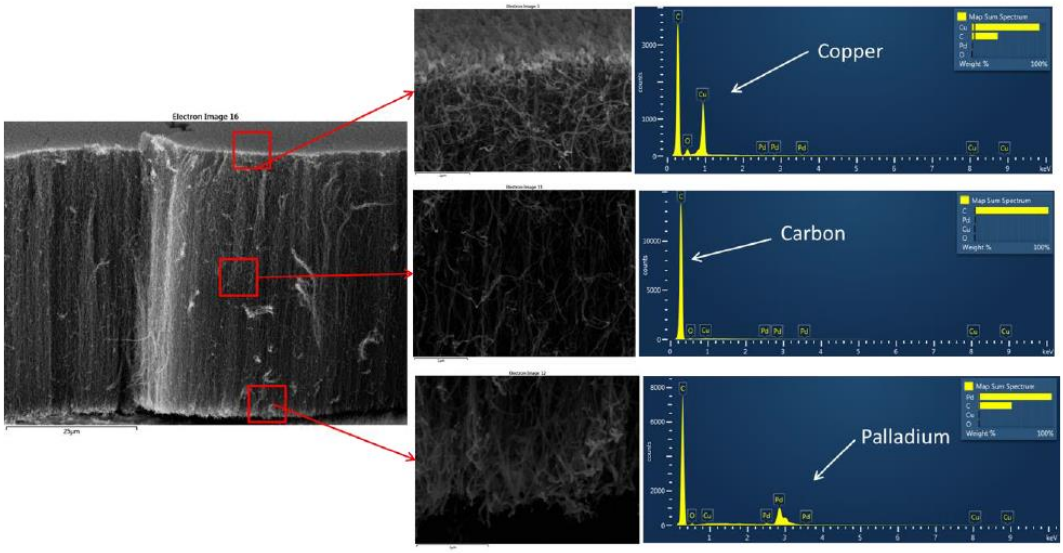


Figure S22. SEM with EDX of a Pd/CNT/CuO forest after treatment in hydrogen for 1 hour at 400 °C.

Supplementary Discussion

Pd and CuO separated on Carbon Nanotubes

Pd and CuO on opposite ends of carbon nanotubes proven using SEM and EDS can be seen in Supplementary Figure 1. According to EDS data at the top of the nanotubes there is 72.2 wt% Cu and 0 wt% Pd, in the middle of the nanotubes there is 0 wt% Cu and 0 wt% Pd, and at the bottom of the nanotubes there is 0 wt% Cu and 68 wt% Pd. Thus, indicating there are no Pd and Cu particles in contact.

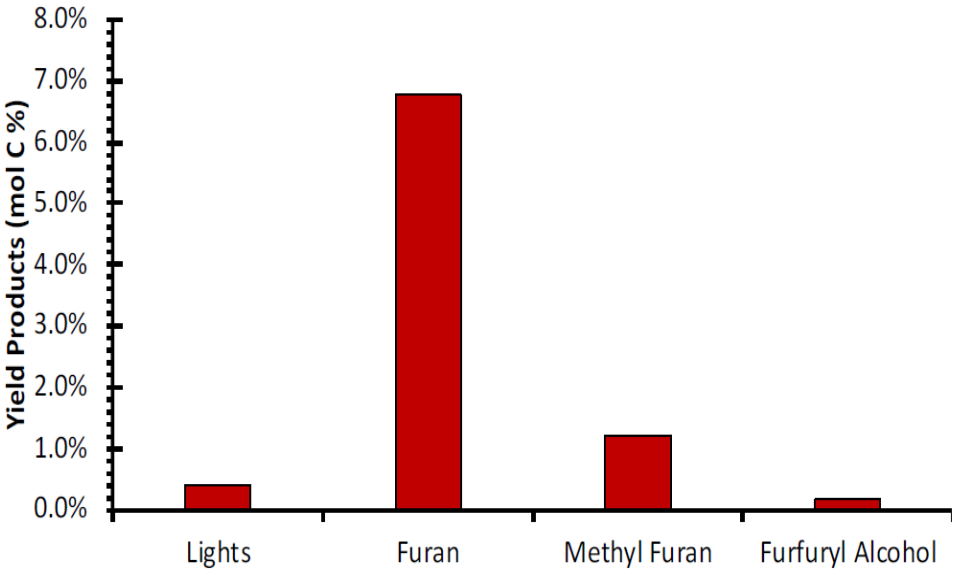


Figure S23. Reaction feeding furfural over physical mixture Pd/CNT and TiO_2/CNT catalyst T= 400 ºC, P = 1 atm, under a H_2 flow, 30 min TOS.

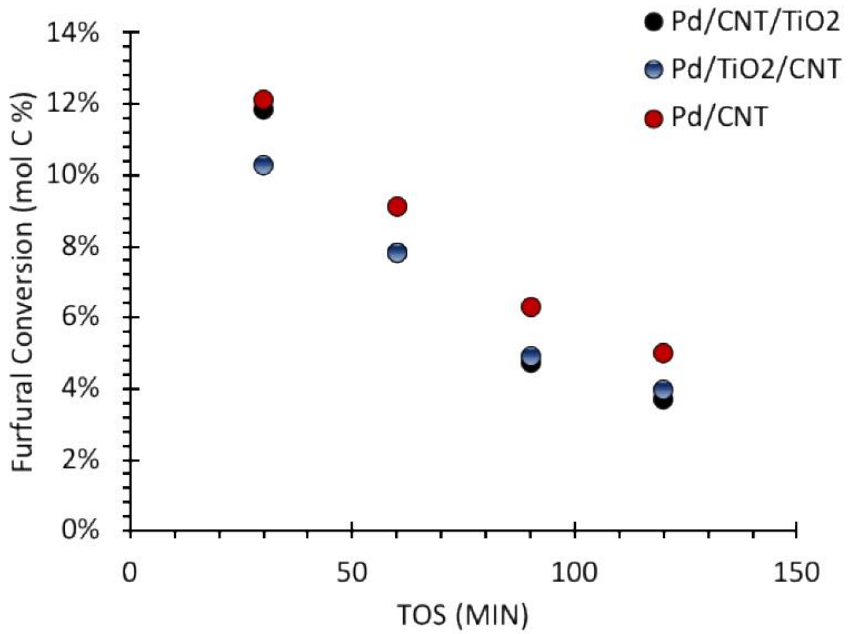


Figure S24. Furfural conversion (estimated based on disappearance of furfural) over Pd and TiO2 catalysts supported on CNTs. T= 400 ºC, P = 1 atm, under atmospheric H_2 flow.

Samples	Mo^{4+}		Mo^{5+}		Mo^{6+}	
*	$Mo3d_{5/2}$	$Mo3d_{3/2}$	$Mo3d_{5/2}$	$Mo3d_{3/2}$	$Mo3d_{5/2}$	$Mo3d_{3/2}$
MoO_3/CNT (Calcined)	--	--	231.06	234.19	232.9	236.10
MoO_3 (commercial)	--	--	231.67	234.80	233.31	236.46
MoO_2 (commercial)	229.91	233.04	232.08	235.21	233.56	236.69

Table S4. Binding energies of Mo 3d doublet for $Mo^{4+,}$ Mo^{5+}, and Mo^{6+} as determined by XPS characterization.

XPS results for calcined MoO_3/CNTs were compared with commercial MoO_2 and MoO_3 to evaluate if Mo^{0+} species were fully oxidized to Mo^{6+}, which is the oxidation state desired as the initial state of the catalyst. During deoxygenation chemistry, Mo^{4+} species can radically reduce activity and increase coke production. **Figure S20a** shows that the deposited material has been fully oxidized to Mo^{5+} and Mo^{6+}. **Table S4** indicates the binding energies of Mo 3d doublet for Mo^{4+}, Mo^{5+}, and Mo^{6+} for all three samples.

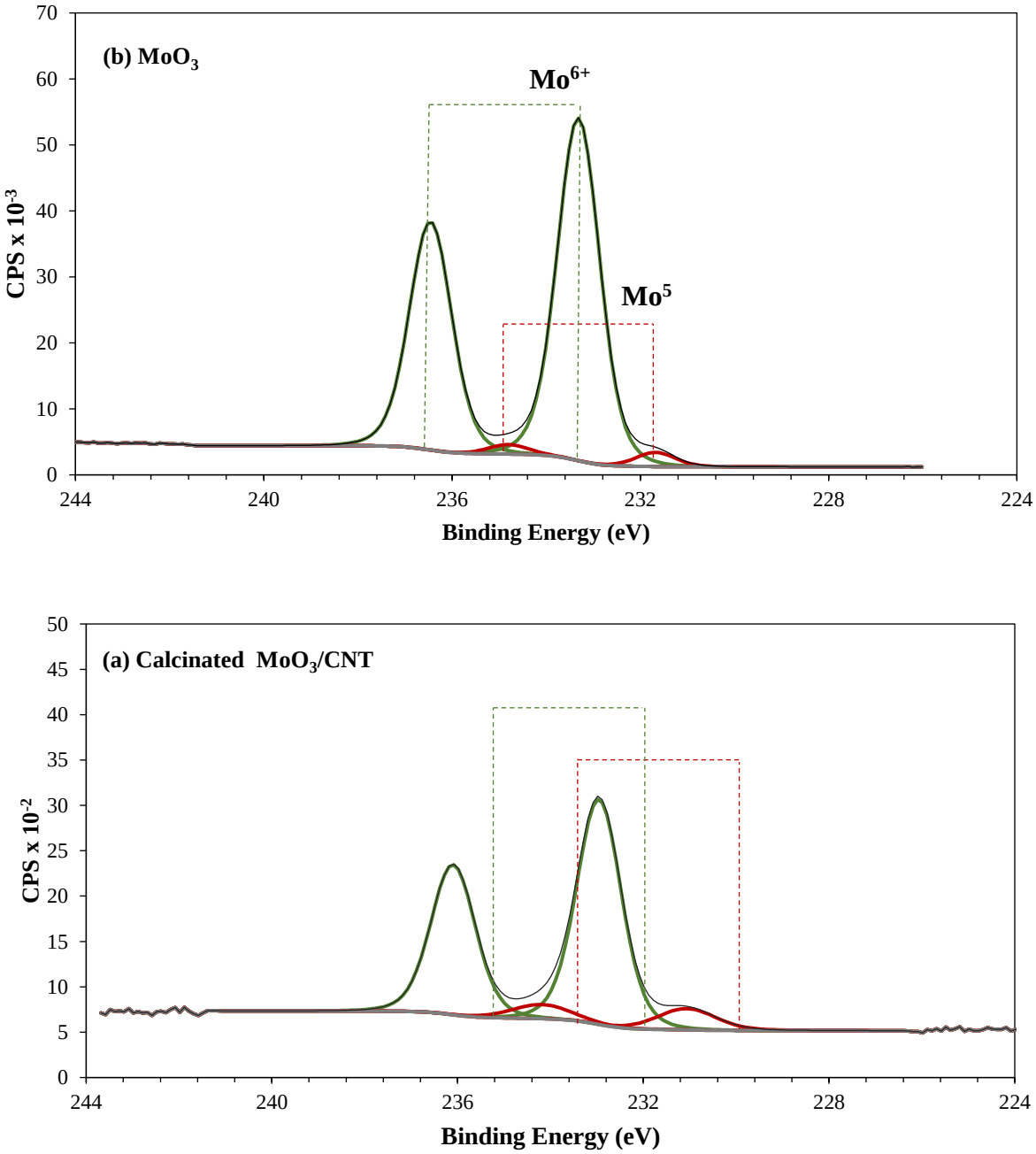


Figure S25. XPS results for (a) calcined MoO_3/CNT, and (b) MoO_3. The calcination for MoO_3/CNT was done for 1 hour at 400 °C.

	ICP-MS (wt %)	QCM (wt%)	EDS (wt%)	
Sample	Pt	Mo	Pt	Mo
$Pt/CNT/MoO_3$	0.169	3.40	0.1-0.2	1.8-4.2
$Pt/MoO_3/CNT$	-----	3.41	0.1-0.2	1.8-4.2

Table S5. Weight percentages of all deposited metals on $Pt/CNT/MoO_3$ and $Pt/MoO_3/CNT$.

The loadings of Mo were calculated by using a quartz crystal microbalance (QCM). Since Pt is present in very low concentrations, the loading of Pt on both samples was determined using inductively coupled plasma-mass spectrometry (ICP-MS). It was not feasible to determine the Pt loading in the $Pt/MoO_3/CNT$ sample due to the encapsulation of Mo-Pt caused by the high temperature utilized during the CNTs ashing process, which is necessary for sample digestion.

To verify the metal loading on the samples, we used energy-dispersive X-ray spectroscopy (EDS). To account for the uncertainty of this technique, a range of metal loading is reported instead of a specific value. This range represents the possible values the instrument detected, accounting for the instrument's margin of error or sensitivity limitations. **Table S5** reports the results obtained with EDS for both samples. Overall, EDS confirms that the Pt loading for both samples is in the same order of magnitude.

APPENDIX A5. Supporting information for chapter V: Vapor-phase ring rearrangement of furfural to cyclic over Ru/TiO_2 catalyst.

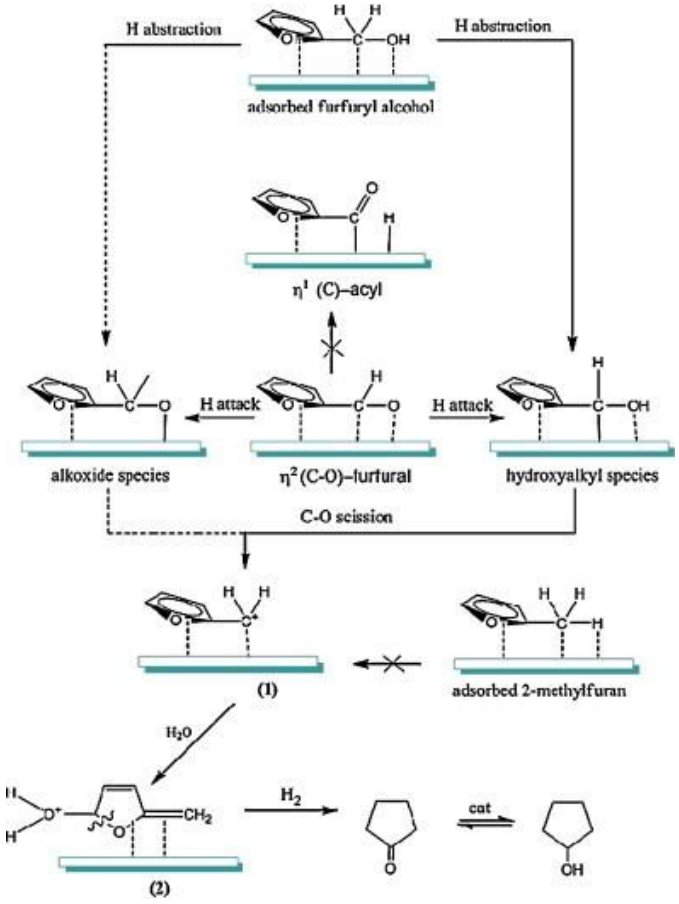


Figure S26. Proposed reaction mechanism for the furan ring rearrangement to cyclopentanone.